THÈSE

En vue de l'obtention du

DOCTORAT DE L'UNIVERSITÉ DE TOULOUSE

Délivré par :

Institut National Polytechnique de Toulouse (Toulouse INP)

Discipline ou spécialité :

Dynamique des fluides

Présentée et soutenue par :

M. MATTHIEU QUEGUINEUR

le vendredi 26 juin 2020

Titre :

Stability and control of unsteady phenomena in rotor/stator cavities using Large Eddy Simulation.

Ecole doctorale :

Mécanique, Energétique, Génie civil, Procédés (MEGeP)

Unité de recherche :

Centre Européen de Recherche et Formation Avancées en Calcul Scientifique (CERFACS)

Directeur(s) de Thèse :

M. LAURENT GICQUEL
M. GABRIEL STAFFELBACH

Rapporteurs :

M. LUTZ LESSHAFFT, ECOLE POLYTECHNIQUE PALAISEAU
Mme FRANCOISE BATAILLE, UNIVERSITE DE PERPIGNAN

Membre(s) du jury :

M. FRANCK NICOUD, UNIVERSITE DE MONTPELLIER, Président
M. GABRIEL STAFFELBACH, CERFACS, Membre
M. LAURENT GICQUEL, CERFACS, Membre
M. PATRICE LE GAL, AIX-MARSEILLE UNIVERSITE, Membre

Résumé

Les phénomènes instationnaires dans les cavités de types rotor/stator sont connus pour être la source de dangereuses vibrations dans les turbopompes spatiales. Bien que plusieurs mesures palliatives aient été prises en comptes durant les phases de conception, des campagnes d'essais ont mis en évidence de fortes oscillations des écoulements internes pouvant menacer certains composants mécaniques ainsi que le moteur cryogénique des lanceurs. Aujourd'hui, l'origine de ces instabilités d'écoulement, connues sous le nom de « phénomène de bandes de pression », est peu comprise et difficile à prédire numériquement. L'objectif principal de cette thèse est d'analyser les mécanismes physiques de ce phénomène afin d'apporter des solutions techniques pour le contrôler. Pour répondre à cette problématique, deux types de configuration sont étudiés: une cavité annulaire académique de type rotor/stator et une cavité réelle de turbopompe spatiale.

Plus largement et d'un point de vue historique, Les couches limites tournantes dans ces cavités sont connues pour être 3D et réceptives à plusieurs types d'instabilités prenant entre autre la forme de spirales ou d'anneaux. Les simulations basées sur la moyenne de Reynolds (RANS) ont par le passé échoué à prédire ce type d'écoulement. Cependant, les Simulations aux Grandes Echelles (SGE) se sont avérées être une alternative efficace à ce problème et sont donc été utilisées tout au long de cette thèse. Des Densités Spectrales de Puissance (DSP) ainsi que des Décompositions modales dynamiques (DMD) appliqués aux résultats SGE, ont permis de montrer que le phénomène de bandes de pression est visible également dans une cavité annulaire de type académique et composé de trois modes dictant toute la dynamique du système. Afin d'établir l'organisation de ces modes et leurs possibles interactions, une nouvelle méthode appelée Dynamic Mode Tracking/Control (DMT/DMTC) a été proposée durant cette thèse. Basée sur des filtres temporels, la DMT est construite pour extraire des structures cohérentes pour une ou plusieurs fréquence(s) donnée(s) dans une simulation SGE. De plus, en ajoutant un terme de relaxation dans les équations de Navier-Stokes couplées avec la DMT, sa variante appelée DMTC permet de contrôler et de suivre en temps réelle un ou plusieurs modes et donc de pouvoir analyser de possibles interactions. Appliqué à la cavité académique annulaire, cette méthode a permis de montrer que le mode basse fréquence est généré dans l'écoulement par le mode dominant du système. Pour aller plus loin, des analyses de stabilité linéaire de type global (GLSA), connues pour permettre d'étudier des écoulements instables, sont effectuées sur la cavité académique. Grâce à des méthodes adjointes, la GLSA a permis de mettre en avant l'origine spatiale de chacun des trois modes et de montrer que le mode basse fréquence et le mode dominant sont générés dans la couche limite du stator ce qui valide les résultats obtenus par DMTC. Enfin et afin de mettre en place des stratégies de contrôle, la sensibilité à la modification de l'écoulement de base, obtenue par GLSA, est analysée. L'objectif est d'identifier la région à modifier pour stabiliser un mode donné ou décaler sa fréquence. Appliqué au cas académique, il est montré que contrairement à la plupart des études dans la littérature, contrôler la couche limite du stator est le moyen le plus efficace de supprimer le phénomène de bandes de pression à travers des injections/aspirations. En rassemblant toutes le études précédentes, la SGE permet de valider notre compréhension des phénomènes et d'illuster l'efficacité des stratégies de contrôle mises en place sur le cas académique pour des amplitudes d'aspiration très basses. Pour finir, le phénomène de bandes de pression est analysé dans une cavité de turbopompe spatiale.

En particulier, la sensibilité de ce phénomène aux changements géométriques est abordée à travers deux configurations: une première sans les aubes du stator de la turbopompe et une deuxième avec. Bien que les aubes génèrent un écoulement complexe notamment avec la présence de chocs, des fréquences similaires de fluctuation de pression sont retrouvées dans les deux configurations avec cependant des nombres azimutaux caractéristiques différents. En se basant sur les études faites sur la cavité académique, une version adaptée de GLSA pour la dynamique non-linéaire de la turbopompe permet de mettre en avant que malgré que le phénomène de bandes pression soit particulièrement présent dans l'écoulement principal (veine de la turbopompe), la source de ces modes se situe dans les cavités inférieures entre le rotor et le stator. De plus les résultats de GLSA mettent en avant que deux moyens de contrôle pourraient être appliqués pour supprimer le phénomène de bandes de pression dans ce cas industriel: modifier le joint d'étanchéité ou modifier la fuite présente autour du moyeu.

Abstract

Unsteady phenomena in rotor/stator cavity are well known to be the source of dangerous vibrations in space turbopump. Even though many palliative measures have been taken during their design, experimental campaigns often reveal high flow oscillations that can jeopardize turbomachinery components and even the rocket engine. Today, the origin of such flow instabilities usually called 'pressure band phenomenon' is not well understood and difficult to predict numerically. The main goal of this thesis is to investigate such phenomenon mechanism to find technical solutions so as to control it. This problematic is addressed here trough two types of configuration: an academic smooth rotor/stator cavity and a space turbopump cavity.

When it comes to cavity flows, their rotating boundary layers are known to be three dimensional and receptive to several instabilities taking the form of spirals or annuli. Reynolds Averaged Navier-Stokes Simulations (RANS) failed in the past to predict such unsteady systems. However, Large Eddy Simulation (LES) proved to be a relevant alternative in many similar applications and is therefore chosen for the present work. Using Power Spectral Analysis (PSD) and Dynamic Mode Decomposition (DMD) on LES predictions, one shows that the pressure band phenomenon is retrieved in an annular smooth rotor/stator cavity and it is composed of three modes driving all the system dynamics. To investigate these mode organization and their possible interactions, a new tool called Dynamic Mode Tracking /Control (DMT/DMTC) is introduced. Based on temporal filters, DMT is constructed so as to extract "on-the-fly" flow coherent structures with a given frequency on the basis of LES. Furthermore, augmenting the Navier-Stokes equations with a relaxation term coupled to DMT, DMTC allows to control and follow the evolution of a controlled mode as well as non controlled ones and thereby observe interactions. This strategy after validation is applied to the annular rotating cavity and shows that the low frequency mode is generated by the dominant mode of the system. To go further, Global Linear Stability Analysis (GLSA), a well known approach to study oscillatory flows, is used on the academic cavity. Augmented with adjoint methods, GLSA sheds some light on all mode origins and points out that the low frequency and dominant modes are coming from the stationary boundary layer. In order to set up control strategies, the GLSA framework is further developed introducing the concept of the sensitivity to base flow modifications which gives the location where the flow should be modified if one wants to stabilize or at least shift a frequency mode. Applied to the academic cavity, one shows that contrary to most studies in the literature, controlling the stator boundary layer is the more efficient way to damp the pressure band phenomenon through suction/injection devices. Finally, gathering all the previous understanding of this flow, the LES framework enables to validate the control strategies proposed and to stabilize the pressure band phenomenon for very low suction amplitudes. To finish, the pressure band phenomenon is analyzed in real space turbompump cavities. In particular, the sensitivity of this specific phenomenon to geometry changes is investigated through two configurations: one without and one with the blades of the stator of the turbopump. Even though the introduction of the blades in the LES creates a more complex flow with the presence of shocks, similar pressure fluctuation spectra are retrieved in both configurations but with azimuthal wavenumber modes that are shifted. Following the studies on the academic cavity, an adapted GLSA to the non-linear dynamics of the turbopump enables to point out that even though the pressure band phenomenon modes are particularly marked in the mainstream of the system, the source of these modes is located in the subcavity in the rotor-stator wheel space. In particular, GLSA results indicate that two possible ways to control the phenomenon are possible: modifying the flow around the seal rim and or modifying the leak around the hub.

Contents

Chapter 1

Foreword

Contents

This chapter introduces the context of this PhD work which is born from a collaboration between the CNES (Centre National des Etudes Spatiales) and Ariane Group. Indeed, space industry has been recently shaken by new objectives and visions, especially with the arrival of low orbit satellites and constellations. To answer this new demand, actors from private sector have emerged and changed the rules forcing the well implemented launcher manufacturers to evolve and optimize their existing systems. This PhD participates to this technology optimization by focusing on a specific phenomenon called "pressure bands" apt to appear in the turbopumps of rocket engines. Indeed, this phenomenon characterized by self-sustained oscillations of the flow can be particularly dangerous to the integrity of the launcher and the payload. To introduce this subject, a detailed description of space industry is provided along with the more recent evolutions. Finally the configuration of interest to this PhD work, i.e the rocket engine turbopumps, are introduced along with its working principle and the different unsteady phenomena that can occur in such a device.

1.1 Space industry

1.1.1 Market

Since the time when Youri Gargarine was sent around earth in april 1961, space industry has evolved with new objectives and visions. At first, security and military were the two subjects on the table that motivated the two dominant and active countries in the field: URSS and US. In fact, as stated by Barbaroux (2016), two thirds of all the satellites launched between 1957 and 2011 have been under military, governmental or spatial agency decisions. However, as shown in Fig. 1.1, the market has drastically changed in the last decades. Due to the increasing demand of ultra high-speed broadband services, commercial and telecommunication satellites are now the most common satellites put into orbit around Earth. In this specific context, constellation satellites (smallstas) provide a promising solution to the increasing demand. These particular architecture systems are however forcing launcher manufacturers to change their strategies and methods along with parts of their launchers and their conception. In parallel, new actors in the field have taken advantages of this high and new demand. Indeed, when governments are focused on exploration, new fast developing private companies of billionaires tend to create new rockets targeting human travel and space tourism. This competition, also known as 'billionnaire space race', began with Richard Branson who developed new ideas and new launchers but also promised the beginning of space tourism and space travel. In order to develop their own technologies and business, these new actors have also entered the market of commercial satellites. In particular, Elon musk has clearly been the game-changer by announcing a 30% reduction of the actual launch cost. Indeed, he forced the well-established companies to change their strategies and to optimize more and more their existing launchers. Apart from the billionaire companies, the industry of low orbit launchers and small payloads (under 500kg) started also to take an important share of the market, especially with the arrival of constellation satellites. Northrop Grumman Innovation Systems,Virgin Orbit or Rocket lab are examples of small companies that are now dominating this market sector due to their low cost launchers.

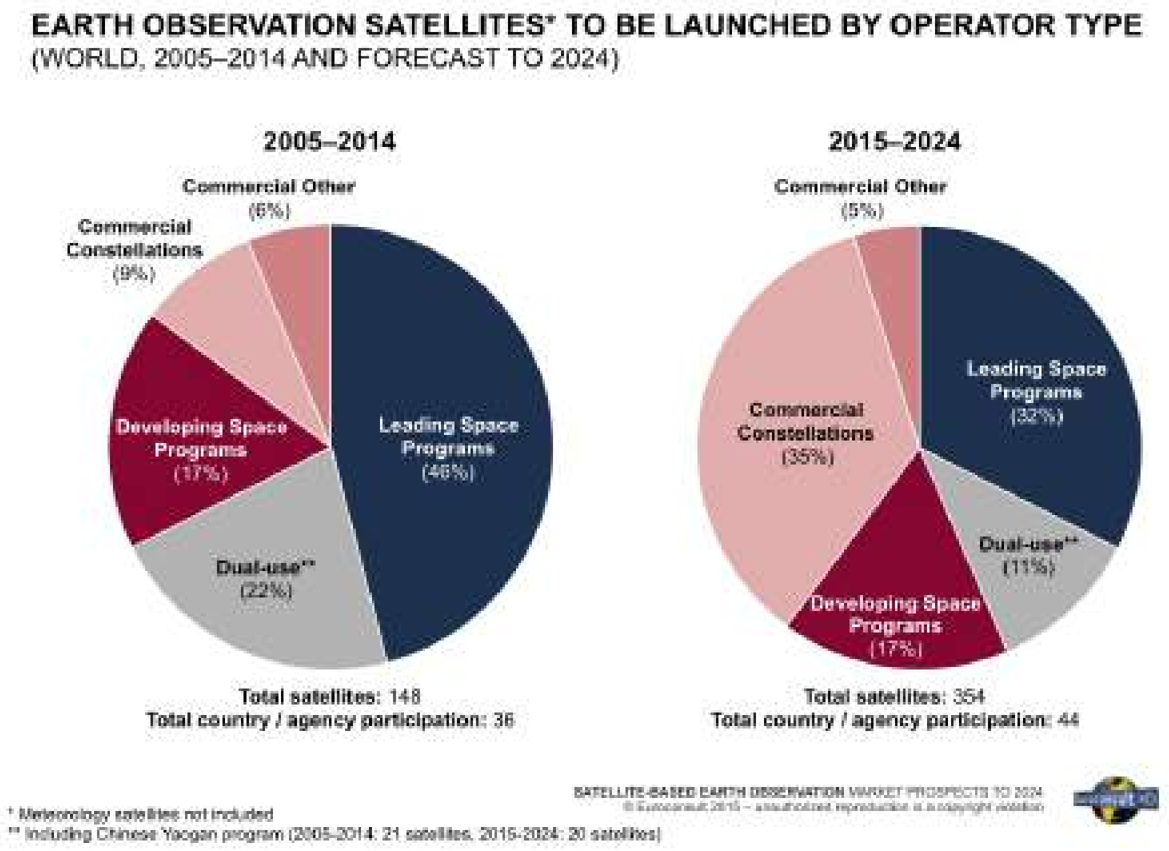

Figure 1.1 – Space market trends: Earth Observation satellites launched in 2005-2014 and prospects for 2015-2024, Source: Euroconsult

1.1.2 Launcher technology evolution

Space conquest has always been the biggest source of new technologies. Even nowadays, a large part of the general public still doesn't understand the primordial benefits of space exploration for both the future and our technology development on Earth. History has shown that projects like Apollo with the moon landing or the first satellite Spoutnik in 1957 were the source of many innovations that changed our lyfestyle. For example[1]: the embedded system of the Apollo program was the predecessor of microcomputer that can be found in all smartphones today. Likewise, thanks to research on space fires, clothes have become far more fire-resistant. Finally astronauts, who have their health constantly followed, helped scientists find new cures on Earth.

---

[1] Space: how far have we gone – and where are we going: The Guardian

Nowadays, to stay competitive in this fast developing market, new technologies still need to be developed. The more recent and striking ones are:

- **Reusable launcher:** The first success of a resuable launcher has been achieved in November 2015 by Blue origin New Shepard rocket which is also the first vertical take-off/landing rocket to reach the Kármán line. Space X achieved the same technological exploit with an orbital rocket stage (See Fig. 1.2). In Europe, the CNES (Centre National d'Etudes Spatiales) and the German space agency (DLR) started the *Callisto* demonstrator in 2015 (Sippel & Klevanski (2004)) in collaboration with the Japanese space agency (JAXA). The purpose of this project is to conduct flight tests, develop new complex technologies and prepare cost plans for future launchers such as *Ariane 6* or *Ariane Next.*
- **Re-ignition engine**: For space engine manufacturers, re-ignition is of primary importance as it increases flexibility and allows much more complex missions. For example, to deliver supplies to the International Space Station, the ESA's Automated Transfer Vehicle (ATV), requires multiple firings of the Ariane 5 ES upper stage engine. The European engine VINCI which will equip Ariane 6, will enable to put different satellites in several orbits in geostationary orbit (GEO) instead of geostationary transfer orbit (GTO). On the other side of the Atlantic, Space X created the Merlin rocket engine re-ignitable for different purposes. The first one was to develop the first reusable launcher. Besides, their strategy was also to use the same engine for all the stages of the launcher.

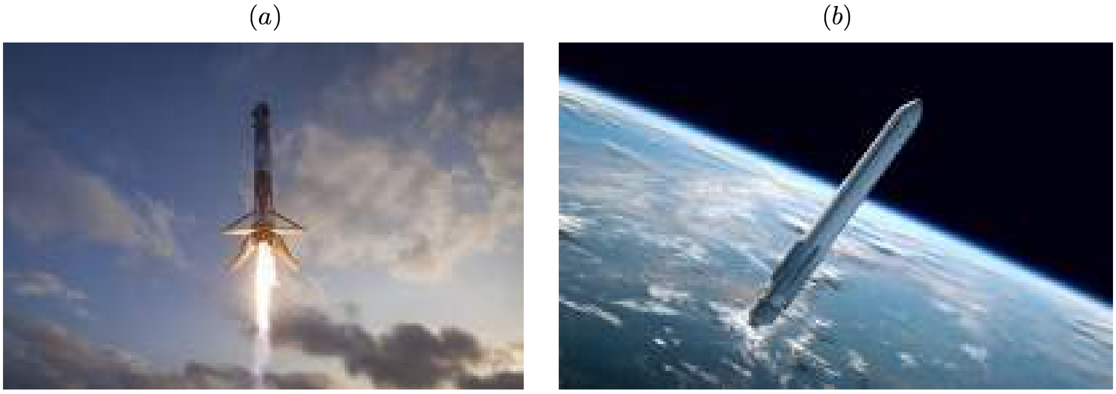

Figure 1.2 – Reusable rockects: (a) Falcon 9 of Space X and (b) Callisto demonstrator of the CNES

The next project that challenges all actors of the space industry is the promise for interplanetary travel. Mars is actually the closest planet resembling Earth in our solar system. The objective of reaching this planet mainly started with Elon Musk, helped and supported by NASA. To make this project a success, multiple new technologies will need to be developed. Among others, one can site radiation protections, advanced communication systems, cooling systems to handle high speed on long distance or advanced environmental control and life support systems for crew members. Finally, the actual engines will need to be optimized or new systems to be developed to assure long travel and a high maneuvering capabilities.

1.1.3 PhD context

Liquid propellant rocket engine

Liquid propellant rocket engine is the most common engine found in the current rockets worldwide. As shown by Fig. 1.3, its principle is to inject fuel and oxidizer at a high pressure in the combustion chamber which after fast chemical reaction results in hot gases that are ejected at high speed through a nozzle. This last specific component purpose is to turn the subsonic flow of the combustion chamber into a supersonic flow or, in other words, to turn the static pressure in dynamic pressure. Contrary to the boosters, the liquid propellant power can be controlled, and is hence used to precisely put into orbit satellites.

For analysis and design, the thrust, F, generated by a rocket engine can be approximated by;

$$F = \dot{m}v_e + (P_e - P_0)S_e, \tag{1.1.1}$$

with $\dot{m}$ the mass flow rate, v_e and P_e respectively the speed and the pressure of the gases exhausted at the nozzle exit. P_0 finally refers to the external pressure while S_e is the cross-section surface of the nozzle exit. Rocket engine performances are often defined through their specific inpulse (I_{SP}) expressed as;

$$I_{SP} = \frac{F}{g \cdot \dot{m}}, \tag{1.1.2}$$

with g the gravitation constant.

Thanks to this specific definition, one can show that the power of an engine can be controlled by the pressure of the combustion chamber or the propellant used. As a consequence, history has shown that different possible configurations can be used to feed the combustion chamber. The three main configurations also known as 'cycle' are usually applied:

- **Pressure-fed cycle** : This configuration has the simplest design. The propellants are directly pressurized in their respective tanks and are directly injected in the combustion chamber to generate thrust. Thanks to this system, quick and high efficiency reactions are possible. However, it doesn't enable to control its pressure and imposes thick structures to sustain the high constraints. This specific cycle can be found in the AJ10 hypergolic rockets family or even the Space shuttle OMS engine.

- **Gas-generator cycle:** Often referred to as open system, engines configured with this type of cycle have one or two turbopumps entrained by a turbine itself activated by a preburner. The oxidizer pump, the fuel pumps and the turbine are usually mounted on a unique shaft. The main drawback of such a configuration is the loss of the exhaust gases coming from the preburner and, due to high thermal constraints,

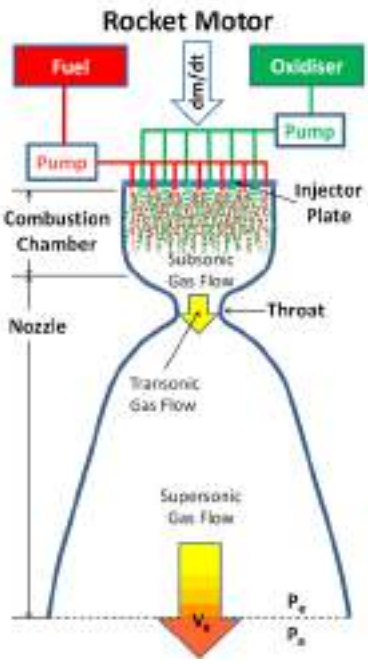

Figure 1.3 – Principle of a liquid properllant rocket engine

the difficulty to burn at an optimal equivalence ratio. This cycle can be found in Saturn V's F-1, Ariane 5's HM7B, Ariane 5's Vulcain or Falcon 9's Merlin.

- **Expander** : Contrary to the gas generator cycle, the turbine of this configuration is entrained by gases issued from the cryogenic propellant used to cool the combustion chamber. The main benefit of this system is that the turbine does not have to undergo high temperature. Advanced systems close the cycle by re-injecting the gazified cryogenic propellant in the combustion chamber to increase its pressure. This cycle can be found in Ariane 6's Vinci.
- **Staged combustion cycle**: Most known cycle, its principle is to feed each propellant pumps by multiple preburners through a rich or lean fuel combustion. This indeed enables to obtain engines with high thrust and efficiency. This cycle can be found in the BE-4 (Blue origin), RS-25 (SLS) and RD-180 (Atlas V).

Typical liquid propellant engines are presented Fig. 1.4. Two different generations can be distinguished: The ones developped before 2000 with the RD-180 (Atlas V), F-1 (Saturn V), Vulcain 2 (Ariane 5) and RS-25 (SLS) and the more recent ones like the Merlin, BE-4, Raptor and Prometheus are recent and future engines. From this presentation, one can first notice that the main difference is the fuel used by the recent engines. The choice of Methane/Oxygen (CH_4/LOx) to power a rocket engine has indeed been the subject of many studies (Burkhardt *et al.* (2004); Haidn *et al.* (2008)) and this specific mixture showed to be a good compromise between kerosene/Oxygen ($RP-1/LOx$) and Hydrogen/Oxygen (LH_2/LOx) in terms of combustion efficiency and tank weight. CH_4/LOx proved also to be the easiest to produce and store. This was the main reason why Space X created such an engine. In fact, the atmosphere of Mars being mainly composed of CO_2, it will be easier to create methane from water through electrolysis and a Sabatier process. Finally, in terms of pollution, CH_4/LOx produces carbon dioxide and water vapor which is less advantageous than the hydrogen while polluting far less than RP-1.

Even though new generation of engines have most of the time adopted a stage combustion cycle, Space X has chosen a gas generator cycle for the Merlin. As said previously, it enables to simplify the design of the engine. One can also note that the RD-180 is not a usual engine that is composed of two combustion chambers for one single turbopump. As shown in Fig. 1.4, the bigger the engine is the higher the thrust will be. However, one interest for a rocket manufacturer is first of all a thrust/weight ratio as high as possible even though it implies to add more engines on a rocket. New generation of engines such as Prometheus confirms this idea, Merlin being the most powerful of all with a ratio of 198 : 1. Efficiency is the main characteristic of an engine that is usually defined by its I_{SP}. The old generation of engines reaches the highest performances with first the RS-25 American engine closely followed by the Vulcain 2 European engine Finally, one can clearly see that new engines have been designed to have a development and production cost as low as possible. Merlin and Prometheus (in development) will be the two engines in competition in a close future due to lower cost ($1M\$$). Re-usability is to finish a factor to be taken into account and that can be defined as a cost/flights ratio but is also more difficult measure.

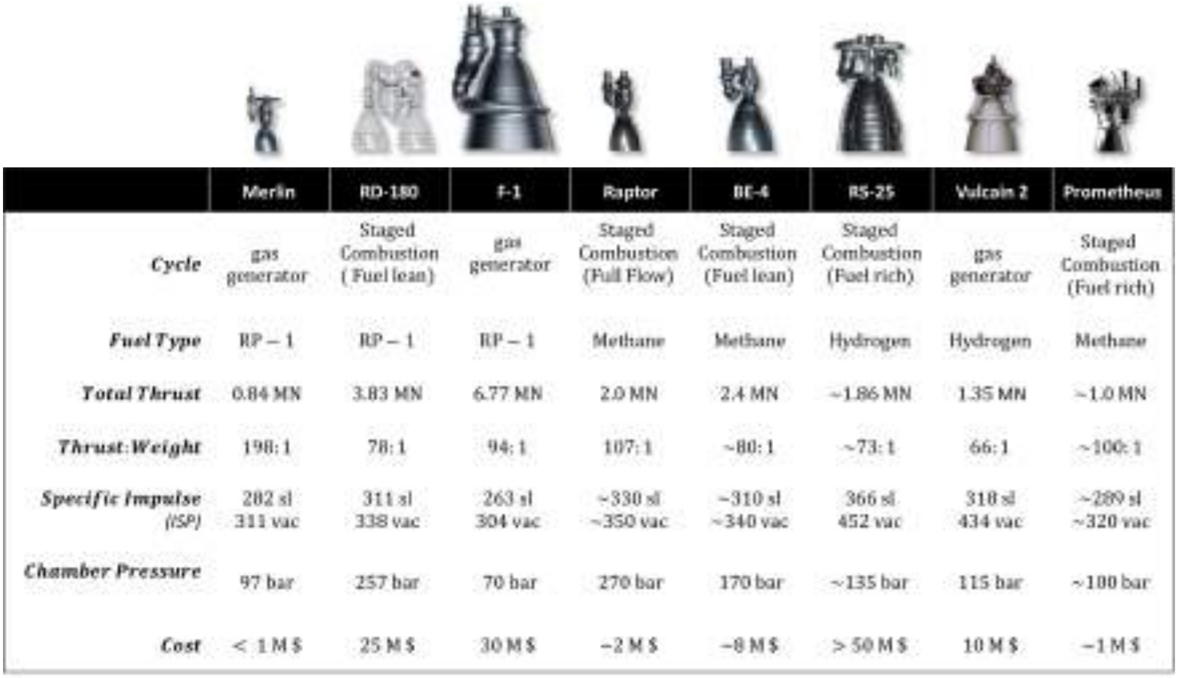

	Merlin	RD-180	F-1	Raptor	BE-4	RS-25	Vulcain 2	Prometheus
Cycle	gas generator	Staged Combustion (Fuel lean)	gas generator	Staged Combustion (Full Flow)	Staged Combustion (Fuel lean)	Staged Combustion (Fuel rich)	gas generator	Staged Combustion (Fuel rich)
Fuel Type	RP – 1	RP – 1	RP – 1	Methane	Methane	Hydrogen	Hydrogen	Methane
Total Thrust	0.84 MN	3.83 MN	6.77 MN	2.0 MN	2.4 MN	~1.86 MN	1.35 MN	~1.0 MN
Thrust:Weight	198:1	78:1	94:1	107:1	~80:1	~73:1	66:1	~100:1
Specific Impulse *(ISP)*	282 sl 311 vac	311 sl 338 vac	263 sl 304 vac	~330 sl ~350 vac	~310 sl ~340 vac	366 sl 452 vac	318 sl 434 vac	~289 sl ~320 vac
Chamber Pressure	97 bar	257 bar	70 bar	270 bar	170 bar	~135 bar	115 bar	~100 bar
Cost	< 1 M $	25 M $	30 M $	~2 M $	~8 M $	> 50 M $	10 M $	~1 M $

Figure 1.4 – Sum up main engines in the world

Turbopumps

The components of interest to this PhD work are the turbopumps. As shown in the previous section this turbomachinery is of first importance for rocket engines to generate high thrust. These systems are composed of two main components: a rotodynamic pump and a driving gas turbine, usually both mounted on the same shaft or sometimes geared together. Its principle is to produce a high-pressure fluid to feed the combustion chamber. In 1942, this new technology appeared as a revolution for propulsion devices. In fact, rockets of this time were suddenly able to sustain a maximum velocity of 1600 m/s thanks to these systems. Vulcain 2 developed by ArianeGroup and headed by the French space agency (CNES) was designed with two types of turbopumps: the TPO for the liquid oxygen LO_2 (see example Fig. 1.5) and a TPH for the liquid hydrogen LH_2. The Vulcain 2 TPH turbine is a two-staged supersonic/transonic impulse type turbine, working in a gas generator cycle.

Figure 1.5 – Example of LOx turbopump mounted on the japanese rocket engine LE-7A

Vibrations have been a source of many problems in turbomachinery design and can come from many parts of the system like the turbine disks, cavities, shafts, blades, etc. A critical speed is always defined to avoid a resonance phenomenon between a natural frequency of a component of the system and the frequency of the rotating shaft. At this critical state, a slight unbalance can be amplified and impact the pump system, the bearing supports or create other damages. To stay versatile, operation points are therefore higher or lower than the critical speed. Note also that optimizing the system by taking for example stiff bearing supports, rigid bearing or greater shaft diameters can increase this critical speed but will produce unwanted mass. Furthermore, many excitations other than the ones related to the rotating parts can appear through unsteady flow fluctuations (D'Agostino *et al.* (2017)). For example, as described in Sutton & Seifert (1950) or Hengli & Zuoyi (2002), these systems can be subject to oscillating pressure loads, cavitation, rotating stall instabilities, surge upstream shocks, fluttering, pogo or any other pressure-wave vibration that can then couple and interact with the structure.

"Pressure band phenomenon"

Experimental campaigns have often evidenced undetermined unsteady phenomena around the cavity of the first stage of turbopump turbines. The one of interest to this PhD, usually called *'Pressure band phenomenon'*, corresponds to oscillations that are characterized by multiple dominant frequencies which can be measured everywhere in the cavity. Those self-sustained oscillatory motions of the fluid can become dangerous and if uncontrolled, impact the structural integrity of the engine. This phenomenon has the particularity to be very sensitive to geometry changes, appears for particular operating points and is also sensitive to thermal conditions of the turbine cavities.

The frequencies linked to this phenomenon could not be retrieved through RANS (Reynolds Average Navier Stokes equations) simulations due to the high unsteadiness of the flow. In fact, for the highly turbulent flow presents in space turbopumps, the mean flow can be of the order as the unsteady perturbations. Time dependent simulations like URANS (Unsteady Reynolds Average Navier Stokes equations) or LES (Large Eddy Simulations) are still too expensive for industry but proved to be best to solution to capture complex and highly unsteady phenomena. The hosting laboratory of this PhD work, CERFACS, has been hence chosen for its expertise in the domain and especially LES.

The *'Pressure band phenomenon'* has been first studied at CERFACS by Bridel-Bertomeu during his PhD Bridel-Bertomeu (2016). His work was organized in two steps. The first one was focused on academic rotating closed cavities for which he was able to retrieve the pressure band phenomenon. In fact, he showed through LES that in a case of an annular cavity, three dominant frequencies could be distinguished through Power Spectral Density (PSD) and were present everywhere in the domain. He confirmed the 3D features of these modes and was able to demonstrate that almost all the dynamics of the annular flow was dictated by the sum of those three modes. Specific structures were pointed out in the flow boundary layers that are common to the infinite rotating disk boundary layer model. Small and high cylindrical rotor stator cavity were also studied and have been the fruit of a paper (Bridel-Bertomeu *et al.* (2017*a*)). To improve our understanding of these modes' origin, Linear Stability Analyses (LSA) were then used and a solver called *AVLP* was developed at this occasion. In particular, the 'wavemaker' of each mode was spatially evidenced. In the case of the industrial turbopump, LES showed to retrieve the specific modes behind 'the pressure band' phenomenon (Bridel-Bertomeu *et al.* (2017*b*)). Once again, modal decomposition enabled to compute their complex structures in the different cavities of the system and their sensitivity to geometry changes and thermal conditions was finally confirmed.

The current PhD work main objectives is to extend the investigation realized on academic rotor/stator cavities through the conjuction use of LES and Linear Stability Analysis. In particular, a global stability approach needs to be developed to deeper investigate the modes' settlement, organization and interactions. Control strategies for such problems also need to be proposed in order to suppress the pressure band phenomenon. From the industrial point of view, the impact of stator blades on the pressure band phenomenon still needs to be characterized. Finally, new linear stability analysis tools are needed to analyse the highly turbulent and highly unsteady turbopump cavities so as to identify the origin of these oscillations and propose relevant control strategies.

1.2 Overview of this thesis

The present PhD work is divided in three main parts and focuses on the pressure band phenomenon in two types of rotating cavities: academic and industrial. The two first parts of this manuscript are dedicated to academic cavities with a first part on their dynamics prediction through Large Eddy Simulation and a second part focused on linear stability analysis and control. The last part then deals with a space turbopump and gathers all previous founding. The following items summarize the main elements of this document that were obtained through the course of this research work of three years and detail the chapters constituting the different parts of the present PhD:

Chap 1, Foreword:

Space industry has recently evolved with new objectives in an explosive market. Telecommunication and commercial satellites' high demand are forcing the launcher manufacturers to optimize their technologies or develop new systems. In this context, the main type of liquid engines composing the market are first compared in this chapter. In order to optimize a rocket engine, unsteady phenomena occurring in space turbopumps and especially in turbine cavities need to be precisely investigated. Flow oscillations, besides being able to reduce engine performances, can indeed be very dangerous and jeopardize the integrity of turbomachinery parts. The "pressure band phenomenon" corresponding to self-sustained motions of the flow is particularly discussed in this chapter and will be investigated all along this PhD work.

PART 1, Large Eddy Simulation of enclosed rotor/stator cavity:

Chap 2, Flow dynamics of academic rotor/stator cavity through Large Eddy Simulations:

This specific chapter focuses on the structures appearing in smooth rotor/stator cavities. In particular, the unstable rotating boundary layers are discussed. Although, the main configuration of interest to this PhD work is an annular enclosed rotor/stator cavity due to its relevance with real turbomachinery, a cylindrical cavity is also studied here to highlight the shaft impact on the dynamics of such systems. Following Bridel-Bertomeu (2016), the Large Eddy Simulation (LES) framework is used to extract the pressure band phenomenon modes. This numerical tool indeed enables to simulate complex flows with highly unsteady phenomena. The mean flows obtained are first analyzed and good agreement is found with configurations coming from experimental studies with close characteristics. In conjunction with Dynamic Mode Decomposition (DMD) and

Power Spectral Density (PSD), LES shows that three specific modes with distinct azimuthal wave numbers $m = 0$ (annular shape), $m = 12$ (12-arms spiral) and $m = 29$ (29-arms spiral) are demonstrated as the main drivers of the global annular rotor/stator cavity. The cylindrical cavity activity is found on its side to synchronize around a unique frequency mode composed of multiple azimuthal wavenumbers.

Chap 3, Mode dominance and interactions:

In the previous chapter, Large Eddy Simulation (LES) demonstrated that three modes defined the pressure band phenomenon in an annular rotor/stator cavity. However, the sources and the mechanisms of this complex flow could not be identified. In fact, no clear understanding can be found in the literature on how can one control a multi-frequency phenomenon and more specifically how these modes effectively interact. In this context, a new method called Dynamic Mode Tracking (DMT) aiming at tracking dynamically modes or flow features thanks to time filters is proposed. Contrary to classical flow feature analyses, DMT has indeed the benefit to be easy to implement in a Navier-Stokes solver while giving a direct possibility to visualize a mode evolution over time. By computing a mode "on-the-fly", DMT furthermore offers gain in memory and CPU time. Thanks to these properties, a second method called Dynamic Mode Tracking and Control (DMTC) corresponding to a mode artificial controller can also be easily created using a relaxation method. A complete set of test cases and sensitivities of these new tools is given in this chapter and compared to the more classical "post-mortem" method like DMD. In the annular cavity context, the link between modes $m = 29$ and $m = 12$ observed in Chap. 2 needed more understanding to identify which mode is to be tempered with in priority. To do so, the DMTC method which enables the control of individual modes is used. As a result, damping mode $m = 12$ proves to have no effect on mode $m = 29$. At the opposite, suppressing mode $m = 29$ induces mode $m = 12$ to be progressively attenuated, signifying that it can not live without mode $m = 29$. By analyzing the response of the $m = 0$ annular mode to the two cases, one can show that this mode is independent of the two other ones. At the end, this study provides the information that to stabilize the whole cavity, controlling mode $m = 29$ will be the most efficient approach.

PART 2, Global Stability analysis of an enclosed rotor/stator cavity

Chap 4, Mode identification and stability analyses:

The self-sustained oscillations driving the above discussed simple rotating cavities proved to be originating from complex phenomenon whose origins stay almost unknown. To study these instabilities in more details, linear stability analysis framework is applied in this chapter to investigate the becoming of local disturbances. To do so, two types of approach are developed and confronted: local and global stability analyses. Results show that the two methods complement one another but also point out the limits of the local approach. In fact, this latter provides the location of absolute instabilities (primordial to generate a global mode) but fails to retrieve the complex mode of the cylindrical cavity or the $m = 0$ mode of the annular cavity. On the contrary, the global approach enables to retrieve with good agreement the modes obtained by DMD not only in terms of frequency but also their spatial distribution. Adjoint global analysis also enables finding the origin of each mode while giving a description of each mode mechanisms by use of structural sensitivity analysis. Finally, the instability mechanisms of a cylindrical cavity is compared to the annular ones and the role of the shaft on the complex dynamics of the annular cavity is provided.

Chap 5, Control of a rotor/stator cavity flow:

The previous chapters shed some light on the mode interactions and indicated a strategy to control the multi frequency pressure band phenomenon in an annular rotor/stator cavity. However, no physical controller could be derived for stabilizing this system. To overcome this problem, the global stability framework is further developed addressing the notions of sensitivity to base flow modifications. Indeed, contrary to the wavemaker obtained through structural sensitivity analysis, the sensitivity to base flow modification enables to point out the exact location where a given mode should be modified to shift its frequency or growth rate. After a brief introduction of the rotating flow control studies, the principle and the steps to obtain the base flow sensitivity are detailed. Applied to the annular cavity, injection and suction show to be relevant solutions to suppress the pressure band phenomenon. In fact and contrary to the literature where the rotating disk is usually controlled, the sensitivity analysis preconizes to position these passive controllers in the stator boundary layer. Indeed, one shows that for very low suction axial amplitudes, the overall instabilities in the cavity can be damped. Care is however recommended since it is also shown that increasing the controller amplitudes too much results in a new limit cycle with frequencies and amplification rates that shift. These new limit cycles can finally be explained through the stability analysis of the controlled cavity which are shown to be unstable.

PART 3, Investigation of the unsteady phenomena in a space turbopump turbine

Chap 6, Industrial application: Turbine cavities of a rocket engine turbopump:

This chapter focuses on the study of the flow in a space turbopump turbine stage. The Large Eddy Simulation (LES) framework is hence first applied to this complex geometry to extract the coherent structures coming from the three dimensional boundary layers. Even though these boundary layers are far more turbulent than the academic annular case, similar velocity profiles can be highlighted. Furthermore, the 'pressure bands' captured in the academic cavities are also observed here in this industrial case where a high Reynolds number and a complex geometry affect the dynamics of the system. Known to be very sensitive to geometry parameters, two different configurations are studied in this chapter: **Case 1** corresponds to the turbine stream channel and the rotor/stator cavity with smooths disks while **Case 2** also takes into account the stator blades present in the turbine stream channel. Power Spectral Density (PSD) on pressure enables first to unveil the modes polluting the whole system and it is shown that the blades increase directly the overall pressure fluctuation level of the retrieved instabilities. In a second time, the 3D spatial distribution of the modes are studied thanks to Dynamic Mode Decomposition (DMD) and Dynamic Mode Tracking (DMT). Equivalently to the academic problems, DMD is found in a good agreement with PSDs and DMT both capturing the multi-azimuthal wave number modes appearing in the low cavities. Finally, to shed some light on the flow dynamics, the global stability framework of Chap. 4 is resumed to highlight the source of these self-sustained oscillations of the flow. In particular receptivity and structural sensitivity analyses tend to preconize two possible ways to control this limit-cycle: modifying the flow around the seal rim and or modify the leak around the hub.

Part I

Large Eddy Simulation of enclosed rotor/Stator cavity

Chapter 2

Flow dynamics in an academic rotor/stator cavity by use of Large Eddy Simulations

Contents

Self-sustained oscillations of rotor/stator cavity flows are well known to industry. In aeronautical engines, this unsteady phenomenon can be very dangerous and jeopardize the structural integrity of the entire system by damaging turbomachinery components or turbopumps in the context of space applications. Today, the origin of such a flow instability and resulting limit-cycle is not well understood and is still difficult to predict numerically. The present investigation purpose is to shed some light on this phenomenon relying on numerical simulations. Large Eddy Simulations (LES) indeed showed in previous studies to be a good candidate to simulate such unsteady flows and is applied here to two different rotor/stator academic cavities: an annular and a cylindrical one. The annular cavity is the closest configuration to the space turbopump cavities and will be of main interest to this PhD. However, the cylindrical cavity enables to give more insight on the impact of the hub on the dynamics of the system. For both cases, the mean flow resulting from LES is found in good agreement with the literature. Furthermore, the 'pressure band phenomenon' corresponding to the modal content of the system is well captured through Power Spectral Density (PSD) and Dynamic Mode Decomposition (DMD). In case of the annular cavity, three modes are found to drive totally the flow. For the cylindrical cavity, the whole dynamic is synchronized around a unique frequency composed of multiple azimuthal wave number modes differing with the radius.

2.1 State-of-the-art of enclosed cavity flows

Rotating enclosed cavities raised a new interest in the last decades mostly because of the many industrial applications relying in these flows: centrifugal separator process, computer storage devices, turbomachinery, etc. These complex systems are also found to be representative of the turbompumps presented in Chap. 6 and have been the source of many experimental and theoretical studies (Schouveiler (2001); Bridel-Bertomeu *et al.* (2016);Séverac *et al.* (2007)). In the context of this PhD work, simple enclosed rotor/stator cavities with annular and cylindrical shapes will be first particularly analyzed (see Fig. 2.1). To discover the variety of flows and structures that can be found in this kind of systems, interested readers can refer to Owen & Rogers (1989) These flows are indeed a source of complex phenomena and confinement has quickly been identified as the key driver affecting the dynamics of enclosed cavities compared to simple infinite disks (Healey (2007),Littell & Eaton (1994)). In fact, two geometrical features can distort and generate different disturbances in such flows: finite radius configurations and end walls (shroud and/or hub for annular cavity). Indeed, finite disk lenght is one of the form of confinement that impacts the usual parallel flow assumption introduced for infinite disk studies. This also makes the self-similarty solution of Batchelor (1951) or Stewartson (1953) inconsistent especially for high Reynolds numbers (Viazzo *et al.* (2012)) even though there may be qualitative resemblance far from the end walls as shown by Brady & Durlofsky (1987) or Lopez (1998). Contrarily to infinite disks, outward travelling modes are expected but so do inward travelling disturbances appearing at the ends of the disks.

In that respect, Appelquist *et al.* (2015) noted that if the radius of the finite disk r_{max} results in a larger local Reynold number $Re_r = r/h$ than the critical local Reynolds number Re_{r_c}, the frequency and shape of the global mode will be directly imposed by the boundary condition at r_{max}. This was confirmed experimentally by Pier (2013). Likewise, in the particular case of an annular cavity, if the central hub local Reynolds number is greater than the critical Reynolds number then the stator instability will be transmitted to the rotor boundary layer.

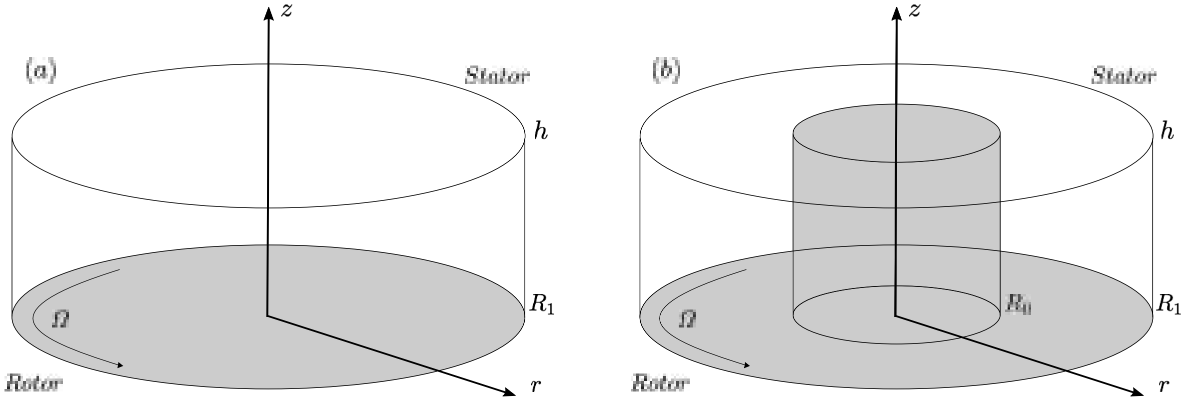

Figure 2.1 – Academic enclosed rotor/stator cavities with a cylindrical shape in *(a)* and an annular shape in *(b)*. The rotating part of both configurations are filled in grey.

To introduce the different regimes potentially present in an annular or cylindrical rotor/stator cavity, characteristic numbers need first to be defined. To do so, one uses Figs. 2.1(a) and (b) that represent respectively an academic cylindrical and an annular enclosed cavity. The upper disk is said stationary while the lower one rotates at the speed Ω. One then defines h, the height of the cavity, R_1 the external radius and R_0 the internal radius. The aspect ratio, defined as $G = h/R_1$, is another important characteristic number but one also often talks about the curvature parameter defined as $R_m = (R_1 + R_0)/(R_1 - R_0)$. Note that, in gas-turbine systems, the aspect ratio is usually $G < 1$ corresponding to radially elongated cavities. For all academic cavities, besides the local Reynolds number Re_r, note that two other Reynolds numbers can be used to define the flow of such systems:

- The boundary layers Reynolds number: $Re_\delta = (h/\delta)^2$ with $\delta = (\nu/\Omega)^{1/2}$,
- The global Reynolds number : $Re = Re_{r_{max}} = \Omega R_1^2/\nu$.

When it comes to the steady, mean and axisymmetric flow structure of rotating cavities, studies showed a long time ago that it is usually composed of two boundary layers, one on each disk, and a central core flow in near solid-body rotation. Figure 2.2 shows a map of the different regimes found for cavities with $G << 1$ as a function of the global Reynolds number Re and classified by Daily & Nece (1960) in four different regimes:

- The two laminar regimes (category I for merged boundary layers, II for separated) are separated by a line $Re\, G^{11/5} \simeq 2.9$,

- The transition to turbulence for flows with separated boundary layers (regime II to IV) occurs at $Re \simeq 1.58 \times 10^5$,
- The common boundary to the two turbulent regimes: category III for merged boundary layers and IV for the turbulent separated one is defined by $Re\ G^{16/3} \simeq 7.8 \times 10^{-3}$,
- The curve between regimes I and III is such that $Re\ G^{10/9} \simeq 366$,
- Finally, the common boundary to regimes II and III satisfies the equation $Re\ G^{16/15} \simeq 4.6 \times 10^6$.

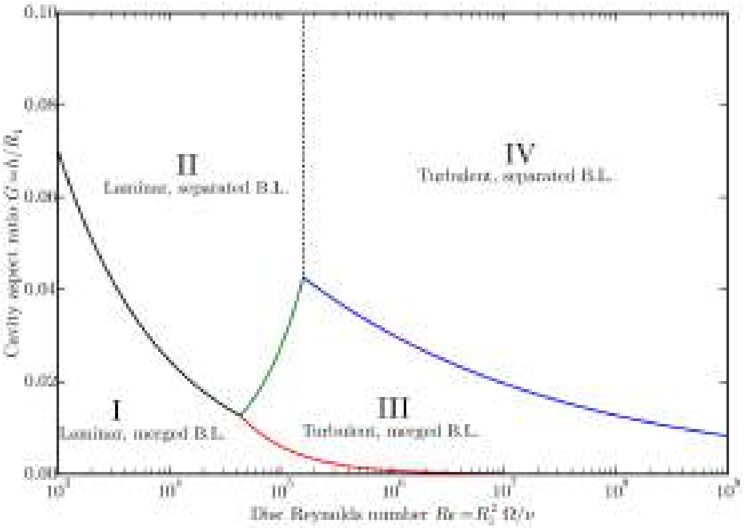

Figure 2.2 – Map of the four regimes found in rotor/stator cavities function of the aspect ration G and the global Reynolds Number Re. Source: Daily & Nece (1960).

Although many different flows can appear, the present PhD focuses on the so called Batchelor type flows corresponding to two separated boundary layer flows. The more relevant experimental studies linked to these configurations are Itoh *et al.* (1992) and Schouveiler (2001). In this latter, the authors provide a map of all the instabilities present in these cavities as a function of the global Reynolds number Re and the cavity aspect ratio G, Fig. 2.3. For these flows, two types of wave have been identified: circular waves around the edge of the disks and spiral waves driving all the dynamics of the flow. In the present chapter, a specific enclosed cavity with a similar operating point that the turbopump one, is studied through Large Eddy Simulation (LES) (Sagaut (2006)). Even though this type of study has been already realized in the past (Bridel-Bertomeu (2016), Séverac *et al.* (2007)), this investigation is primordial for the next chapters and will be taken as reference results. Note that the LES framework will be further developed to understand the mode interactions in Chap. 3.

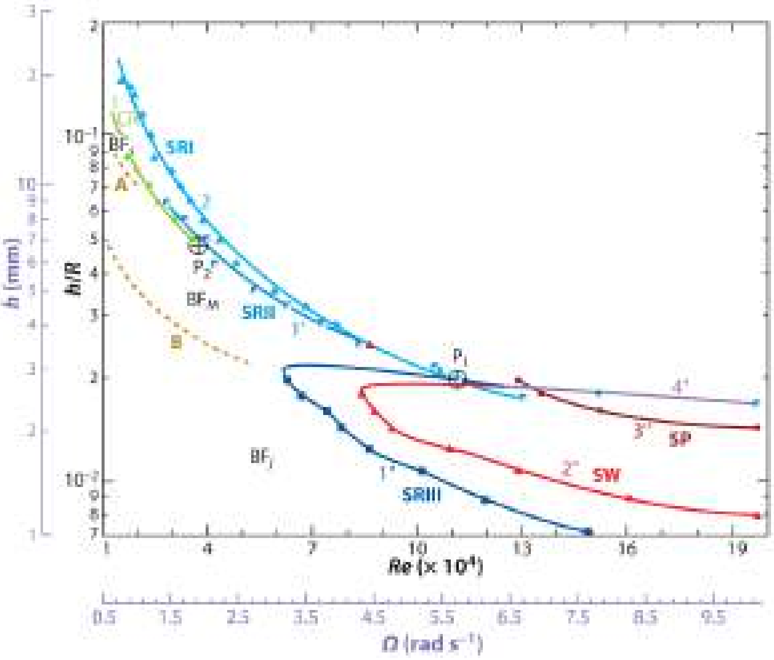

Figure 2.3 – Transition diagram of a rotor/stator cavity function of the aspect ration G and the global Reynolds number Re with Circular Rolls (CR), Spiral Rolls (SRI, SRII, SRIII), Solitary Waves (SW), tubulent SPots (SP). The different states generating different structures are separated by numbered curves. Letter annoted curves enable to distinguish the different base flows (Separated (BF_s), joined BF_j and mixed (BF_m). Source: Launder *et al.* (2010).

The present chapter is organized as follows. First, LES concepts and equations are introduced in Sec. 2.2. After a brief description of the numerical set up and the configurations of interest in Sec. 2.3 and in Sec. 2.4, LES predictions and flow dynamics are discussed in Sec. 2.5.

2.2 Large Eddy Simulations

In industry, most numerical studies are based on the Reynolds-Averaged Navier-Stokes (RANS) equations (Pope (2001)) due to their low computational cost but are however restrained to stationary flows. In the context of turbomachinery, the unsteady nature of the flows is critical and RANS failed multiple time to describe the good beahavior of such a flow (Su *et al.* (2013)). Unsteady Reynolds-Averaged Navier-Stokes (URANS) simulations could hence be a good alternative to provide more physical understanding but as reported in the review of Launder *et al.* (2010), eddy viscosity models failed to predict rotating boundary layer thicknesses, the rotation rates of the central core and hence the transition to turbulence. Finally, Wu & Squires (2000) performed the first LES on a simple disk and a few years later, Séverac *et al.* (2007) analyzed an enclosed rotating cavity with also a LES using a spectral vanishing viscosity (SVV) technique. Thanks to this advanced method, both were able to retrieve a good agreement with the corresponding experimental data. According to these sucesses, LES is therefore the more relevant alternative for this specific problem and will be retrieved in the present study.

2.2.1 Filtered Navier Stokes Equations

LES equations and concept for compressible flows are provided in this section. Note that throughout this introduction, i, j, l, will be the 3 space directions following Einstein's notation. Note also that the index k will refer to the k^{th} species and does not follow the summation rule unless specifically mentioned or implied by the $\sum$ sign.

In a turbulent flow, different scales of structures can be generated going from the integral scale length l_t to the more dissipative and smallest scale usually called the Kolmogorov scale (Kolmogorov (1991)). The main difference between DNS, RANS and LES is the ratio of scales resolved by the model. When DNS resolves all the turbulence scales with very refined meshes (of the order of the Kolmogorov scale) and RANS models all the turbulence, LES corresponds to a compromise where the largest structures are resolved and the more dissipative structures are modeled. This difference between LES and RANS is translated through different mathematical operators applied to the original set of Navier-Stokes equations. RANS is based on a temporal or ensemble average operator while LES introduces a spatial filter dependent on the mesh grid size. For any variable $f(x,t)$, this LES operation corresponds to a convolution product:

$$\bar{f}(x,t) = \int_{\Omega} G_{\delta}(x,x')f(x',t)dx', \tag{2.2.1}$$

where $\bar{f}$ is the resolved field and G_{δ} is the spatial filter. From this filter, the unresolved quantity usually noted f' and usually referred to as the subgrid scale is defined so that,

$$f' = f - \bar{f}. \tag{2.2.2}$$

Finally, note that for the compressible Navier-Stokes equations, the mass-weighted Favre filtered variables $\tilde{f}$ (Favre (1983)) are usually introduced following,

$$\tilde{f} = \frac{\overline{\rho f}}{\bar{\rho}}. \tag{2.2.3}$$

with $\bar{\rho}$ is the filtered density.

Thanks to these definitions, one obtains the LES conservation equations that read,

Filtered mass flow conservation

$$\frac{\partial \bar{\rho}}{\partial t} + \frac{\partial}{\partial x_j}(\bar{\rho}\tilde{u}_j) = 0, \tag{2.2.4}$$

where $\tilde{u}_j$ are the filtered velocity components.

Filtered momentum conservation:

$$\frac{\partial \bar{\rho}\tilde{u}_i}{\partial t} + \frac{\partial}{\partial x_j}(\bar{\rho}\tilde{u}_i\tilde{u}_j) = -\frac{\partial}{\partial x_j}[\bar{P}\delta_{ij} - \bar{\tau}_{ij} - \bar{\tau}_{ij}^t], \tag{2.2.5}$$

where P is the pressure and δ_{ij} stands for the Kronecker symbol. The resolved viscous stress tensor $\bar{\tau}_{ij}$ is then given by:

$$\bar{\tau}_{ij} = 2\mu(\tilde{S}_{ij} - \frac{1}{3}\delta_{ij}\tilde{S}_{ll}), \tag{2.2.6}$$

where $\tilde{S}_{ij}$ is the rate of strain tensor defined as:

$$\tilde{S}_{ij} = \frac{1}{2}(\frac{\partial \tilde{u}_j}{\partial x_i} + \frac{\partial \tilde{u}_i}{\partial x_j}), \tag{2.2.7}$$

and μ is the mixture molecular viscosity, described with a Sutherland or a Power law.

Filtered species conservation:

$$\frac{\partial \bar{\rho}\widetilde{Y}_k}{\partial t} + \frac{\partial}{\partial x_j}(\bar{\rho}\widetilde{Y}_k\tilde{u}_j) = -\frac{\partial}{\partial x_j}[\overline{J_{j,k}} + \overline{J_{j,k}}^t], \tag{2.2.8}$$

where $\rho_k = \rho Y_k$ with k^{th} specie's mass fraction Y_k. $J_{j,k} = V_{j,k}Y_k$ represents the diffusion flux with $V_{k,j}$ the components of the diffusion velocity of species k.

Filtered Energy conservation:

$$\frac{\partial \bar{\rho}\widetilde{E}}{\partial t} + \frac{\partial}{\partial x_j}(\bar{\rho}\widetilde{E}\tilde{u}_j) = -\frac{\partial}{\partial x_j}[\overline{u_j(P\delta_{ij} - \tau_{ij})} + \bar{q}_j + \bar{q}_j^t], \tag{2.2.9}$$

where $E = \int_T^{T_0} C_p dT + \frac{1}{2}u_i u_j - \frac{P}{\rho}$ and q_j is the heat flux.

The state equation which closes the Navier-Stokes equations is hereafter assumed to be an ideal gas mixture so that,

$$\frac{P}{\rho} = rT, \tag{2.2.10}$$

where r is the gas constant of the mixture, $r = \mathcal{R}/W$ where W is the mean molecular weight of the mixture:

$$\frac{1}{W} = \sum_{k=1}^{N} \frac{Y_k}{W_k}, \tag{2.2.11}$$

with W_k is the molecular weight of the k^{th} species.

In Eqs. (2.2.4)-(2.2.9), $\bar{\tau_{ij}}^t$, $\bar{q_j}^t$ and $\overline{J_{k,j}}^t$ correspond to the turbulent or subgrid terms which need to be modeled. Only details on the subgrid-grid scale Reynolds stress tensor are provided hereafter, more details being found in the book of Sagaut (2006).

The subgrid-grid scale Reynolds stress tensor can be expressed as,

$$\bar{\tau_{ij}}^t = -\bar{\rho}(\widetilde{u_i u_j} - \tilde{u}_i \tilde{u}_j). \tag{2.2.12}$$

A Boussineq approximation (Boussineq (1897)) is usually used to model this term so that,

$$\bar{\tau_{ij}}^t = 2\bar{\rho}\nu_t(\widetilde{S}_{ij} - \frac{1}{3}\delta_{ij}\widetilde{S}_{ll}). \tag{2.2.13}$$

This expression relates the subgrid stress to a quantity that takes the form of a viscosity and also called subgrid-scale turbulent viscosity ν_t. The ν_t model used in the present work is WALE (Wall-adapting local eddy-viscosity) originally proposed by Nicoud & Ducros (1999) and is of the form,

$$\nu_t = (C_w\Delta)^2 \frac{(s^d_{ij}s^d_{ji})^{3/2}}{(\widetilde{S}_{ij}\widetilde{S}_{ij})^{5/2} + (s^d_{ij}s^d_{ji})^{5/4}}, \tag{2.2.14}$$

where $\widetilde{S}_{ij} = \frac{1}{2}\left(\frac{\partial \tilde{u}_i}{\partial x_j} + \frac{\partial \tilde{u}_j}{\partial x_i}\right)$, and $s^d_{ij} = \frac{1}{2}\left[\left(\frac{\partial \tilde{u}_i}{\partial x_j}\right)^2 + \left(\frac{\partial \tilde{u}_j}{\partial x_i}\right)^2\right] + \frac{1}{3}\delta_{ij}\left(\frac{\partial \tilde{u}_k}{\partial x_k}\right)^2$, for which, the closure coefficient is $C_w = 0.325$.

2.3 Studied cavities

In this chapter, as represented by Fig. 2.1, the cavities of interest to be simulated by LES have a cylindrical and annular shapes. Two specific configurations already studied theoretically and experimentally at $Re = 10^5$ are used, Table 2.1 summing up all the parameters of both cases as well as their rotor rotation rate:

- **Case 1** is a **cylindrical cavity** designed with $G = 0.2$ and is a first order approximation of a real life turbine rotor/stator cavity. Such an aspect ratio is indeed often considered in the literature (Serre *et al.* (2001*b*, 2004); Tuliszka-Sznitko & Zielinski (2007); Lopez *et al.* (2009)) as relevant to model industrial cavities without the complex flow effects induced by the presence of a hub. Experimental results for such a configuration can be found in Daily & Nece (1960) or Czarny *et al.* (2002).

- **Case 2** is an **annular cavity** with $G = 0.2$ and $R_m = 1.8$. It only differs from **Case 1** by the presence of a hub ($R_0 > 0$). It hence allows to illustrate the effect of a non-unit curvature parameter on the rotor/stator cavity flow response to destabilizing effects. This specific value of $R_m = 1.8$ is chosen because the corresponding in-cavity flow was extensively studied by Séverac *et al.* (2007) experimentally as well as numerically and later by Tuliszka-Sznitko *et al.* (2009).

	Case 1	Case 2	
R_0	—	71	mm
R_1	178	250	mm
h	35	35	mm
Ω	615	315	rad/s
Re	10^5	10^5	—
G	0.2	0.2	—
R_m	1.0	1.8	—
Stator z	35	35	mm
Rotor z	0	0	mm

Table 2.1 – Characteristic parameters of the two rotor/stator cavities shown in Fig. 2.1.

Note that the wall resolved LES predictions and validations for both cases under considerations have been comprehensively detailed and validated in Bridel-Bertomeu *et al.* (2016). Features of interest for each prediction are detailed hereafter with the objective of identifying the origin of the observed flow large structures and dynamics.

2.4 Numerical model

2.4.1 Mesh

In order to create **Case 1** and **Case 2** meshes, $2D$ disk and annular unstructured meshes have been first generated through the software CENTAUR[1] and finally 3D extruded along the z-axis via the mesher HIP[2]. Figure 2.4 presents a view of the results obtained for **Case 2**, only a sector of the 3D mesh is given. One can note that the final 3D grids of each configuration are only composed of prismatic elements with a constant thickness z_1. Table 2.2 sums up the spatial resolution adopted and measures for both cases. N_{nodes}, N_{cells} and Δt correspond respectively to the number of nodes, number of cells and the average LES time step. Note that z_1 has been taken of the same order of δ (rotating boundary layer thickness usually defined as $\delta = \sqrt{\nu/\Omega}$). In order to evaluate the good quality of the mesh at the walls, the first grid node wall normal coordinate $z^+ = z_1 u_\tau/\nu$ has been computed where u_τ is the total wall-friction velocity defined as $u_\tau = \sqrt{\tau_w/\rho}$ with τ_w standing for the flow shear stress at the wall. Table 2.2 shows the z^+_{min} and z^+_{max} for both cases and for each disk (the values in the brackets represent the rotor and stator values). Two or three points for both cases have been introduced in the viscous

---

[1] https://www.centaursoft.com/

[2] www.cerfacs.fr/avbp7x/hip.php

	Case 1	**Case 2**
δ [m]	5.65×10^{-4}	7.91×10^{-4}
z_1 [m]	3.90×10^{-4}	5.14×10^{-4}
N_{layers}	91	70
N_{nodes}	4.7×10^{6}	5.5×10^{6}
N_{cells}	9.2×10^{6}	10.8×10^{6}
Δt [s]	7.1×10^{-7}	7.6×10^{-7}
z^+_{min}	$[0.321, 0.153]$	$[0.975, 1.1]$
z^+_{max}	$[2.79, 5.79]$	$[2.87, 5.45]$

Table 2.2 – Mesh characteristic parameters of the two rotor/stator cavities shown in Fig. 2.1.

sublayers (usually defined as $z^+ \simeq 11$ (Schlichting & Gersten (2001); Sagaut (2006)) as recommended for wall resolved LES (Sagaut (2006)).

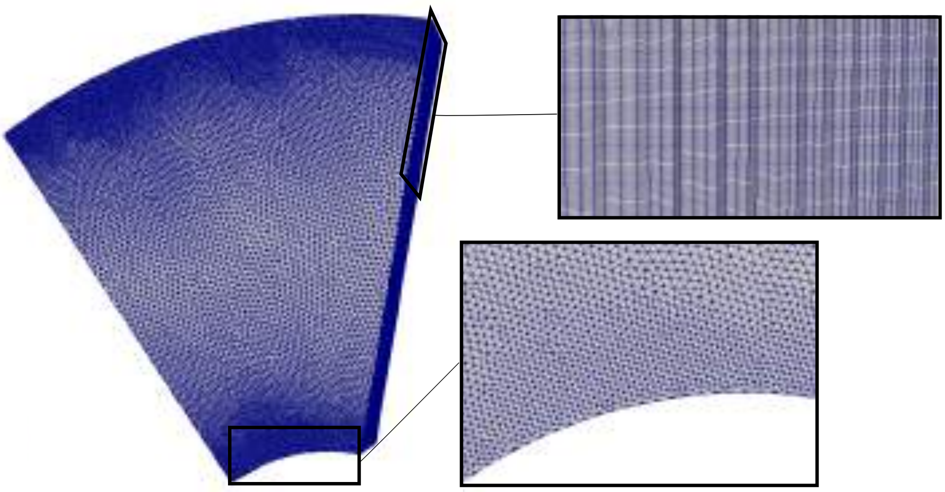

Figure 2.4 – Sector of the 360 3D mesh of the annular cavity of Tuliszka (**Case 2**).

2.4.2 Numerical Scheme

LES described in this chapter have been performed with the AVBP (Gourdain *et al.* (2009)) code. This code has been widely used for many well known industrial and academic configurations (Seguí *et al.* (2018)) and especially highly unsteady flows. It solves the filtered compressible Navier-Stokes equations and can be used on massively parallel machines. For the configurations of interest, the TTGC (Two-Step Taylor Galerkin) scheme (Colin & Rudgyard (2000)) based on finite elements is used. This centered scheme is an explicit two time step integration with low dissipation and dispersion properties. It is third order accurate in time and space making it suitable for LES of compressible flows. As introduced in Sec. 2.2.1, the subgrid model used is the WALE model (Nicoud & Ducros (1999)). Its construction makes it more suitable than a classical Smagorinsky model (Smagorinsky (1963)) to wall bounded flows since adapted for scaling laws near walls.

2.5 LES results and discussion

The LES results for the two cavities are presented in this section. After an evaluation of the mean flow against the literature in Sec. 2.5.1, the flow activity is extracted through Power Spectral Density (PSD) and Dynamic Mode Decomposition (DMD) (Schmid (2010)) in Sec. 2.5.2.

2.5.1 Mean flow validation

For the time-dependent solutions, the computing time is determined by the largest characteristic time in rotating flows, i.e.

Note that the wall resolved LES computations have both been conducted until at least $\tilde{t} = t\, F_0/G \approx 1350$ (with $\Omega = 2\pi F_0$) so as to be coherent with the viscous time-scales (largest characteristic time in rotating flows) of the problems that can be expressed as $G^2 Re/\Omega$ (Serre *et al.* (2001*a*)). Once the statistically stationary state of the flow is reached, data and statistical analysis of the flows is produced. In this case and to enhance statistical convergence, mean flow quantities are obtained thanks to a temporal and azimuthal average of the LES variables thereafter denoted by $\langle \cdot \rangle$.

Figure 2.5 presents the averaged radial component of velocity for (a) **Case 1** and (b) **Case 2** respectively. Note that the 2D cuts presented through sketches in these figures will be used all along this work. In both figures, the radial velocity component has been normalized by its ∞-norm, i.e. $\langle u_r \rangle / \max(\langle u_r \rangle)$, where the maximum is taken over the whole (r, z) domain of definition. Note that to improve the readability of the figures, the axial coordinate has been transformed using the following ad-hoc iso-parametric function to thicken artificially the boundary layers on the disks: $arctanh\left((2z/z_{max} - 1)(1 - \epsilon)\right)$ with $\epsilon = 0.08$. This transformation will be used in all the chapters of this manuscript. Although the spatial evolution of both top, bottom and outer wall flows are clearly similar, differences appear as expected in the central region. Indeed, the presence of the wall connecting the top and bottom flows via the central part of the cylindrical cavity induces the generation of an additional wall flow which can not establish in the annular cavity. This flow redirection introduces a direct communication between the top and bottom wall flows accompanied by strong flow streamline curvatures near the top and bottom central connecting regions. This specificity explains the noted differences of flow boundary layer thicknesses in this region. It is indeed clear from Fig. 2.5 that

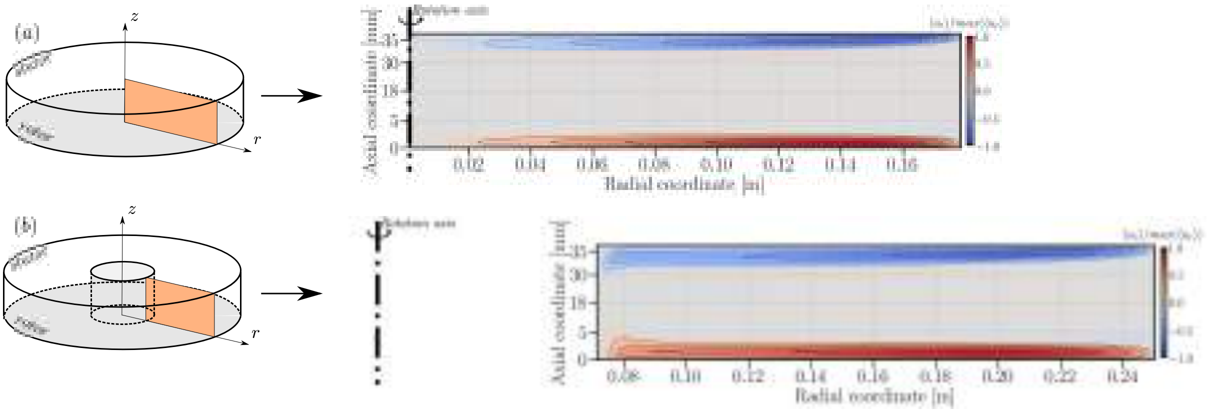

Figure 2.5 – Contours of the averaged radial component of velocity normalized by its ∞-norm, $\langle u_r \rangle$ / max $(\langle u_r \rangle)$ with (a) **Case 1** (a) **Case 1** and (b) **Case 2**. Note that these specific 2D cuts will be used all along this work. The stator is located at the top and the rotor at the bottom. Axial coordinate is transformed to thicken artificially the boundary layers.

Case 1 boundary layer is thinner in the central region. This feature plays a significant role in the development of the flow turbulence and hence the modal distribution of each configuration. Such differences have however already been evidenced and discussed in Bridel-Bertomeu *et al.* (2016). They are here also identified as a potential reason for the two different flow limit-cycles and energetic contents as briefly recalled in the coming discussion.

To validate both LES results, the radial and azimuthal mean velocity profiles have been extracted and compared to the literature in Fig. 2.7 and Fig. 2.6 respectively for **Case 2** and **Case 1**. The axial velocity component, being negligible compared to the two other ones, this latter is not analyzed here. Note that both components are normalized by $r\Omega$. **Case 2** configuration was chosen for the exhaustive study realized by Séverac *et al.* (2007) and as shown in Fig. 2.7 a good agreement is found with this experimental study. Furthermore, a comparison with the auto-similar solution of Rogers & Lance (1962) shows that despite retrieving the rotation core rate and the rotor boundary layer, confinement plays a main role on the stator boundary layer dynamics. For **Case 1**, one of the objectives is to evaluate the impact of the hub on the annular cavity dynamics. To do so, the exact same Reynolds number and aspect ratio were picked up for this cylindral cavity. However, no precise experimental results at **Case 1** operating point could be obtained. When compared with Itoh *et al.* (1992) results ($Re = 10^6$, $G = 0.08$), one can see that the rotation rate speed is retrieved as well as the rotor boundary layer but discrepencies are present in the stator boundary layer. In fact, in **Case 2**, the stator boundary layer is in a transitional state while in Itoh *et al.* (1992), it is fully turbulent. Finally, by comparing **Case 1** results with Rogers & Lance (1962) auto-similar solution, a better agreement is found here contrary to **Case 2** due again to the presence of the hub.
In the next section, an analysis of both flow cavity dynamics is presented and the pressure band phenomenon extracted thanks to dedicated post processing tools.

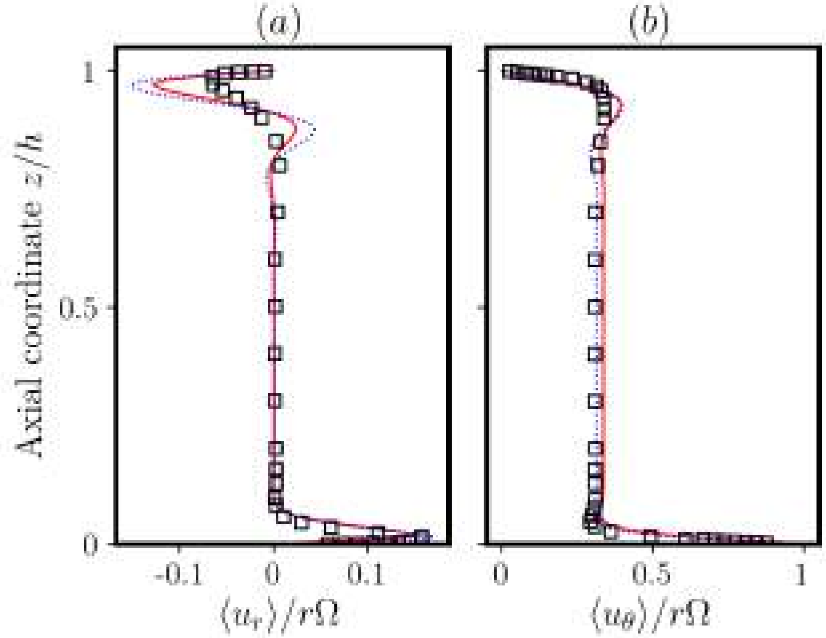

Figure 2.6 – **Case 1** base flow at $r/R_1 = 0.4$: Dimensionless mean radial velocity *(a)*, azimuthal velocity *(b)* with current LES results (—), Itoh *et al.* (1992) experiment (□) and Rogers & Lance (1962) (- - -) auto-similar solution.

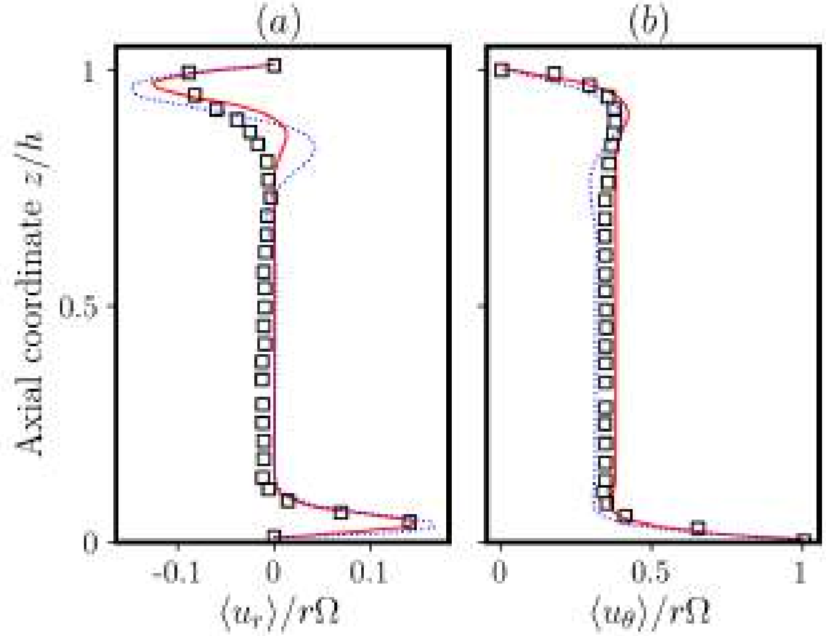

Figure 2.7 – **Case 2** base flow at $r/(R_1 + R_0) = 0.5$: Dimensionless mean radial velocity *(a)*, azimuthal velocity *(b)* with current LES results (—), Séverac *et al.* (2007) experiment (□) and Rogers & Lance (1962) (- - -) auto-similar solution.

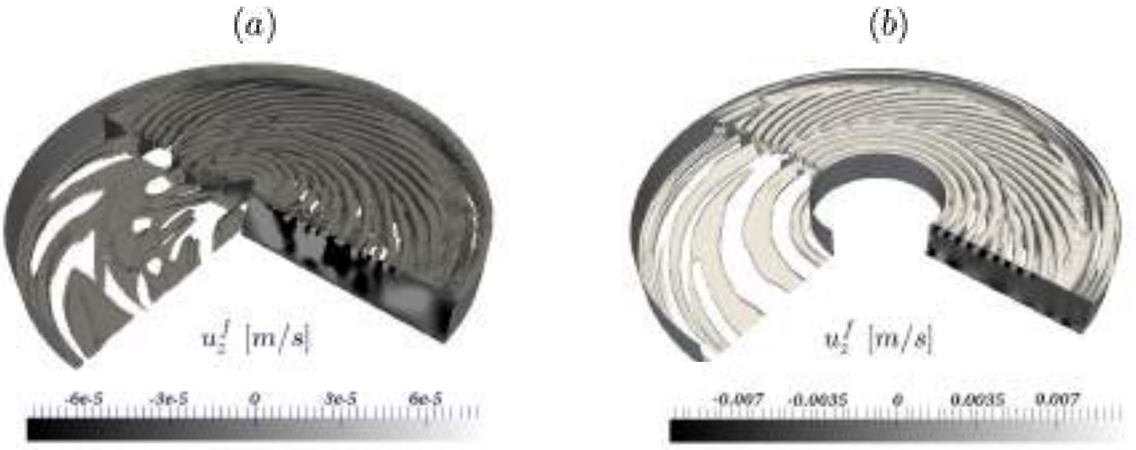

Figure 2.8 – Three-dimensional iso-contour of the axial velocity fluctuations $u_z^f = u_z - \langle u_z \rangle$ of (a) **Case 1** and (b) **Case 2** complemented by a two-dimensional colour-mapping in a plannar slice at $\theta = 0$ with associated colorbar.

2.5.2 Flow activity

Instantaneous views of the flow organization for the two limit-cycles are provided on Fig. 2.8 through the use of the three-dimensional velocity fluctuations (noted as $\mathbf{u^f} = \mathbf{u} - \langle \mathbf{u} \rangle$). To do so, the time-dependent fluctuations are computed at specific instants $\tilde{t}_k$ and the average flow solutions are taken out of multiple instants $\tilde{t}_p \ldots \tilde{t}_n$, where $\tilde{t}_n, \tilde{t}_k \gg \tilde{t}_p$ with $\tilde{t}_p \approx 200$ for both **Cases 1** & **2**. This procedure is chosen because when instability arises (refer to e.g. Smith, 1947; Gregory *et al.*, 1955; Faller, 1963), the base flow is known to depart from a purely parallel flow and the perturbations can be measured by the magnitude of the axial velocity fluctuations which then vary around a zero mean Lopez *et al.* (2009); Serre *et al.* (2001*b*). Figure 2.8 are representations of the major features present in **Case 1** and **Case 2** respectively, based on three-dimensional iso-contours of the axial velocity fluctuations u_z^f. In both considered cases, the stationary disk boundary layer shows evidence of instability patterns. The rotating disk boundary layer on the other hand displays instabilities as strong as the statoric ones only in the presence of an inner hub (**Case 2**) and a spiral-like perturbation with a very low magnitude in **Case 1**. Aside from the viscosity-driven boundary layers, it is of note that the homogeneous core flow also exhibits characteristic patterns and a coherent azimuthal organization. In addition it is also noted that the fluctuations in **Case 2** have much stronger amplitudes than in **Case 1** confirming the effect of the geometry.

In **Case 1**, Fig. 2.8(a), the colour-mapped slice reveals that the perturbations are strongest in the stationary disk boundary layer and in the inviscid-like core, whereas the rotating disk boundary layer displays a very weak spiral instability. The major feature of the flow is a spiral-like structure located in the upper stationary disk boundary layer. The vortices are contained within a fixed radial range $r \in [0.025, 0.14]$ m, out of which the flow is either laminar (close to the z-axis) or interactions with the outer cylindrical boundary layer lead to a loss of coherence. From the analysis of

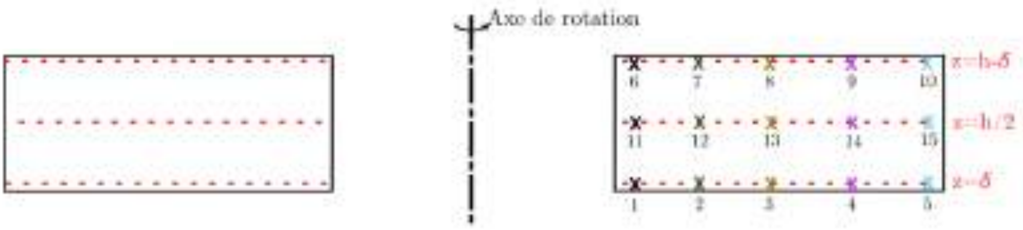

Figure 2.9 – Locations of the numerical probes in the cavity associated with **Case 2** at $\theta = 0$. The bottom disk, the homogeneous core and the top disk have been instrumented, the radial positions of the probes being referenced through the use of the colour code.

Fig. 2.8(a), an azimuthal number of $m = 28$ is found for $r \in [0.09, 0.128]$ m. As the radius decreases, the number of arms of the spiral structures tends to be difficult to define. However, at the axis of the cavity for $r \in [0.0, 0.059]$ m an azimuthal number of $m = 8$ has been clearly identified. The buffer zone between those two types of structure can be due to an interaction of azimuthal modes or even the presence of an other type of mode. The large-scale structure visible in the inviscid-like core of the flow is also noteworthy, as it appears to exist up to a greater radial location than the statoric spiral's limit and presents a radically different azimuthal organization. Finally, the spiral confined in the rotor boundary layer exists mostly close to the outer cylindrical boundary layer and seems to exhibit approximately 12-arms.

In **Case 2**, Fig. 2.8(b), it appears that the presence of the rotating hub has a deep impact on the organization and dynamics of the rotor/stator flow. Like **Case 1**, the stationary disk boundary layer features a 29-arms spiral structure existing at high radii $r > 0.12$ m. However for $r < 0.12$ m, the cylindrical boundary layer present along the hub induces the dislocation of the spiral into a quasi-concentric annular structure. Finally, it is noteworthy that with a hub, the rotating disk boundary layer also becomes unstable and displays spiral-like macro-structures (see Fig. 2.8(b)) that are clearly connected to the upper disk boundary layer structures through the inviscid-like core.

The purpose of this investigation was first of all to extract the driving modes of the cavities and their constituent frequencies. To do so, numerical probes have been placed in both cavities to analyze the temporal dynamics of these flows. Figure 2.9 gives a representation of the probes distribution at $\theta = 0$ for **Case 2**. Note that three range of probes have been used: mid-cavity ($z = h/2$), stationnary disk ($z = h - \delta 2$) and rotating disk ($z = \delta$).

Thanks to these temporal series, Power Spectral Density (PSD), Fig.2.10, have been extracted from both LES limit-cycles and reveal the presence of:

Case 1 : Throughout the cavity, one major peak is identified at a frequency of $3.55F_0$ indicating that the flow oscillates as a whole (where F_0 stands for the rotor frequency). Two more peaks appear at mid-height and in the stator layer at frequencies $3.27F_0$ and $3.85F_0$ respectively but their amplitude is significantly lower than the main

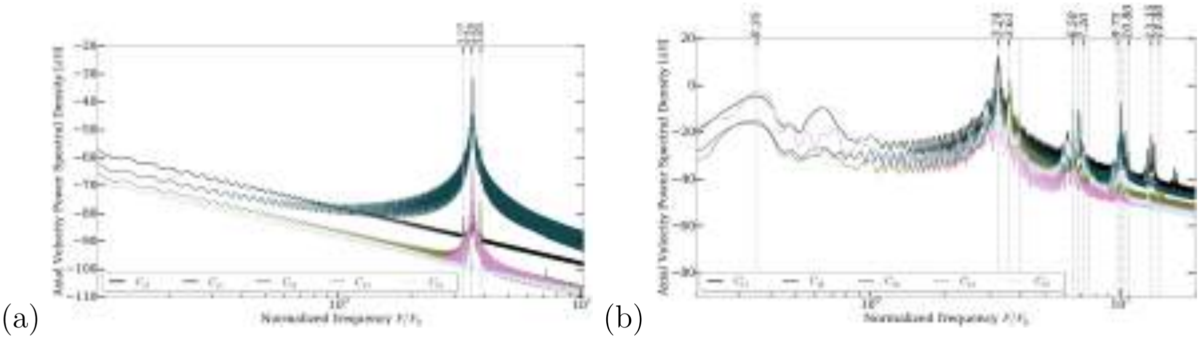

Figure 2.10 – Power Spectral Densities (PSD) of the fluctuations of axial velocity u_z^f at mid-height of the two cavities and different radial locations for (a) **Case 1** and (b) **Case 2**. In all cases, darkest to lightest shades, respectively, correspond to an increasing radial position of the probe as identified in the simulations.

identified one and will therefore not be addressed hereafter. From the PSD and the isocontours of Fig. 2.8, one can deduce that this cavity has the particularity to exhibit different m azimuthal wave number modes synchronized at a unique frequency.

Case 2 : The annular cavity displays a much richer spectral content. Throughout the cavity, three main frequencies can be identified, *i.e.* $0.35F_0$, $3.24F_0$ and $3.61F_0$, all other peaking frequencies being either harmonics or linear combinations of these three frequencies. Similarly to **Case 1**, the magnitudes of the peaks at different radial locations are coherent with the location of the three-dimensional structures in the cavity. Typically, the stator boundary layer appears disturbed only close to the hub and up to $r \simeq 0.18$ m.

Dynamic Mode Decomposition (DMD)

PSD enabled to distinguish through probes oscillating phenomena in both cavities. One particular drawback of this tool is that it doesn't enable to retrieve the spatial distribution of each modes. From all available data-based analyses or modal decomposition methods (Taira *et al.* (2017)), DMD (Schmid (2010)) is one of the most widely used in the CFD community today. On top of giving access to the mode spatial distribution of each modes, a spectrum of all the flow frequencies and their growth rate associated can also be retrieved.

DMD has been therefore applied to both **Case 1** and **Case 2**. Their respective spectra (not shown) confirm the PSD findings. For **Case 1**, a unique frequency is retrieved at $F = 3.55F_0$. For **Case 2**, as for its PSD, the DMD spectrum is much richer and complex. In fact, five frequencies are found common with the PSD : $F = 0.35F_0$, $F = 3.24F_0$, $F = 3.6F_0$, $F = 6.5F_0$ and $F = 6.84F_0$. Only the three first modes will be taken into consideration for the rest of this PhD work, other local maxima being attributed to noise or lack of snapshots for the adequate decomposition.

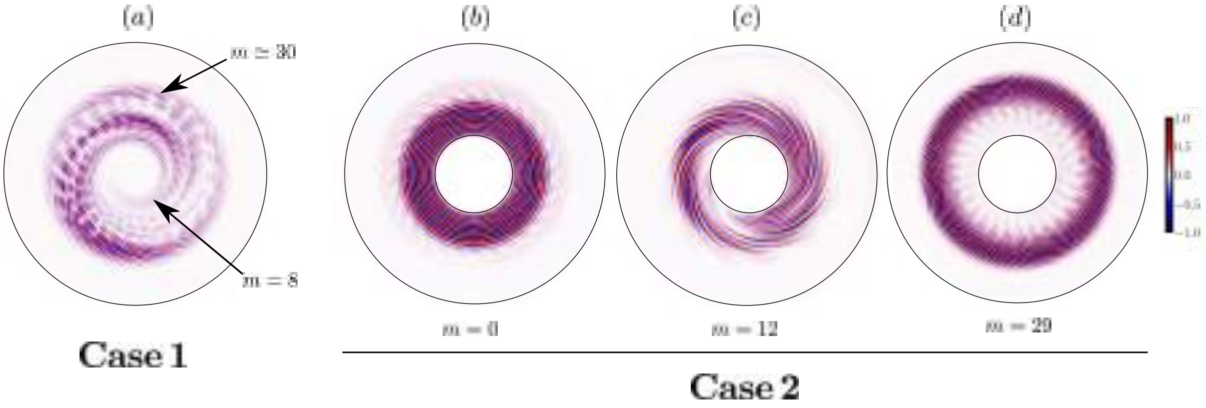

Figure 2.11 – Axial velocity DMD in a (r, θ)-cut at $z = 0.035$: **Case 1** *(a)* $F/F_0 = 3.55$ and **Case 2** with *(b)* $F/F_0 = 3.24$ $(m = 0)$, *(c)* $F/F_0 = 0.35$ $(m = 12)$, *(d)* $F/F_0 = 3.6$ $(m = 29)$.

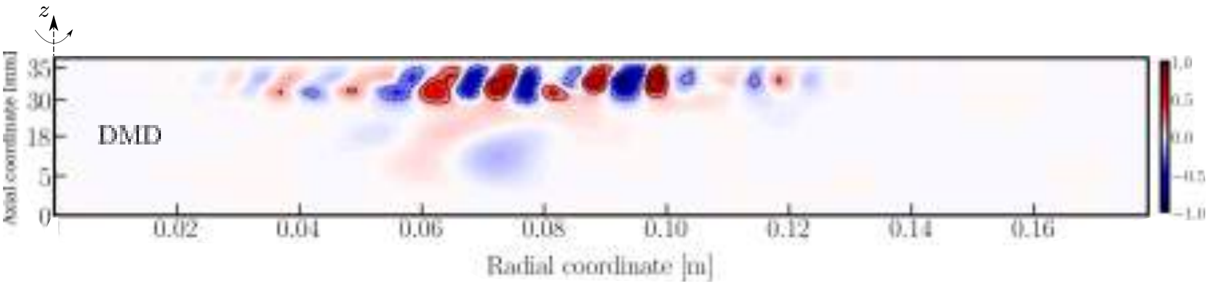

Figure 2.12 – Axial velocity DMD of **Case 1** in a (r, z)-cut of $F/F_0 = 3.55$.

The main benefit of DMD is the possibility to access the spatial distribution obtained for each modes. As stated in Sec. 2.8, for **Case 1,** instantaneous fields of axial velocity enabled to point out different azimuthal wave numbers at different regions of the cylindrical cavity. DMD confirms here these observations and highlights that those different azimuthal wavenumbers are synchronized at a unique frequency. As one can see from Fig. 2.11(a), DMD enables also to refine the regions where each azimuthal wave number is dominant: for $r > 0.10$, $m \simeq 30$ is present. For $r < 0.05$, a unique azimuthal wavenumber $m = 8$ is observed. Finally between $0.05 < r < 0.1$, coherent structures with the same order of amplitude as the low and high radii ones are observed but with no characteristic wavenumber. As shown in Fig. 2.12, this mode is generated around the stator boundary layer. A more detailed analysis of this complex mode is provided in Sec. 4.4.2.

For **Case 2**, the three dominant frequencies observed in the DMD spectrum have respectively a unique azimuthal wavenumber. As shown in Fig. 2.11(b), the first mode considered as an annular shape $(m = 0)$ with a frequency $F/F_0 = 3.24$ mainly present around the hub and the stator disks (see Fig.2.13(a)). Finally, two spiral modes $m = 12$ and $m = 29$ respectively given in Fig. 2.11(c) and in Fig. 2.11(d) are observed around the rotor and the stator disks (see Fig.2.13(b)-(c)). For the aspect ratio and Reynolds number of the present configuration, these three specific modes and shapes are in good agreement with the transition diagram presented in Fig. 2.3.

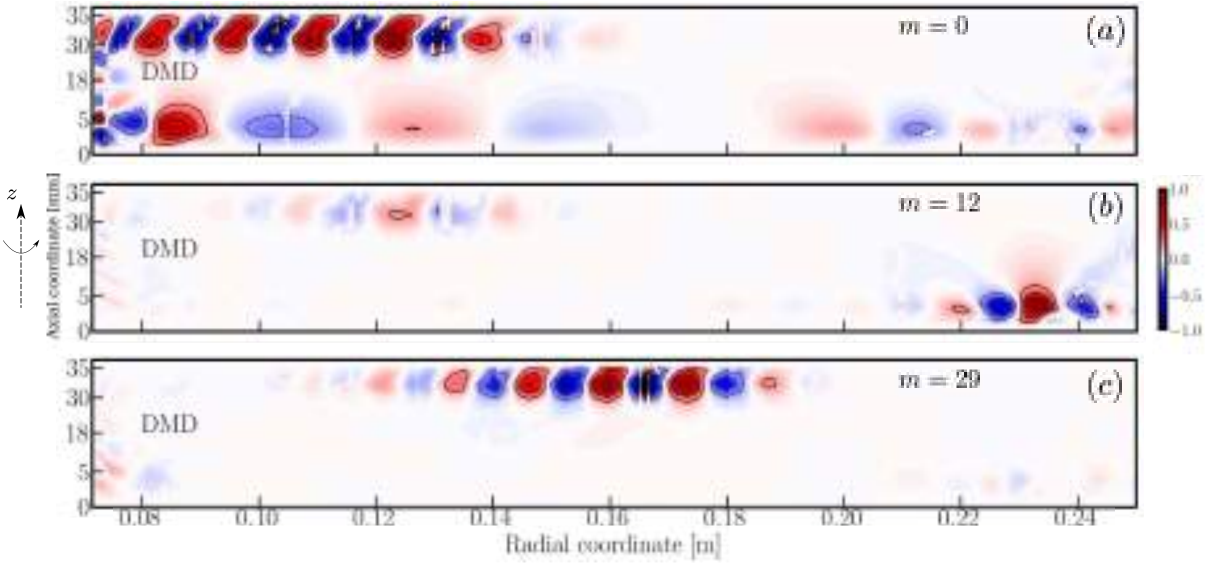

Figure 2.13 – Axial velocity DMD of **Case 2** in a (r, z)-cut with: *(a)* $m = 0$, $F/F_0 = 3.24$ *(b)* $m = 12$, $F/F_0 = 0.35$ *(c)* $m = 29$ $F/F_0 = 3.6$.

2.6 Conclusion

This first investigation focused on Large Eddy Simulations, realized with AVBP, for two rotor/stator cavites: an annular and cylindrical shapes. These configurations are indeed a first order representation of more complex turbomachinery cavities and enable to study the activity and modes that dictate the unstable regime of such flows. First, the mean velocity profiles are detailed and validated against literature (Schouveiler (2001); Lopez *et al.* (2009)). These are indeed of first importance for the next stability study of Chap. 4. The activity of the flows is then studied thanks to Power Spectral Density. and the results show that **Case 1** exhibits a unique mode present everywhere in the cavity. At the opposite, **Case 2** reveals a richer spectrum with three dominant modes. Even though, LES enables to obtain a full description of the annular rotor/stator cavity and DMD allows to extract the coherent structures, deeper understanding of these mode origins and interactions still needs to be acquired to eventually produce control strategies. In the next chapter, a new tool is proposed to do so. The objectives are indeed through numerical control to investigate how the modes interact with each other so as to identify which mode is to be controlled first. Note that for this specific investigation only **Case 2** will be directly addressed.

Chapter 3

Mode dominance and interactions

Contents

Mode interaction is a complex phenomenon particularly difficult to predict and model. In the previous chapter, three modes with distinct frequencies have been found to constitute the global activity of the annular rotor/stator cavity. From this observation, non linearities can be suspected to generate interactions between these modes and in particular a dominant mode can create low frequency modes. To evaluate such a specific property of an oscillating flow, a new method named Dynamic Mode Tracking/Control (DMT/DMTC) is proposed. Based on temporal filters, DMT is constructed so as to track flow features on the basis of LES. The benefit of this new method is to extract "on-the-fly" flow coherent structures with a given frequency saving simulation time and memory compared to more classical post processing techniques. Furthermore, augmenting the Navier-Stokes equations with a relaxation term coupled to DMT, DMTC allows to control and follow the evolution of a controlled mode as well as non controlled ones and thereby observe interactions. Thanks to such numerical experiments, one can access to mode dominance of an established limit-cycle. This last strategy is therefore applied here to the annular rotating cavity and shows that the low frequency mode is as assumed generated by a dominant mode. This information will then be used to guide the design of physical control strategies aiming at damping the whole pressure band phenomenon.

3.1 Introduction

Theoretical as well as experimental or numerical works on turbulent flows have very early evidenced the presence of coherent structures (Davies & Yule (1975); Pope (2001)). Although not clearly defined, these structures have been extracted thanks to different methods taking advantage of a spatial or temporal analysis of flow features even in industrial applications. From the review of Taira *et al.* (2017), those mathematical tools can be classified in two categories: operator-based or data-based analyses. Operator based analyses such as global stability analysis have recently gained interest (Theofilis (2011)) and will be evaluated in Chap. 4. At the opposite, data-based analyses or modal decomposition methods are widely used in flow dynamics, most of the time as post processing tools which impose the saving and manipulation of a large amount of data. A typical example has been presented in Sec. 2.5.2 with DMD. For this technique, one requires access to a spatial and temporal representation of an entire flow field (set of snapshots) to obtain a complete set of modes with indications of frequency, growth rate and their specific spatial distribution. In opposition to the more classical Proper Orthogonal Decomposition (POD) (Lumley (1967)), DMD gives a decomposition on a non-orthogonal spatial basis which results in a more meaningful representation of the flow dynamics. In the previous chapter this tool typically enabled to extract the pressure bands phenomenon in an annular rotor/stator cavity and showed that three main modes with three specific azimuthal wave numbers $m = 0$, $m = 12$ and $m = 30$ were driving this academic cavity. For future control purpose, the question remaining as shown in the scheme of Fig. 3.1 is **how does these modes interact ?** Unfortunately such a question can not be answered today in the context of LES and AVBP or through the use of data-based analyses

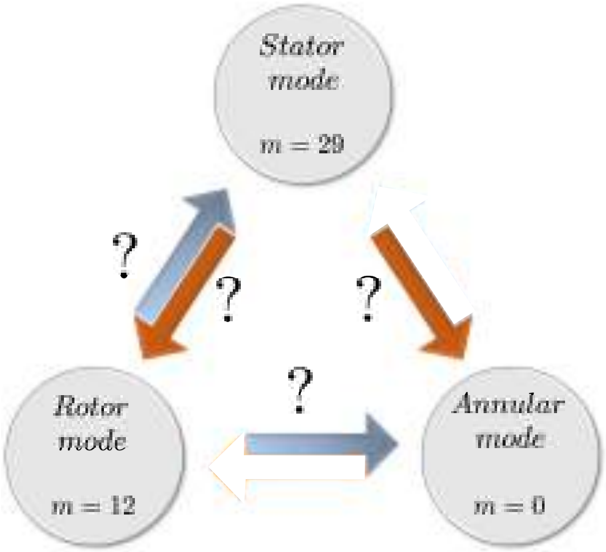

Figure 3.1 – Schematic of mode interactions studied during this chapter

In this chapter, as a first attempt to answer this question, a new tool called Dynamic Mode Tracking (DMT) is presented to address this problem. Since one knows that tracking and damping structures can be linked to spatial and temporal filtering techniques and have been widely used in the context of CFD. One of the most known application of such tools remains indeed LES where the large scales of motion are resolved and the small ones filtered with a low pass linear filter allowing coarser meshes while alleviating the weight of turbulence modeling in the flow prediction. Likewise, Localized Artificial Dissipation (LAD) is also a well known example which uses spatial filtering to prevent wiggles emergence and smooth large gradients Mathew *et al.* (2006, 2003). In an other context, the Selective Frequency Damping (SFD) (Åkervik *et al.* (2006)) was created to compute a steady state flow by filtering the unstable temporal frequencies, essential to conduct linear stability analysis. Following this latter method, DMT is proposed to identify dynamically with band pass filters, a mode with a given frequency so as to have access to its spatial as well as temporal evolution in a non-linear context. Contrary to other typical data-based analyses like DMD or POD, this ”on-the-fly” method does not require to save data, hence saving non negligible memory. Once validated, such an information can then be used as a support to actively control a mode by adding a relaxation term in the CFD solver, as done with SFD. This simple strategy, named hereafter Dynamic Mode Tracking and Control (DMTC), hence allows to follow the evolution of a controlled mode as well as non controlled modes and thereby observe the interactions.

The chapter is organized as follows: SFD method is recalled first in Sec. 3.2 followed by the mathematical formulation of DMT/DMTC in Sec.3.3. The capacity of this new approach is not detailed here but can be retrieved from App.B where three types of flows are opposed (1D cavity with 3 acoustics eigenmodes, a cylinder wake and an academic premixed swirl burner). Instead, DMT/DMTC are exploited on the enclosed annular cavity in Sec. 3.5 to give a first answer on how the three main modes interact.

3.2 Selective Frequency Damping (SFD)

Being in the context of fluid dynamics, the original set of governing equations are the non-linear compressible Navier-Stokes (NS) equations symbolically expressed by,

$$\dot{q} = F(q), \tag{3.2.1}$$

where F corresponds to the non-linear NS operator and q stands for the state vector of the conservative variables: *i.e.* $q = (\rho, \rho u_i, \rho E)$ with $i \in [1, 2, 3]$ for a fully 3D problem where ρ is the fluid density, u_i are the velocity components and E is the total energy. In the following, notations are such that for any quantity X, dependent of time, t, the notation $\dot{X}$ refers to as the derivative of X with respect to time and $\hat{X}$ stands for its Fourier transform,

$$X(t) = \int_{-\infty}^{\infty} \hat{X}(\omega) exp(i\omega t) d\omega, \tag{3.2.2}$$

where ω is a pulsation.

With this formulation, the SFD method (Åkervik *et al.* (2006)) seeks a steady state flow solution relying on the application of a low-pass filter noted T in the time domain to suppress high frequencies related to flow instabilities. The transfer function $\hat{H}$ associated to this low pass filter T in the Fourier space usually reads,

$$\hat{H}(\omega, \delta) = \frac{1}{1 + i\omega\delta}. \tag{3.2.3}$$

where δ is the characteristic filter width as represented on Fig. 3.2. Applying this filter yields the filtered variables, usually denoted by $\bar{q}(t)$, and is obtained thanks to a convolution product of $\hat{q}$ with $\hat{H}$.

$$\hat{\bar{q}}(\omega) = \hat{H}(\omega) * \hat{q}(\omega), \tag{3.2.4}$$

An inverse Fourier transformation can then be applied to yield the temporally dependent filtered signal,

$$\bar{q}(t) = \int_{-\infty}^{\infty} \hat{H}(\omega)\hat{q}(\omega) exp(i\omega t) d\omega. \tag{3.2.5}$$

It results that in the spectral domain, $\hat{H}$ corresponds to the ratio $\hat{\bar{q}}/\hat{q}$ and that by differentiating Eq. (3.2.4) and using the Fourier transform properties, one can show that the last expression satisfies an ordinary differential equation of the form,

$$\dot{\bar{q}} = \frac{q - \bar{q}}{\delta}. \tag{3.2.6}$$

Thanks to this property, the filtering operation is equivalent to solving the above ordinary equation in time. The main benefit of using this specific equation is that it allows working directly in the time domain rather than in the frequency domain and back. It can also be easily implemented in a time stepping code giving access to $\bar{q}(t)$ for a given or observed $q(t)$.

SFD has been at the origin of many different applications. For example, Garnaud *et al.* (2012) have shown recently that it is possible to solve an eigenvalue problem in a specific range of frequencies by replacing the low pass-filter of SFD by a band-pass filter, saving computational time and memory. Jordi (2015) has also shown that it is possible to find optimal SFD parameters with successive stability analyses using partially converged base flows.

As detailed in the introduction, an extension of SFD called DMT/DMTC is presented in this chapter to extract a mode with a given frequency. The next paragraph is dedicated to the mathematical formulation of this new method.

3.3 Dynamical Mode Tracking (DMT)

The extension proposed here consists in taking a classical second order band-stop filter T_{sf} with a transfer function $\hat{H}_{sf}$ of the form,

$$\hat{H}_{sf}(\omega, \omega_0, \beta) = \frac{\hat{\bar{q}}}{\hat{q}} = \frac{\omega_0^2 - \omega^2}{\omega_0^2 + i\beta\omega - \omega^2}, \tag{3.3.1}$$

where β is defined as the filter width, f_0 the central frequency so that $\omega_0 = 2\pi f_0$ and ω a pulsation. A band-stop filter has the benefit of passing all the frequencies with the exception of a band of frequencies limited by the so called cutoff frequencies noted respectively f_- and f_+. As shown in Fig. 3.2, the bandwidth is a crucial parameter as it dictates the selectivity of the filter but also the attenuation / gain of the output variables. Small values of β, for which the band-stop filter is referred to as a Notch filter (thin line in Fig. 3.2) are recommended to capture a given feature or mode at a given frequency.

As for the original approach, the filtered variables $\bar{q}$ can be expressed as a convolution product,

$$\bar{q}(t) = \int_{-\infty}^{\infty} \hat{H}_{sf}(\omega)\hat{q}(\omega) exp(i\omega t) d\omega, \tag{3.3.2}$$

which then becomes solution to a second order ordinary differential equation only function of time,

$$\ddot{\bar{q}} - \ddot{q} + \beta\dot{\bar{q}} + \omega_0^2(\bar{q} - q) = 0. \tag{3.3.3}$$

The main benefit of this method comparatively to SFD is to be able to dynamically track a given feature at a given pulsation ω_0 thanks to Eq. (3.3.3). The counterpart of having access to $\bar{q}$: *i.e.* the flow without the frequency $\omega_0/2\pi$, is that one can easily access $q - \bar{q}$ which is the flow response at ω_0 as time evolves. Contrary to the new approach proposed, most known methods available to compute modes are used as post processing tools.

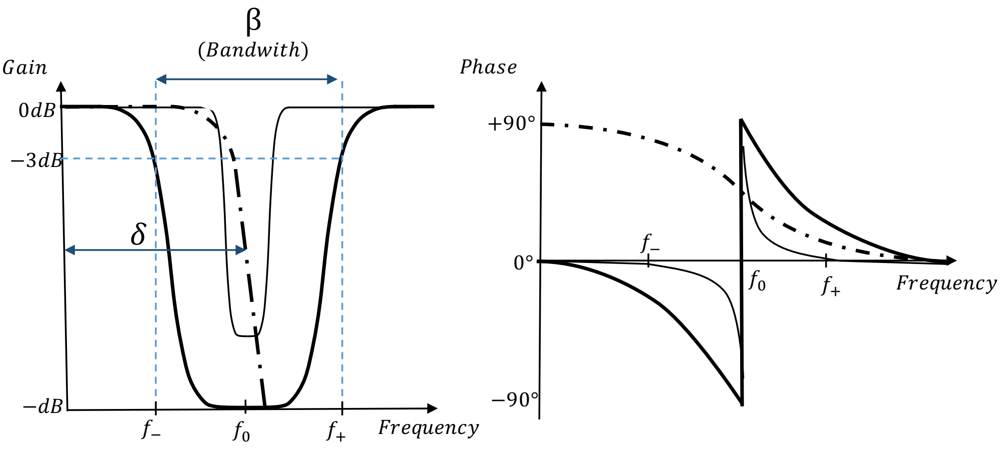

(a) (b)

Figure 3.2 – Ideal filters characteristics: *(a)* Gain and *(b)* Phase as functions of frequency for a classical band-stop filter (━), a narrow band-stop filter also referred to as a Notch filter (—) and a low pass filter (·━).

They can be sensitive to noise and memory demanding. In the following, the proposed solution will be referred to as *Dynamic Mode Tracking* (**DMT**) and will correspond to the NS system augmented by a set of second order ordinary differential equations whose inputs are the instantaneous NS solutions provided by the CFD solver and $(\omega_0^{(n)}, \beta^{(n)})$ values for each equations if multiple modes are to be retrieved (for example N_{modes}). The final CFD solver hence will solve,

$$\begin{cases} \dot{q} = F(q), \\ \text{For } n = 1 ... N_{\text{modes}} \\ \qquad \ddot{\bar{q}}^{(n)} - \ddot{q} + \beta^{(n)}\dot{\bar{q}}^{(n)} + (\omega_0^{(n)})^2(\bar{q}^{(n)} - q) = 0. \end{cases} \tag{3.3.4}$$

Just like for SFD, critical parameters that define the filtering process are for DMT: $(\omega_0; \beta)$. To help understanding the impact of these parameters, the filter equation, Eq. (3.3.3), is rearranged into,

$$\ddot{\bar{q}} + \beta\dot{\bar{q}} + \omega_0^2\bar{q} = \ddot{q} + \omega_0^2 q. \tag{3.3.5}$$

With this form, one notes that the original system corresponds to a forced oscillator problem for which the solution $\bar{q}$ can be expressed as the sum of a homogeneous solution $\bar{q}_h$ and a particular solution $\bar{q}_p$. The exact solution of the homogeneous equation is well known and can be compared to a classical mass-spring-damper model where the speed of convergence is directly associated to the coefficient β. In this context, if one defines $\tau_{90\%}$ the time for the mode/feature to be converged to 90% of its final amplitude, then the following approximation holds,

$$1 - exp^{-\beta\tau_{90\%}/2} = 0.9, \tag{3.3.6}$$

so that,

$$\tau_{90\%} = -2\, ln(0.1)/\beta. \tag{3.3.7}$$

This last expression confirms that the larger β is, the quicker the convergence toward the final mode amplitude is. It also demonstrates that $\tau_{90\%}$ is independent of the filter frequency f_0. Equivalently, the above analysis also indicates that for a system with activity nearby f_0, β needs to be chosen carefully so as to be selective enough and retrieve exactly the good amplitude of the features under study otherwise bias may be introduced due to the spurious forcing of the dynamic system used for identification. In the particular case of single frequency flows, β can be taken very large to obtain a fast convergence of the time filter making DMT suitable to capture accurately mode amplitude variations.

3.4 Dynamical Mode Tracking and Control (DMTC)

One interest behind the above data-based approach aside from having a quick and efficient access to given flow dynamics is that it also allows to actively control the flow so as to avoid the establishment in a solution of the identified activity. In that respect, the initial need for SFD was to force the flow to be steady: *i.e.* $F(q(t)) \to F(\bar{q})$ along with the constraint $\dot{\bar{q}} = 0$ or $q(t) = \bar{q}$. To do so a relaxation term is added to the momentum and energy NS-equations to yield,

$$\begin{cases} \dot{q} = F(q) - \chi(q - \bar{q}), & \text{(3.4.1a)} \\ \delta\dot{\bar{q}} = q - \bar{q}, & \text{(3.4.1b)} \end{cases}$$

where χ is the relaxation coefficient with the dimension of a frequency. With the same objective but with the purpose of avoiding dynamics at given frequencies, a generalized relaxation term can be introduced in the NS operator, Eq. (3.3.4), for the control of specific modes as identified by DMT. The benefit of this frequency dependent feedback control loop is to keep the unsteady solution of the flow while avoiding the presence of specific flow instabilities which is well adapted for linear problems. For more complex flows, such a loop provides access to more understanding of mode coupling in multi modal systems or limit cycles. This variant of DMT will be referred to as *Dynamic Mode Tracking and Control* (**DMTC**) and corresponds to the following system,

$$\begin{cases} \dot{q} = F(q) - \displaystyle\sum_{m}^{M_{\text{controlled modes}}} \chi^{(m)}(q - \bar{q}^{(m)}), & \text{(3.4.2a)} \\ \text{For } n = 1 \ldots N_{\text{modes}} & \\ \quad \ddot{\bar{q}}^{(n)} - \ddot{q} + \beta^{(n)}\dot{\bar{q}}^{(n)} + (\omega_0^{(n)})^2(\bar{q}^{(n)} - q) = 0. & \text{(3.4.2b)} \end{cases}$$

3.4.1 Implementation and effect of DMTC

For all the cases studied hereafter, DMT as well as DMTC have been implemented in the fully compressible Navier-stokes solver AVBP Gourdain *et al.* (2009) by use of second order finite difference operators. Note that for linear problems, the authors have been able to demonstrate the efficiency of DMTC for acoustic phenomeca (see Ãpp. A.2.1). However for hydrodynamics instabilities or strongly non-linear flows, damping a dominant frequency of a system will only shift the operating point of the problem. The new state generated by the artificial control can be predicted by analyzing the eignmodes associated to the DMTC system, Eq. (3.4.2), in the spectral domain. The analysis presented here is inspired by the study of Garnaud *et al.* (2012) who proposed a method to compute modes of a system only in a specific frequency band through linear stability analysis.

For that case, L is the operator associated to the linearized Naviers Stokes equations, and $\mathbf{x}$ the set of coordinates. By decomposing the flow fluctuations as $\dot{q}'(\mathbf{x},t) = \hat{q}(\mathbf{x})exp(i\omega t)$, the linearized version of Eq (3.2.1) can be expressed as,

$$i\omega\hat{q} = L\hat{q}. \tag{3.4.3}$$

By defining Ω, the eigenvalues obtained after activation of DMTC, Eq. (3.4.2) can be written in the spectral domain introducing the operator L' whose associated eigenvectors $\hat{Q}$ satisfy,

$$i\Omega\hat{Q} = L'\hat{Q}. \tag{3.4.4}$$

The key point is then to note that the filtered variables $\hat{\hat{q}}$ and the conservative variables $\hat{q}$ are linked by the filter transfer function,

$$\hat{\hat{q}} = \frac{\omega_0^2 - \Omega^2}{\omega_0^2 + i\beta\Omega - \Omega^2}\hat{q}. \tag{3.4.5}$$

This expression can thus be introduced in Eq. (3.4.2a) to finally obtain,

$$f(\Omega)\hat{q} = L\hat{q}, \tag{3.4.6}$$

with $f(\Omega) = i\Omega + \chi(1 - \frac{\omega_0^2 - \Omega^2}{\omega_0^2 + i\beta\Omega - \Omega^2})$.

This expression shows that the new eigenvalues generated by DMTC can be retrieved by solving a problem of the form,

$$f(\Omega) = \omega. \tag{3.4.7}$$

Corresponding to a 3^{rd} order polynomial with 3 roots associated to the new potential modes issued by the control of the initial ω mode. An application on the cylinder wake of this analysis can be found in App. A.2.2.

In the next section, DMTC is applied to the annular cavity already studied in the previous chapters to extract information about the mode interactions present in this specific flow problem.

3.5 Enclosed annular rotor/stator cavity: Mode interactions

From the previous chapter, DMD showed potential mode feedbacks. Indeed, as already pointed out by Serre *et al.* (2001*b*) and retrieved by Bridel-Bertomeu (2016) through

LES, the mode $m = 12$ is fully expressed in the limit cycle in the rotating disk, it could come from the stator boundary layer and could be amplified though the hub boundary layer. However, the true origin of mode $m = 12$ is therefore particularly difficult to explain. For example, Bridel-Bertomeu (2016) who studied the exact same cavity, mentioned that mode $m = 29$ was the possible source of mode $m = 12$. This section aims at verifying this hypothesis thanks to the new tools introduced in the previous section. To do so, one offers a direct view of the total flow and its reaction when the different modes are controlled one by one and on-the-fly. Note that thereafter and throughout the study, the modes $m = 29$, $m = 12$ and $m = 0$ will be respectively called **stator mode**, **rotor mode** and **annular mode**.

The section is organized as follow: First, **DMT** is used to retrieve the shape of the three main modes driving the annular cavity. Note that in this case; it will correspond to the modes expressed in the fully developed limit cycle of the configuration in opposition to the linear modes computed with a linear stability approach. To obtain these results, only one simulation is conducted. In Sec. 3.5.2, **DMTC** is then applied to understand mode dominance and potential interactions as produced by LES. In particular, the interest is here to evidence the link between the rotor mode and the stator mode. For this study, two different simulations are presented and both are initialized with the simulation results obtained with DMT. Each simulation corresponds to the control of **one mode** and a direct evaluation of the reaction of the non controlled modes. The *stator mode* control is first analyzed followed by the control of the *rotor mode.*

3.5.1 Mode Tracking (DMT)

DMT is first used along with LES to track the three main modes of the cavity with a narrow bandwidth: $\beta = 20Hz$. The trace of the three modes axial velocity component captured by DMT are displayed in Fig. 3.3(a)-(c), respectively for the stator, rotor and annular modes, all taken in a plane located in the stator boundary layer at $z = 0.034\,m$ for three different instants. To complement this spatial vision of the modes, the temporal signal of a numerical probe placed around the location of the axial velocity fluctuation maximum for each mode is displayed in Fig. 3.3(d)-(f) respectively for the stator, rotor and annular mode. Clearly, DMT retrieves here the characteristic spiral patterns with $29-$arms for the stator mode, $12-$arms for the rotor mode and the annuli of the annular mode. Note that each feature requires only 3 periods of oscillation to yield an accurate shape of the mode. Furthermore, as shown in Sec. 3.3, a time $\tau_{90\%} = -2\,ln(0.1)/\beta = 0.23$ s is necessary to retrieve 90% of each mode amplitude. In this particular study, a limit of the method can be observed with the annular mode. As shown by Fig. 3.4, the same DMT filters have been taken for the annular and stator mode extraction. Both modes having a frequency very close, DMT captures for both modes approximately 5% of the other mode. However, the stator mode having an amplitude 40% higher than the annular mode, it is not unexpected that the DMT results of this latter mode are marked by the spirals of the stator mode. The snapshot of Fig. 3.3(c)I indeed shows residues of the spiral mode $m = 29$ marking the annular mode spatial distribution. A narrower bandpass filter width could be taken to avoid such bias but would also involve longer convergence time (See Eq. (3.3.7))

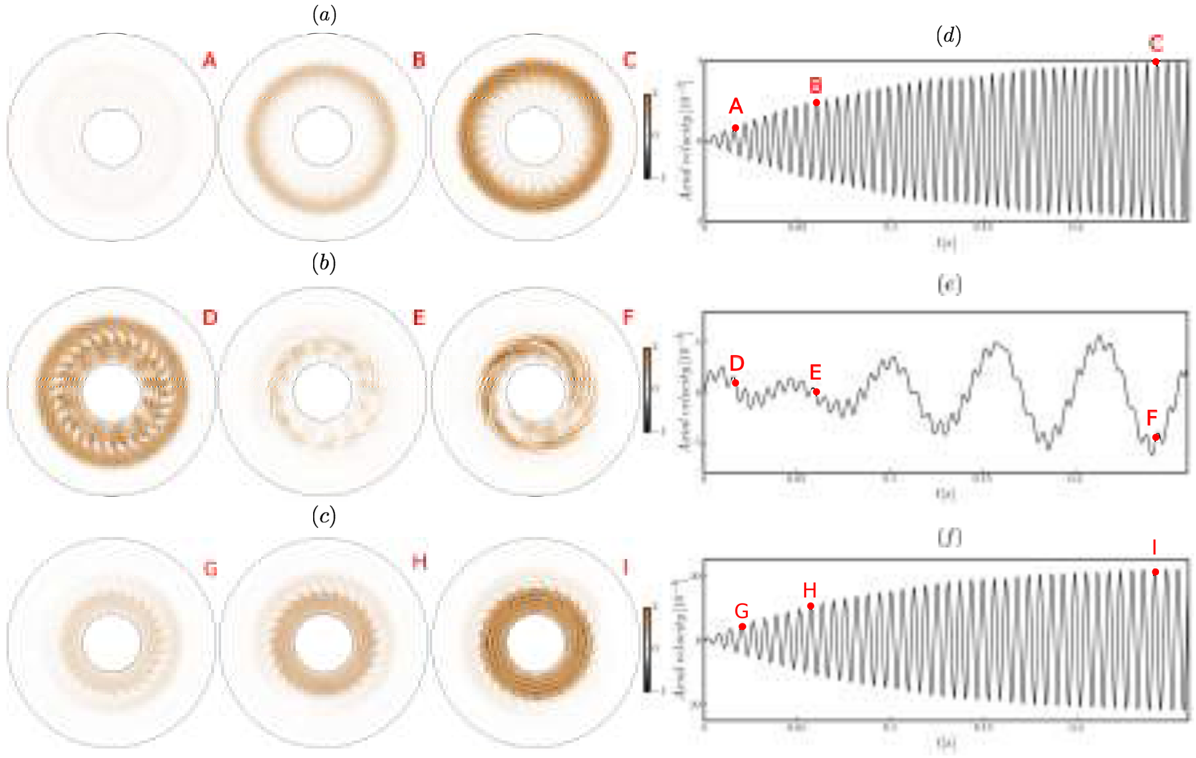

Figure 3.3 – Axial velocity perturbation: 3 instantaneous at $t = [0.02s, 0.06s, 0.24s]$ are displayed for the stator mode in *(a)*, the rotor mode in *(b)* and the annular mode in *(c)* in a plan located at $z = 0.034\,m$. Axial velocity perturbation at the probes (r,θ,z) = (0.16,0,0.0352), (r,θ,z) = (0.225,0,0.001) and (r,θ,z) = (0.08,0,0.0352) is also plotted for respectively the stator mode in *(d)*, the rotor mode in *(e)* and the annular mode in *(f)*.

3.5.2 Mode Control (DMTC)

Thanks to DMT "on the fly" capacity, one uses in the following DMTC to analyse mode interactions. In that case and to evaluate the temporal response of the system, one defines E_v^m the kinetic energy associated to the m^{th} mode over the domain,

$$E_v^m = \int_V \rho \frac{(u - \bar{u}^{(m)})^2}{2} dv \quad m = 0, 12, 29 \tag{3.5.1}$$

which is then followed in time.

In the next paragraphs, two separated simulations are conducted both from the converged results of DMT. First, the stator mode is suppressed with DMTC while following the three modes of the system with DMT. This investigation enables to see the reaction of the rotor mode to the suppression of the stator mode. To ensure the dominance of the

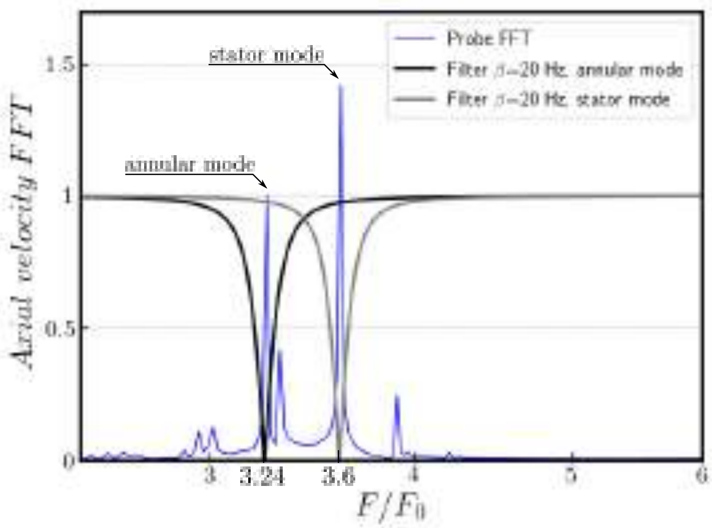

Figure 3.4 – Axial velocity on a probe and the time filters used on the annular mode ($F/F_0 = 3.24$) and stator mode ($F/F_0 = 3.6$).

stator mode over the rotor mode the inverse simulation is also realized: *i.e* the suppression of the rotor mode and the investigations of the two remaining mode reactions.

Stator mode control

As said, only the stator mode is controlled using a relaxation coefficient of $\chi = 50$. Figures 3.5(a)-(c) display respectively the non dimensional energy E_v^m/E_{max}^m, where E_{max}^m is the converged kinetic energy of a mode m obtained with DMT; *i.e.* either of the stator, rotor and annular modes (the two lattest being not controlled).

Three instantaneous axial velocity fields in Fig. 3.5(d)-(f) have been extracted from the simulation to visualize respectively the stator, rotor and annular modes as they evolve in time. As seen, the stator mode is damped really quickly: *i.e* after 3 transitional growths Fig. 3.5(a). The corresponding instantaneous field, in Fig. 3.5(c), shows that only residues of the mode are present after a long simulation time. At the same time, the rotor mode is also progressively suppressed. The response of this mode is however slower than the stator mode. Indeed, as shown in the instantaneous fields of Fig. 3.5(e), the mode is progressively altered and becomes disymmetric, indicating that the rotor mode can not exist without the stator mode. This observation is in adequacy with Bridel-Bertomeu (2016) hypothesis.

The feedback of the annular mode to the stator mode damping can be observed in Fig.3.5(c). Even though the annular mode is impacted, no clear link between these two modes can be effectively highlighted. Indeed, the results show that the mode amplitude is decreased by a half but remains and tends to reach a stable state. As evoked in the previous section with Fig. 3.4, this effect is more likely due to the bandwidth of the filter

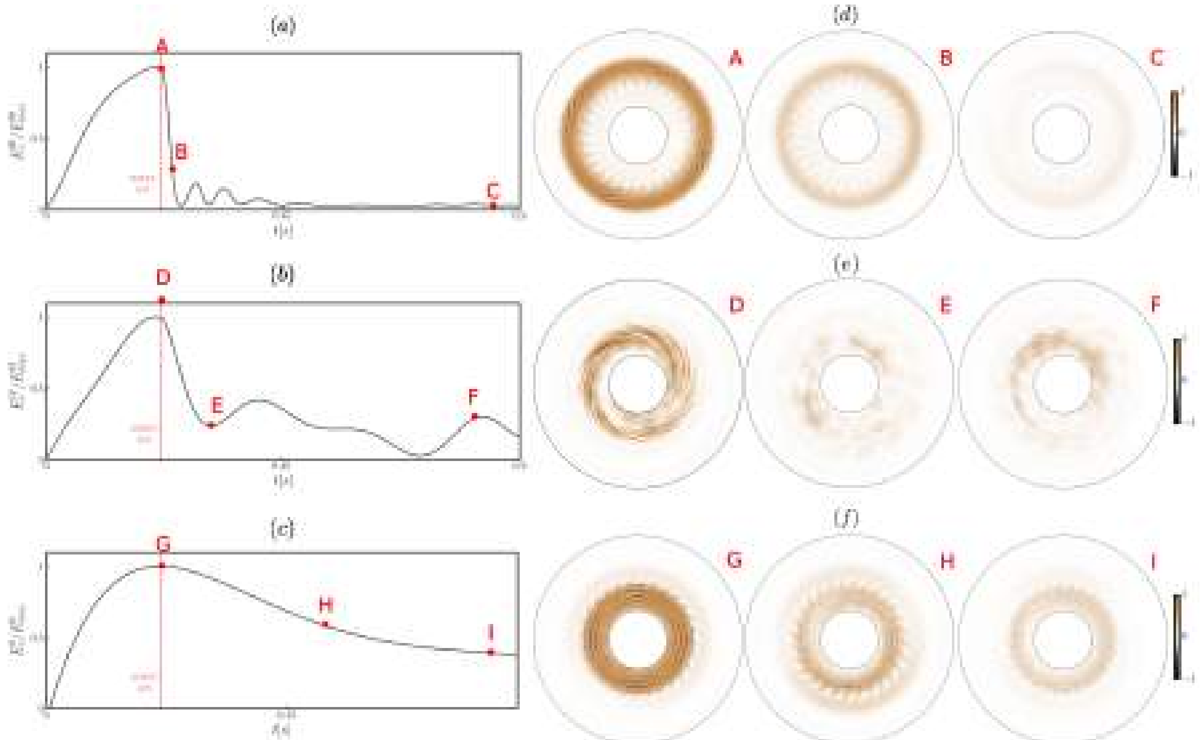

Figure 3.5 – Kinetic energy (Eq. (3.5.1)) of *(a)* the stator mode ($m = 29$), *(b)* the rotor mode ($m = 12$) and *(b)* the annular mode ($m = 0$) obtained with the DMTC. 3 axial velocity fields at $t = [0.25s, 0.3s, 0.8s]$ are displayed for the stator mode in *(d)*, the rotor mode in *(e)* and the annular mode in *(f)* in a plan located at $z = 0.034\,m$.

chosen. Since the annular mode is marked by the spiral of the stator mode, by controlling the latter, one expects to observe an impact on the annular mode amplitude.

Rotor mode control

In this second study, the rotor mode is damped while the stator and annular mode remain uncontrolled. Figure 3.6 presents the assocaited results associated following the organization of Fig. 3.5. As one can see, the stator mode is not really impacted by the rotor damping while the rotor mode disappears as time progresses. These results confirm that the stator mode is at the origin of the rotor mode which agrees also with the sensitivity analysis to be conducted in Chap. 4. In case of the annular mode, no impact is observed as the mode rotor disappears. Those observations are also in adequation with Serre *et al.* (2001*a*) who studied a similar configuration. He indeed showed that the stator-layer instabilities are convected along the hub and induce disturbances in the rotor layer triggering first axisymmetric (annular mode) and later three-dimensional convective modes characterized by an opposite angle spiral (rotor mode).

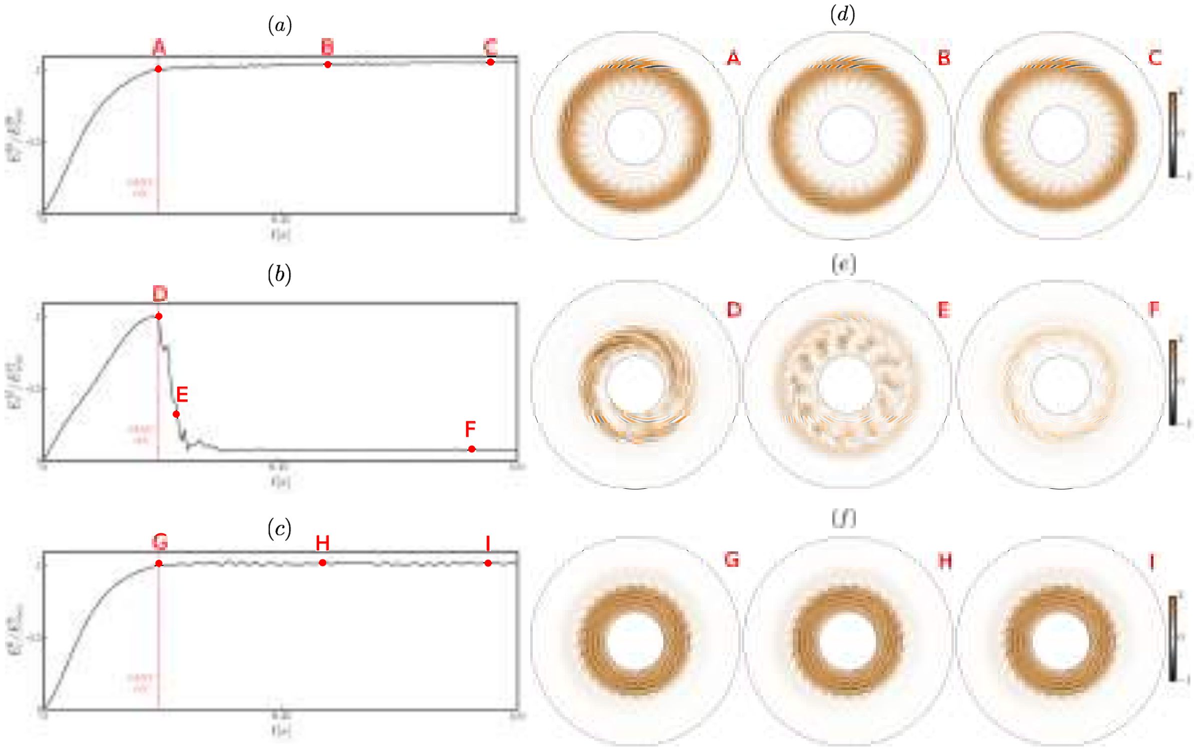

Figure 3.6 – Kinetic energy (Eq. (3.5.1)) of *(a)* the stator mode ($m = 29$), *(b)* the rotor mode ($m = 12$) and *(b)* the annular mode ($m = 0$) obtained with the DMTC. 3 axial velocity fields at $t = [0.25s, 0.3s, 0.8s]$ are displayed for the stator mode in *(d)*, the rotor mode in *(e)* and the annular mode in *(f)* in a plan located at $z = 0.034\,m$.

3.6 Conclusions

The main goal of this chapter was first to study mode interactions of the enclosed rotor/stator annular cavity and in particular point out the link between the dominant mode and low frequency modes. In fact, in order to set up a control system to damp a multi-frequency phenomenon, strategies need to be chosen. To find answers to this problematic, a new tool called Dynamic Mode Tracking/Control (DMT/DMTC) was introduced to track dynamically modes or flow features thanks to time filters. Contrary to classical flow feature analyses, DMT has the benefit of being easy to implement in a Navier-Stokes solver and gives a direct possibility to visualize a mode evolution over time. Furthermore, by computing a mode on-a-fly, DMT also offers gain in memory and time of computation compared to classical post-processing methods like DMD. With DMTC, modes can also be artificially controlled thanks to a relaxation method. A complete set of test cases with parameter sensitivity analyses was proposed (see App. B) to validate this two new methods.

Whenever applied to the annular rotor/stator cavity, DMT is able to retrieve the spiral and annular patterns of the DMD analysis. In its DMTC version, the method is also shown to enable the control of individual modes as desired. In this context, damping the rotor mode proves to have no effect on the stator nor the annular modes. On the contrary, suppressing the stator mode induces the rotor mode to be progressively attenuated, signifying that it can not live without the stator mode. The link between the annular and the stator mode is however particularly difficult to analyse through this method. Indeed a significant decrease of the annular mode is observed when the stator mode is controlled: the gap between the mode frequencies being very narrow, one can directly conclude that this damping is due to a too wide DMT filter. Conclusions could be obtained by reducing the filter width but would involve longer time convergence. At the end, this study still highlights that to stabilize the whole cavity, controlling the stator mode would be the more efficient. Finally, even though a first insight on the mode organization has been highlighted through their interactions, a complete understanding of their sources and mechanisms still needs to be produced. As evoked in the introduction of this chapter, one of the widely used method to analyze an unstable flow is linear stability analysis. In the next chapter, this specific method is developed to investigate each mode separately and to set up control strategies.

Publication:

These results of the present part have been the subject of a conference paper and a A ranked journal publication:

- Queguineur, M., Gicquel, L. Y. M., Dupuy, F., Misdariis, A., Staffelbach, G. Dynamic mode tracking and control with a relaxation method. **Physics of Fluids**, 2019,
- Queguineur, M., Gicquel, L. Y. M., Stafflebach, G. Modes identification and interactions in a rotor/stator academic cavity. 13th European Turbomachinery Conference on Turbomachinery Fluid Dynamics and Thermodynamics, **ETC**, 2019.

Part II

Global stability analysis of an enclosed rotor/stator cavity

Chapter 4

Modes identification and stability analyses

Contents

Although rotating cavity flows are essential components of industrial applications, their dynamics is still largely misunderstood. From computer hard-drives to turbo-pumps of space launchers, designed devices often produce flow oscillations that can either destroy the component prematurely, produce disturbing noise or undesired operating modes of the system. Fundamentals of encountered static and rotating flow boundary layers have evidenced, a long time ago now, the presence of specific boundary layer instabilities and structures for low Reynolds numbers. For higher Reynolds numbers and fully enclosed systems, features are however more complex with the apparition of multi-frequency oscillations populating the entire cavity limit cycle. Large Eddy Simulation (LES) has illustrated in Part 2 its capacity of reproducing these features and limit cycles. Complemented by the developed approaches that are DMT/DMTC, mode dominance could also be identified thanks to LES. However, identifying the origin and region within these flows that are responsible for mode selections remains difficult if not impossible using such Computational Fluid Dynamics (CFD) tools. The present chapter evaluates a global stability analysis framework to identify the potential mechanisms responsible for the observed limit-cycle in the annular cavity. In parallel, a study of the cylindrical rotor/stator cavity is also realized to shed some light on the impact of a central body (or hub) and the instability selection. Results issued by the conjunct use of Global Linear Stability Analysis (GLSA) and sensitivity analysis confirm the observed LES dynamics and DMD/DMT results. Most importantly GLSA gives access to the triggering mechanisms at the root of the limit-cycle expression as well as hints on the mode selection. In that respect, the cylindrical cavity is shown to sustain more complex features than the annular cavity because of an enhanced flow curvature near the central hub.

4.1 Flow instabilities

In fluid mechanics, flow transition from laminar to turbulent has been a complex subject of studies for more that 150 years. In this context, hydrodynamic stability theory has been a key to explain this phenomenon that was first studied by Reynolds with the famous "Reynolds experiments" (Reynolds (1883)). As a follow up to this experiment, many famous scientists have attached their names to various instabilities. For instance, Kelvin for the Kelvin-Helmhotz instabilities has highlighted how two fluids flowing at different velocities can create a shear velocity responsible of instabilities. Figure 4.1(a) gives an example of such a process with the formation of typical cloud patterns formed between two layers of air traveling at different speeds. Likewise, the Rayleigh-Taylor instabilities Rayleigh (1883) occur between two fluids but for two different densities. All of these instabilities appear in a number of different situations and can be easily evidenced for instance by dropping coloured oil into water, creating tiny upside-down mushroom clouds as shown in Fig. 4.1 (b). Less known, but still very complex, the Rayleigh-Bernard instabilities happen inside a fluid confined between two infinite horizontal planes at different temperatures (see Fig.4.1 (c)). For more details on the occurence and specifities of instabilities, interested reader can refer to Drazin & Reid (2004) for a complete review.

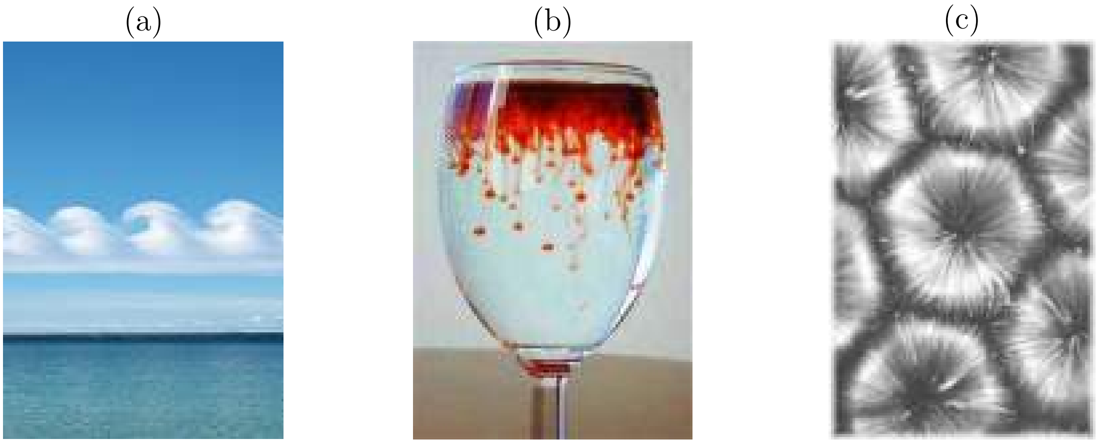

Figure 4.1 – 3 examples of instabilities: (a) Kelvin-Helmotz (b) Taylor-Rayleigh instability, source : experiment of James Riodon, AIP (c) Rayleigh-Benard instability, source: The Parabolic Press. Van Dyke, M., 1982

In the specific context of rotating flows over disks, complex three-dimensional instabilities have been observed and studied for more than a century with the first studies being carried out by Ekman (1905) and his attemps to understand how Earth rotation influences wind-driven ocean currents. Rotating flows over disks are still today a subject of interest of many industrial applications (atmospheric and oceanic flows, rotating cavity flows, centrifugal separator process, computer storage devices, chemical vapor deposition (Lingwood & Henrik Alfredsson (2015)) and in particular in turbomachinery devices. In the two previous chapters, LES helped capturing the pressure band phenomenon in the boundary layers of the annular and cylindrical cavity disks. Furthermore, DMT/DMTC gave a first information on the $m = 29$ and $m = 12$ link. However, the precise origins and mechanisms of these modes could not be identified especially for the annular mode $m = 0$. This chapter introduces a linear stability analysis framework and details their application on academic rotating cavities to find answers to this problematic. In a first section, features of infinite rotating disks similar to the one found in enclosed rotor/stator cavities are presented. In Sec. 4.3, a complete description of the stability analysis principle and the associated tools are provided. Finally, the results from dedicated stability analyses on the cavities are detailed and discussed in Sec. 4.4.

4.2 Rotating boundary layers and cavity flows

Over the years, many academic rotating flows have been studied. A classification of these flows has hence been realized by introducing on top of the Reynolds number, the Rossby number Ro which characterizes the ratio of advection to the Coriolis effect:

$$Ro = \frac{U}{L\Omega}, \tag{4.2.1}$$

where U, Ω and L refer respectively to the velocity of the fluid, the rotation rate of the rotating parts and the length scales which will vary depending on the rotating flow studied. Note that in the particular case of a flow induced by a rigid-body in rotation over a disk, one can define Ω_f, the rotation rate of the homogeneous core of fluid, Ω_d the rotation rate of the disk (if rotating) and δ the viscous characteristic length usually defined as $\delta = (\nu/\Omega_d)^{1/2}$ with ν the kinematic viscosity of the fluid. Based on this new reference numbers and lenght-scale, Faller (1991) suggested a more relevant definition of non-dimensional numbers relating the rotating boundary layer to the Reynolds and Rossby numbers, so that:

$$Re_\delta = \frac{(\Omega_f - \Omega_d) r\delta}{\nu} = \frac{r}{\delta} Ro, \tag{4.2.2}$$

and where

$$Ro = \frac{\Delta\Omega}{\tilde{\Omega}}, \tag{4.2.3}$$

for which $\tilde{\Omega} = (\Omega_f + \Omega_d)/4 + ((\Omega_f + \Omega_d)^2/16 + (\Omega_f - \Omega_d)^2/2)^{1/2}$, r is the radial coordinate and $\Delta\Omega = \Omega_f - \Omega_d$.

From the above new definitions, one can define three types of rotating boundary layers induced by the differential rotation of a rigid rotating inviscid flow over a disk:

- Ekman (1905) and Von Kármán (1921) flows: In Ekman and Von Kármán rotating boundary layers, the flows are radially thrown outwards because of the centrifugal force and create a downward axial flow. This effect is illustrated in Fig. 4.2(a) where U,V and W denote respectively the mean radial, azimuthal and axial velocities. These two types of flow can be distinguished by the behavior of their homogeneous core of fluid:

  - Ekman (1905) flow: Ekman was the first to describe rotating boundary layers by setting a theory on the influence of the Earth's rotation on ocean currents. More generally, the Ekman layer occurs when a disk and fluid rotate with approximately the same angular velocity, *i.e*, $\tilde{\Omega} = \Omega_f = \Omega_d$ and $Ro = 0$.
  - Von Kármán (1921) flow: A few years later, Von Kármán formulated the similarity equations giving the exact solution to the Navier-Stokes equations for a laminar flow over an infinite disk spinning in an unbounded fluid at rest sufficiently far above the disk, *i.e*, $\Omega_f = 0$, $\tilde{\Omega} = \Omega_d$ and $Ro = -1$.

  A complete review on these specific rotating boundary layers can be found in Lingwood & Henrik Alfredsson (2015).

- Bödewadt (1940) flow: Much later, Bödewadt studied the flow produced over an infinite stationary plane in a fluid rotating with a uniform angular velocity at an infinite distance from the plane, *i.e*, $\Omega_d = 0$, $\tilde{\Omega} = \Omega_f$ and $Ro = 1$. Much less studies have however been realized on this type of boundary layer flow because of the difficulty to reproduce it experimentally. The Bödewadt layer contrary to the first boundary layer flows corresponds to an equilibrium between the centrifugal, Coriolis forces and the radial pressure gradient forces in the core flow. The viscous dissipation and the radial pressure gradient flow yield therfore an inward axial flow close to the disk, Fig.4.2(b). Batchelor (1951) showed that the ratio of the fluid and disk rotation velocities are sufficient to characterize the steady laminar flow over an infinite disk.

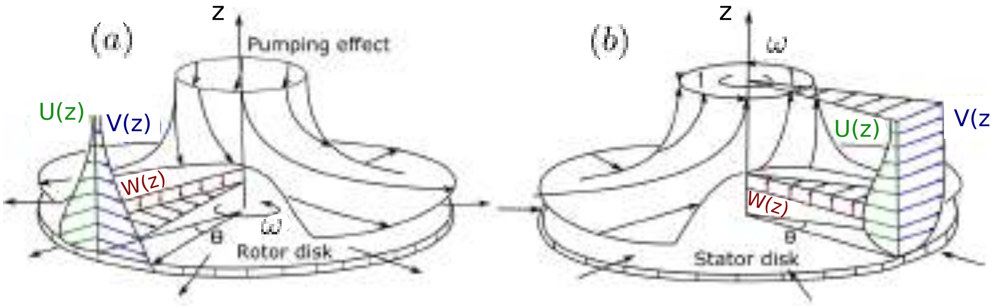

Figure 4.2 – Flow behaviour of a fluid initially at rest put in motion by a rotating disk (a) and a rotating fluid over a stationary disk (b). From Schlichting & Gersten (2001).

Note that, by adopting a dimensionless form of the continuity and momentum equations in cylindrical coordinates for axisymmetric steady flows (Lingwood (1995)), these three specific flows can be generalized and are usually referred to as the BEK (Bödewadt Ekman Kármán) family .

BEK Characteristic instabilities

It is now well known that the above discussed undisturbed boundary layer flows become unstable when Re_δ exceeds a critical value. Table 4.1 from Crespo del Arco *et al.* (2005) sums up these different critical values for the different types of rotating boundary layers. Many stability studies on the BEK model have therefore been realized during the last decades and have permitted to classify the different instabilities of rotating flows apt to support the laminar/turbulent transition in 3 types:

- Cross flow Instability, referred to as Type-1: This type of instability has been first discovered by Smith (1947) and occurs if the mean velocity component profiles are inflectional. Gregory *et al.* (1955) observed experimentally that this instability occurs in the case of the Von Kármán and Ekman boundary layers which was confirmed a few years later by Faller (1991). These specific instabilities mark the flow as 3D **spiral** patterns .

- Convective instability, referred to as Type-2: Malik (1986) extended the work of Gregory by computing the neutral curves for stationnary disturbances. He confirmed the existence of the Type-1 instability and showed an additional mode. This last one is due to the viscous part of the flow and comes from the Coriolis forces

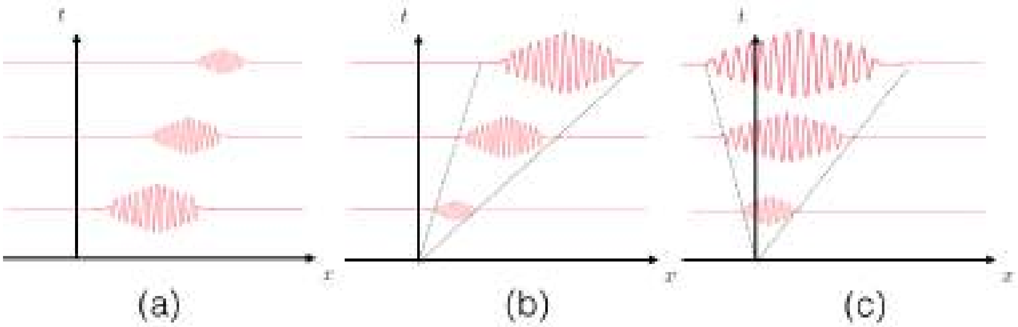

Figure 4.3 – The 3 types of responses of a perturbation: (a) Stable, (b) Convectively unstable, (c) Absolutely unstable.

which curve the flow streamlines. Contrary to Type-1, these specific instabilities appear as **annular** patterns.

- Absolute instabilities. Lingwood (1996) pointed out a third instability called absolute instabilities first described in Huerre & Monkewitz (1990). This specific instability differs from the convective instability by the way it propagates and grows in the system. As shown in Fig. 4.3, if the flow is convectively unstable, a spatially unstable wavepacket is typically advected away from the source and let it eventually undisturbed. On the other hand, if the flow is absolutely unstable, the unstable wavepacket surrounds the source and eventually contaminates the whole medium. Absolute instabilities can be also seen as an over production of fluctuations compared to their transport. Contrarily, for a convective instability, the transport of fluctuations will be dominant. The absolute instabilities are known to be responsible for the laminar-turbulent transition and the onset of the nonlinear behavior of the flow. More details on these instabilities are given in Sec. 4.3.1.

Rossby number	Type II	Type I	Neutral stability for stationary waves	Absolute instability
$Ro = -1$ (Von kármán)	69.4	285.3	290	507
$Ro = 0$ (Ekman)	54.3	113.1	116.3	198
$Ro = +1$ (Bödewadt)	15.1	[15.1; 25]	27.4	21.6

Table 4.1 – Critical Reynolds numbers Re_{δ_c} obtained by stability analysis for the three basic types of rotating boundary layer flows by Faller (1991) and Lingwood (1996).

Local stability analyses (see Sec. 4.3.1 for more details) were at the root of the discovery of the different instabilities that can trigger the flow of the BEK family. It futhermore enabled to discover the convectively unstable mode (Type-2) of the Von Kármán boundary layer (Faller & Kaylor (1966)). The same authors also confirmed that this instability is also present in the Ekman boundary layer, dominates at low Reynolds numbers and becomes stable in the inviscid limit. Both Type-1 and 2 instabilities are unstable to stationnary disturbances and also to disturbances traveling relative to the disk surface but with different critical local Reynolds numbers (See 4.1). Traveling Type-2 disturbances were observed in expermients (Faller (1991); Tatro & Mollo-Christensen (1967)) and theoretically studied for the Ekman boundary layer by Lilly (1966).

From local to global instabilities

For the specific Von Kármán boundary layer, local absolute instabilities corresponding to disturbances growing in time at fixed radial postions (see Sec 4.3.1 for more information) were found by Lingowood through a spatio-temporal linear stability analysis (Lingwood (1996)) and for Reynolds numbers much higher than the Type-1 and Type-2 instabilities (See 4.1). These specific instabilities were obtained in a local context and are often associated to the transition to turbulence but their link to the global beahviour of the flow is still an open subject of research. However, Davies & Carpenter (2003) showed through linearized Navier–Stokes equations submitted to a specific impulse excitation that local instabilities do not produce global linear instabilities. Their link with a global mode (real self-sustained oscillation oberved in experiments) were only clarified by Pier (2003, 2007) through non linear stability analyses. He indeed showed that the primary local absolute instabilities are unstable to secondary absolute disturbances generating disorder and triggering global modes. This type of mode has then been referred to as an *elephant mode* in the litterature Pier *et al.* (1998); Pier (2007). Besides the Von Kármán boundary layer, from the author's knowledge, only a few studies focusing on the two other flows of the BEK family and on the mechanisms triggerring a global mode have been realized. One can site at least the study of Davies & Thomas (2016), who used a global stability framework to evidence that the BEK family is globally linearly stable. However, only Rossby numbers in the range $-1 \leq Ro \leq 0.6$ were studied. When it comes to the Bódewadt boundary layer ($Ro = 1$), it was not investigated due its highly unstable nature.

4.3 Linear Stability Analysis (LSA) of Rotating flows

Stability analyses can be used in many different fields from the simple stability of a tree in a windstorm James *et al.* (2016) to the complex studies of the evolution of a star structure Chandrasekhar (1984). In fluid dynamics, a "base flow" can be said stable in the sense of Lyapunov (1992), if an infinitesimal perturbation of this base flow stays infinitesimal over time or if the perturbed flow stays around the base flow. In addition of telling us if a flow is stable or unstable, the main goal of a linear stability analysis is to give the physical features of the response of a little perturbation around the base flow: frequency, amplification rate (also called growth rate), spatial and temporal evolution.

This section intends to descibe how this method works in details in the particular case of a rotating flow. The interested reader can find more information about this theory in the book of Drazin & Reid (2004).

Base flow versus Mean flow

From theory, all linear analysis has to be done around a base flow solution of the Navier Stokes equations that can be stationnary or time-periodic. For simple cases, one can use analytical solutions as done for a simple rotating disk (see Sec. 4.2). For complex configurations, recent methods were developped to construct a base flow from unsteady simulations (Selective Frequency Damping (SFD) Åkervik *et al.* (2006); Jordi *et al.* (2015)). For limit-cycle studies, non linearities can become predominant and cause a so called base flow distorsion. This last phenomenon can make difficult the use of such framework especially of one intends to retrieve the good frequencies resulting of non-linear processes (like the frequencies observed in experiments or numerical simulations of high *Re* cases). For such complex flows, the mean flow is usually taken after manipulation (time-averaged solution typically) and can be obtained thanks to CFD for example. This last choice is however still a great subject of debate, Beneddine *et al.* (2016). Indeed, even if the mean flow is most of the time not a fixed point of the Navier-Stokes equations, it still enables to take into account a part of the non linearities of the flow. For example, in the case of a flow around a cylinder, Pier (2002) showed very good predictions of the vortex shedding frequency, even far from the critical Reynolds number by using its mean flow. A good review of the mean flow properties and its impact on linear stability analysis can be retrieved in Turton *et al.* (2015) and Bengana *et al.* (2019).

Governing equations

One describes here the construction principle of the governing equations for an axisymmetric rotating flow. In the following, p and $\mathbf{u} = (u_r, u_\theta, u_z)^T$ represent respectively the pressure and velocity perturbations while $\mathbf{U} = (U_b, V_b, W_b)^T$ stands for the base flow solution of the steady Navier-Stokes equations.

After linearization of the Navier-Stokes equations around the base flow, the following first order system of equations in the cylindrical-polar coordinates (r, θ, z), are obtained:

$$\frac{1}{r}\frac{\partial(ru_r)}{\partial r} + \frac{1}{r}\frac{\partial u_\theta}{\partial \theta} + \frac{\partial u_z}{\partial z} = 0, \tag{4.3.1}$$

$$\frac{\partial u_r}{\partial t} + u_r\frac{\partial U_b}{\partial r} + U_b\frac{\partial u_r}{\partial r} + W_b\frac{\partial u_r}{\partial z} + u_z\frac{\partial U_b}{\partial z} + \frac{V_b}{r}\frac{\partial u_r}{\partial \theta} + \frac{u_\theta}{r}\frac{\partial U_b}{\partial \theta} - \frac{2V_b u_\theta}{r} = -\frac{1}{\rho}\frac{\partial p}{\partial r} + \nu\left(\frac{\partial^2 u_r}{\partial z^2} + \frac{\partial^2 u_r}{\partial r^2} + \frac{1}{r^2}\frac{\partial^2 u_r}{\partial \theta^2} + \frac{1}{r}\frac{\partial u_r}{\partial r} - \frac{u_r}{r^2} - \frac{2}{r^2}\frac{\partial u_\theta}{\partial \theta}\right), \tag{4.3.2}$$

$$\frac{\partial u_\theta}{\partial t} + U_b\frac{\partial u_\theta}{\partial r} + u_r\frac{\partial V_b}{\partial r} + W_b\frac{\partial u_\theta}{\partial z} + u_z\frac{\partial V_b}{\partial z} + \frac{U_b u_\theta}{r} + \frac{u_r V_b}{r} + \frac{V_b}{r}\frac{\partial u_\theta}{\partial \theta} + \frac{u_\theta}{r}\frac{\partial V_b}{\partial \theta} = -\frac{1}{r\rho}\frac{\partial p}{\partial \theta} + \nu\left(\frac{\partial^2 u_\theta}{\partial z^2} + \frac{\partial^2 u_\theta}{\partial r^2} + \frac{1}{r^2}\frac{\partial^2 u_\theta}{\partial \theta^2} + \frac{1}{r}\frac{\partial u_\theta}{\partial r} - \frac{u_\theta}{r^2}\right), \tag{4.3.3}$$

$$\frac{\partial u_z}{\partial t} + U_b\frac{\partial u_z}{\partial r} + u_r\frac{\partial W_b}{\partial r} + W_b\frac{\partial u_z}{\partial z} + u_z\frac{\partial W_b}{\partial z} + \frac{V_b}{r}\frac{\partial u_z}{\partial \theta} + \frac{u_\theta}{r}\frac{\partial W_b}{\partial \theta} = -\frac{1}{\rho}\frac{\partial p}{\partial z} + \nu\left(\frac{\partial^2 u_z}{\partial z^2} + \frac{\partial^2 u_z}{\partial r^2} + \frac{1}{r}\frac{\partial u_z}{\partial r} + \frac{1}{r^2}\frac{\partial^2 u_z}{\partial \theta^2}\right). \tag{4.3.4}$$

This set of equations can be reformulated in the following matrix system:

$$B\frac{\partial q}{\partial t} = Jq \tag{4.3.5}$$

for which $q = (u_r, u_\theta, u_z, p)^T$ is the perturbation vector and J the Jacobian of the Navier-Stokes equations.

Stability analysis around the base flow is then given by the spectrum of eigenvalues of the matrix J. Depending on the nature of the base flow (parallel, weakly non-parallel, two or three-dimensional flow), different types of analyses can be realized:

- Local stability analysis: Simple flows with the parallel flow assumption (reduced system of equations),
- Global stability analysis: More complex flows with a non parallel assumption (full set of equations).

In the following two sections, the local and global methods are described and applied to enclosed cavities.

4.3.1 Local Stability

Flow instabilities were particularly difficult to study in the past because of the lack of computational resources or even analytical tools. Most of the investigations therefore assumed that the wavelength of the underlying instability mechanism is short compared to the typical scale over which the flow develops in the streamwise direction. Under such an assumption, parallel base flow rotating around an axis z has the form:

$$\begin{aligned} \mathbf{U} &= (U_b(z), V_b(z), W_b(z))^T, \\ P &= P_b(z). \end{aligned} \tag{4.3.6}$$

By imposing perturbations of the form $[u_i, p] = [u_r(r,\theta,z,t), u_\theta(r,\theta,z,t), u_z(r,\theta,z,t), p(r,\theta,z,t)]$ on the base flow with the following global decomposition:

$$\begin{cases} U(r,\theta,z,t) = & U_i(z) + u_i(r,\theta,z,t), \\ P(r,\theta,z,t) = & P_b(z) + p(r,\theta,z,t), \end{cases} \tag{4.3.7}$$

the set of Eqs. (4.3.1)-(4.3.4) can be simplified and becomes separable in r, θ and t. The perturbations can hence be represented with a normal mode formulation so that:

$$[u_r, u_\theta, u_z, p]^T = [\hat{u}_r, \hat{u}_\theta, \hat{u}_z, \hat{p}]^T(z)\ exp[(i(\alpha r + m\theta - \omega t)] \tag{4.3.8}$$

In this case, a given mode is said normal because it is considered independent of the other modes of the systems. Each mode can hence be represented by a pair of parameters (α, ω) with α a complex wavenumber $\alpha = \alpha_r + i\alpha_i$ and ω a complex frequency $\omega = \omega_r + i\omega_i$. With this notation, $\alpha_r = \mathfrak{Re}(\alpha)$ corresponds to the real wavenumber of the perturbation and $\alpha_i = \mathfrak{Im}(\alpha)$ is the amplification rate in space of the mode. A similar physical interpretation of ω can be given *i.e*, $\omega_r = \mathfrak{Re}(\omega)$ represents the real frequency and $\omega_i = \mathfrak{Im}(\omega)$ is the amplification rate in time of the mode. Finally m represents the azimuthal wavenumber. In case of a rotating cavity, modes corresponding to $m = 0$ will be axisymmetric and for $(|m| > 0, |\alpha| > 0)$, modes will show spiral patterns with $m-$arms.

By introducing the normal modes in the linearized equations, Eqs. (4.3.1)-(4.3.4), one can formulate a dispersion problem which reads

$$D_L(\omega, \alpha, m, \hat{q}) = 0, \tag{4.3.9}$$

where D_L denotes the problem dispersion relation of a general local stability analysis. (The detailed equations of this problem can be retrieved in App. A.1). Thanks to this dispersion relation, several types of analysis can be done as detailed hereafter.

Temporal analysis:

The temporal analysis purpose is to find the complex frequency ω by fixing a real wavenumber $(\alpha \in \mathbb{R})$. In other words, find the response of the flow to an α given spatial excitation. The dispersion problem of Eq. (4.3.9) is in such a case reduced to the following eigenvalue problem (EVP) :

$$A\hat{q} = \omega B\hat{q}, \tag{4.3.10}$$

with $\hat{q} = [\hat{u}_r, \hat{u}_\theta, \hat{u}_z, \hat{p}]^T$

The growth of the infinitesimal perturbations $\hat{q}$ is then governed by $\mathfrak{Im}(\omega) = \omega_i$ (the imaginary part of ω):

- if $\omega_i > 0$: The base flow is said linearly and locally unstable. The perturbation grows exponentially with time,
- if $\omega_i < 0$: The base flow is said linearly and locally stable. The perturbation decays exponentially with time,
- if $\omega_i = 0$: The base flow is said neutrally stable and the perturbations do not change with time. Deeper investigation is necessary usually using a non-linear analysis.

Note that it is possible to simplify the system of Eq. (4.3.10) by introducing the stream function ϕ of the perturbations. This operation yields the famous Orr-Sommerfeld equation (Orr (1907); Sommerfeld (1908)).

Temporal analyses are well suited for bounded flows for which located perturbations can not spatially grow. However, even if this type of analysis can give the evolution of perturbations in time, it does not enable to access a global mode.

Spatial analysis:

In this case the unknown is the wavenumber α. One looks for the response of the flow to time periodic oscillations. Hence, $\omega \in \mathbb{R}$ is fixed. The set of equations, Eqs. (1.1.1)-(1.1.4), bring out quadratic terms in α and the eigenvalue problem can be formulated as:

$$A\hat{q} = \alpha B\hat{q} + \alpha^2 C\hat{q}. \tag{4.3.11}$$

Given that $\hat{p}$ does not have a term with α^2, taking $\phi = \alpha\hat{u}_i$ one can recast the problem into:

$$\begin{bmatrix} A & 0 \\ 0 & I \end{bmatrix} \begin{bmatrix} \hat{q} \\ \phi \end{bmatrix} = \alpha \begin{bmatrix} B & C \\ -I & 0 \end{bmatrix} \begin{bmatrix} \hat{q} \\ \phi \end{bmatrix} \tag{4.3.12}$$

or,

$$A'\tilde{q} = \alpha B'\tilde{q} \tag{4.3.13}$$

with $\tilde{q} = [\hat{q}, \phi]^T$.

The spatial analysis has proven to be very efficient for open flows. The main benefit over the temporal analysis is that it enables to reconstruct a 2D global shape of a global mode. Many studies have been done with this type of analysis during the last decades. One can cite the work of Lesshafft *et al.* (2006) on hot jets, Oberleithner (2012) on swirling flows under vortex breakdown or more recenlty the work of Lacassagne (2017) on the stability of corner shedding vortices in solid-propellant rocket.

Spatio-temporal analysis

In the last section, two types of analysis have been presented, one for bounded flows and one for open flows. In some cases, some spatially developing flows can sustain self-excited global modes without external forcing. These are in general characterized by a dominant frequency ω_G. Huerre & Monkewitz (1990) have shown that a global mode comes from a region of what is usually called '**absolute instabilities**'.
In that case, to find such particular instabilities, a spatio-temporal analysis is performed to study the local group velocity of the flow. An absolute instability indeed corresponds to a perturbation moving with zero group velocity and is marked by a saddle point of ω in the complex α-plane. In other word, for this type of study, the wavenumber is taken complex ($\alpha \in \mathbb{C}$) and one tries to find an eigenvalue ω_0 solution of the following eigenvalue problem:

$$\begin{cases} A\hat{q} = \omega_0 B\hat{q}, \\ c = \left.\dfrac{\partial \omega}{\partial \alpha}\right|_{\omega_0} = 0. \end{cases} \tag{4.3.14}$$

The sign of the resulting ω_0 gives the behavior and evolution of the local perturbation as shown in Fig. 4.3(b)-(c):

- $\omega_0 < 0$: The perturbation is amplified and is convected away from its source. The base flow is convectively locally unstable.
- $\omega_0 > 0$: The perturbation expands around its local source and perturbs all the flow. The base flow is absolutely locally unstable.

Enclosed cavities stability analysis

For a few years, the BEK family has been studied through local stability analyses and a review can be found in App. A. However, due to their industrial relevance, stability of an enclosed rotor/stator cavity has been rapidly a subject of interest. From an experimental point of view, the complete study of Schouveiler (2001) or Lopez *et al.* (2009) can be read to discover the different transition scenarios possible as a function of the aspect ratio G and the Reynolds number Re. From the linear stability analysis point of view, the first studies were done between two infinite disks. In that cases, auto similar Batchelor profiles were used in Itoh (1991) for the base flow. However for the rotating-disk boundary layer, Healey (2007) showed that confinement has a singular effect on waves that both propagate and grow in the cross-stream direction. Tuliszka confirmed this phenomenon by extending the work of Itoh (1991) and Lingwood (1996) to an enclosed cavity (Tuliszka *et al.* (2002)). Good agreement was found in that case between a DNS and a local stability analysis. Finally, they confirmed the existence of the spiral paterns and travelling circular waves as described in Schouveiler (2001).

Following these studies, the local stability framework is retrieved in this work to study enclosed cavity. The principle to obtain the set of equations associated to these specific systems is similar to the one presented in Sec. 4.3.1 and will not be more discussed here but can be retrieved in App. A.3.

AVLP: Local stability Solver

The linear local stability solver used for the configurations of interest in this PhD work, is called *AVLP* and has been developped by Bridel-Bertomeu (2016) in collaboration with *CNES* and *ArianeGroup*. This code has been implemented in Python, is massively parallel and enables to solve the linearized incompressible Navier-Stokes equations. Due to its efficiency in the context of stability analysis, a spectral collocation method has been used based on Chebyshev polynomials. Different types of stability analysis can be realized thanks to this solver: spatial (fixed ω unknown α) and temporal (fixed α unknown ω). Options also enable to track absolute and convective instabilities and allow reconstruction of the 2D global modes. Routines from ARpack and LAPack librairies are used to resolve the various eigenvalue problems. A full description of the code, solving parameters, and all its capabilities can be found in Bridel-Bertomeu (2016).

4.3.2 Global Stability

The analysis introduced so far relied on the parallel flow assumption. Unfortunately for many applications such a hypothesis does not hold. To overcome this problem, the weakly non-parallel flow theory has been created (Monkewitz *et al.* (1993)) and as an example, the Parabolised Stability Equations (PSE) proved to be efficient to capture simple boundary layer flows. However, the resulting method is not powerful enough to capture the effect of recirculations and boundary layer detachment situations. It is only in the 1980s, with the progress in computing science and the increase of computing power that the local stability theory has been extended to two dimensional base flows. The first global stability analysis was performed by Pierrehumbert, R & Widnall (1982) based on the solution of the eigenvalue problem pertaining to the essentially 2D basic states of a shear layer. As a result, many applications appeared and interested reader can refer to Theofilis (2011) for a complete review of the existing global stability methods.

Governing equations

This section describes the main steps to obtain the governing equations of a global stability analysis for any azimuthally periodic flows. The steps are organized as in the local stability section for the reader to precisely see the difference between the two methods.

By assuming infinitesimal perturbations evolving onto strongly non parallel two dimensional flows, the following base flow form is retained:

$$\begin{gathered}\mathbf{U} = (U_b(r,z), V_b(r,z), W_b(r,z))^T, \\ P = P_b(r,z).\end{gathered} \tag{4.3.15}$$

By introducing perturbations of the form $[u_i, p] = [u_r(r,\theta,z,t), u_\theta(r,\theta,z,t), u_z(r,\theta,z,t), p(r,\theta,z,t)]$ above a base flow following the global decomposition:

$$\begin{cases} U(r,\theta,z,t) = & U_i(r,z) + u_i(r,\theta,z,t), \\ P(r,\theta,z,t) = & P_b(r,z) + p(r,\theta,z,t), \end{cases} \tag{4.3.16}$$

the set of equations Eqs. (4.3.1)-(4.3.4), can be simplified and becomes separable in r, θ and t. The perturbations can then be represented using a normal mode formulation following:

$$[u_r, u_\theta, u_z, p]^T = [\hat{u}_r, \hat{u}_\theta, \hat{u}_z, \hat{p}]^T(z)\, exp[(i(m\theta - \omega t)]. \tag{4.3.17}$$

The same description as for the local stability analysis of Sec. 4.3.1 can be done here for m and ω. However, in that case the frequency ω_r and the growth rate ω_i correspond directly to the global characteristics of a given global mode. The second main change compared to the local stability analysis is the loss of radial wavenumber. The direct consequence is that a spatial analysis is impossible with a global approach.

Introducing the normal modes in the linearized Naviers-Stokes equations, Eqs. (4.3.1)-(4.3.4), one obtains a dispersion problem of the form:

$$D_G(\omega, m, \hat{q}) = 0, \tag{4.3.18}$$

where D_G denotes the problem dispersion relation of a global stability analysis (the detailed equations of this problem can be retrieved in App. A.4). Note that this set of equations, at the opposite of the local approach, enables to simulate any kind of axysymmetric base flow and is not restricted to enclosed cavities. No assumption being realized, the size of the problem is also considerably larger.

Thanks to the resolution of this specific dispersion problem, the stability behavior of fluid systems can be characterized. However, a simple global analysis is usually not enough to describe the full dynamics of a flow and its origin. In fluids dynamics, adjoint approaches are often used for optimal design methods. It gives indeed new insight in the flow and can be interpreted as a measure of its sensitivity, qualifying its robustness to changes, an information of importance to design passive control strategies for example. To address these issues in the context of the above dispersion problem, Eq. 4.3.18, two concepts are detailed. These are receptivity and structural sensitivity.

Receptivity:

This flow characteristic has been introduced by Hill (1992). It is usually defined as the response to additive changes to the governing equations, *i.e* modeling external sources of influence (such as free-stream turbulence, wall roughness, harmoning forcing, etc) or the optimal initial condition which will excite the most a global mode.

In such a context, the direct global modes are first obtained as described before by discretizing the system in space and solving the matrix eigenvalue problem corresponding to Eq. (1.4.1). For the purpose of the discussion, this latter is reformulated as:

$$\mathcal{L}\hat{q} = \omega\hat{q}. \tag{4.3.19}$$

The adjoint global mode $\hat{q}^+$ also referred as the receptivity of a mode $\hat{q}$ will be then solution of the problem:

$$\mathcal{L}^+\hat{q}^+ = \omega^*\hat{q}^+, \tag{4.3.20}$$

where $\mathcal{L}^+$ is the adjoint operator of $\mathcal{L}$ and $\omega^* = \mathfrak{Re}(\omega) - i\mathfrak{Im}(\omega)$.

Note that if one considers a discrete linear operator $\mathcal{L}$, then the corresponding adjoint operator $\mathcal{L}^+$ is defined as the conjugate transpose of $\mathcal{L}$, *i.e.* $\mathcal{L}^+ \equiv \mathcal{L}^H$. It can furthermore be shown that the adjoint global modes $\hat{q}^+$ are simply the left eigenvectors of $\mathcal{L}$ (when transposed and conjugated). The computation of the adjoint global modes is therefore implicit from the resolution of the linear system expressed by Eq. (1.4.1).

Structural sensitivity:
In opposition to receptivity, the structural sensitivity describes the response to structural changes in the governing equations, while modelling the internal sources of influence (such as base-flow modifications or changes in geometry). As originally described by Hill (1992), this information is given by the dyadic product of the direct and adjoint solution vectors of the linear problem, that is $\hat{\mathbf{u}}(\hat{\mathbf{u}}^+)^H$ where $\hat{\mathbf{u}}$ represents the velocity solution vector.

Following the definition given by Giannetti & Luchini (2007) based on Hill (1992), this resulting tensor shows how feedback between the components of the linearized velocity vector affects the growth rate $\mathfrak{Im}(\omega)$ and frequency $\mathfrak{Re}(\omega)$ of a global mode. Finally, Giannetti & Luchini (2007) showed that by taking the norm of the dyadic tensor, it becomes possible to identify where a modification in the linearized equations produces the greatest drift of the eigenvalue:

$$S(r,z) = \frac{\| \hat{u}^+ \|_2 \| \hat{u} \|_2}{|< \hat{u}^+, \hat{u} >|}, \tag{4.3.21}$$

where $< \cdot, \cdot >$ denotes the inner product defined as $< a, b >= \int a^* b \, dS$ and $\| \cdot \|_2$ stands for the Frobenius-norm.

The location of maximum structural sensitivity will therefore correspond to the greatest drift of the eigenvalues for a given modification of the system. This maximum is usually defined as the trigger of a global mode and can be assimilated to the notions of wavemaker described in the local stability approach. Receptivity and structural sensitivity are applied on the two academic rotating cavities in Sec. 4.4 two shed some light on each mode mechanism and to give first insight on how one can control them.

GIFIE: global stability solver

To compute linear global modes with a global stability approach, the solver called GIFIE has been developed and used in this PhD work. Its implementation started with Bridel-Bertomeu during his post-doc at CERFACS and resumed in the present PhD. Thanks to this solver, Eqs (1.4.1) are discretized using the Finite Element Method (FEM). Since the pressure fluctuations are expected to be continuous over the domain, one solves the problem on Taylor-Hood elements (Taylor & Hood (1973)), *i.e.* a standard P2 quadratic approximation of the fluctuation velocity components and a standard linear P1 approximation of the pressure on a partition of triangles (Rannacher (2000)). To assemble the FEM matrices, Freefem++ (Hecht (2012)) is used for its ease in defining variational formulations. The implementation of the equations using FEM has been validated using reference cases from the literature. The size of the eigenproblems are undoubtedly substantial and a note has to be made about computational cost. In the global stability framework, the matrices involved in the eigenproblem are very large: they scale like $(N_L + 3N_Q)^2$, where N_L and N_Q are respectively the linear and quadratic number of elements. Fortunately, the differentiation operators yield by the FEM on P2/P1 mixed elements (Taylor & Hood (1973)) are very sparse, leading to assembled matrices with a level of sparsity as high as 99 %. To take advantage of this specific aspect, the linear solver PETSc (Balay *et al.* (2019)) is preferred to manipulate the sparse matrices and the massively parallel librairy SLEPc (Roman *et al.* (2019)) is used to solve the eigenproblems with a shift-and-invert spectral transformation. Note that GIFIE was actually developed to compute multiple types of incompressible equations: 2D/3D cartesian and 2D periodic in azimuth. As explained above, from a discrete linear operator the adjoint modes are straight forward to obtain from the direct problem and can be also treated with GIFIE.

When it comes to the use of the local stability analysis, only a part of the annular cavity dynamics observed in Chap. 2 could be retrieved with this method. In fact, the dominant mode and the low frequency mode respectively referred to as $m = 29$ and $m = 12$ in Chap. 2 were found by LSA and were both in good agreement with DMD results. However the annular mode, $m = 0$, could not be retrieved due to the parallel flow assumption. Furthermore, the local approach failed to retrieve the unique mode driving **Case 1**: *i.e.* the cylindrical cavity. Such limitations were not observed when using GIFIE so, in the following, only the results obtained with the global approach will be presented. Note that a complete comparison of the two methods for **Case 2** has however been obtained and published during this PhD (Queguineur *et al.* (2018)). These comparisons can be retrieved in App. E.

4.4 Enclosed rotor/stator cavities global stability analysis

The modes driving the enclosed rotor/stator cavity dynamics of the configurations presented in Sec. 2.3 were identified in Sec 2.5.2 through DMD and DMT. In particular, the conjunct use of LES and DMD enabled to highlight that the cylindrical cavity, referred to as **Case 1** is composed of a unique mode synchronized around a unique temporal frequency composed of multiple azimuthal wave numbers m. At the opposite, the annular cavity, referred to as **Case 2** and taken at the same operating point, exhibits 3 independent modes with for each a unique temporal frequency and azimuthal wave number. Even though LES/DMD enabled to capture these peculiar modes, their mechanism and origins still need to be clarified.

The following discussion has therefore three purposes: First the global linear stability analysis (GLSA) is applied to both cases and results are compared to DMD results to avaluate such a tool capacityto retrieve identified modes. Receptivity and structural sensitivity are also obtained to produce more information on the source of each modes. Finally, comparing both configurations also helps us discussing the impact of the hub on the dynamics of a rotor/stator system. Note that the following results have been published in Queguineur *et al.* (2019).

4.4.1 Mesh and cost of the global analysis

Prior the presentation of the results of both **Case 1** and **Case 2**, it has to be noticed that whenever performing a global stability analysis, the homogeneity and the level of mesh refinement have an impact on the found eigenvalues and associated eigenvectors. As a consequence, for the **global approach**, the maximum edge length was fixed at 4×10^{-4} m and the cell-to-cell aspect ratio at 1.1, which is sufficient for the eigenvalues to change by only $\mathcal{O}(10^{-6})$ when the resolution is increased. The characteristics of the corresponding 2D meshes are summarized in Table 4.2.

The main consequences of these choices for the cases considered, is that the size of the eigenproblems is undoubtedly substantial and a note has to be made about the computational cost of the investigation presented here. As explained in Sec 4.3.2, in a global stability framework, the matrices involved in the eigenproblem are very large and scale like $(N_L + 3N_Q)^2$, meaning for **Cases 1** & **2** $\mathcal{O}(10^{11})$ elements.

All eigenproblems are solved using the shift-and-invert spectral transformation to compute the eigenvalues, which yields an overall cost of approximately 2800 s_{CPU} for one problem on an Intel Xeon (E5-2605, 2.45GHz) core. An exhaustive study of the possible global linear modes of **Cases 1** or **2** thus requires about 90 such computations (Adjoint modes, direct modes), hence a total CPU time per case of approximately 70 $\mathrm{h_{CPU}}$. The solver is however massively parallel and scales like SLEPc (Roman *et al.* (2019)), meaning

	Case 1	**Case 2**
Number of triangles	88 041	93 404
Number of vertices	44 555	47 238
Linear d.o.f N_L	44 555	47 238
Quadratic d.o.f N_Q	175 016	185 739
Matrices size $(N_L + 3N_Q)^2$	$(569\ 603)^2$	$(604\ 455)^2$

Table 4.2 – Summary of the finite element meshes characteristics used for the global stability analysis of **Case 1** and **Case 2**. Acronym "d.o.f" stands for degrees of freedom.

	Global Stability	Local Stability
Number of elements	$\mathcal{O}(600\ 000^2)$	$\mathcal{O}(1\ 000^2)$(one radius)
Sparsity	> 99 %	> 99 %
Resolution of 1 eigenproblem	2800 s_{CPU}	1200 s_{CPU}
Number of resolution for 1 case	90	–
Time for 1 case and 1 mode wavemaker	$1.5h_{CPU}$	$12h_{CPU}$
Overall time for 1 case	$70, h_{CPU}$	$37h_{CPU}$

Table 4.3 – Summary of computational time data for the linear global analyses based on Intel Xeon E5-2605 cores at 2.4Ghz.

that the total computational time per case can be decreased to 2.8 h when the solver runs on 25 cores.

To obtain the global modes of a system through a local approach a complex process needs to be followed (see Sec 4.3.1). The method being 1D and spectral elements being used, the local approach eigenvalue problem is far smaller than the global stability approach (around 1000 nodes for a radius) and for a unique eigenvalue resolution only 1200 s_{CPU} is necessary. However, for a temporal analysis, 3 parameters need to be varied to map all the possible existing modes of such a system: radius r, radial azimuthal wave number α, and azimuthal wave number m and absolute/convective instabilities also need to be computed. For a configuration like **Case 2**, an estimated overall time simulation of $37h_{CPU}$ is hence necessary to retrieve all the wavemakers of the possible eignemodes and their corresponding global reconstruction. All above-discussed details are summarized in Table 4.4.1. As one can see, the local approach even though based on 1D simulations needs to follow a complex process to obtain the wavemakers.

4.4.2 Note on the projected dynamic mode decomposition

Although DMD is widely used in Computational Fluid Dynamics (CFD) to extract full $3D$ modes of a simulated limit cycle, the current analysis will rely on the azimuthal periodicity of the problem and flow, a fundamental property of Navier-Stokes for the problems at hand. As a consequence all quantity of interest can be decomposed in a contribution of a mean axisymmetric stationary flow obtained by temporally and azimuthally averaging the flow realization within the limit cycle. Deviations from such a mean can then be further decomposed into azimuthally periodic contributions specified by their azimuthal wave numbers m. In that case, the previously discussed decomposition ensures an unambiguously characterized mode consistent with the global stability analysis (as detailed thereafter Sec. 4.3.2). As a consequence and instead of doing a conventional use of a DMD decomposition on the basis of the full $3D$ data basis, the following procedure is proposed.

First, all fluctuation fields $q' = (\mathbf{u}', p')$ (with $\mathbf{u}'$ and p' respectively the velocity vector and pressure fluctuations) are first Fourier decomposed in azimuth so that,

$$q'(r,\theta,x,t) = \sum_m \phi_m(r,x,t)cos(m\theta) + \psi_m(r,x,t)sin(m\theta), \quad \text{with } m\text{=0, }\pm1\text{,}\pm2\text{,..} \tag{4.4.1}$$

with ϕ_m and ψ_m the associated Fourier coefficients:

$$\begin{aligned} \phi_m(r,x,t) &= \tfrac{1}{2\pi}\textstyle\int_0^{2\pi} q'(r,x,\theta,t)cos(m\theta)d\theta, \\ \psi_m(r,x,t) &= \tfrac{1}{2\pi}\textstyle\int_0^{2\pi} q'(r,x,\theta,t)sin(m\theta)d\theta. \end{aligned} \tag{4.4.2}$$

DMD can then be applied to the ϕ_m and ψ_m $2D$ fields to extract the frequencies and reconstruct the spatial distribution of each mode ζ given an azimuthal wave number m through,

$$\zeta(r,\theta,x,m) = \mathfrak{Re}\left\{\phi_m(r,x)_{DMD}\right\}cos(m\theta) + \mathfrak{Re}\left\{\psi_m(r,x)_{DMD}\right\}sin(m\theta), \tag{4.4.3}$$

where $\phi_m(r,x)_{DMD}$ and $\psi_m(r,x)_{DMD}$ are respectively the 2D DMD modes obtained from the time series $\phi_m(r,x,t)$ and $\psi_m(r,x,t)$

Note that a direct consequence of the above described strategy is that a DMD mode is now uniquely characterized by its complex frequency (oscillation frequency and growth rate) and wave number, a feature that conventional DMD cannot produce since modes are only qualified by their frequency and spatial structure which is *a priori* arbitrary.

4.4.3 Case 1: Cylindrical shape cavity

The first case under study is the cylindrical rotor/stator cavity. As shown in Sec. 2.5.2, this system is synchronized around a unique frequency composed of multiple m azimuthal wavenumbers along the radius. In order to clarify these different zones an azimuthally

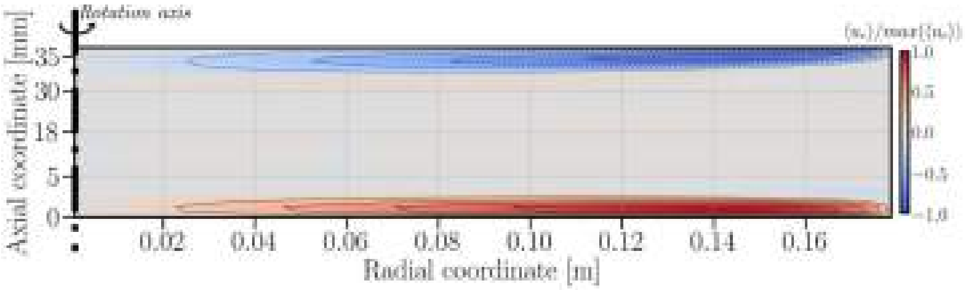

Figure 4.4 – Contours of the averaged radial component of velocity normalized by its ∞-norm, U_b / max $(\langle U_b \rangle)$ in **Case 1**. The stator is located at the top and the rotor at the bottom. Axial coordinate is transformed to thicken artificially the boundary layers.

projected DMD is first presented to ease its comparison with the stability analysis. Note that, the local stability analysis failed to reproduce these projected modes and will hence not be discussed here. Finally, the mean flow obtained by LES in Sec. 2.5.1 is used here for the global stability analysis as the fixed point of the Navier-Stokes equations. Figure 4.4 gives a reminder of the specific shape of this mean flow. One retrieves here the characteristic boundary layers of **Bödewadt** and **Von Kármán** respectively on the stationary disk and the rotating disk.

Mode maps

Resolution of the direct global stability problem provides access to a discrete set of eigenmodes (frequency and growth rates) and associated eigenvectors (spatial evolution) representative of perturbations potentially carried by the mean flow. First, a view of **Case 1** eigenvalues is detailed as a function of the azimuthal wave number m in Fig. 4.5. For the representation, the frequencies $(m, \mathfrak{Re}(\omega))$ and growth rate $(m, \mathfrak{Im}(\omega))$ planes are respectively provided in Fig. 4.5*(left)* and Fig. 4.5*(right)*. Each curve represented by a specific symbol/color corresponds to a stability branch. Note that, all modes belonging to a specific branch, share a physical feature: *i.e.* a common spatial structure. In our configuration, the branches differ by the number of lobes along the radial direction, *i.e.* the intersections of the spiral arms of the modes with a $x - r$ plan (see Fig. 4.6(c) as an example).

From the amplification rate results (right column), it appears that **Case 1** mean flow is capable of sustaining unstable modes at high azimuthal wavenumbers $m \geq 10$ and the most amplified mode is identified at $m = 30$. Although it is commonly stated in the literature dealing with stability analyses (see e.g. Meliga *et al.*, 2009; Qadri *et al.*, 2013; Chomaz, 2005) that only the most unstable mode is of interest to define the stability of the base flow, non linearities allow for mode interactions and operating conditions that can sustain multiple modes at once, some of which are not necessarily coinciding with the most amplified mode. Figure 4.5(left) exhibits eigenfrequencies for **Case 1** with very similar behaviors and convergence of all branches indicative of a potential synchronization of all the branches. Based on this spectral vision, one can identify a correspondence between the

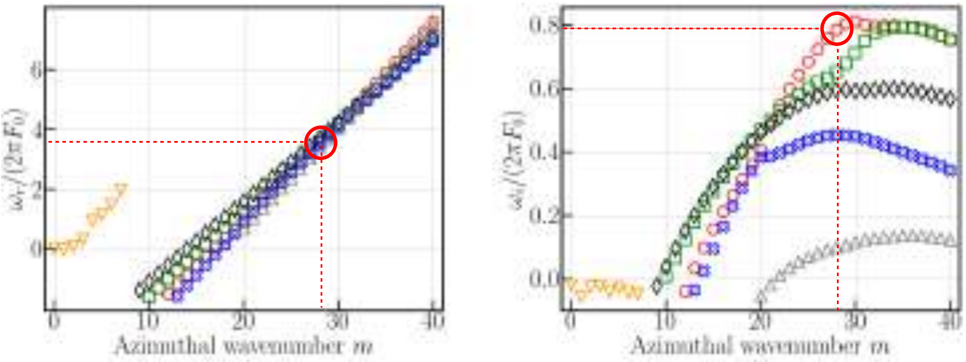

Figure 4.5 – Scatter plot of the frequency (left) and amplification rate (right) versus the azimuthal wavenumber of the linear global modes obtained of cylindrical cavity . The ordinates have been normalized by the pulse of the rotor, i.e. $2\pi F_0$. Different branches are represented by distinct color/symbol pairs.

Case 1	**DMD**	**GLSA**
Mode $m = 28$	3.55	3.6

Table 4.4 – Sum up of the modes frequency obtain by stability analysis compared to DMD for **Case 1.** The results have been normalized by F_0

eigen-frequencies and positive values of the growth rates of GLSA with peak frequencies registered in the LES (see the Table 4.5). The mode $m = 28$ is also seen to have a good agreement with the LES which dominates this cylindrical cavity. Furthermore, this linear analysis indicates that the other modes observed in the LES: *i.e.* $m = 8$, comes from non linear interactions that cannot be captured by the global stability analysis. In the following, all branches remaining very similar in terms of frequency, only the mode $m = 28$ with the highest growth rate will be retained for the discussion around **Case 1**. Table 4.4 sums up the different frequencies obtained for both methods

Comparison of the global mode shapes

Figure 4.6 presents a comparison between the real part of the fluctuations of the axial velocity u'_z generated by the DMD mode (top part of the figure) and obtained by use of the spatial Fourier decomposition for $m = 28$ along with the mode obtained by global linear stability analysis (bottom part of the figure). This specific comparison supports the conclusion that the global mode indeed matches the high radius part of the DMD mode for **Case 1**, both analyses displaying the same radial overall distribution with a maximum amplitude spanning the range $r \in [0.1, 0.13]$ m. All these spatial traces also generate spiral structures in the stationary disk boundary layer that has 28 arms for $r \gtrsim 0.09$ m.

Structural sensitivity and receptivity analysis

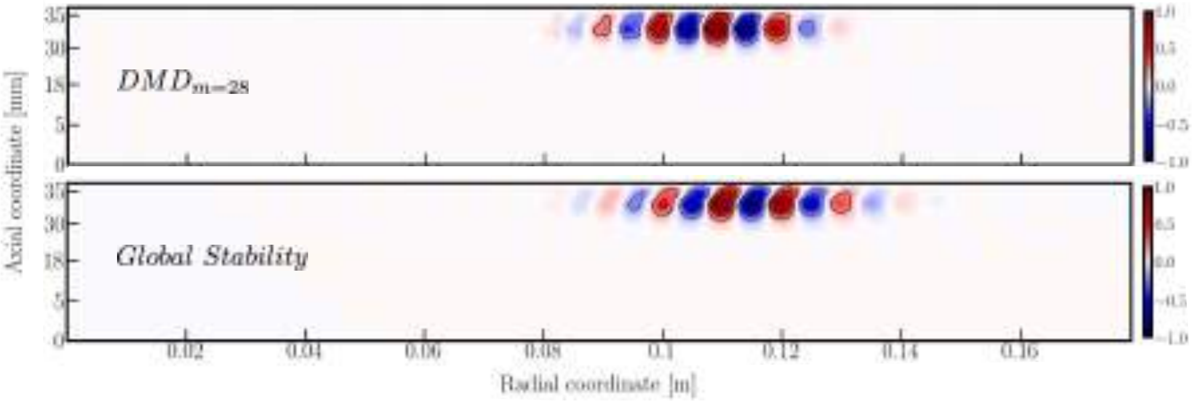

Figure 4.6 – **Case 1**, comparison between the axial velocity fluctuations $u_z^f/\max(|u_z^f|)$ of the $m = 28$ component of the decomposition of DMD in Fourier series (top) and the global mode issued by the linear analysis (bottom). Note that the axial coordinate has been transformed as in Fig. 2.5 to thicken artificially the boundary layers.

Corresponding adjoint axial velocity fluctuations $\tilde{u}_z^+$ are shown on Fig. 4.7. The adjoint mode results from the resolution of Eq. (4.3.20) for the base flow of **Case 1** and represents the receptivity of the direct mode to external forcing. It can also give as stated by Chomaz (2005), an indication on the initial condition that most optimally excites the direct mode. In the present case and for the first selected mode at $m = 28$, the adjoint expresses mostly in a region localized close to the top-right corner, i.e. at the intersection between the external stationary shroud and the upper stationary disk. Note also that, direct and adjoint modes do not coincide spatially, which is indicative of a flow with convective non-normality (Chomaz, 2005), i.e. a flow in which the streamwise advection of the perturbations by the flow is not negligible. Interestingly, this is a feature that is often referred in the literature as a characteristic of open flows (see e.g. Chomaz, 2005; Qadri *et al.*, 2013), and insofar and to the authors knowledge, has never been mentioned or evidenced for an enclosed flow. Based on (Chomaz, 2005), the region that is crucial in determining the global mode frequency, *i.e.* the wavemaker region, corresponds to the region where the direct and the adjoint modes overlap. This specific notion is detailed in the following subsection along with a discussion on the potential coupling and initiation mechanisms behind the expression of the various identified modes.

Mode origin and sensitivity tensor

As indicated above, the notion of wavemaker is coincident with the construction of the structural sensitivity; Eq. (4.3.21) for the mode issued by the linear analysis. Such maps are shown for the modes of interest in Fig. 4.8. For the most unstable direct mode, the sensitivity of Fig. 4.8*(a)* & *(b)* shows that the region of most amplification is located around $r \simeq 0.13$ m, above and slightly upstream of the recirculation region as confirmed by Fig. 4.8*(b)* that is a zoom of Fig. 4.8*(a)* complemented by streamlines of

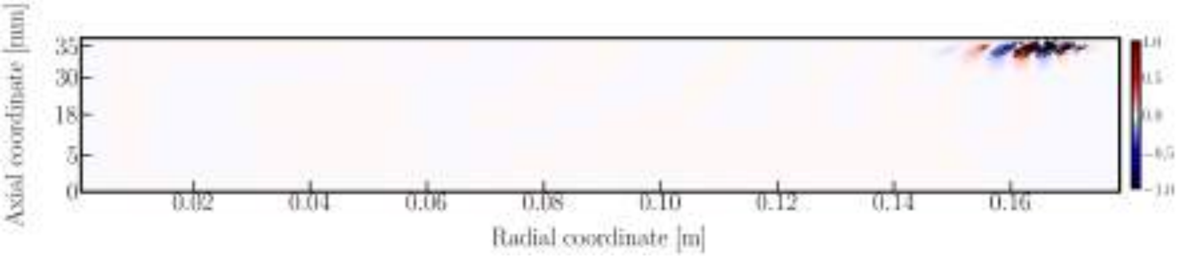

Figure 4.7 – **Case 1**, adjoint axial velocity fluctuations $\tilde{u}_z^+/\max(|\tilde{u}_z^+|)$ $m = 28$ (see Fig. 4.6*(bottom)* for the corresponding direct mode). The axial coordinate has been transformed to highlight the structure of the modes within the boundary layer.

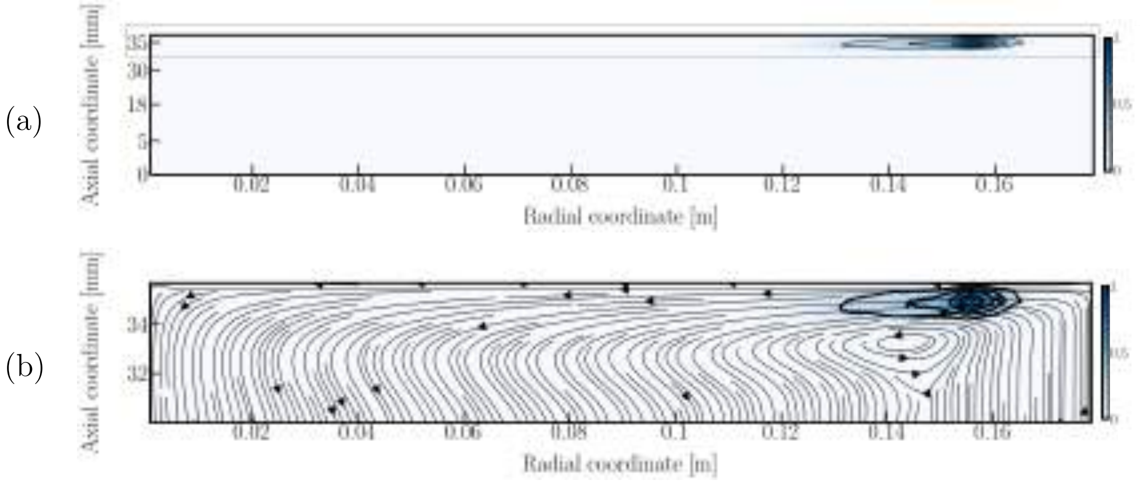

Figure 4.8 – **Case 1**, mode $m = 28$ (a) structural sensitivity map as defined by Eq. (4.3.21); (b) same as a, zoomed in and with the base flow (Fig. 2.5) streamlines. Axial coordinate has been transformed. Isocontours at ±20%, ±40%, ±60%, ±80% and ±100% of the absolute maximum (solid lines are positive values and dotted lines are negative values).

the corresponding mean base flow.

To understand the physical mechanism(s) by which the mode can be triggered, one can consider the nine components of the structural sensitivity tensor rather than just its trace (as shown on Fig. 4.8*(a)*-*(b)*). Indeed, according to previous investigations (see e.g. Chomaz, 2005; Giannetti & Luchini, 2007; Qadri *et al.*, 2013), these different components provide a measure of the influence on the eigenmode of the feedback between the three components of $\tilde{\mathbf{u}}$ and the three components of the linearized momentum equations. The maps of the absolute values of the different tensor components are shown on Fig. 4.9. Following Qadri *et al.* (2013), these frames can then be compared to the nine components of the strain tensor of the mean flow $\varepsilon_{ij} = \nabla\langle\mathbf{u}\rangle + (\nabla\langle\mathbf{u}\rangle)^T$, shown in Fig. 4.10. The three frames on the main diagonal represent the radial ε_{rr}, azimuthal $\varepsilon_{\theta\theta}$ and axial ε_{zz} strain components respectively, whereas the other frames represent the shear components (note the symmetry of the frames issued by the symmetry of the tensor).

First, along both disks, the $\theta - z$ shear component is strong, with local maxima at the intersections between the disks and the outer shroud. Second, the middle row

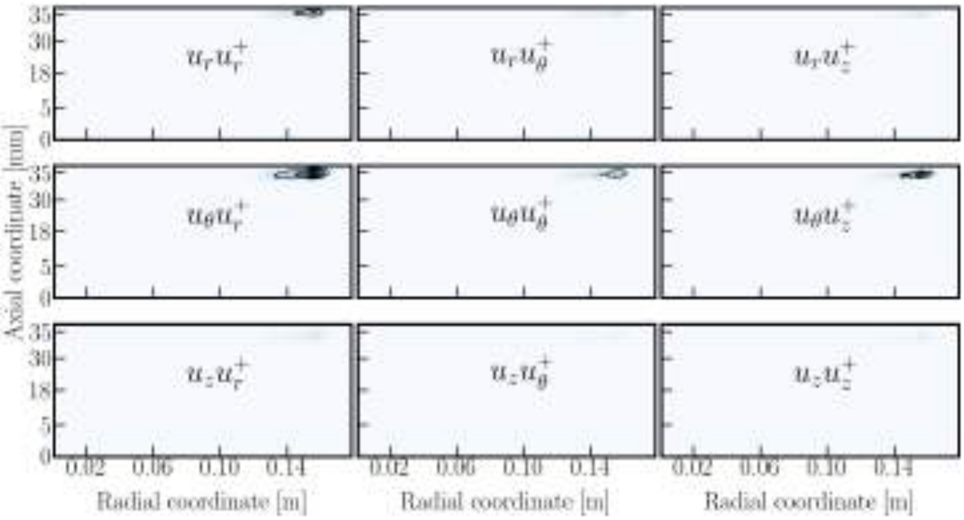

Figure 4.9 – **Case 1**, mode $m = 28$. Absolute value of the components of the sensitivity tensor, with the shading on all the plots scaling from 0 (light) to 1 (dark). Axial coordinate has been transformed as aforementioned. Isolevels at 20%, 40%, 60%, 80% and 100% of the maximum.

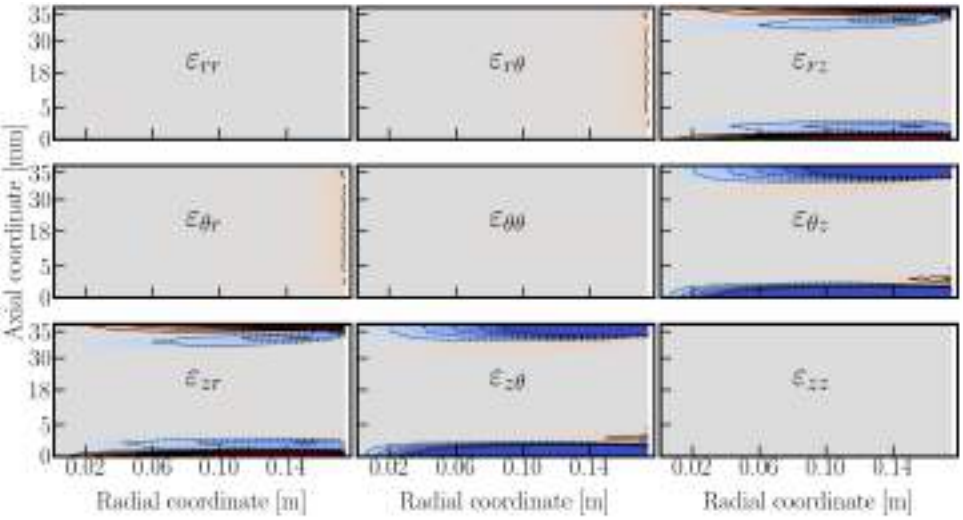

Figure 4.10 – **Case 1**, components of the rate-of-strain tensor $\varepsilon_{ij} = \nabla\langle\mathbf{u}\rangle + (\nabla\langle\mathbf{u}\rangle)^T$ for the base flow $\langle\mathbf{u}\rangle$. The shading on all the plots scales from -1 to 1. Axial coordinate has been transformed as aforementioned. Isolevels at ±20%, ±40%, ±60%, ±80% and ±100% of the absolute maximum have been added for clarity (solid lines are positive values and dotted lines are negative values).

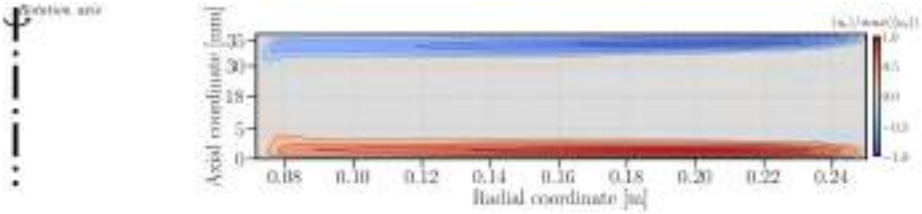

Figure 4.11 – Contours of the averaged radial component of velocity normalized by its ∞-norm, $\langle u_r \rangle$ / max $(\langle u_r \rangle)$ in **Case 2**. The stator is located at the top and the rotor at the bottom. Axial coordinate is transformed to thicken artificially the boundary layers.

of Fig. 4.9 shows that the $u_\theta u_r^+$, $u_\theta u_\theta^+$ and $u_\theta u_z^+$ components, which correspond to the influence of the azimuthal velocity, have high amplitudes in the region in which there is a strong $\theta - z$ shear component. Similarities with the behavior of a fully parallel azimuthal shear layer flow leads the authors to believe that both the non-zero azimuthal and radial velocity components are responsible in equal parts for the behavior of the flow in this region and for this specific mode. A small perturbation advected by the rotor flow and moving towards the stationary disk within the outer shroud boundary layer will be amplified when it reaches the top-right corner and enters a region of very strong azimuthal shear. The centripetal statoric motion then participates in the advection of the corresponding structure away from the corner and exclusively within the top-disk boundary layer since $\langle u_r \rangle$ is null in the quasi-inviscid core of the cavity. These remarks explain why the wavemaker region (see Fig. 4.8*(b)*) is located upstream of the direct mode structure and in close proximity to the secondary recirculation bubble representative of the non-zero shear components. Those observations can be linked to previous studies (Poncet *et al.* (2009); Crespo del Arco *et al.* (2005)) where the spiral instabilities of such a cavity is identified as the Type I instability Lingwood & Henrik Alfredsson (2015) found in simple rotating disk boundary layer. Also known as crossflow instability, one retrieves here the effect of the centripetal forces and even the inflectional characteristic profile in Fig. 4.10(ϵ_{zr}).

4.4.4 Case 2: Annular shape cavity

This second case concerns the annular rotor/stator cavity. The mean flow used in the present global stability analysis was obtained with LES as **Case 1** in Chap. 2 and is showed here as a reminder in Fig. 4.11. The characteristic boundary layers presented in Sec. 4.2 are retrieved here with the **Bödewadt** boundary layer on the statioannary disk and **Von Kármán** on the rotating disk.

As shown in Sec. 2.5.2, this system presents three distinct modes $F/F_0 = 0.35$, $F/F_0 = 3.24$ and $F/F_0 = 3.6$ with respectively an azimuthal wave number of $m = 12$, $m = 0$ and $m = 29$. As a reminder, this second cavity has been taken with the same aspect ratio $G = 0.2$ and the same global Reynolds number $Re = 10^5$ as for **Case 1** to put in parallel the activity of both cavities and highlight the role of the hub into the dynamics of the present case.

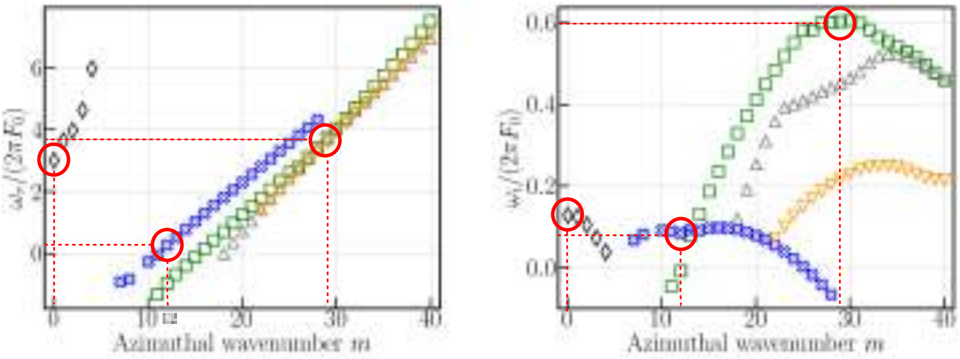

Figure 4.12 – Scatter plot of the frequency (left) and amplification rate (right) versus the azimuthal wavenumber of the linear global modes obtained of cylindrical cavity . The ordinates have been normalized by the pulse of the rotor, i.e. $2\pi F_0$. Different branches are represented by distinct color/symbol pairs.

Mode maps

Following the presentation of **Case 1** results, the spectrum obtained by use of the global stability analysis for azimuthal wavenumbers from $m = 0$ to $m = 40$ is displayed in Fig. 4.12 for **Case 2**. Note that the same representation as in Fig. 4.5 is adopted. From the amplification rate results (Fig. 4.12*(right)*), one can observe that **Case 2** mean flow is capable of sustaining unstable modes at high azimuthal wavenumbers $m \geq 10$ as **Case 1** and the entire range of m including the $m = 0$ value. As observed for **Case 1**, the most amplified modes are identified for $m \approx 30$ for **Case 2**.

A more detailed analysis of both spectra evidences first hand differences. Figure 4.5*(left)* exhibits eigen-frequencies for **Case 1** with very similar behaviors and convergence of all branches indicative of a potential synchronisation of all the branches. On the contrary, the spectrum of **Case 2**, Fig. 4.12*(left)*, exhibits three seemingly independent unstable branches:

- a set of unstable branches at high values of azimuthal wavenumber $m \gg 10$ similar to the branches obtained in **Case 1**,
- an unstable branch spanning over the medium values of azimuthal wavenumber, $8 < m < 25$ and,
- an unstable branch at very low azimuthal wavenumbers, $m < 5$.

Based on this spectral vision, one can identify a correspondence between the eigenfrequencies and positive values of the growth rates of GLSA with peak frequencies registered in the LES (see the Table 4.5). Therefore, for **Case 2** the most unstable modes with $m = 0, m = 12$ and $m = 29$ are found to match closely the spectral content of the LES as well as the corresponding DMD decomposition.

Case 2	**DMD**	**GLSA**
Mode $m = 0$	3.24	3.1
Mode $m = 12$	0.35	0.31
Mode $m = 29$	3.61	3.7

Table 4.5 – Sum up of the modes frequency obtain by stability analysis compared to DMD. The results have been normalized by F_0

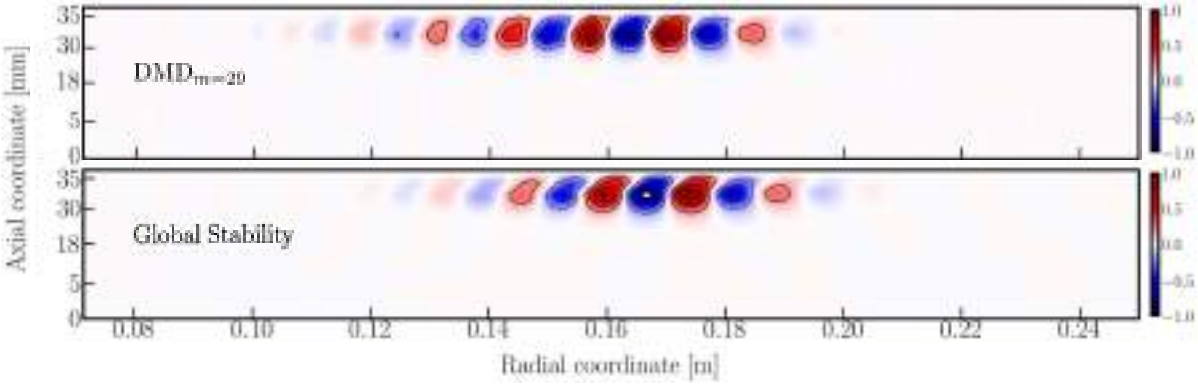

Figure 4.13 – **Case 2**, comparison between the axial velocity fluctuations $u_z^f/\max(|u_z^f|)$ of the $m = 29$ component of the DMD decomposition in Fourier series (top) and the global stability analysis (bottom). The axial coordinate has been transformed as in Figs. 2.5 to thicken artificially the boundary layers.

Comparison of the global mode shapes

The correspondence between the DMD and the direct mode spatial structures issued by a global approach is detailed for the three modes selected above. As done for **Case 1**, a spatial Fourier decomposition is applied for each DMD mode in order to be consistent with the global stability approach. Figure 4.13 shows iso-contours of the axial velocity fluctuations of the $m = 29$ mode identified either by the projected DMD Fig. 4.13*(top)* or global stability analysis Fig. 4.13*(bottom)*. Clearly similar spatial organizations are retrieved and just like for **Case 1**, the structure appears to exist mainly in the neighborhood of the inner cylindrical hub.

For this second case, it is found that the instability mechanism in the stationary disk boundary layer and for the apparition of the spiral structure therein is similar to the one described in Sec. 4.4.3 for the cylindrical cavity. In fact, mode $m = 28$ of **Case 1** was found to be sensitive only in the external part of the cavity and coming from perturbations amplified at the shroud. By modifying only the central zone (addition of

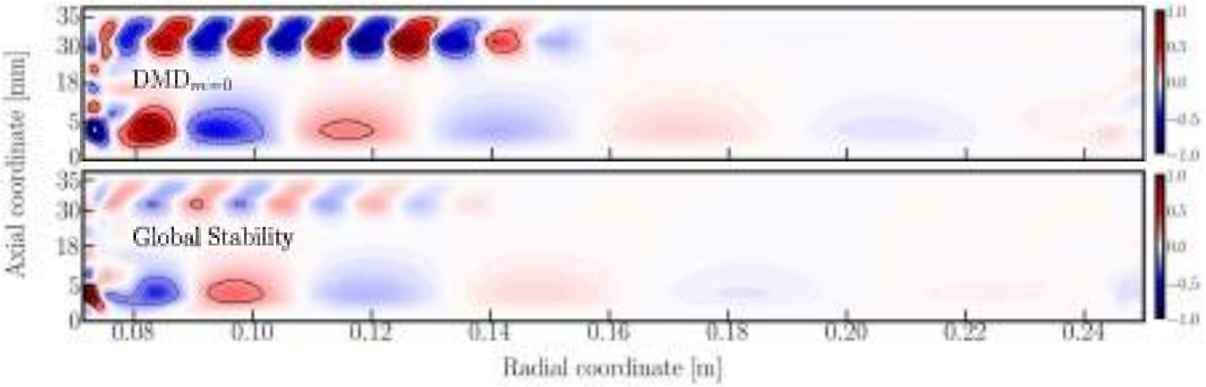

Figure 4.14 – **Case 2**, comparison of the $m = 0$ component of the DMD decomposition in Fourier series and global stability analysis (see Fig.4.13 for the full caption details).

the hub), this high azimuthal mode is naturally expected to persist as confirmed here. This stationary disk instability of **Case 2** will therefore not be further developed in this section.

The next modes produced by the global linear stability analysis and of interest in this investigation are: the $m = 0$ & 12 modes. The results are shown and compared to the projected DMD in Figs. 4.14 & 4.15 respectively for $m = 0$ and $m = 12$. Note that, as said in the end of Sec. 4.3, no result was found for $m = 0$ using local stability analysis. For both modes, the agreement between the spatial organization of the linear mode from the global approach and projected DMD is remarkable. Such spatial agreements come as a complement to the observation that the pulsation of all identified paires do correspond. Similarly to the $m = 29$ mode, the structure of the $m = 12$ mode expresses mainly in the neighborhood of the inner cylindrical hub. The flow being particularly not parallel around this region can explain why no result could be obtained at low radii for this mode with a local stability approach (see App. E). According to the projected DMD, the vortices along the rotor and along the stator of the $m = 12$ mode have approximately the same magnitude, when stability analysis yields a mode that is strongest in the inner top corner between the rotor and the hub. The structures in both frames are however very similar near the intersection between the hub and the stator as well as at the edge of the rotor.

Structural sensitivity and receptivity analysis

As discussed before in Sec. 4.4.3 for **Case 1**, there is a non-negligible interest in looking at the adjoint modes. Figure 4.16*(a)* presents the adjoint axial velocity fluctuations $\tilde{u}_z^+$ for the $m = 0$ mode and (b) for the $m = 12$ mode. The $m = 0$ adjoint mode, Fig. 4.16(a), has two distinct local extrema, one located in the upper disk boundary layer while the other is found in the inner hub cylindrical boundary layer, both being of the same order of magnitude.

One can also note that the direct, Fig. 4.14, and adjoint modes, Fig. 4.16(a), coin-

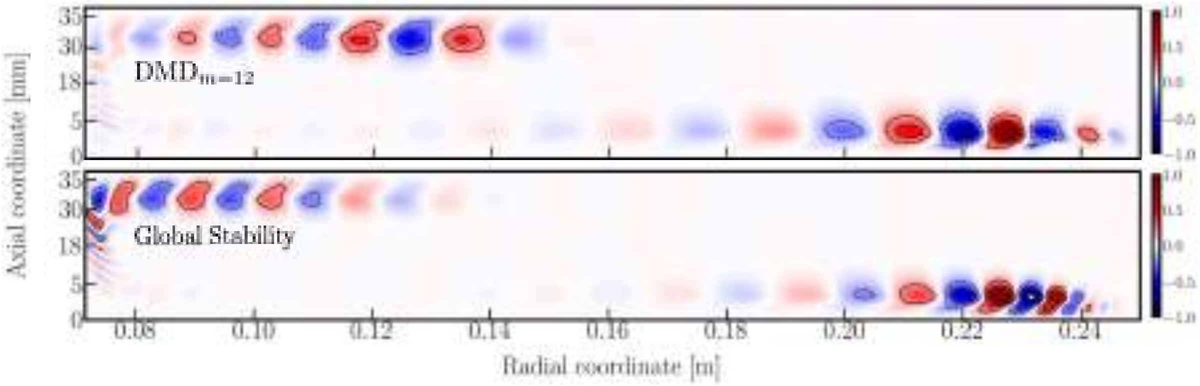

Figure 4.15 – **Case 2**, comparison of the $m = 12$ component of the decomposition of DMD in Fourier serie and global stability analysis (see Fig.4.13 for the full caption details).

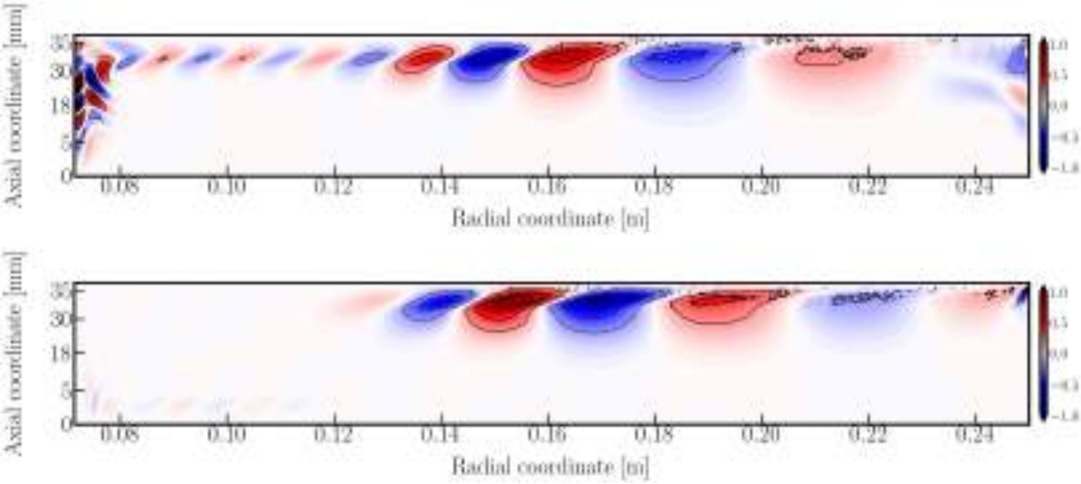

Figure 4.16 – **Case 2**, adjoint modes of (a) the $m = 0$ direct mode and (b) the $m = 12$ direct mode (see Fig. 4.15).

cide spatially, implying that contrary to the mode present in the stator boundary layer (common to **Case 2** and **Case 1** as discussed before), the perturbations at $m = 0$ are less susceptible to mean flow advection.

For the $m = 12$ mode, the conclusions are somewhat different. Figure 4.16(b) shows that the adjoint mode expresses mainly in the stationary disk boundary layer for $r > 0.12$ m, *i.e.* this location not coinciding with the direct mode, Fig. 4.15. The situation is therefore similar to the case of the $m = 28$ mode of the cylindrical cavity (see section 4.4.3), which points to the fact that the $m = 12$ mode is affected by the base flow convection. This convective non-normality is here even more marked given that the direct mode has two local extrema, one being at the edge of the rotor disk, *i.e.* very far downstream of the adjoint maximum. There is however a reason for the vortices on the rotor to have a non-zero magnitude only at high radial locations: it is indeed well documented in the literature (see e.g. Daily & Nece, 1960; Lingwood, 1995; Séverac *et al.*, 2007; Appelquist *et al.*, 2015) that the rotating disk boundary layer is sensitive to any external excitation and is capable of sustaining coherent macro-structure for Reynolds numbers $r^2\Omega/\nu \gtrsim 5 \times 10^4$.

Structural Sensitivity

As discussed before in section 4.4.3, structural sensitivity maps help gathering more information about the modes' triggering mechanisms. Figure 4.17 presents such maps for (a) the $m = 0$ mode and (b) the $m = 12$ mode of **Case 2**.

The structural sensitivity map of the $m = 0$ mode confirms that contrary to the mode $m = 28$ present in the stator boundary layer of **Case 1** (and **Case 2** as discussed before), the perturbations at $m = 0$ are less susceptible to base flow advection. Furthermore and as a consequence of the presence of both the direct and adjoint modes in the hub boundary layer, this region becomes crucial in determining the global mode behavior as supported by the high levels of sensitivity shown in this specific flow region. It is also noted that Fig. 4.17*(a)* confirms that the mechanisms behind the existence of the $m = 0$ are exclusively related to the boundary layers along the cavity walls. This latter could explain why the local stability approach could not retrieved the wavemaker and mode $m = 0$ 2D shape.

For the $m = 12$ mode, the structural sensitivity map, Fig. 4.17(b) shows that the wavemaker region is here mainly located in the stationary disk boundary layer around $r \simeq 0.13$ m, in a zone where the effects of confinement due to the presence of the inner hub start to be non-negligible. A second highly localized peak appears also in the lower right corner near the junction between the rotating disk and the external static hub. To conclude this discussion, recall that by nature the adjoint mode represents the initial condition that most optimally excites the corresponding direct global mode (Chomaz, 2005). It is therefore natural that the region of highest sensitivity be correlated to the region where the amplitude of the adjoint mode is also close to a maximum (here the hub

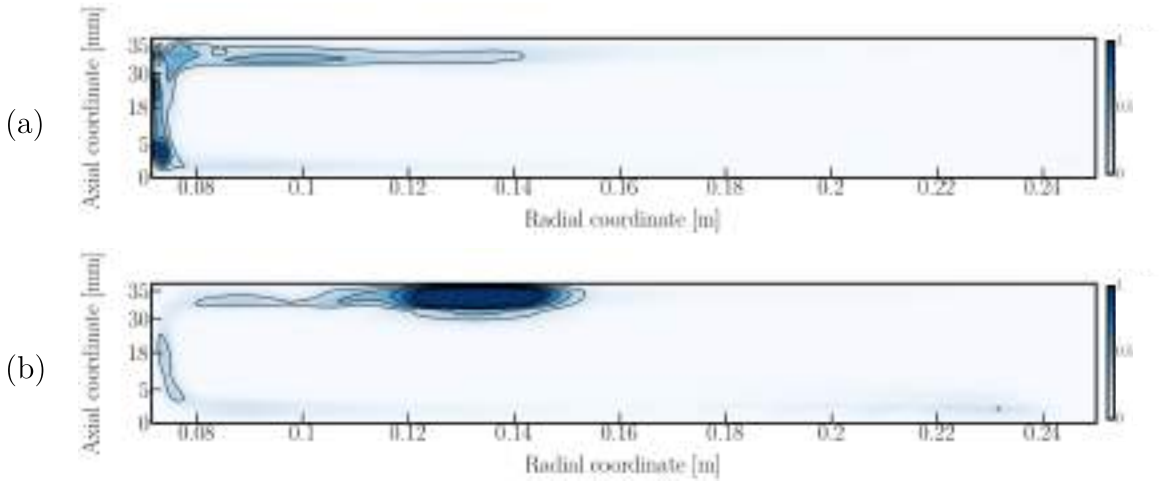

Figure 4.17 – **Case 2**, structural sensitivity maps of (a) the $m = 0$ and (b) the $m = 12$ modes as defined by Eq. (4.3.21).

and hub boundary layers). This feature is however complemented by the appearance of a second maximum located in the stator boundary layer for both modes, 0.12 m $\lesssim r \lesssim$ 0.20 m. It is indeed remarkable that this second spot matches exactly the region where the statoric constituent $m = 29$ mode is the strongest. Perturbations generated this way are hence amplified so the mode becomes globally unstable. The mechanism by which the perturbations get amplified by the presence of the hub will be discussed later in this section.

Mode origin and sensitivity tensor

The only question left aside for **Case 2** deals with the triggering mechanism of the $m = 0$ and $m = 12$ modes. As mentioned in the introduction of section 4.4.4, the mechanism behind the spiral $m = 29$ mode present in the stator boundary layer is found to be similar to what is described in section 4.4.3. To support this observation, one presents in Fig. 4.18 the nine components of the strain tensor of the base flow ε_{ij} as we did in section 4.4.3 for **Case 1**. Contrary to the maps of the corresponding flow (Fig. 4.10), **Case 2** features strong $\theta - r$ shear close to the hub due to the cylindrical boundary layer and the necessity for the flow to adapt to the rotation speed of the hub, other regions remaining highly similar.

Similarly to the discussion about the cylindrical cavity, the components of the strain tensor are compared to the components of the sensitivity tensor, exhibited in Fig. 4.19 for the $m = 0$ mode and in Fig. 4.20 for the $m = 12$ mode. For the $m = 0$ mode, the $u_\theta u_r^+$, $u_\theta u_\theta^+$ and $u_\theta u_z^+$ components, corresponding to the influence of the azimuthal velocity, are the only non-negligible components and have very high amplitudes in the region where $\varepsilon_{\theta r}$ is strong. Similarly to the analysis conducted in Sec. 4.4.3, it seems reasonable to conclude that the perturbations related to the cylindrical shear layer close

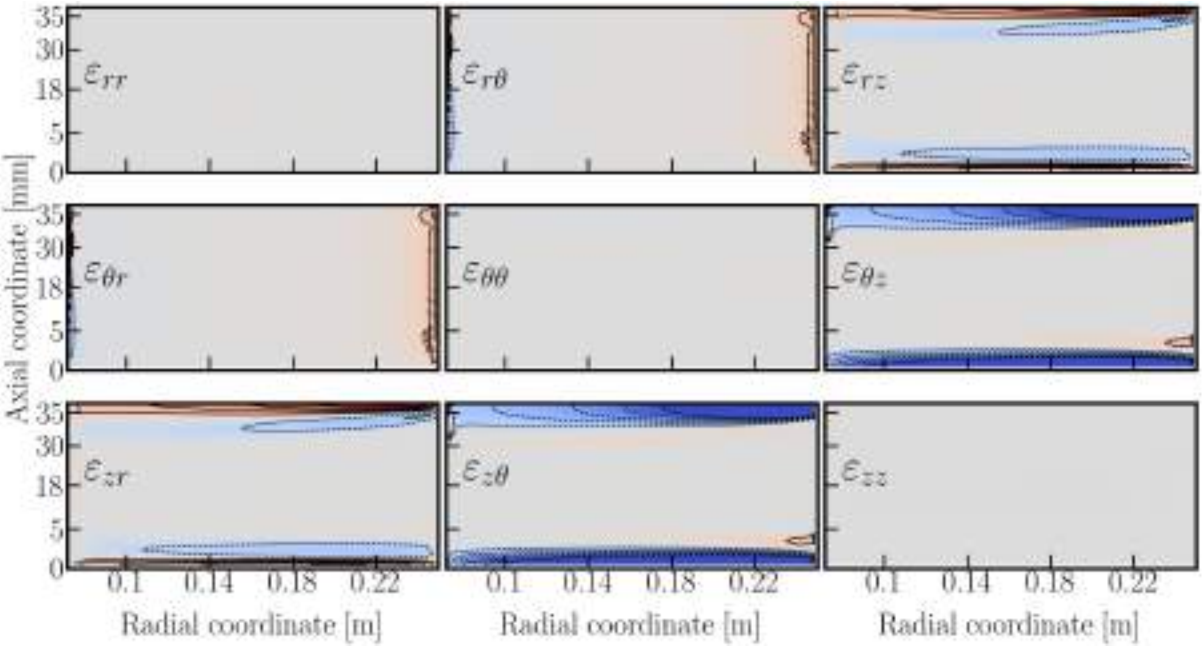

Figure 4.18 – **Case 2**, components of the rate-of-strain tensor $\varepsilon_{ij} = \nabla\langle\mathbf{u}\rangle + (\nabla\langle\mathbf{u}\rangle)^T$ for the base flow $\langle\mathbf{u}\rangle$. The shading on all the plots scales from -1 to 1. Axial coordinate has been transformed as aforementioned. Isolevels at ±20%, ±40%, ±60%, ±80% and ±100% of the absolute maximum have been added for clarity (solid lines are positive values and dotted lines are negative values).

to the hub play an important role. In fact, they amplify the infinitesimal perturbations coming from the stator boundary layer (where the adjoint is maximum), thus triggering the strong downstream vortices located at the corner between the hub and the rotor seen on Fig. 4.14. The second feature to consider is the high value of the $u_\theta u_r^+$ component in a region where, from Fig 4.18, no component of the base flow shear tensor is large. It has already been mentioned in the literature (e.g. Leibovich & Stewartson, 1983; Gallaire & Chomaz, 2003; Qadri *et al.*, 2013), for flows with a strong swirl component, conservation of angular momentum in some regions of the flow can be the cause of an instability which can then trigger global instabilities. In the present case, this conservation of momentum could potentially help explaining the origin of the mode $m = 12$ in the region just upstream of the hub in the stator layer.

Indeed, considering a fluid particle centripetally displaced in the stationary disk boundary layer where it possesses a weak azimuthal velocity, as it gets closer to the hub, it is suddenly accelerated in the azimuthal direction and entrained by the rotating cylindrical wall. At the same time, its radial velocity is markedly reduced and axial velocity increased to follow the stream. As a consequence, the fluid particle is strongly compressed in the radial direction and stretched in the azimuthal and axial directions. By conservation of angular momentum, the vorticity in the azimuthal and axial directions is bound to increase while the vorticity in the radial direction decreases. Vorticity is, in turn, increased. As the perturbation reaches the cylindrical boundary layer, it is then amplified (peak of sensitivity in this region, see Fig. 4.17) so vortices are generated and advected by the base flow along the rotor. In summary, it is the belief of the authors that in the specific case of the $m = 0$ mode, both a mechanism based on conservation of momentum and a Kelvin-Helmholtz like instability are active and both are due to the presence of the hub. This new approach can be related to the convective instability of simple rotating disk boundary layer also known as Type II (Lingwood & Henrik Alfredsson (2015)). In fact, as shown above, the streamline-curvature plays a main role in the destabilization of **Case 2** hub.

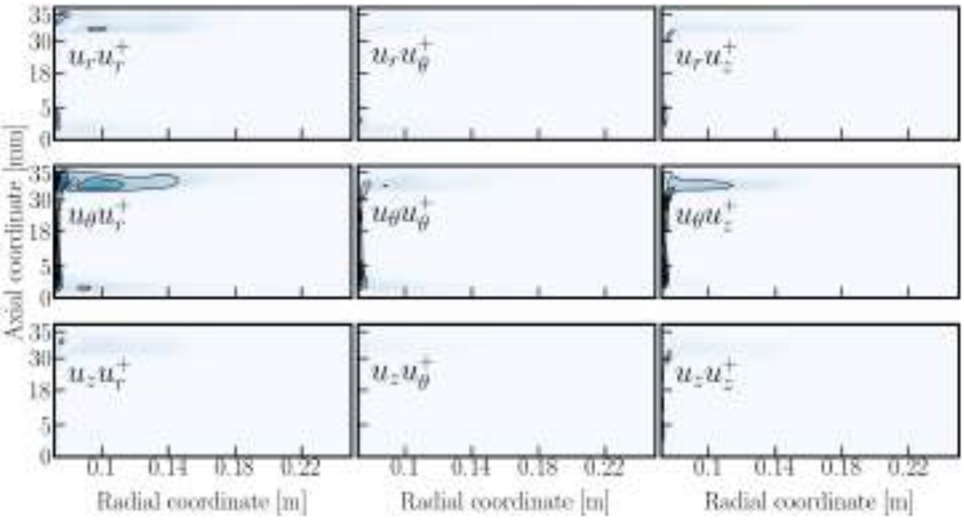

Figure 4.19 – **Case 2**, mode $m = 0$, absolute value of the components of the sensitivity tensor, with the shading on all the plots scaling from 0 (light) to 1 (dark). Isolevels at 20%, 40%, 60%, 80% and 100% of the maximum.

Focusing on the components of the sensitivity tensor for the $m = 12$ mode, Fig. 4.20 again points to the importance of the azimuthal velocity as the source of production of this mode. In this case, one can also note the influence of the radial velocity as well, given the top frames of Fig. 4.20 which show strong magnitudes for $u_r u_r^+$ and $u_r u_\theta^+$. If linked to Fig. 4.18, these high amplitude regions correspond to regions of mild shear, making it difficult to conclude on the underlying mechanisms. Nonetheless, it is still of importance to consider other features. First, paying attention on the adjoint base of the $m = 12$ mode, the vortices visible bear a striking resemblance to the vortices generated by the direct $m = 29$ mode shown on Fig. 4.13. This leads to the thinking of a sequentiality process, where the $m = 12$ mode is linked to the $m = 29$ mode. Following this line of thought, it has been said that the mechanism behind the $m = 29$ mode is the same as the mechanism behind the modes of **Case 1**, *i.e.* a strong amplification of any perturbation reaching the shroud/stator corner in that region. All this being considered, the $m = 12$ mode may also be linked to that same mechanism. Second, because the direct and adjoint bases do not coincide, the $m = 12$ mode is subject to convective non-normality (Chomaz, 2005), which is known to lead to extreme sensitivity to forcing. In other words, even though the probability of a perturbation triggering the mode is high, if it is active in the wavemaker region (see Fig. 4.17(b)), a perturbation can become active in any region where $\mathbb{S}$ is non zero and can be enough to initiate that mode. Finally, it was noted that on Fig. 4.17(b) or Fig. 4.20 ($u_\theta u_r^+$), the region close to the hub and also a small region at the edge of the rotor exhibit a positive sensitivity. In both regions, strong shear due respectively to the cylindrical boundary layer and the rotor boundary layer serve as amplifiers for any perturbation passing through, promoting the apparition of the $m = 12$ mode. In summary, we find that for $m = 12$ there is no evident mechanism of instability contrarily to the $m = 0$ mode or the stator spiral found in **Case 1**. One conclude simply that when it comes to the triggering of this mode, perturbations generated by the apparition of the statoric spiral $m = 29$ mode may be influenced by three regions of the flow acting as amplifiers and therefore promoting the $m = 12$ mode. Likewise any source of oscillation equivalent to an external forcing can explain the appearance of this specific mode. Note finally that these results match the observations given in Chap. 3 with the mode interactions study obtained with DMTC for which damping the dominant mode $m = 29$ proved to also suppress the low frequency mode $m = 12$.

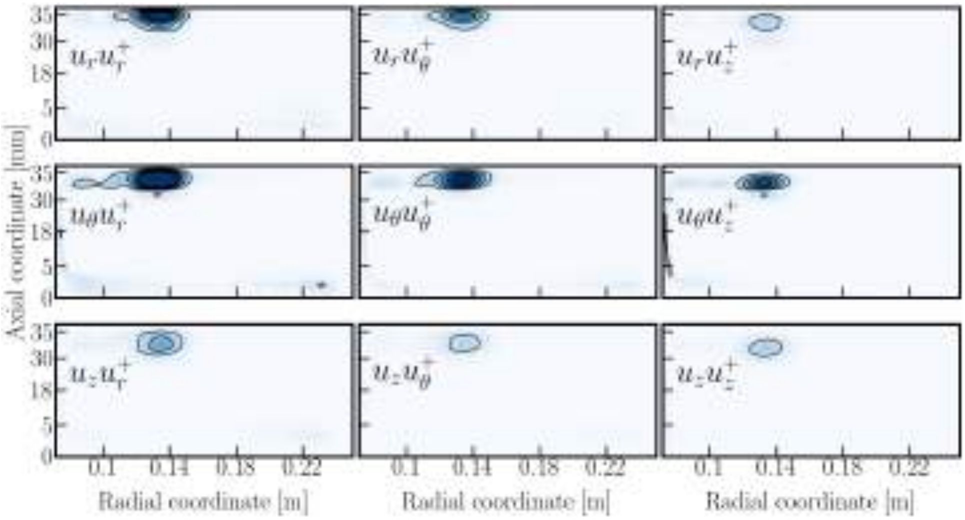

Figure 4.20 – As Fig. 4.19 for $m = 12$ and levels from 0 (light) to 1 (dark).

4.5 Conclusion

This chapter introduced a global stability analysis framework to extend the investigation of the pressure band phenomenon in rotating cavities realized with LES in Chap.2. This latter enabled to extract the driving modes of two types of academic cavities: A cylindrical and an annular rotor/stator cavity but could not explain the mechanism and origin of each mode. Global stablity analysis is well known to provide such efficient tools to study unsteady phenomena and their origin through adjoint/sensitivity analyses and was applied here on both configurations of interest. Particular attention was dedicated to the annular cavity which comparatively to the cylindrical cavity, allows to expose the impact of a hub on rotating cavity instabilities, a known interest to industrial problems. The three modes driving the annular cavity already capture by DMD in Chap.2 are retrieved trough a global stability analysis contrary to a local stability approach. A very good agreement is found in terms of mode spatial distribution but also in terms of frequencies. However, this investigation was conducted before everything else to shed some light on the mode mechanisms of the annular cavity. Sensitivity analysis pointed that the origin of each modes is in the stationnary boundary layer. In particular, one showed that the dominant mode of the annular cavity is purely due to perturbations generated in the external parts of the rotor and amplified along the shroud to finally be advected by the centripetal forces of the stator. Furthermore, one showed through sensitivity tensor analysis that the unique mode of the cylindrical cavity is only sensitive to perturbations in the external part of the stator boundary layer. This observation explains why adding a hub at low radii does not damp this particular mode and is hence retrieved in the annular configuration. For the two other modes of the annular cavity, the triggering mechanisms are linked to the boundary layer around the hub. The annular mode $m = 0$ comes directly from small perturbations generated at the corner between the stator and the hub. These vortices are also amplified to finally be advected along the rotor. The mechanism linked to the mode $m = 12$ is however not clearly identified. The sensitivity tensor analysis points out different possibilities. The first one is similar to the one identified for the mode $m = 0$ while the second one directly links the existence of mode $m = 12$ to the presence of the $m = 29$. Although not demonstrated, the similarities between the adjoint of the mode $m = 12$ (optimal forcing of the mode) and the direct mode of $m = 29$ is clearly observed. Cumulated to the fact that the non-normality property of mode $m = 12$ makes it very sensitive to external forcing and hence to perturbations generated by mode $m = 29$. This second possibitity was found in good agreement with the results obtained through DMTC in Chap. 3 where one observed that suppressing the dominant mode $m = 29$ cancels at the same time the low frequency mode $m = 12$.

This chapter enabled to shed some light on the different mode origins and confirmed that to control the overall pressure band phenomenon a focus on the $m = 29$ mode damping should be realized. However, concrete and physical control actuators still need to be set up and will be the subject of the next chapter.

Chapter 5

Control of a rotor/stator cavity flow

Contents

This chapter proposes to set up control strategies to stabilize the modes driving the pressure band phenomenon in the enclosed annular rotor/stator cavity. The previous chapters indeed helped capturing the dynamics of this system while understanding the mode interactions and dominance. However, no physically implementable solution could be proposed to control this flow with the tools and analyses proposed. To overcome this problem, the GLSA framework is further developed here to make use of the sensitivity to a base flow modification, first introduced by Marquet et al. *(2008). Contrary to the wavemaker obtained through structural sensitivity analysis, the sensitivity to a base flow modification enables to point out the exact location where a given mode should be modified to shift its frequency or growth rate. In this context, this method provides a first order tool to set up a passive controller. After a brief introduction of the rotating flow control studies, the principle and the steps to obtain the base flow sensitivity are detailed. Thanks to this analysis, the conjunction use of LES and GLSA shows to be a promizing method to suppress the pressure band phenomenon thanks to very low amplitude injection/suction controllers to be added to the original cavity at locations indicated by the base flow sensitivity tool.*

5.1 Introduction

In the previous chapters, the pressure band phenomenon was reproduced by LES and analyzed through GLSA for an academic annular rotor/stator cavity. These different tools shed light on the different origins of the three main modes driving this cavity and how they interact. In this chapter, a control framework still based on GLSA is proposed to overcome this pressure bands problem of the annular academic cavity. To do so, a review of the control systems and studies realized first in the general context of rotating boundary layers are provided in Sec. 5.1.1 while Sec. 5.1.2 details the work specifically dedicated to enclosed cavities.

5.1.1 Rotating boundary layer control

Turbomachine efficiency has always been optimized by controlling its inner flow and many passive or active actuators have been developed in the last decades to delay or promote the transition to turbulence (Lord *et al.* (2000)). One can cite for example fluid suction/injection methods of Lee & Greitzer (1990), vortex generators by Chima (2002) or riblets. A review of this latter system can be found in Koepplin *et al.* (2017). Among all possible solutions present today, boundary layer control is a well known concept (Prandtl (1904)) and blowing or suction devices have already proved to delay separation and are still in use today in the area of supersonic inlets Caraballo *et al.* (2009) for example.

For rotating disks, the main control system studied over the years has been grooves (roughness), suction/blowing devices but also magnetic fields. The latter will not be detailed in this introduction but the last progresses can be retrieved from Thomas & Davies (2013). Spatial inhomogeneities of rotating disk effects have been particularly studied by Davies & Carpenter (2003). In this specific work, the authors showed that grooves affect directly the global response of this locally absolute unstable flow. From these observations, grooves or specific surface roughness have been specifically investigated for the Von Kármán boundary layer to study the laminar to turbulence transition but also in the long term to set up drag reduction systems. For example, partial slip boundary conditions were used in Cooper *et al.* (2015) to approximate roughness (grooves) of small scales compared to the boundary layer thickness. In this context, they used the approach to analyze the Type-I (spiral shape) and II (annular shapes) instability behavior. It was found that the groove organization plays a main role in the stabilization of these modes. In effect, even though Type-I instability can be stabilized for any kind of grooves, more complex behaviors were found for the viscous Type-II instability and this latter is still a source of debate (Garrett *et al.* (2016); Stephen (2017)).

The second most common control systems encountered are suction devices and were used early on in the experiments of Gregory & Walker (1960). The results of this study showed that the greater the suction amplitude is the higher will be the critical Reynolds number of the transition to turbulence. This is however not in agreement with Stuart (1954) who suggested through a linear stability analysis that suction had a little effect on the flow stability. The first investigation of suction device effects on the absolute instabilities of the Von Kármán boundary layer was obtained in Lingwood (1997). In particular and using LSA with a parallel flow assumption, they showed that suction has a stabilizing effect for all Type-I modes as well as for the stationnary Type-II modes. In agreement with Gregory & Walker (1960), they also proved that the critical Reynolds number associated to the appearance of absolute instabilities increases with suction. A decade latter, Thomas & Davies (2010) showed also through LSA that using a suction system on the Von Kármán boundary layer, the absolute instability will be transformed into a global instability. This observation was supported by Ho *et al.* (2016) experimentally.

For the Bödewadt boundary layer, much less control studies have been conducted. However, based on the work of Cooper & Carpenter (1997) and Cooper *et al.* (2015), Alveroglu *et al.* (2016) was able to demonstrate using a local stability analysis and an integral energy balance that the Type-I instability is stabilized for isotropic grooves and destabilized for the anisotropic roughness (radial grooves). On the contrary, the same authors showed that in case of the Type-II instability, radially anisotrpic grooves have a destabilizing effect contrary to isotropic and azimuthally anisotropic grooves which are stabilizing. Venkatachala & Nath (1980) then studied the bahavior of the Bödewadt boundary layer with suction/injection. In that case, and with high levels of injection, they found that the inflow is destabilized due to an inversion of the axial velocity direction. Suction showed however to be stabilizing. This last result was confirmed by Lingwood & Garrett (2011) who extended Lingwood (1997) LSA to the BEK family.

5.1.2 Enclosed rotor/stator cavity control

The system of interest to the present work deals with enclosed rotor/stator cavities as introduced in Chap. 2. However, due to the complex nature of the 3D flow coming with such a configuration, little literature exists on their control.
Özkan *et al.* (2017) showed through experiments and simulations that changing the geometric characteristics of a cylindrical rotor/stator cavity has the same effect as adding roughness on the rotor disk. Wilson & Schryer (1978) showed that by activating a suction device on the rotating disk, both rotor and stator boundary layer thicknesses were decreased. The same author also showed that by increasing the suction mass flow amplitude, the stationary boundary layer becomes more and more unsteady. One major benefit of suction when applied to the rotating disk is that it offers the possibility to synchronize the rotating core speed with the rotating disk speed and hence suppress its boundary layer.

Effectively, multiple ways to control a rotating flow is possible although most of the studies focused on the control of the rotating boundary layer. Furthermore, no argument was really given for such a specific choice rather than the control of the stationary disk. In this chapter, the GLSA framework is once again probed to find the optimal position for the introduction of a passive control device that can stabilize an annular rotor/stator cavity. To do so, the sensitivity to base flow modification is introduced in Sec. 5.2 and applied in Sec. 5.3. After setting the strategies taking into account all the studies described in the previous chapters, a relevant controlled system: *i.e.* that could be implemented in an experiment, is tested through LES in Sec. 5.4.

5.2 Sensitivity to base flow modifications

In Chapter. 4, a complete framework was developed to extract and understand the dynamics of an annular rotor stator cavity. In addition to the wavemaker analysis also known as structural sensitivity, the eigenvalue sensitivity to a perturbation of the base flow defines another important quantity which provides physical insight on the instability mechanism, especially for control purposes. Indeed, it provides a useful tool to predict how the mean flow should be varied by a passive controller so it significantly affects the leading global mode. First introduced by Marquet *et al.* (2008), this analysis enabled to explain the experimental results obtained by Strykowski & Sreenivasan (1990) for which small cylinders where postionned to remove the vortex shedding of a classical cylinder wake. Since its first use, this type of analysis has been applied to many configurations: D-shape cylinder (Carini *et al.* (2017)), open cavities Mettot *et al.* (2014) and so on.

As done in Chap. 4, the base flow is hereafter defined as $Q = [\mathbf{U}, P]$ with $\mathbf{U}$ and P respectively the velocity and pressure base flow. Each mode under study will be qualified by their complex eigenvalue ω for which $\omega_r = \mathfrak{Re}(\omega)$ and $\omega_i = \mathfrak{Im}(\omega)$ are respectively the mode frequency and growth rate.

The main steps to obtain the sensitivity to base flow modifications $\nabla_Q \omega$ of a given mode are as follows. For a base flow modification $\delta Q = [\delta \mathbf{U}, \delta P]$, the eigenvalue shift, denoted $\delta\omega$, will result from the expression,

$$\delta\omega =< \nabla_Q \omega, \delta Q >, \tag{5.2.1}$$

where $< \cdot, \cdot >$ corresponds to the inner product $< a, b >= \int a^* \cdot b \, dS$ with a^* the conjugate of a. Note that the sensitivity $\nabla_Q \omega$ is a complex vector, which is decomposed into a real and an imaginary part corresponding respectively to the frequency sensitivity $\nabla_Q \omega_r = \mathfrak{Re}(\nabla_Q \omega)$ and the growth rate sensitivity $\nabla_Q \omega_i = -\mathfrak{Im}(\nabla_Q \omega)$ or,

$$\delta\omega_r =< \nabla_Q \omega_r, \delta Q > \quad , \delta\omega_i =< \nabla_Q \omega_i, \delta Q > . \tag{5.2.2}$$

The sensitivity to a base flow modification computation corresponds in the end to an optimal control problem where Q is the control function, Eq. (4.3.19) the eigenvalue problem to solve (a constraint), (ω, $\hat{\mathbf{q}}$) the state function and ω is the cost function that one wants to maximize (the most sensitive parts correspond to the highest variation of ω). To solve this optimal problem, the Lagrangian functional $\mathfrak{L}$ (Airiau *et al.* (2003)), is introduced so that,

$$\mathfrak{L}(\omega, \hat{\mathbf{q}}, \hat{\mathbf{q}}^+, Q) = \omega - < \hat{\mathbf{q}}^+, D(\{\omega, \hat{\mathbf{q}}\}, Q) >, \tag{5.2.3}$$

where D is a reformulation of the direct eigenvalue problem expressed by Eq. (4.3.19) so that $D(\{\omega, \hat{\mathbf{q}}\}, Q) = \mathcal{L}(m, Q)\hat{\mathbf{q}} - \omega\hat{\mathbf{q}}$ and $\hat{\mathbf{q}}^+$ is the adjoint mode here defined as the Lagrange multiplier. Cancelling the gradient functional with respect to the state variable (ω,$\hat{\mathbf{q}}$), the multiplier $\hat{\mathbf{q}}^+$ and the control variable Q enable to retrieve respectively the direct eigenvalue problem, Eq. (4.3.19), the adjoint eigenvalue problem, Eq. (4.3.20), and the expression of the sensitivity to base flow modifications. The latter can thus be formulated as,

$$< \nabla_Q \omega, \delta Q >=< \frac{\partial \mathfrak{L}}{\partial Q}, \delta Q >= \delta\omega. \tag{5.2.4}$$

Note that, one can show that this sensitivity for incompressible flow is independent of the pressure base flow modification and can therefore be expressed by,

$$\nabla_{\mathbf{U}} \omega = -(\nabla \hat{\mathbf{u}})^H \cdot \hat{\mathbf{u}} + \nabla \hat{\mathbf{u}}^+ \cdot \hat{\mathbf{u}}^*. \tag{5.2.5}$$

The first term on the right hand side of Eq. (5.2) is usually interpreted as the sensitivity to a base flow transport (advection) modification and is usually denoted $\nabla_{\mathbf{U}_T} \omega$. The second term in such a case is the sensitivity to a base flow production modifications and is usually referred to as $\nabla_{\mathbf{U}_P} \omega$. The investigation of both terms can be useful to deeply investigate the source of a given mode which can then be opposed to the convective/absolute instability notions of a local stability analysis.

In order to validate the sensitivity to a base flow modification as implemented in our global stability code, a cylinder wake has been simulated and compared to the results of Marquet *et al.* (2008). Good agreement was found and details of this test case can be retrieved in App. C.

5.3 Application to the annular rotor stator/cavity

The dynamics of an annular rotor/stator cavity has been deeply investigated in the previous chapters. In particular, DMTC showed that the $m = 12$ mode is generated by the dominant mode ($m = 29$) of the system which therefore needs to be suppressed if one wants to control the overall pressure band phenomenon. The sensitivity to a base flow modification based on the GLSA framework introduced in the previous chapter is applied here to define a physical control system that could stabilize or at least shift the frequencies of the observed pressure bands.

5.3.1 Control strategies

Figures (5.2) and (5.1) show respectively the results obtained for the magnitude of the frequency sensitivity to a base flow modification $\nabla_U \omega_r$ and the magnitude of the growth rate sensitivity to the same base flow modification $\nabla_U \omega_i$ for each modes present in the cavity of interest: *i.e.* **Case 2** of Chap. 4. In each case, the results are normalized by their infinity norm ($\|\nabla_U \omega_r\|_\infty$ for the frequency sensitivity and $\|\nabla_U \omega_r\|_\infty$ for the growth rate sensitivity). For any given mode, the same regions of the cavity are globally sensitive to changes, either for the frequency or the growth rate. Table (5.1) gives the location of maximum sensitivity found for each component and each mode. The stator and rotor modes are clearly more sensitive in the Bödewadt boundary layer which was also found to be the source of these modes (Queguineur *et al.* (2018)). Note finally that the annular mode has a particular spatial distribution of sensitivity similar to its adjoint mode computation (see Fig. 4.16(a)).

	$\|\nabla_U \omega_r\|_\infty$	$\|\nabla_U \omega_i\|_\infty$
Stator mode	(0.19 m, 34.9 mm)	(0.20 m, 34.9 mm)
Annular mode	(0.13 m, 33 mm)	(0.13 m, 32.4 mm)
Rotor mode	(0.12 m, 34,8 mm)	(0.13 m, 34,8 mm)

Table 5.1 – (r, x) Position of maximum sensitivity for each modes

The purpose of the upcoming discussion is to investigate base flow sensitivity maps in more details so as to identify strategies to control this rotating cavity flow. Two ways can be taken: For an industrial purpose, the first one would be to apply a base flow modification susceptible to shift the frequency in order to establish a new limit-cycle less dangerous for the integrity of the whole system. The second one would be to

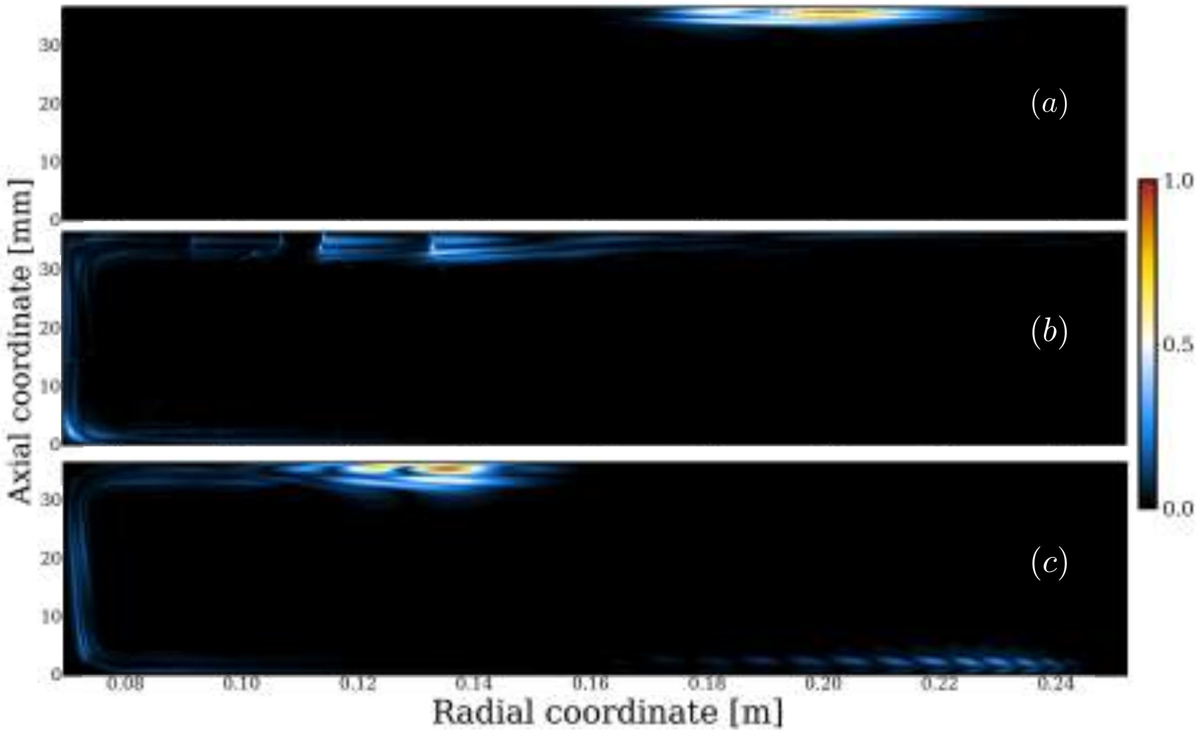

Figure 5.1 – Spatial distribution of the growth rate sensitivity to base flow modification: The magnitude of $\nabla_U \omega_i$ is represented with (a) the stator mode ($m = 29$) (b) the annular mode ($m = 0$) and (c) the rotor mode ($m = 12$).

suppress the modes by decreasing their growth rate until they become stable. From these results, the Bödewadt boundary layer (stator) needs to be thickened or reduced to alter the dominant mode appearance. As said previously, global stability analysis has been successfully used in previous studies to control unstable boundary layers (Carini *et al.* (2017)) with suction/injection slots. In the present case the whole dynamics of the system is concentrated around the two boundary layers of the disks and hence the more efficient way to control the modes would be to change the structure of the flow near the disk walls. The questions remaining are, where should one put a flow controller and which type should be used? Grooves showed to be an efficient tool but would be difficult to link in terms of physics with the sensitivity flow analysis. At the opposite, low amplitude suction/injection can be directly linked to the local velocity base flow modification δU introduced in Sec. 5.2 or at least the local thickness of the above boundary layer. These latter actuation systems are therefore chosen for the configuration studied here.
To set up such a control system, Fig. 5.3 and Fig. 5.4 provide views of the axial component respectively for the growth rate sensitivity to a base flow modification and the frequency sensitivity to a base flow modification. Thanks to these results, if one takes a purely axial velocity modification, the expression behind Eq. (5.2) can give us directly the sign of the mode eigenvalue shift. If the main purpose of the controller is to stabilize the dominant mode (stator mode), Fig. 5.3(a) shows that one can add a suction device ($\delta U > 0$)

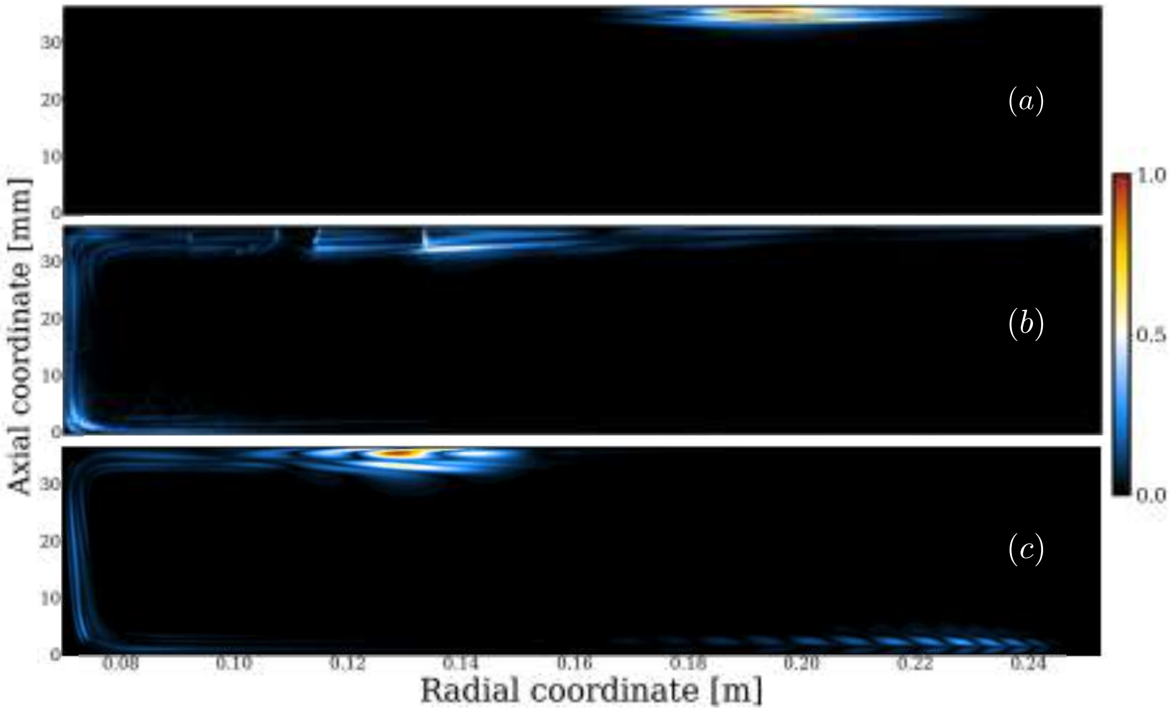

Figure 5.2 – Spatial distribution of the frequency sensitivity to base flow modification: The magnitude $\nabla_U \omega_r$ is represented with (a) The stator mode ($m = 29$) (b) The annular mode ($m = 0$) and (c) The rotor mode ($m = 12$).

between $r \in [0.195 \text{ m}, 0.21 \text{ m}]$ on the stator disk. According to Eq. (5.2) one will obtain a negative growth rate shift. For this exact same device, Fig. 5.4(a), shows that a positive shift of the frequency will be obtained which can be also an interesting approach if one purpose of the controller system is, for example, to avoid a resonance of the flow with the structure. Note that this solution will however not guarantee an optimal shift of the frequency. In fact, the maximum of axial frequency sensitivity to a base flow modification is found around 0.1925 m. Note also that the growth rate sensitivity has a sign change around $r = 0.19$ m, the diameter of the suction device needs therefore to be precisely adapted to fulfill all the wanteed conditions and avoid a destabilization of the dominant mode. The last benefit of the position and orientation of the proposed control device is that it doesn't impact *directly* the other modes. Indeed the growth rate sensitivity of the rotor and annular modes in the range $r \in [0.195 \text{ m}, 0.21 \text{ m}]$ are almost equal to zero, so, any modification δU of the boundary layer should not change their properties. However, as demonstrated in Chap. 3 and by Bridel-Bertomeu (2016), the stator mode was found at the origin of the low frequency rotor mode; a reaction of this mode is hence expected with the activation of the controller.

The drawback with the proposed suction actuator is that even if used with a low total mass flow rate, the operating point of the system will be changed which may not be acceptable for an industrial case. To overcome this problem, a second actuator oriented inward (injection slot) with an appropriate section is necessary. The first possibility is to simply place this second actuator in the external part of the cavity ($r \in [0.24\ \text{m}, 0.25\ \text{m}]$) where the sensitivity of the flow is almost equal to zero for all modes. The second possibility is to position it near the hub, also on the stator disk around ($r \in [0.12\ \text{m}, 0.13\ \text{m}]$). Indeed, the latter would directly stabilize the annular and rotor modes.

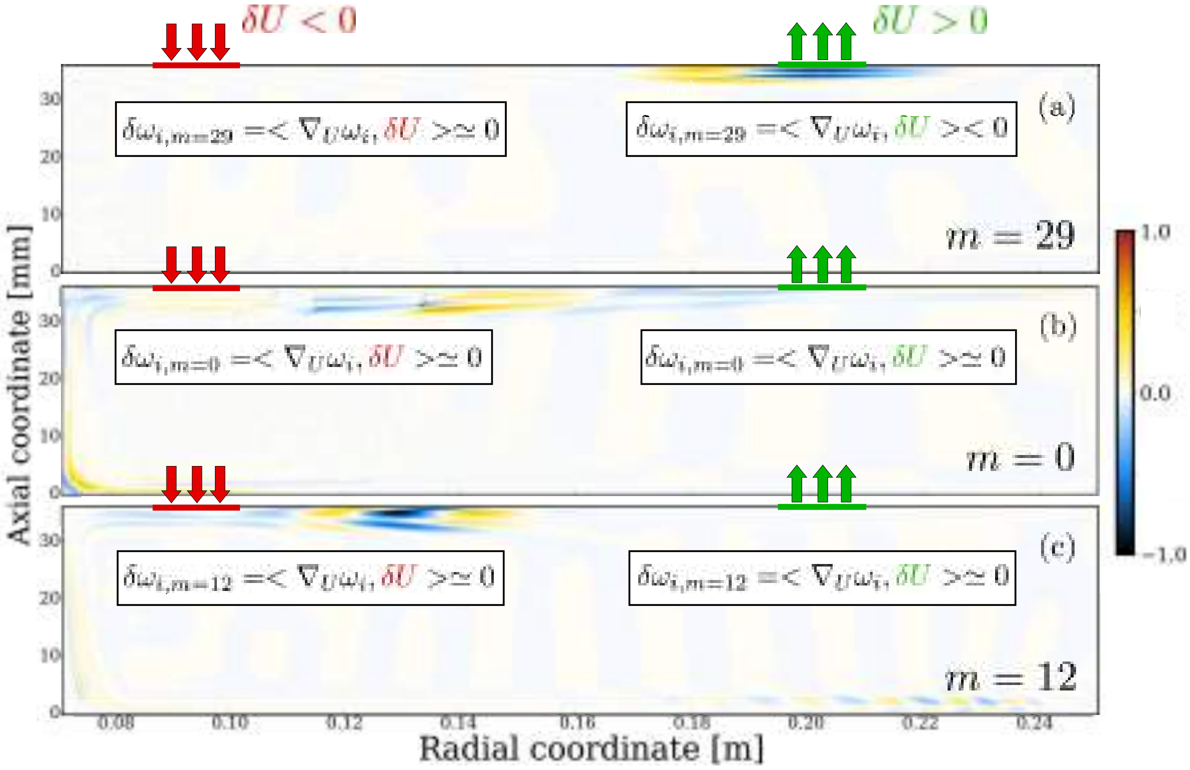

Figure 5.3 – Spatial distribution of the growth rate sensitivity to base flow modification: The axial component $\nabla_U \omega_i \cdot x$ is represented with (a) the stator mode ($m = 29$) (b) the annular mode ($m = 0$) and (c) the rotor mode ($m = 12$). The red arrows represent the injection and the green one the suction. Note that the exact surfaces for each actuators is displayed. The growth rate shift generated by the controllers are also displayed for each modes.

5.3.2 Effect of a flow modification: transport and production mechanisms

The sensitivity to a base flow modification can be linked to the local stability approach. In fact, as described in Sec. 5.2, the sensitivity gradient can be decomposed into a production and a transport term. As introduced by Huerre & Monkewitz (1990), a global mode comes from the competition between production and advection of fluctuations by the base flow. When the production (respectively the transport) dominates, the flow is said locally absolutely (respectively convectively) unstable. A region of absolute instabilities is necessary to generate a global mode and can be retrieved in the present sensitivity analysis. Figure 5.5 presents the results of this decomposition with the growth rate sensitivity to a base flow production/transport modification for the *stator mode*

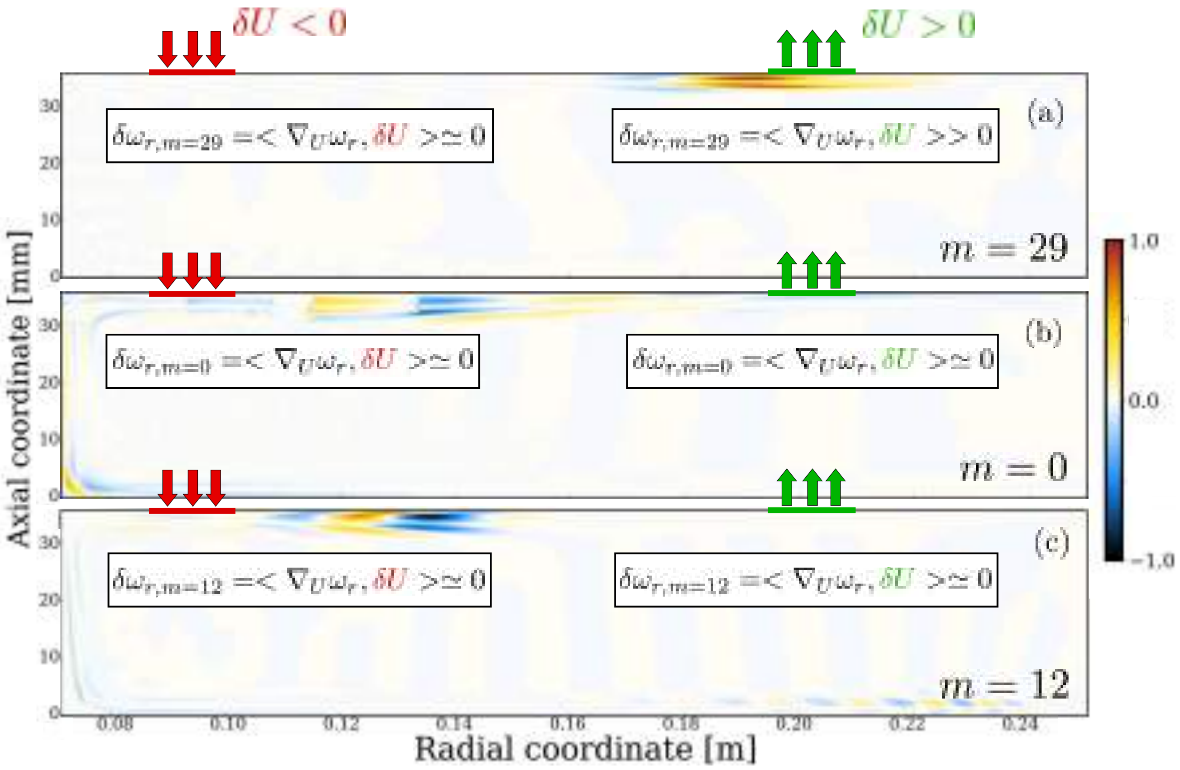

Figure 5.4 – Spatial distribution of the frequency sensitivity to base flow modification: The axial component $\nabla_U\omega_r \cdot x$ is represented with (a) the stator mode ($m = 29$) (b) the annular mode ($m = 0$) and (c) The rotor mode ($m = 12$). The red arrows represent the injection and the green one the suction. Note that the exact surfaces for each actuators is displayed. The frequency shift generated by the controllers are also displayed for each modes.

$m = 29$. The production $\nabla_{U,P}\omega_i$ is represented in Fig. 5.5(a) and the transport $\nabla_{U,T}\omega_i$ in Fig. 5.5(b). The magnitude is provided for each plot and a zoom in the zone of interest is also performed to visualize the orientation of the sensitivity gradients using arrows. Both magnitudes have been normalized by $max(\|\nabla_{U,T}\omega_i\|_\infty, \|\nabla_{U,P}\omega_i\|_\infty)$. As one can see, higher values of sensitivity are generally observed for production than for transport. This indicates that to change the stator mode stability properties, a modification of the base flow production mechanisms would be necessary in the zone $r \in [0.175 \text{ m}, 0.21 \text{ m}]$.

Note that the orientation of both sensitivities is interesting to understand the mechanisms at the source of the mode stability. In Fig. 5.3(a), a sign inversion has already been noted around $r = 0.19$ m, this is due to a complete inversion of the sensitivity to the base flow production orientation in this zone as shown in Fig. 5.5(a). However, the transport sensitivity stays oriented downward in all the zone of high sensitivity. In the previous argumentation, a suction device has been chosen to be located around $r \in [0.19 \text{ m}, 0.21 \text{ m}]$ to stabilize the mode (negative shift of the growth rate). One can see that the small base flow modification generated by this controller ($\delta U > 0$) is almost oriented in the opposite direction to the transport sensitivity and hence generates a $\delta\omega_i < 0$. Contrarily, the production sensitivity is almost completely orthogonal to δU and hence generates a $\delta\omega_i \simeq 0$. One can conclude that the stabilization of this mode for the chosen control system comes from the transport mechanism which is in agreement with the fact that to suppress an absolute instability region, one needs to balance the excess of fluctuation production compared to the fluctuation transport (see Sec. 4.2 for more details about absolute/convective instabilities).

Finally, the global stability analysis gave the structural sensitivity of each mode (wavemaker) but no direct comparison could be done with the notion of absolute instabilites of the local approach. In Fig. 5.5(c), the convective/absolute nature of each instabilily for all radial positions found with a local stability analysis of (Queguineur *et al.* (2018) and Bridel-Bertomeu (2016) are displayed and compared with the sensitivity to the base flow production/transport modification of Fig. 5.5(a)-(b). In these results, the region of absolute instabilities (defined for a positive growth rate) is found quite larger than the present analysis where production of perturbations dominates transport of perturbations. These observations highlight again the limit of the local stability approach and the better precision of the global approach. However, for both approaches the wavemakers were found at similar radial locations (see Queguineur *et al.* (2018)).

In the next section, the control strategy developed previously is effectively tested so that expected results presented here can be validated. To do so, LES of the exact same cavity studied in Chap. 2 augmented with the control devices are produced and analyzed.

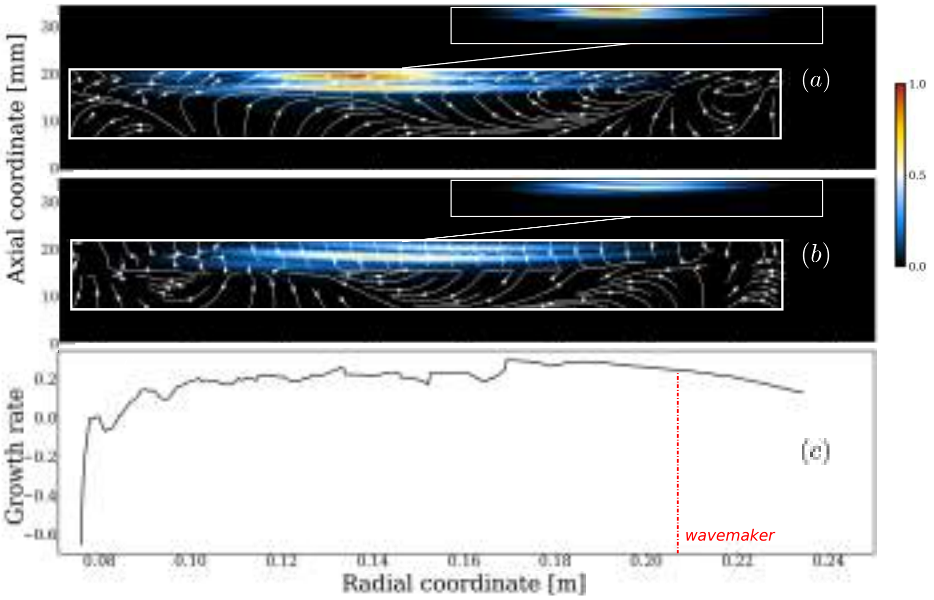

Figure 5.5 – Stator mode mechanisms: Spatial distribution of the growth rate sensitivity to base flow modification of (a) Production $\|\nabla_{U,P}\omega_i\|$ (b) Transport $\|\nabla_{U,T}\omega_i\|$. For each case, a zoom between $x \in [28, 35mm]$ displays their orientation with arrows. The radial distribution of the growth rate obtained for the stator mode with a local approach is displayed in (c) (Bridel-Bertomeu (2016)).

5.4 Validation of the control strategy through LES

This section intends to confirm the sensitivity to base flow modification results while validating the control strategies proposed in the previous section. To do so, a LES as described in Chap. 2 is repeated taking into consideration the identified suction and aspiration actuators. After a brief description of the numerical set up, results for different suction/injection mass flow rates are presented. Then an investigation of the mode evolutions is provided for one specific mass flow rate that was found optimal. Finally, a stability analysis of the controlled system is analyzed to show the evolution of the linear global modes and the new flow state.

5.4.1 Numerical set up

The numerical parameters used for the present validation are taken from the uncontrolled case introduced in Sec. 2.4. The following paragraph details the meshing strategies adopted to incorporate the two new controllers and a description of the specific boundary conditions used.

Mesh

As a reminder, the original mesh of the uncontrolled configuration introduced in Sec. 2.4 was constructed from a 2D fully triangular mesh and extruded along the rotation axis. In order to add the two new boundary conditions following the control strategies developed in the previous section, the original mesh needed to be modified. To be consistent with the previous mesh, the same extrusion method is applied. To do so, five 2D annuli have been meshed and extruded as presented in Fig. 5.6 (small sector in gray). The resulting annular rotor/stator cavity is thus obtained by assembling all five 3D annuli with HIP while maintaining the two surfaces acting as controllers (injection and suction devices respectively represented in red and green in Fig. 5.6).

Boundary conditions

To set up the suction and blowing controllers, the multiperforated boundary condition available in AVBP are used (Mendez *et al.* (2006)). In its actual version, two types of these specific boundary conditions exist: injection side wall-model and suction side wall-model for multiperforated walls. The benefit of these boundary conditions is that they both allow to impose a mass flow even in the case of a suction which is difficult to do with a classical outlet boundary condition. To stay coherent with the control strategies, a porosity (ratio of the holes surface over the total surface) has been set to 1 and the orientation of the corresponding perforated holes is supposed to be orthogonal to the direction of the main flow.

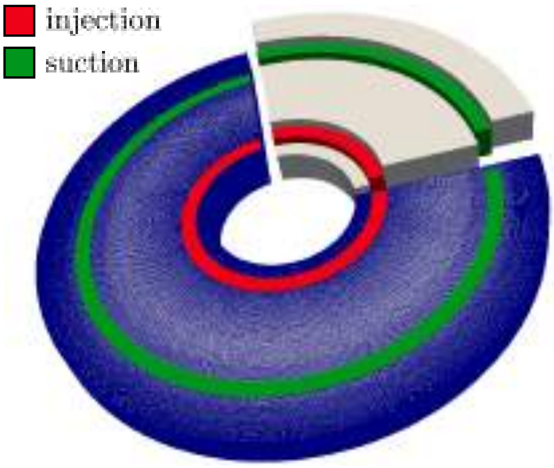

Figure 5.6 – Controlled system mesh: The 5 rings forming the mesh is represented by an exploded sector. The red ring corresponds to the suction actuator and the green one the injection actuator.

5.4.2 Results

In this section, the results of the controlled annular cavity are presented for different suction amplitudes. In the literature on rotating flow control, the parameter $a = -U_x/\sqrt{\nu\Omega}$ where U_x is the wall-normal velocity at the disk surface of the injection/suction controller is usually used (Stuart (1954), Ho *et al.* (2016)). Note that $a > 0$ will denote suction while $a < 0$ for an injection control.

Mass flow rate effect

To stay in the linear assumption usually needed for the analysis used to design the controllers, low suction parameters are necessary. However, fixing a limit is impossible so seven values ranging from $a = 0.001$ to $a = 0.2$ have been tested. First, the convergence of the flow kinetic energy $\bar{E}_k$ integrated over the domain and normalized by the uncontrolled cavity kinetic energy in its limit cycle $\bar{E}_{k_{NC}}$ is shown in Fig. 5.7. This figure presents the results obtained for an increasing suction parameter going from $a = 0.001$ to $a = 0.2$ with an increasing shading: *(light)* for low values to *(dark)* for high values. Time is normalized such that $t' = t\,F_0$ and one can see that a stable state is obtained for each case after $t' = 20$. From this result, one can also notice that the overall kinetic energy of the controlled system is decreased by 1 to 2% compared to the uncontrolled case and this level decreases with an increasing suction parameter.

The new limit cycles obtained are analyzed in the following through pointwise power spectral density of the axial velocity component. Note that the same probe notationas in Chap. 2 is resumed here. Figures 5.8(a)-(e) give the PSDs obtained as a function of a respectively for probes with an increasing radial position going from $r = 0.08$ m to $r = 0.24$ m, the position of the probes being reminded in Fig. 5.8(f). Finally, the results obtained for the uncontrolled cavity are added in black in each plot for

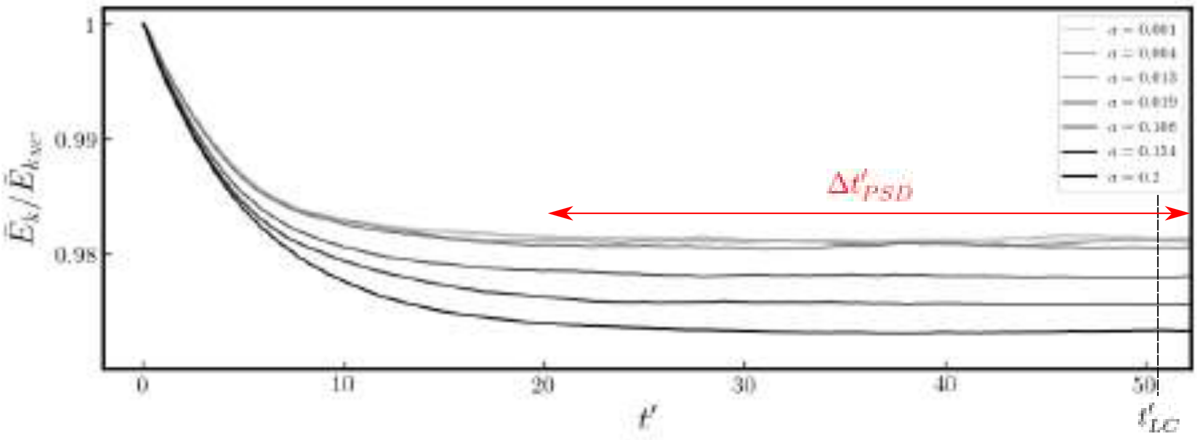

Figure 5.7 – Convergence of the kinetic energy $\bar{E}_k$. Each curve corresponds to a given suction parameter scaling from $a = 0.001$ (light) to $a = 0.2$ (dark). The results are normalized by the uncontrolled cavity kinetic energy $\bar{E}_{k_{NC}}$. t'_{LC} is the time at which the 2D shape of each final limit cycles obtained for each parameter a will be displayed in Fig. 5.9. $\Delta t'_{PSD}$ is the time range on which PSDs will be applied on each limit cycles.

reference. For all cases, the exactly same range of time $\Delta t'_{PSD} = 32$ (see Fig. 5.7) has been taken to rigorously compare the different results. From a general point of view, one can see that for all suction parameter values, it is really difficult to distinguish a global frequency. When one looks closely, 3 regions can however be identified: For very low suction, no global frequency is distinguished but the overall PSD level is increased by about 20% around the controllers (see Fig. 5.8(d)-(e)). The PSD level is however not impacted between the two controllers (see Fig. 5.8(b)-(c)) where the dominant mode was initially observed in the uncontrolled case. Increasing the suction parameter values results in an overall level decrease and for the highest suction values, a new limit cycle is detected with new frequencies: $F/F_0 = 1.18$ and $F/F_0 = 2.2$ at low radii as shown in Fig. 5.8(a)-(b). However compared to the uncontrolled case, one can see that these modes are not advected all around the cavity and the actuators can be seen as perturbation transportation absorbers. Note that these observations can also be retrieved by analyzing the PSD of probes located in the middle of the cavity as well as for probes around the rotor. Interested reader can refer to App. D for these specific results.

The evolution of the controlled cases compared to the uncontrolled one can also be retrieved in Fig. 5.9 with instantaneous field of axial velocity taken in a plane around the stator boundary layer at $z = 0.035\,m$ for all suction parameters and the non controlled case at t'_{LC} (see Fig.5.7). In Fig. 5.9(a), one can see that the annular and the spiral patterns are retrieved here with the new mesh. With the activation of the controller, all the patterns are broken leaving only turbulence even for the smallest suction parameter. For $a = 0.004$, new spirals at high radii start to appear locally and grow inward if increasing a. For $a = 0.108$, a new pattern arises to appear around the hub and a clear azimuthal wavenumber $m = 14$ is observed for $a = 0.2$. Note that the frequencies

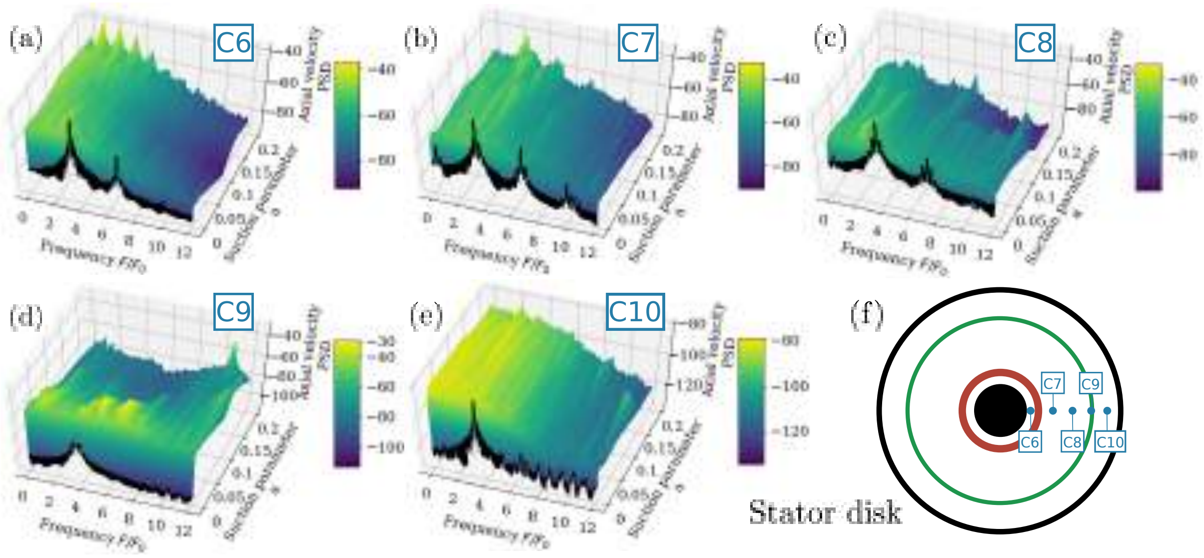

Figure 5.8 – Probes Axial velocity PSD of the controlled cavity function of the suction amplitude a in the stator disk: (a) probe $C6$ ($r = 0.08$) (b) probe $C7$ ($r = 0.12$) (c) probe $C8$ ($r = 0.16$) (d) probe $C9$ ($r = 0.20$) (e) probe $C10$ ($r = 0.24$) . In each plots the black contour represent the results obtained for the non controlled cavity. (f) Schematic of the probes $C6$ to $C10$ probes.

observed in the PSDs of this last case must be linked to the patterns described here. This behavior is in agreement with the theorical results of Venkatachala & Nath (1980) for which the Bödewadt boundary layer was found destabilized by flow injection and stabilzed for suction. However, the present study shows that contrary to Venkatachala & Nath (1980) low values of suction/injection are sufficient to stabilize the boundary layer.

The effect of the controllers on the mean flow is described in the following set of figures. Figure 5.10 gives first the velocity profiles for 3 radial positions : $r' = 0.3$ (injection device position), $r' = 0.5$ (mid-cavity) and $r' = 0.65$ (suction device position) respectively given in columns *(left)*, *(middle)* and *(right)* where $r' = r/(R_0+R_1)$. For these three positions, the three velocity components U_r, U_θ and U_x are provided respectively in rows Fig. 5.10(a)-(c), Fig. 5.10(d)-(f) and Fig. 5.10(g)-(i). From the radial velocity profiles, one can note that the suction device has a direct impact on the stator boundary layer thickness (as expected) and this latter keeps shrinking when increasing the controller strength (see Fig. 5.10(c)). One can also note that the flow injection at $r' = 0.3$ creates locally a negative azimuthal velocity around the stator disk which is increasing with a as shown by Fig. 5.10(d). From Fig. 5.10(i), one can see that the suction device inverts locally the axial velocity component but more importantly reduces the inflection nature of the mean flow profile. Finally, it is noted that activating the suction changes the core flow. In fact, this latter has, in the uncontrolled case, a negative and constant axial velocity due to the pumping effect of the rotor. However, In the controlled cases, the sign of the axial speed changes at mid-height of the cavity. At the opposite location, at the injection device location ($r' = 0.3$) and for relatively low mass flow injections,

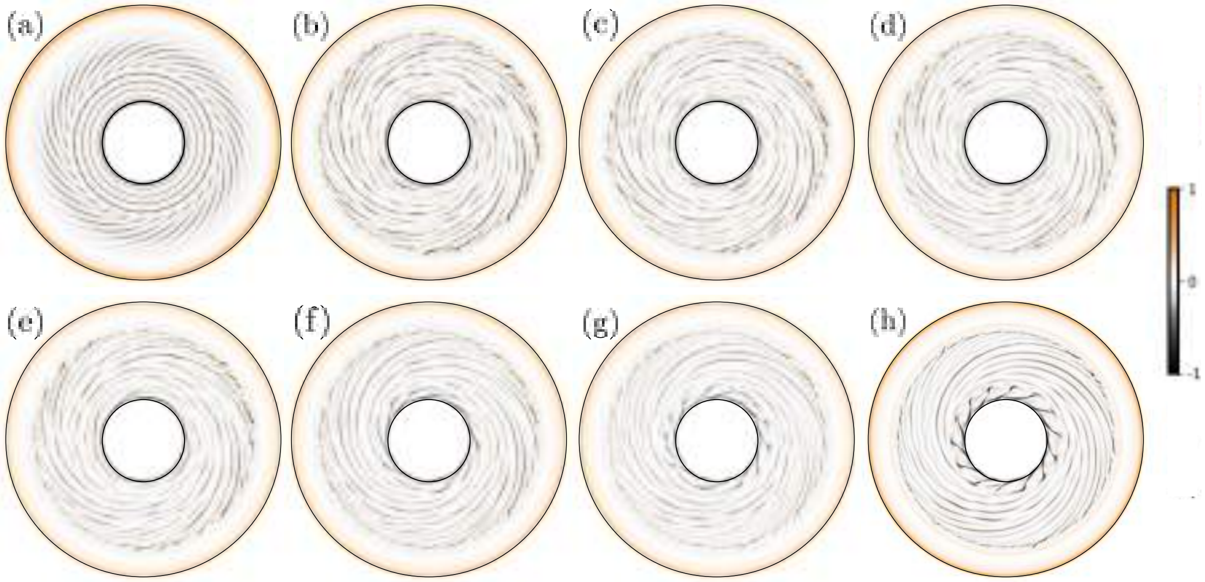

Figure 5.9 – Limit cycles: Instantaneous axial velocity in a plan at $x = 0.035$ in at t'_{LC} (see Fig.5.7): (a) $a = 0$, (b) $a = 0.001$, (c) $a = 0.004$, (d) $a = 0.013$, (e) $a = 0.019$, (f) $a = 0.108$, (g) $a = 0.154$, (h) $a = 0.2$.

Fig. 5.10(g) shows that the mean flow profile is not perturbed and it is only for $a = 0.108$ that strong axial velocity around the stator starts to deform the uncontrolled mean flow. This last observation could be linked to the new limit-cycle appearing above $a = 0.108$ and particularly active around the hub. Finally, at $r' = 0.5$, Fig. 5.10(h), low suctions affect more the core flow axial velocity of the system than high suction. For example, for $a = 0.001$, the axial velocity core flow is increased by about 36% compared to the uncontrolled case. Concerning the Bödewadt boundary layer, one can see that this rotor boundary layer is not impacted at all in the region where the dominant mode $m = 29$ is particularly marked in the uncontrolled cavity. This ensures that the stabilization mechanism of this mode is not linked to a modification of the mean flow around $r' = 0.5$.

Detailed study of the flow limit-cycle for $a = 0.004$

The results obtained for a very low mass flow injection and suction: *i.e.*, $a = 0.004$ are particularly detailed thereafter. First, three instantaneous axial velocity fields taken at $t' = 0, 25$ and 38.7, where $t' = F_0 t$ are given in Fig. 5.11. Note that for this specific case, less than 10 periods are necessary to retrieve a stable state of the system as seen in Fig. 5.7. As shown by Fig. 5.11(c), when ce limit cycle is reached, no clear structures can be identified. The spirals corresponding to the dominant mode appear here broken showing a purely turbulent flow.

To visualize the evolution of the three characteristic modes found previously in Chap. 2, DMT is activated during the simulation starting from the activation of the

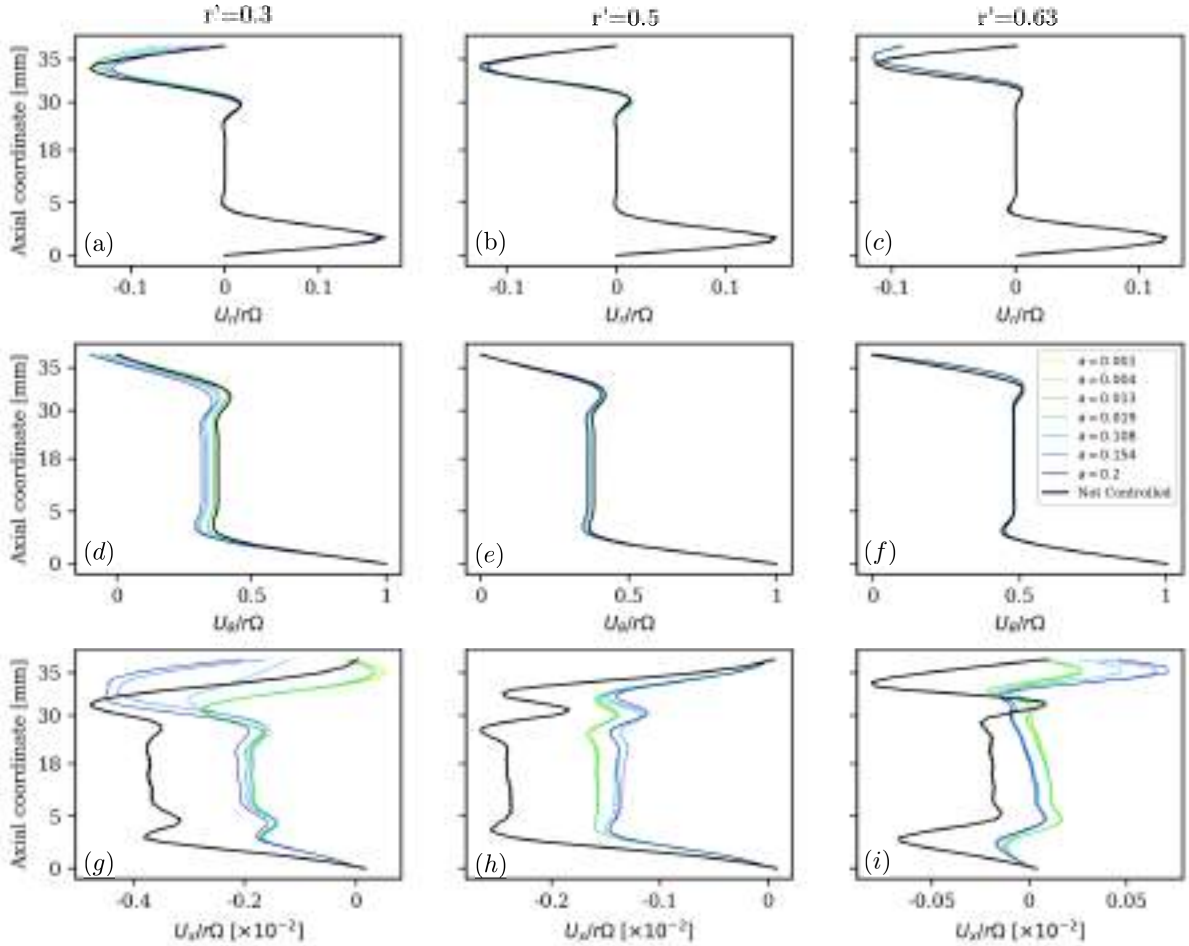

Figure 5.10 – Mean flow velocity profiles of the controlled cavity: (a)-(c) Radial velocity component (d)-(f) azimuthal velocity component (g)-(i) axial velocity component. The three components are normalized by $r\Omega$ and are displayed for the radii $r' = 0.3$ (injection device position), $r' = 0.5$ (mid-cavity) and $r' = 0.65$ (suction device position) respectively in columns *(left)*, *(middle)* and *(right)*.

(a) (b) (c)

Figure 5.11 – 3D instantaneous axial velocity with (a) $t' = 0$, (b) $t' = 25$ and (c) $t' = 38.7$.

actuators. Axial velocity profiles are displayed on Fig. 5.12 for the modes $m = 29$, $m = 0$ and $m = 12$ at the same characteristic times as the ones used in Fig. 5.11 for the plane positioned in the stator boundary layer at $z = 35.7$ mm. With DMT, one retrieves initially the annular and spiral modes that are then progressively broken to finally display all selected frequencies an almost purely incoherent flow.

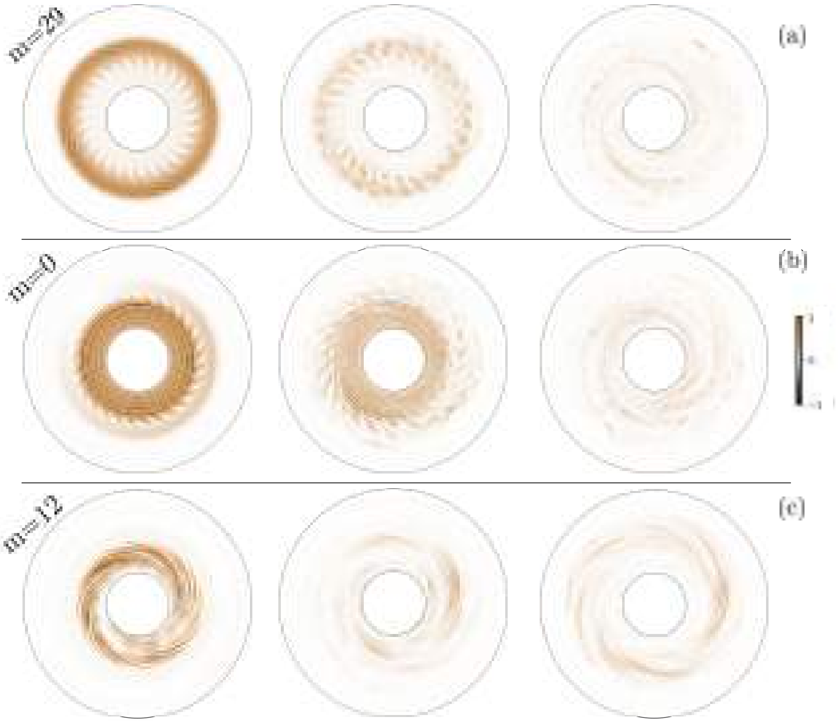

Figure 5.12 – Modes controlled: evolution of the modes driving the uncontrolled cavity dynamics with (a) m=29 , (b) m=0 and (c) m=12. each mode can be visualized at the three characteristic times: $t' = 0$, $t' = 25$ and $t' = 38.7$ in a plane located in the stator boundary layer at $z = 35.7$ mm.

Finally, PSDs of the axial velocity in the stationary disk are again used to evaluate the evolution of the fluctuation levels. As one can see in Fig. 5.13(a), the uncontrolled cavity initially displayed a spectrum concentrated around three main modes. From Fig. 5.13(b), the PSD level of the controlled cavity has increased due to the controllers but no mode can be truly distinguished. Only a few peaks can be observed around the periphery of the cavity (probe C_9) for $F/F_0 = 7.0$. This wave stays however local and no clear global mode seems to appear. The $-5/3$ slope relevant to the inertial range of a Kolmogorov spectrum in a fully turbulent flow Pope (2001) is also present for both cases, thus supporting the turbulent LES flow in the stator boundary layer that are not yet fully turbulent but rather in a transitional state. Higher dispersion can however be observed for high frequencies of the controlled cavity compared to the uncontrolled cavity.

Stability analysis of the controlled cavity for $a = 0.004$

The purpose hereafter is to investigate the modal content generated by the mean flow of the controlled cavity for a suction parameter $a = 0.004$. To do so, stability analysis is produced and results are compared to the sensitivity to a base flow modification

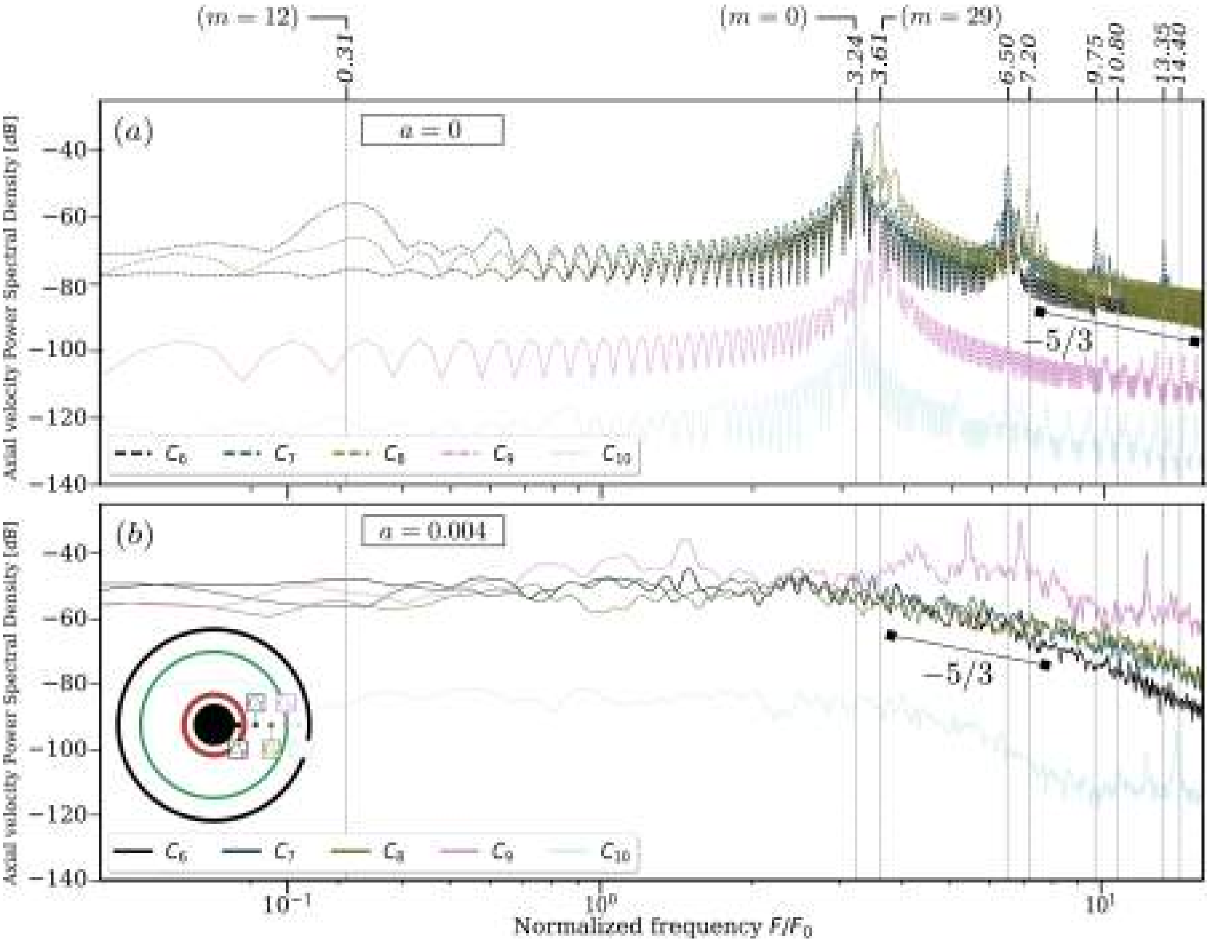

Figure 5.13 – Axial velocity PSD comparison between (a) the uncontrolled cavity ($a = 0$) and (b) the controlled cavity ($a = 0.004$). All the probes from C_6 to $C_1$0 are localized in the stator boundary layer.

analysis described in Sec. 5.3.1.

First, Fig. 5.14 gives a direct comparison of the radial velocity component of the controlled cavity (Fig. 5.14(a)) and the uncontrolled one (Fig. 5.14(b)). As one can see, no impact can be observed on the rotor flow. Around the suction actuator, no significant changes is also identified. This is explained by the low axial velocity introduced by the actuator system as already observed from the velocity profiles, Fig. 5.10. This last observation is important, in the sense that the main purpose of these control systems is to suppress the main mode, preserving the operating condition of the cavity and without disturbing the flow around the hub. Note however that, at the periphery of the cavity, the stator boundary layer is locally decreased by 10% around the suction controller.

In the following, the eigenvalue spectrum issued by the linear stability analysis of the controlled cavity is compared to the uncontrolled case. Figure 5.15 gives the results associated with (a) the amplification rate and (b) the frequency. The first observation

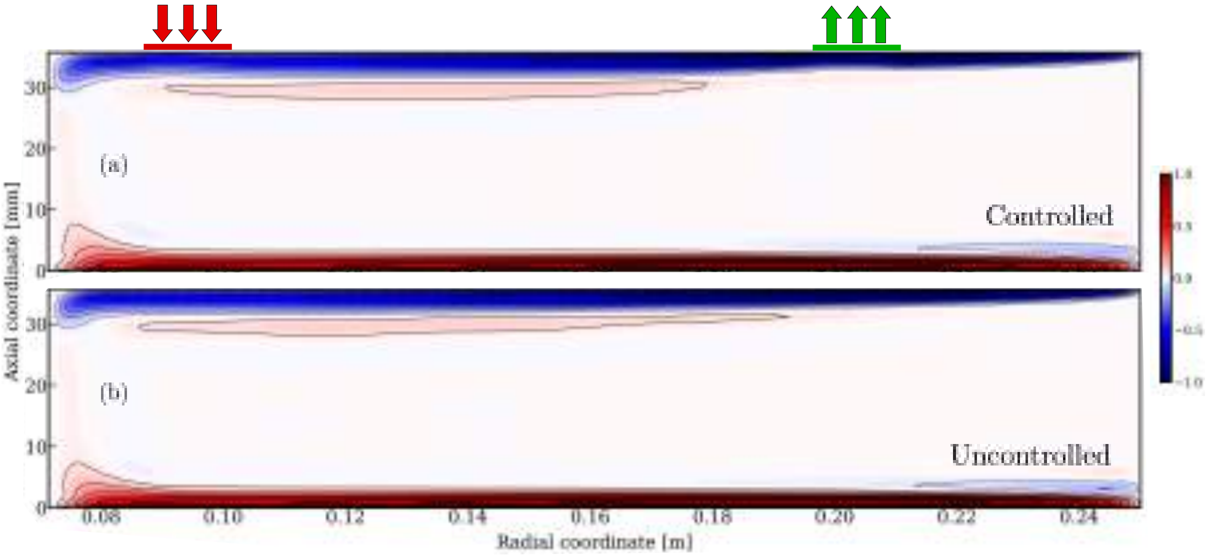

Figure 5.14 – Comparison of the radial velocity component: (a) Controlled case ($a = 0.004$) (b) uncontrolled case ($a = 0$). The red arrows represent the injection and the green ones the suction. Note that the exact surfaces for each actuator are displayed. Both plots have been normalized by the maximum radial velocity of the uncontrolled case.

that can be made is that no physical mode could be retrieved for $m = 12$ as expected since one showed that by controlling the mode $m = 29$, the mode $m = 12$ should disappear (see Chap. 3).

The second point concerns the annular mode $m = 0$. As one can see, even though, LES results predict that this mode is totally damped, LSA predicts only a slight decrease of its amplification rate. This result validates one of the main purpose of the control strategy which was to suppress the dominant mode without impacting the other ones. Furthermore, what is suspected here is that the specific mode around the hub, that can be well observed on Fig. 5.9(h) (for $a = 0.2$), is linked to the annular mode which had a very similar shape around the hub at the mid-height of the cavity in the uncontrolled case. In other words, the mode seen on Fig. 5.9(h) can be the annular mode amplified after the suppression of the $m = 29$ mode. One can also note that the new $m = 0$ mode found by LSA is very close in terms of frequency to the one found in the PSDs for high suction amplitude with LES ($F/F_0 = 2.2$).

Finally, interesting results are found for the mode $m = 29$. Even though not observable in the LES, the frequency of mode $m = 29$ issued by LSA has been increased thanks to the controller systems as expected by the sensitivity analysis and the control strategy set up. However, despite the observation that LES confirmed that control the dominant mode is fully stabilized, from a linear stability point view a large amplification of this mode is obtained. This type of result was already observed in Leu & Ho (2000) where the global mode of a plane wake was indeed eliminated thanks to suction which shrinked the region of absolute instability. But this control also caused at the same time a steep rise of the mode absolute amplification rate.

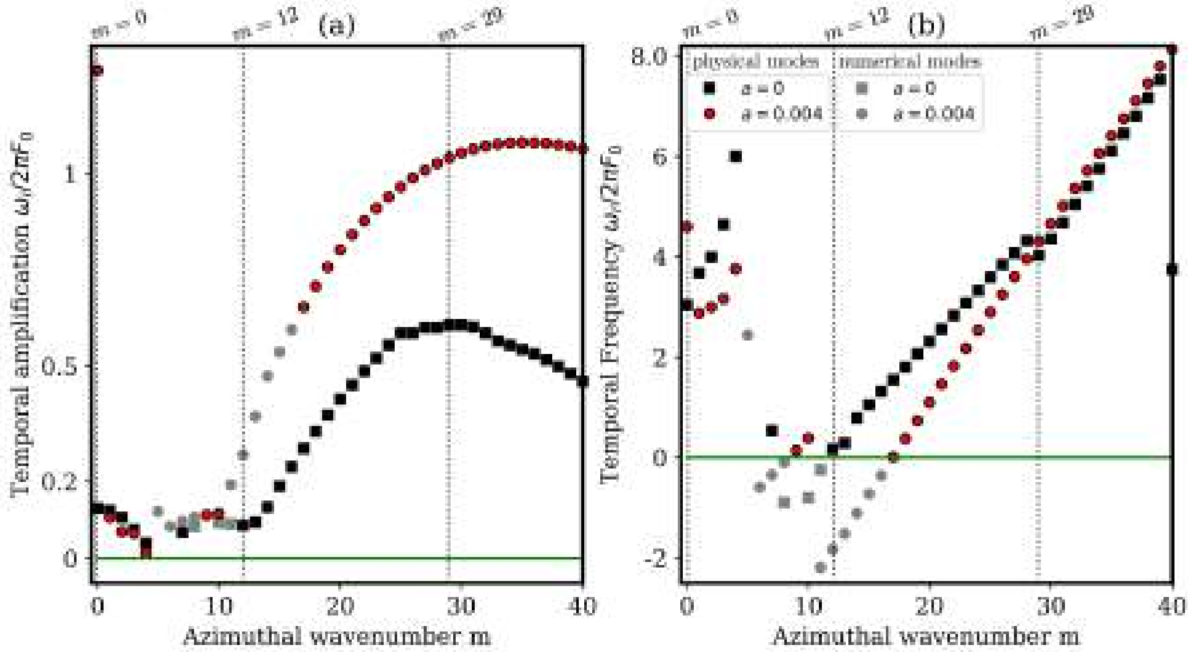

Figure 5.15 – Scatter plot of the controlled cavity stability analysis spectrum: (a) The amplification rate and (b) the frequency versus the azimuthal wavenumber m with $a = 0$ (black square) and $a = 0.004$ (red circle). The coordinates have been normalized by the pulse of the rotor, *i.e.*, $2\pi F_0$. The gray markers represent numerical modes ($\omega_r < 0$).

Interesting information can finally be obtained by looking at the mode shapes obtained by LSA. Figure 5.16 presents the $m = 0$ and $m = 29$, 2D axial velocity fields post control. Note that, LSA results giving only negative frequencies for $m = 12$, the 2D shape associated to this mode corresponds effectively to purely numerical noise. As expected from the last comments, the $m = 0$ mode (Fig. 5.16(a)) is not impacted at all but highest amplitudes compared the uncontrolled mode Fig. 4.14 are found in the stator boundary layer. Finally, even though an increase of the amplification rate was found for the $m = 29$ mode, LSA predicts a mode with a very different shape. One can see that the mode is confined between the shroud and the suction controller which suggests that, due to the centripetal forces, the perturbations can be absorbed by the controllers leaving the rest of the cavity unperturbed.

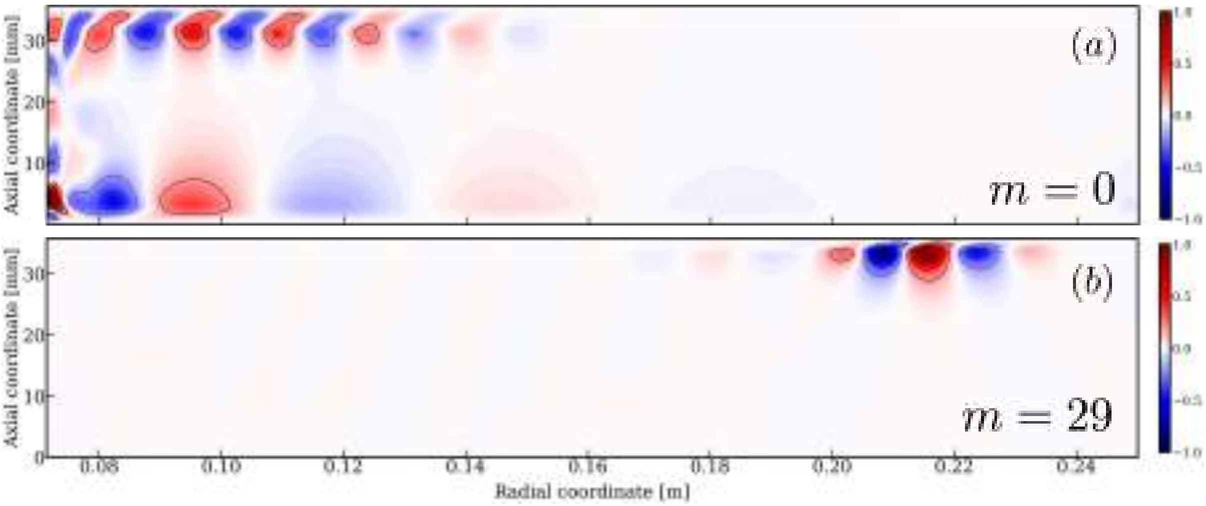

Figure 5.16 – Axial velocity modes of the controlled cavity ($a = 0.004$) with (a) $m = 0$ and (b) $m = 29$, both obtained through linear stability analysis.

5.5 Conclusion

In order to improve our understanding of the pressure band phenomenon and set up control strategies, the annular stator/rotor cavity is investigated in this chapter thanks to global stability analysis. In the previous chapter, the studies were focused on structural sensitivity analyses to point out the origin of each global mode in this cavity, whereas the present study develops the notions of sensitivity to base flow modifications to analyze how the activity of the cavity would evolve under specific base flow changes. For the three modes driving the cavity, the Bödewadt boundary layer (stator) shows to be the most sensitive zone of the cavity according to the frequency and growth rate sensitivities. The sensitivity axial components are then used to set up control strategies. To shift the dominant mode frequency and stabilize it at the same time, activating a suction slot on the stationary disk around $r = 0.20$ m proves to be the best way contrary to the literature where most of the studies focus on the rotating disk. Since to preserve the operating point, an injection actuator is also needed, two different positions of this second controller have been proposed. The first one is identified where a zero sensitivity is noticed for the three modes. This latter would allow to suppress the dominant mode independently from the other modes. The second possible position is a location in the cavity where the two remaining modes are particularly sensitive. Only the first strategy is evaluated though LES in the last section of this chapter. In that case, one shows that for a very small injection/suction mass flow, the three modes can be suppressed leaving a flow purely turbulent with an overall fluctuation level far lower than the uncontrolled cavity. Finally, a stability analysis of the controlled case helps understanding that the annular mode of the system can become predominant as observed for higher level of injection/suction parameters.

To conclude, the conjunction use of LSA and LES shows to be a promising method to construct physical controller and impact directly the pressure band phenomenon. Based on such observations and successes, the tools developed and validated in Part I and II are evaluated on a space turbopump cavity to give more insight on the pressure band phenomenon occurring in these complex systems.

Part III

Investigation of the unsteady phenomena in a space turbopump turbine

Chapter 6

Industrial application: Turbine cavities of a rocket engine turbopump

Contents

The previous chapters have highlighted the capacity of Large Eddy Simulation (LES) to capture the pressure band phenomenon in academic cavities while global stability analysis allowed to point out the origin of each modes. In the present chapter, the same strategy is applied for the cavities of a space turbopump turbine where high Reynolds numbers and large scale dynamics have been observed. The primary goal of this investigation is to evaluate the capacity of LES to retrieve the modal content of the system. Known to be very sensitive to geometrical parameters, the pressure band phenomenon is studied in a second step by addressing a new configuration which includes the blades of the stator. In order to shed some light on the retrieved flow dynamics, the global stability framework is once again applied here to highlight the source of the self-sustained oscillations. In particular, receptivity and structural sensitivity analyses are conducted to identify strategies to delete or at least shift the modes of the observed limit-cycles.

6.1 Introduction

Space engine design still remains challenging for researchers and engineers today. Indeed, each phenomenon and component need to be precisely analysed to produce reliable design which is particularly difficult due to the complexity of the fluid dynamics that operates such devices. For example, experimental campaigns have often evidenced unsteady phenomena around the cavities of space turbopump turbines which is still misunderstood and can be a real source of problem during launches. As introduced in Chap. 1, this PhD focuses on the 'Pressure band phenomenon' corresponding to purely hydrodynamic flow instabilities. This phenomenon has been named as such because of frequencies which can be measured everywhere in the cavity and mark pressure probes. Furthermore, these self-sustained oscillatory motions of the fluid can, under certain circumstances, become dangerous if uncontrolled and potentially impact the structural integrity of the engine. Deeper investigations have highlighted the sensitivity of this unsteady flow to geometric changes but also to the thermal conditions of the system and operation point. In that respect, the PhD work of Bridel-Bertomeu (2016) enabled to shed some light on such devices as well as the origins of this phenomenon. In particular, he proved that contrary to RANS, LES is capable of retrieving such modes. The sensitivity to the thermal conditions and geometry changes evoked previously have also been studied by the same author through three cases: **Case (a)**, a full turbine stage cavity with a cold leak at the hub; **Case (b)** a simplified geometry with a cold leak at the hub and **Case (c)**, a full turbine stage cavity with a warm leak. Through spectral evaluations of the corresponding LES predictions, Bridel-Bertomeu (2016) proved with **Case (b)** that suppressing the higher cavity (C_5 in Fig. 6.2) acts as a band pass-filter of the high frequencies. Likewise, the warm leak of **Case (c)** changed the overall dynamics of the system proving the sensitivity of the system to its thermal operating condition as well as its operating point.

In aeronautical engine turbines, similar unsteady phenomena have been observed. In fact, to avoid overheating the turbine disk, cooling systems are usually set up by imposing a mass flow (or leak) in the wheel rotor-stator space as shown in Fig. 6.1. To minimize the ingress of hot gas coming from the hot main annulus from entering the wheel stator-rotor space, a rim seal which can take different shapes (Phadke & Owen (1988)) is usually added. This specific part of the system creates three dimensional and highly unsteady flows that have been studied for a long time theoretically (Owen (2012)), experimentally (Phadke & Owen (1988),Daniels *et al.* (1992)) and numerically (Pogorelov *et al.* (2018)). Over the years, two specific flow mechanisms have been linked to this ingress/egress unsteady phenomenon. The first one, referred to as externally-induced (EI) ingress (Owen (2011*b*)), corresponds to a non-axisymmetric distribution of the pressure in the hub region between the stator blades and the wheel space. The second one, usually called rotationally-induced (RI) ingress (Owen (2011*a*)) occurs for an axisymmetric pressure distribution in the main annulus and with or without the stator or rotor blades. This is due directly to the rotor disk pumping effect which creates a pressure gradient between the wheel space and the main annulus. Depending of the configuration studied a combinaison of both mechanisms can also be observed and is usually named combined ingress (CI) (Owen (2011*b*)). A complete review of this specific ingestion and blowing processes at rim seal interfaces can be read from Fiore (2019).

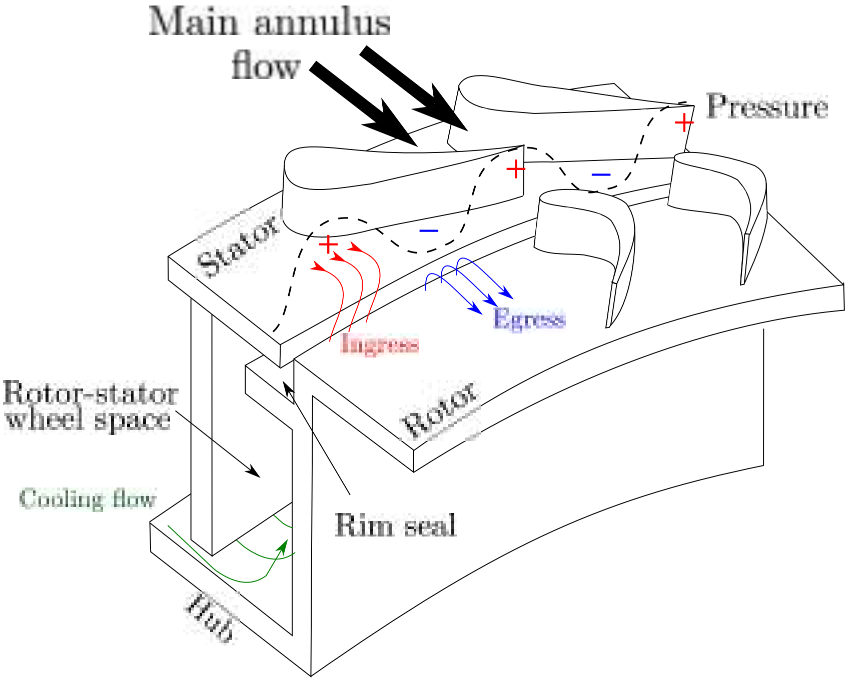

Figure 6.1 – Turbine cavities sketch with ingress/egress process at the rim seal

Folllowing these investigations, two new configurations called **Case 1** and **Case 2** are studied in the present chapter. For **Case 1**, the original geometry of Bridel-Bertomeu (2016) is modified around the hub and a direct comparison with his **Case (c)** will be made. Finally, since experimental observations showed that the pressure band phenomenon was not linked to the turbine blades, these were not considered in Bridel-Bertomeu (2016). This specific point is however partially addressed through **Case 2** hereafter to confirm this finding. To do so, the same geometry as for **Case 1** is retrieved with the addition of the stator blades.

The chapter is organized as follows. First, the two configurations simulated by LES are presented in details in Sec. 6.2 and comparisons with the one studied by Bridel-Bertomeu (2016) are provided. The numerical parameters and meshes adopted to simulate such geometries are then given. The modal behavior of all resulting predictions is then analysed though power spectral analyses and modal decompositions. DMT is also used to evaluate more precisely the characteristic azimuthal and axial wavenumber modes present in the different cavities. Section 6.6 is finally dedicated to the stability analysis of **Case 1** to see if GLSA retrieves the observed modes for such a complex system. To finish, regions of flow, where control could be envisioned, are looked for as done for the academic configuration studied previously.

6.2 Turbompump configurations

The two configurations studied in this chapter are presented in Fig. 6.2 and will be called respectively **Case 1** (Fig. 6.2 (a)) and **Case 2** (Fig. 6.2 (b)) throughout the rest of the discussion. As stated in the introduction, **Case 2** is very close to **Case 1**: it is in fact **Case 1** augmented by the stator blades. Note that as shown in Fig. 6.2(a)(upper) all considered computational domains correspond to 360° axisymmetric simulations. Indeed, as observed for the academic cases, even though such systems are geometrically simple, the structures appearing in the boundary layers are complex and three dimensional imposing to take the full system in any CFD computation.

Figure 6.2(lower) represents (r, z)-cuts of the geometries allowing to see the different parts of the systems. For both cases, the same nomenclature has been chosen to identify the four different cavities present in the considered system:

- C_1: Rotor/stator wheel space of the first rotor being marked by a red line
- C_2: Main annulus corresponding to the main stream flow coming from the gas generator,
- C_3: Throat between the stator and rotor stage linking the C_1 and C_2 cavities,
- C_5: High radius cavity with no specific function.

Note that C_4 (not shown in Fig. 6.2) corresponds to the rotor/stator wheel space of the second rotor and will not be taken into account in the present study. Finally, the C_3 cavity separating the main annulus from the rotor/stator wheel space of the first rotor as a specific shape contrary to rim seal found in classic turbomachinery and will

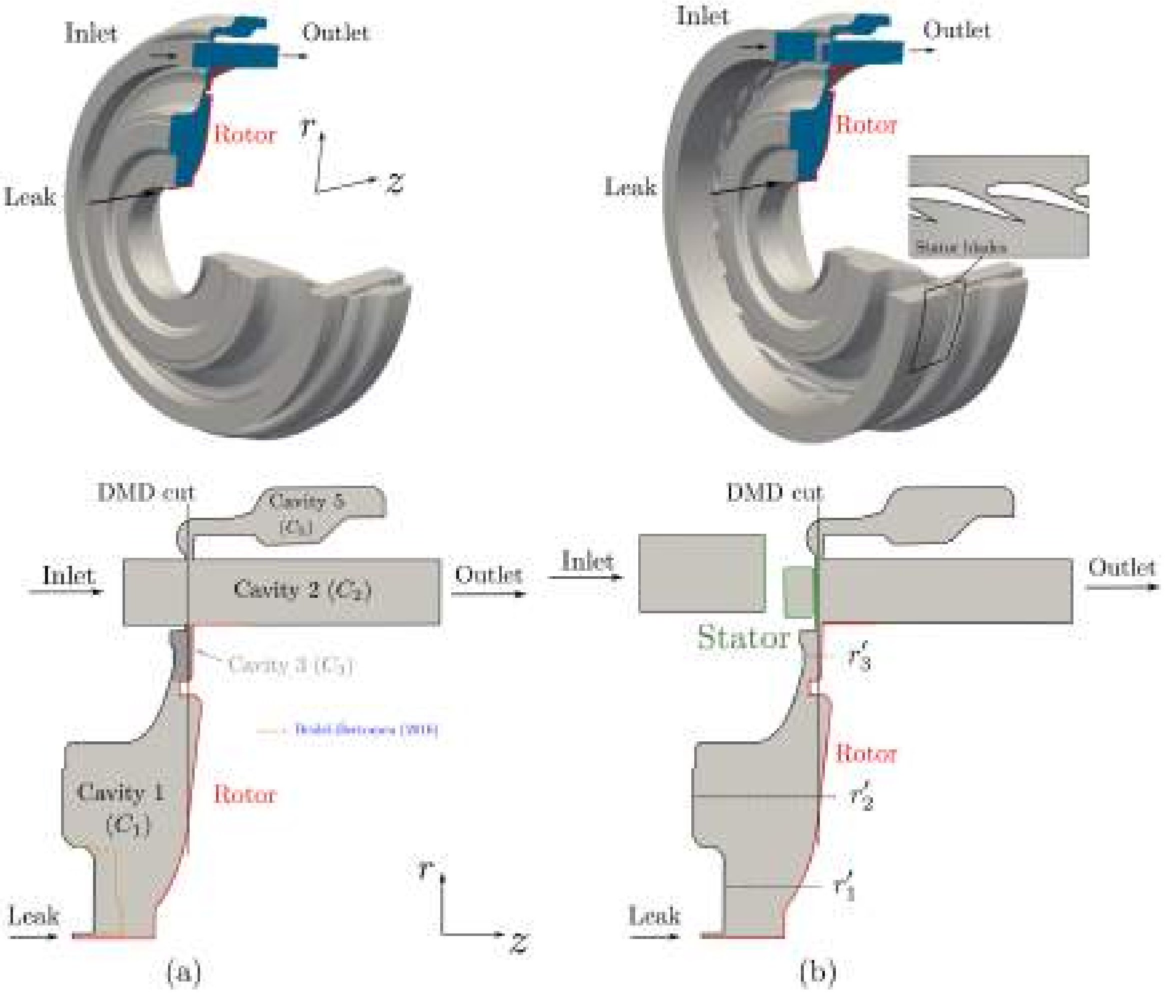

Figure 6.2 – 3D Configurations studied with (a) **Case 1** (the orange dashed line represnet the only diffenrece of the acual configuration with the one studied in Bridel-Bertomeu (2016)) (b) **Case 2** same configuration as **Case 1** augmented by the stator stage blades. Note that the blades profiles have been modified for confidentiality reasons.

be referred to as annular seal.

In order to compare these configurations with the previous academic cases, three radial locations have been specifically chosen in the cavities C_1 and C_3. These regions have the particularity to be between a relatively smooth rotor and stator disks. The respective locations will be referred to as $r_1^{'} = 0.35$, $r_2^{'} = 0.488$ and $r_3^{'} = 0.72$ where $r^{'} = r/r_{max}$ as shown in Fig. 6.2(lower)(b). Note also that in the same figures, the axial position for which 2D DMD cuts will be displayed is represented. Note finally that all geometric values discussed in this chapter are normalized by the maximum radius of the geometries for confidentiality reasons. The rotating parts will furthermore be marked by a red solid line. To finish, for both cases and in all computations, the inlet of cavity C_2

injects hot combustion products coming from the gas generator driving the turbine stage. The leak, located at the lowest radius injects a cold liquid.

6.3 Large Eddy Simulations

This section presents the numerical parameters and boundary conditions chosen for the LES of the previous configurations as well as the meshing strategies adopted.

6.3.1 Boundary conditions

As described in Sec. 6.2, for both cases under study, two inlets (the main annulus and the leak) for one outlet are present. Apart from the rotor, all other boundaries are walls. The leak and the main annulus inlet of **Case 1** have been treated the same way by imposing the three cartesian velocity components (u, v, w), the Temperature T_s and the species mass fractions $Y_{species}$. A new boundary condition made available during the second part of this PhD then enabled to impose total quantities (pressure and temperature) and mass fractions (Odier *et al.* (2019)). Already known to be more efficient for turbomachinery computations, this specific boundary conditions has therefore been applied only for **Case 2** and proved to accelerate convergence of the inlet flow specifications to the expected mass flow. For both cases, only the static pressure is prescribed at the outlet condition. The leaks, inlets and the oulet have finally been all treated thanks to the Navier-Stokes Characteristic Boundary Conditions (NSCBC) formalism Poinsot & Lele (1992) to avoid wave reflection.

When it comes to the walls of the main annulus extension (post C_3 cavity), these are set as no slip conditions while the rotor wall is defined by fixing its tangential velocity as a linear function of its rotation speed Ω and the radial position along the wall. To reduce CPU cost while capturing the good bahavior at walls, wall-laws are furthermore imposed on the remaining conditions. The law from Coles & Hirst (1968) is in this case prescribed so that,

$$\begin{cases} u^+ = n^+ & \text{for } n^+ \leq 11.445, \\ u^+ = k^{-1}\ln(En^+) & \text{for } n^+ > 11.445, \end{cases} \tag{6.3.1}$$

with $k = 0.41$, $E = 9.2$ and for which $u^+ = \bar{u}/v^*$ and $n^+ = nv^*/\nu$ are respectively the normalized velocity and normal wall distance, v^* being the wall-friction velocity defined using the wall shear stress τ_w ($v^{*2} = \tau_w/\rho$) while ν is the kinematic viscosity of the fluid and ρ is its density. The different boundaries are detailed geometrically in Fig. 6.3.

6.3.2 Meshes

The meshing strategies applied to the two configurations are described in the following. Note that for both configurations, the meshes are composed entirely of tetrahedra.

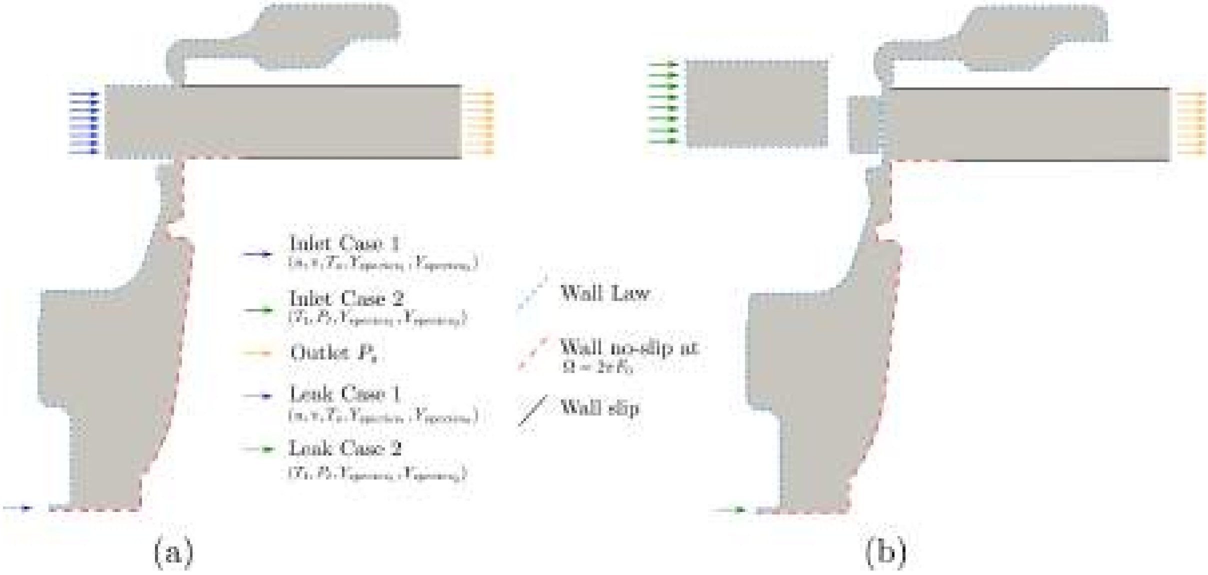

Figure 6.3 – Boundary conditions imposed for the LES of (a) **Case 1** and (b) **Case 2**

Case 1:

A (r, z)-cut of the mesh is given in Fig. 6.4 and highlights the main regions of refinement. At low radii, the mesh has been refined to recover the leak of H_2 interacting with the rotor. An important refinement has also been applied around cavity C_3 where strong mixing has been noted due to the interaction of the lower main annulus boundary layers with the centrifugal flow generated by the rotor. A coarsen mesh is used near the outlet to avoid any flow or numerical wave reflection. Note that, after numerical convergence of the corresponding simulations, the wall coordinate n^+ has been verified. Even though some nodes can cross the recommendation of $n^+ = 30$ (Sagaut (2006)) all nodes are found to be within $1 < n^+ < 30$.

Case 2:

At first, **Case 1** meshing strategy has been reused to mesh **Case 2**. In particular, the mesh in the cavities C_1 and C_5 is taken so as to be exactly the same as for **Case 1**. This first resulting mesh has then been used to numerically converge the simulation and reach the operating point of the system. From this converged result, an automatic mesh refinement has been applied thanks to the library called mmg3D (Dapogny *et al.* (2014)) developed at INRIA Bordeaux. The tool has been implemented to adapt the mesh thanks to a given metric. In our case, the average viscous dissipation given by AVBP and usually called LIKE (Loss In Kinetic Energy) (Daviller *et al.* (2017)) has been chosen to produce this metric based on which a second mesh was obtained for **Case 2**. This quantity indeed provides a good sensor of the regions of the flows with strong velocity and pressure gradients which is useful for **Case 2** to refine the

	Case 1	**Case 2**	Case (C)
Number of cells (N_{cells})[$\times 10^6$]	111	131	109
Number of node (N_{nodes}) [$\times 10^6$]	19	24	19
Minimum Cell volume (V_{min}) [m^3]	0.6×10^{-13}	0.1×10^{-15}	0.7×10^{-13}
Averaged wall normal n^+_{ave}	40	100	35

Table 6.1 – Summary of the meshes characteristics of **Case 1** and **Case 2**. Case (C) corresponding to the Bridel-Bertomeu (2016) PhD configuration shown Fig. 6.2 is given for comparison.

blade boundary layers but also their wakes and shocks as seen in the resulting mesh, Fig. 6.4(b). The normal wall coordinate n^+ has again been checked a *posteriori*. The lower and high radius cavities were not impacted by the automatic refinement and similar n^+ values are obtained as for **Case 1** aside near the blades where an average n^+ of 100 was found.

Note that, Tab. 6.1 sums up the charateristic values obtained for both meshes along with the values reported for Bridel-Bertomeu (2016) (see Fig. 6.2) as reference.

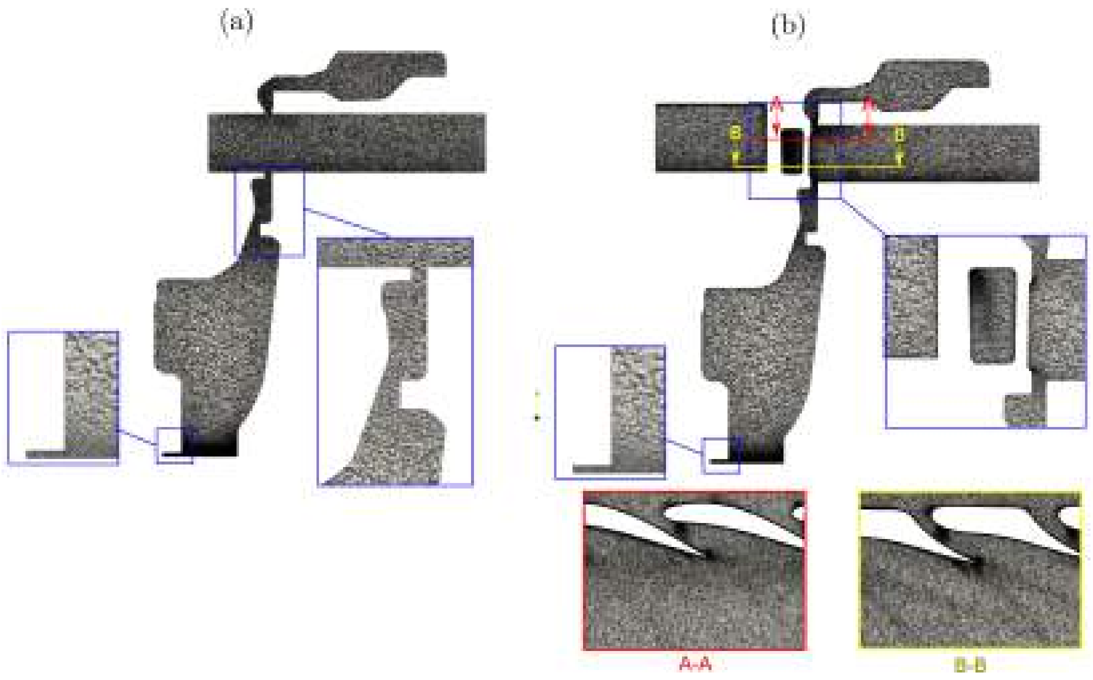

Figure 6.4 – Configurations meshes: (a) **Case 1** (b) **Case 2**. The cuts A-A and B-B show the mesh refinements around the wake and the shocks respectively at $r' = 0.86$ and $r' = 0.8$. Note that the blade shapes have been modified for confidentiality reasons.

6.3.3 Numerics and LES modelling

In order to close the description of the numerical set up of these industrial configurations, the main numerical parameters and adapted subgrid scale model are provided in this section. First, the full compressible multi-species Navier-Stokes equations Solver AVBP is used here. The convection scheme TTGC (Colin & Rudgyard (2000)) (Two-steps Taylor Galerkin) based on finite element and following a cell-vertex formalism is preferred for its low dissipation and dispersion properties (3^{rd} order space and time accuracy). Finally, the WALE subgrid scale model (Nicoud & Ducros (1999)) is chosen for its good behavior in wall bounded flows.

In the particular configuration of **Case 2**, Localized Artificial Dissipation (LAD)(Mathew *et al.* (2006, 2003)) is activated to help the system to numerically converge. This tool has the benefit of using spatial filtering to prevent wiggles and smooth large gradients making it very suitable to stabilize a simulation with shocks. After 2 full rotations of the rotor, LAD which can be intrusive, is then replaced by a Colin artificial viscosity (Colin & Rudgyard (2000)). Finally, to prevent artificial reflections on the outlet, a numerical sponge layer is applied at the end of the main annulus (C_2).

To obtain a satisfying convergence and exploitation of the simulations, two main flow features have been checked: the operating point and the full development of the flow dynamics. To ensure the first criterion, mass flow at the inlet, outlet and leak have been followed in time and are given in Fig. 6.5(a)(left) for **Case 1** and Fig. 6.5(a)(right) for **Case 2**. Inlet and outlet mass flows have been in both cases normalized by the inlet expected mass flow noted here $\dot{m}_0$. In case of the leak, the same approach is adopted, the reference scale being noted $\dot{m}_l$. As one can see, for **Case 1**, the desired targets are obtained quickly after 3 full rotations of the rotor disk and with a final error below 1%. For **Case 2**, the system converges faster thanks to the interpolation of **Case 1** results which has been used as an initial guess for this case. For the inlet and the outlet, one also retrieves a final error below 1%. The leak mass flow of **Case 2** seems however more difficult to retrieve. However, even though an error of 5% is found the leak mass flow being very low ($\dot{m}_0 \simeq 10^3 \dot{m}_0$), these results were considered acceptable.

Ultimately, the parameter which validates the operating point of such simulations is the outlet pressure that is displayed on Fig. 6.5(c). Contrary to the mass flow, it is particularly difficult to converge the outlet of **Case 2** to the good static pressure noted P_{out}. In fact, the blades of the stator generate wakes which produce shocks (see Sec 6.4) that create an unsteady flow at the end of the main annulus. Nevertheless, to ensure a good overall pressure in the entire domain, the NSCBC relax coefficient imposed at outlet can be progressively adjusted to increase convergence as seen from Fig. 6.5(c)(b) through the jumps of the convergence curves. In parallel to these verifications, the convergence of the flow dynamics is obtained by looking at the kinetic energy integrated over the entire domain as function of time. A limit cycle is clearly observed after only a complete rotation for both cases and average values are all taken on the plateau noted E_{max} which has been used to normalize all associated plots.

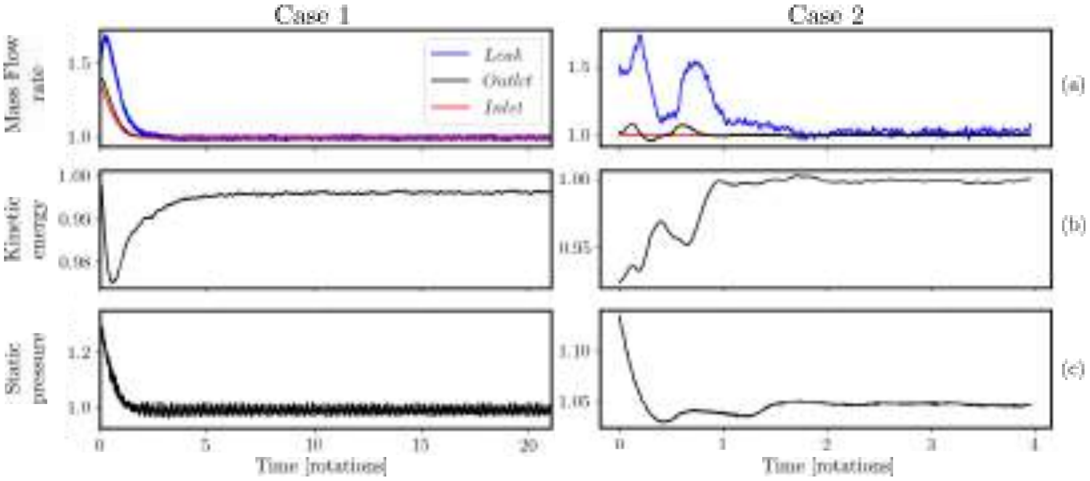

Figure 6.5 – Simulations convergence of **Case 1** *(left column)* , **Case 2** *(right column)* with (a) the inlet, outlet and leak Mass flow rate over time respectively in red, black and blue. The results have been respectively normalized by $\dot{m}_i$, $\dot{m}_i$ and $\dot{m}_l$, (b) the kinetic energy integrated over the domain normalized by its ∞-norm and *(c)* The static pressure outlet normalized by P_{out}.

6.4 Overall flow analysis

In the present section, the three dimensional coherent structures resulting from LES are presented for **Case 1** and **Case 2**. To do so, Fig. 6.6 first depicts instantaneous iso-surfaces of the Q-criterion (Jeong & Hussain (1995)) colored by the absolute Mach number to evidence the vortical structures present in the complete flow field and specifically in the wake regions of the stator blades. One also notes here that for **Case 1**, the flow in the main annulus (C_2) is fully supersonic. Contrarily, the flow of **Case 2** goes supersonic only due to the presence of the stator blades as in the real configuration. Figure 6.6(c) also shows the interactions between the highly tangential wakes and the shocks generated at the blade pressure side close to the trailing edge.

One particular interest behind these configurations is the flow activity appearing in the cavity C_3 which links the main annulus C_2 to the rotor/stator wheel space C_1. Figure. 6.7 shows a comparison of a radial velocity instantaneous of both configurations around this specific region. Note that both results have been normalized by the absolute radial velocity at the $C_3 - C_2$ connection of **Case 1**.

As one can see, in both configurations the egress/ingress phenomenon corresponding to unsteady fluctuations of the radial velocity at the C_2-C_3 connection is observed in both cases. For **Case 2** (Fig. 6.7(b)), the stator blades have however a larger impact on the flow feeding the rotor/stator wheel space C_1. In fact, it has been noted that the ingress magnitude in **Case 2** can be increased by 20% to 30% when compared with **Case 1**.

Figure 6.8 provides the same results in a (r,θ)-cut to show the change of the flow in the azimuthal direction. The major consequence of the presence of the stator blades is as expected an increased azimuthal heterogeneity of the flow dynamics. While **Case 1**, Fig. 6.8(a), shows spiral patterns in C_1, these seem absent in **Case 2**. Overall both predictions seem to produce rather distinct flow organizations and limit-cycles although more validations are required.

FIGURE REMOVED FOR CONFIDENTIALTY REASONS

Figure 6.6 – Instantaneous iso-surfaces of the Q-criterion colored by the absolute Mach number: (a) **Case 1** full domain (b) **Case 2** full domain (c) **Case 2** in the stator hub region.

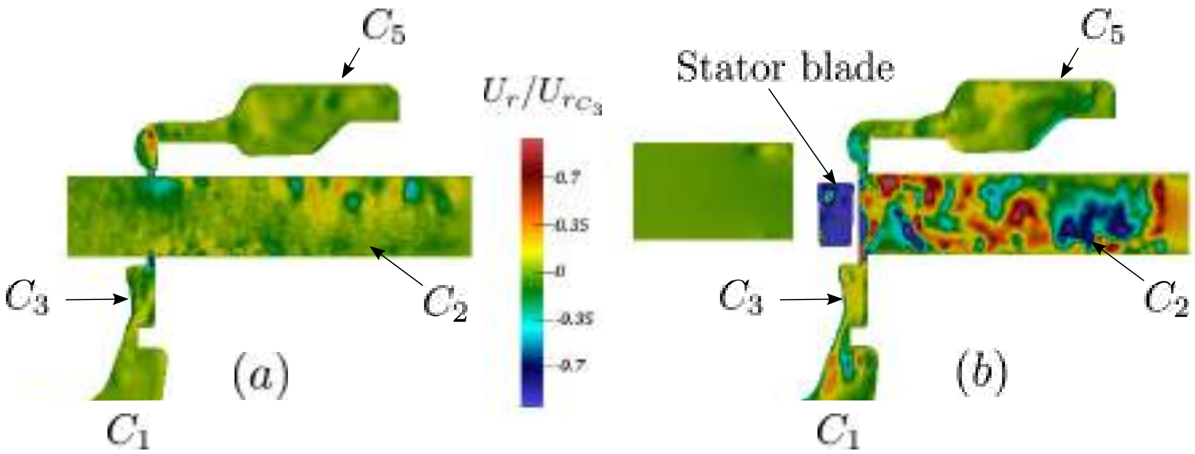

Figure 6.7 – Instantaneous radial velocity component in a (r,z)-cut: (a) **Case 1** (b) **Case 2**. The results have been normalized by $|U_{r_{C_3}}|$ the absolute radial velocity at the $C_3 - C_2$ connection of **Case 1**.

To do so, the following tends to validate the predictions obtained through LES by comparing the flow in the cavities C_1 of **Case 1** and **Case 2** to smooth academic rotor-stator cavities as the ones studied in the previous chapters. Indeed, as demonstrated

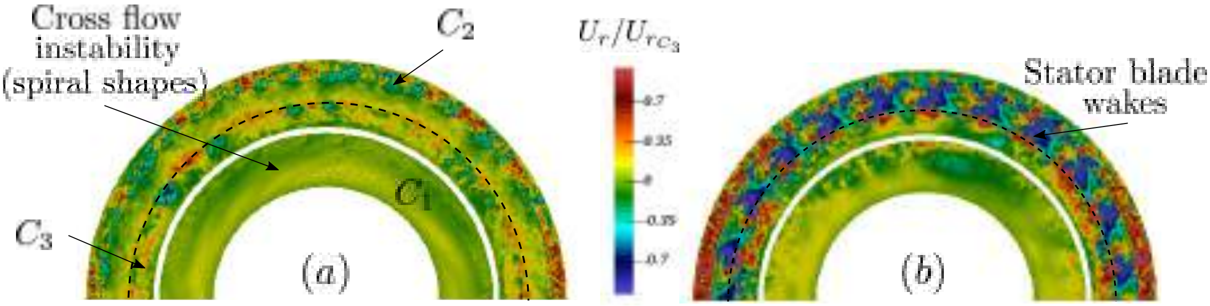

Figure 6.8 – Instantaneous radial velocity component in a (r,θ)-cut: (a) **Case 1** (b) **Case 2**. The results have been normalized by $|U_{r_{C_3}}|$ the absolute radial velocity at the $C_3 - C_2$ connection of **Case 1**.The dashed line highlights the $C_3 - C_2$ connection.

experimentally by Schouveiler (2001) and numercically by Serre *et al.* (2001*a*), the global behavior of a rotating cavity is driven by its Reynolds number and its aspect ratio. In this context, the C_1 cavity characteristic Reynolds number evolutions are provided in Fig. 6.9 as a function of the normalized radial coordinate $r' = r/r_{max}$: *i.e.* for the local radial Reynolds number $Re_r = r^2\Omega/\hat{\nu}$, Fig. 6.9(a), and the axial Reynolds number $Re_h = h^2\Omega/\hat{\nu}$ Fig. 6.9(b). For each Reynolds number, the kinematic viscosity $\hat{\nu}$ has been taken as the mean at each radial position so that $\hat{\nu}(r') = \int_{z_{min}}^{z_{max}} \nu(r',\xi)d\xi/(z_{max} - z_{min})$. Note that ν is the time and azimuthal average of the kinematic viscosity in the cavity C_1 and z_{max} (resp. z_{min}) corresponds to the highest (resp. smallest) axial coordinate at r'. The complex geometry of the cavity C_1 makes both local Reynolds numbers vary as much as an order of magnitude. Recall that in theory, for radial Reynolds number below 10^6, a transitional cavity is expected similarly to the academic cases studied in the previous chapters. One can also see that similar maps are obtained for both **Case 1** and **Case 2** since this part of the geometries does not change. The only impact to note comes from the presence of the stator on the cavity C_3, linking the main annulus and the rotor/stator wheel space C_1 around $r' = 0.72$. From such views, three different regions with approximately a constant axial Reynolds number can be highlighted. These regions are represented by circles and correspond to the radial positions $r'_1 = 0.35$, $r'_2 = 0.488$ and $r'_3 = 0.72$ (see Fig. 6.2 for more details).

Figure 6.10 shows the C_1 axial profiles of the dimensionless mean radial $U_r^* = U_r/(r\Omega)$ and azimuthal $U_\theta^* = U_\theta/(r\Omega)$ velocity components at the three locations of Fig. 6.2(b) and for both configurations. As a complement, the auto-similar laminar solutions from Rogers & Lance (1962) at the corresponding axial Reynolds number Re_h are also provided for comparison. Note that these last solution profiles were obtained for low Reynolds numbers between smooth infinite stationary and rotating disks which hence does not take into account the complex geometry effects like the ones present in the studied turbopumps. Results need therefore to be taken with caution. However and as shown by Daily & Nece (1960) through Fig. 2.2 of Sec. 2.1, rotating cavity flows can be classify in four categories based on such findings. At the locations $r'_1 = 0.35$ and $r'_2 = 0.488$, the rotating boundary layer and the stationary boundary layer can be well distinguished from the rotating core and given their high Reynolds number and aspect

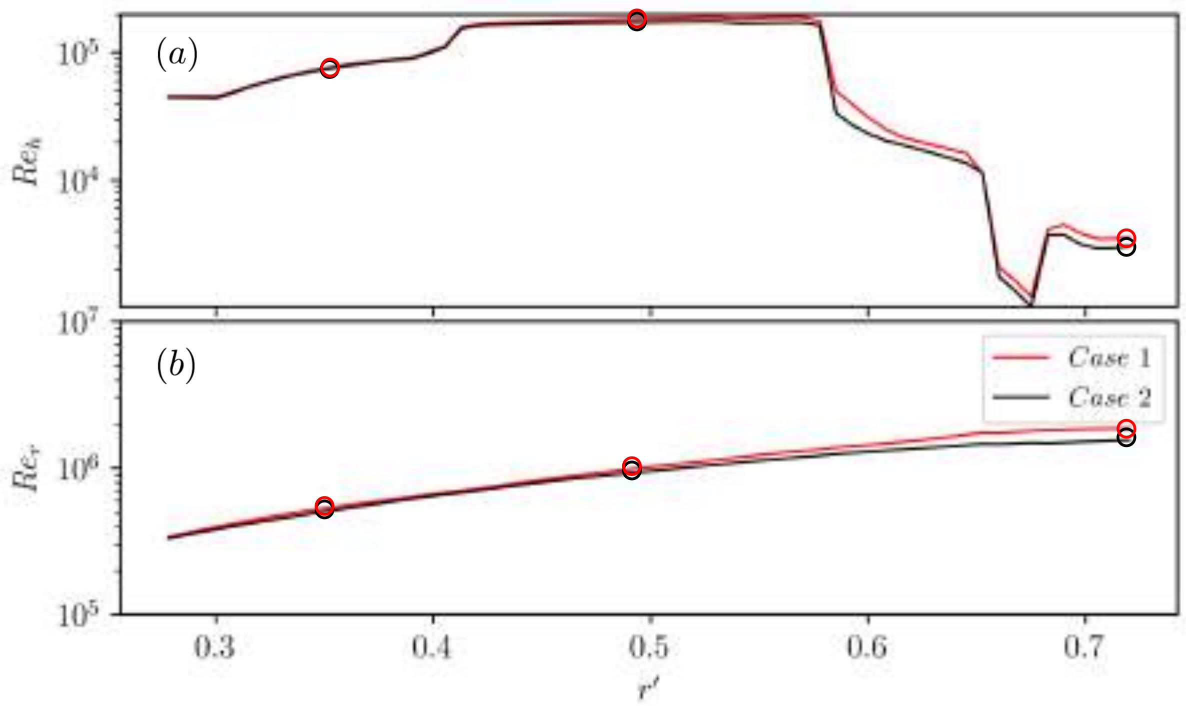

Figure 6.9 – Evolution of the Reynolds number with the radial coordinate in the rotor/stator wheel space C_1: (a) Axial Reynolds Number $Re_h = h^2\Omega/\hat{\nu}$ (b) Radial Reynolds number $Re_r = r^2\Omega/\hat{\nu}$ with $\hat{\nu}$ the kinematic viscosity defined as $\hat{\nu}(r') = \int_{z_{min}}^{z_{max}} \nu(r',\xi)d\xi/(z_{max} - z_{min})$. The radial coordinate has been normalized by r_{max}.

ratio, these belong to category IV. Contrarly, the cavity C_3, at $r'_3 = 0.72$, should belong to category IV of Daily & Nece (1960) classification but clearly shows merged boundary layers. This difference can be explained by the side walls of the cavity where the $C_3 - C_2$ connection effectively corresponds to a radial injection/ejection of fluid that can perturb the mean flow as shown in the previous chapter with the axial injection/suction on academic cases. One main difference compared to the auto-similar solution of Rogers & Lance (1962) is also the boundary layer thicknesses. In fact, one expects turbulent boundary layers to be thinner that the laminar ones. However this is not the case here and this difference can be explained by the lack of mesh refinement around the wall boundary conditions.

If looking at Fig. 6.10(f), one notes here that higher level of radial velocity is reached in **Case 2** compared to **Case 1**. One can see furthermore that a large ingress (negative radial velocity) is found if compared to **Case 1**. This higher level of ingress is also retrieved at mid cavity (r'_2 Fig. 6.10(b) & (d)) where the centripetal force due to the stationary disk imposes a negative radial velocity and a non zero azimuthal velocity contrary to the academic cavities studied in the previous chapters. One finally notes that for this particular region, the auto-similar solution of Rogers & Lance (1962) well predicts the boundary layer thicknesses, although the core rotating rate is increased due the to flow ingress. Finally at low radius, the hub clearly affects the velocity profiles. In particular the leak creates higher level of radial velocity in the rotating boundary layer. These latter results are not unexpected and were already observed for the controlled academic cavity under injection in Chap. 5.

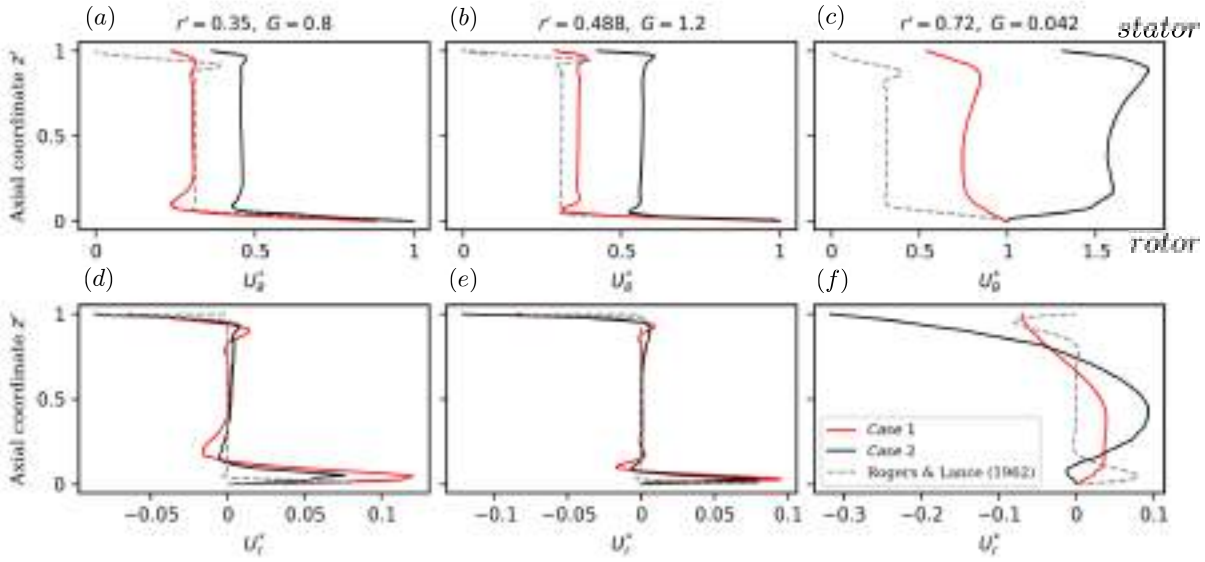

Figure 6.10 – Normalized mean flow profiles: (a)-(c) Azimuthal velocity component and (d)-(f) Radial velocity component. Each colums from left to right correspond respectively to profiles extracted at $r'_1 = 0.35$, $r'_2 = 0.488$, $r'_2 = 0.72$. The black, red and dashed curves correspond respectively to **Case 1**, **Case 2** and the auto-similar solution of Rogers & Lance (1962).

6.5 Modal analysis

The modal content of the two LES predictions is studied in this section. As done in Chap. 2, a point-wise temporal analysis is first realized. To do so, a set of numerical probes has been placed in all cavities as shown in Fig. 6.11. Note that this view and associated probes are also replicated azimuthally every 6 degrees and the exact same positions have been taken for **Case 2**. A PSD of the pressure is then computed for each configuration as shown in Fig. 6.12 and Fig. 6.13 for **Case 1** and **Case 2** respectively. Note that, frequencies have been normalized by the rotor frequency F_0. For **Case 2**, the precision of the spectrum Δ_{F/F_0} ($\Delta_{F/F_0} = 0.12$) is 6 times larger than **Case 1** ($\Delta_{F/F_0} = 0.02$) due to the higher cost of the simulation. The first observation that can be made is that the overall pressure level of each probe of **Case 2** is around 10 dB higher than for **Case 1**. The dominant frequency in terms of amplitude appears for both cases around $F/F_0 = 4.5$ (4.85 for **Case 1** and 4.35 for **Case 2**). Harmonics are also present in both cases: *i.e.* 9.56 and 14.5 for **Case 1** and 8.75 and 13.2 for **Case 2**. The last common point between the two systems is the low frequency around $F/F_0 = 2$. Indeed,

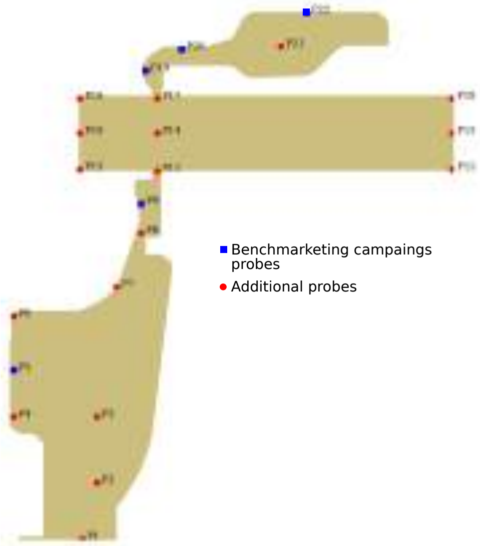

Figure 6.11 – Probes map at $\theta = 0°$.

	F_0	F_1	F_2	F_3	F_4	F_5
Case 1	1.70	–	4.85	–	9.56	14.5
Case 2	1.90	2.90 $(F_2 - F_0)$	4.35	6.00 $(F_4 - F_0)$	8.75	13.20

Table 6.2 – Summary of the frequencies found through pressure PSD in **Case 1** and **Case 2**.

a mode at $F/F_0 = 1.70$ is dominant in cavity C_1 for **Case 1** and could be linked to the cross flow instability identified in Fig. 6.8. A closer look at **Case 2** shows that two new low amplitude but perfectly distinguishable frequencies at $F/F_0 = 2.90$ and $F/F_0 = 6.15$ are present contrary to **Case 1**. These two specific frequencies are found to be a linear combination between the dominant frequency ($F/F_0 = 4.35$), its harmonics and the low frequency ($F/F_0 = 1.9$).

By looking at the radial distribution of the main mode amplitudes Fig. 6.12(right) and Fig. 6.13(right) for **Case 1** and **Case 2** respectively, the highest levels are all found in cavity C_5. Table 6.5 sums up the frequencies found in each configuration.

The previous analysis enabled through several probes to show that both configurations have a rich and complex spectrum. Based on this frequency knowledge that composes both limit-cycles, the extraction of the 2D modes from each flow, *i.e.*, the large scales driving the cavity of the turbopumps is analyzed in the following. To do so, DMD (already presented in Chap. 2) is applied to the (r, θ)-cuts presented in Fig. 6.2. The decomposition is realized on snapshots obtained with a sampling rate of $\Delta t_{sampling} = 10^{-4}\,s$ for **Case 1** and **Case 2** and a duration of $4.6 \cdot 10^{-3}\,s$. As listed in Fig. 6.14 and Fig. 6.15, good agreement is found between DMD frequencies and the one obtained with the local PSDs.

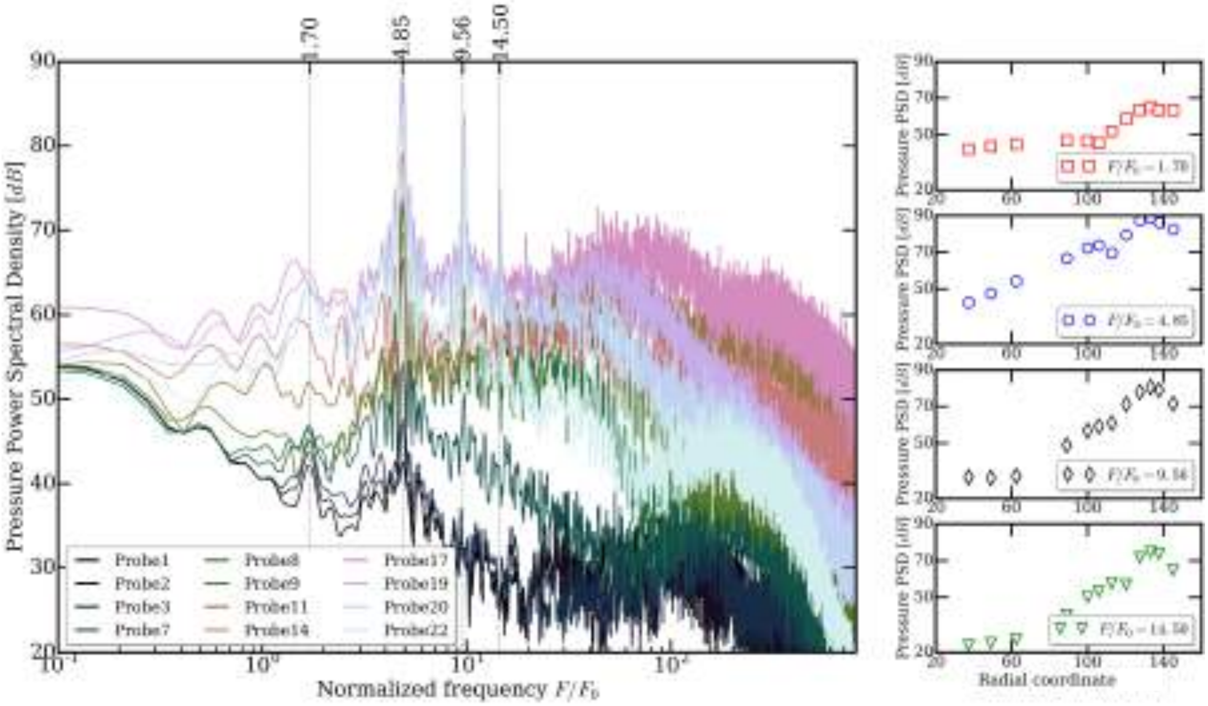

Figure 6.12 – Power Spectral Densities (PSD) of the pressure fluctuations in **Case 1** *(left)* and radial evolutions of the amplitudes of the dominant frequencies *(right)*.

A maximum frequency difference of 1.4% for $F/F_0 = 9.7$ has been observed by comparing both methods. Analyzing the pressure phase contours associated to each main mode found by DMD, one can see that the azimuthal wavenumbers of both cases are ranging from $m = 1$ to $m = 12$ and are not linked to the Blade Passing Frequency (BPF) of 24. Furthermore, the addition of the stator blades decreases the azimuthal wavenumbers found in **Case 1** of $m = 4, 8$ to $m = 2, 4$ in **Case 2**. It is also of note that this range of wavenumbers were also obtained in previous studies for similar configurations (Bridel-Bertomeu (2016), Pogorelov *et al.* (2018)). Finally, these modes have all the features associated to the phenomenon introduced Sec. 6.1 called rotationally-induced (RI) ingress. In fact, as stated by Owen (2011*a*), one retrieves that the azimuthal wavenumbers are not linked to the BPF and that the mean pressure in the stator-rotor wheel space is axisymmetric (not shown here). Comparing both cases, one also retrieves that this specific phenomenon appears with or without the stator blades.

Even though DMD enables to give more information about the spatial distribution of the modes in each configurations, a full understanding of their 3D composition is not accessible due to a too high cost and memory need. To overcome this problem, DMT, presented in Sec. 3.3, is applied here to obtain a full 3D cartography of the turbopump modes. The input frequencies adopted to track the modes are the ones taken from the PSDs and a bandwidth of 20 Hz is chosen for the DMT temporal filter. The results for **Case 1** and **Case 2** are presented respectively in Fig. 6.16 and Fig. 6.17. Note that for these figures, to help visualizing the evolution of the structures in the turbopumps,

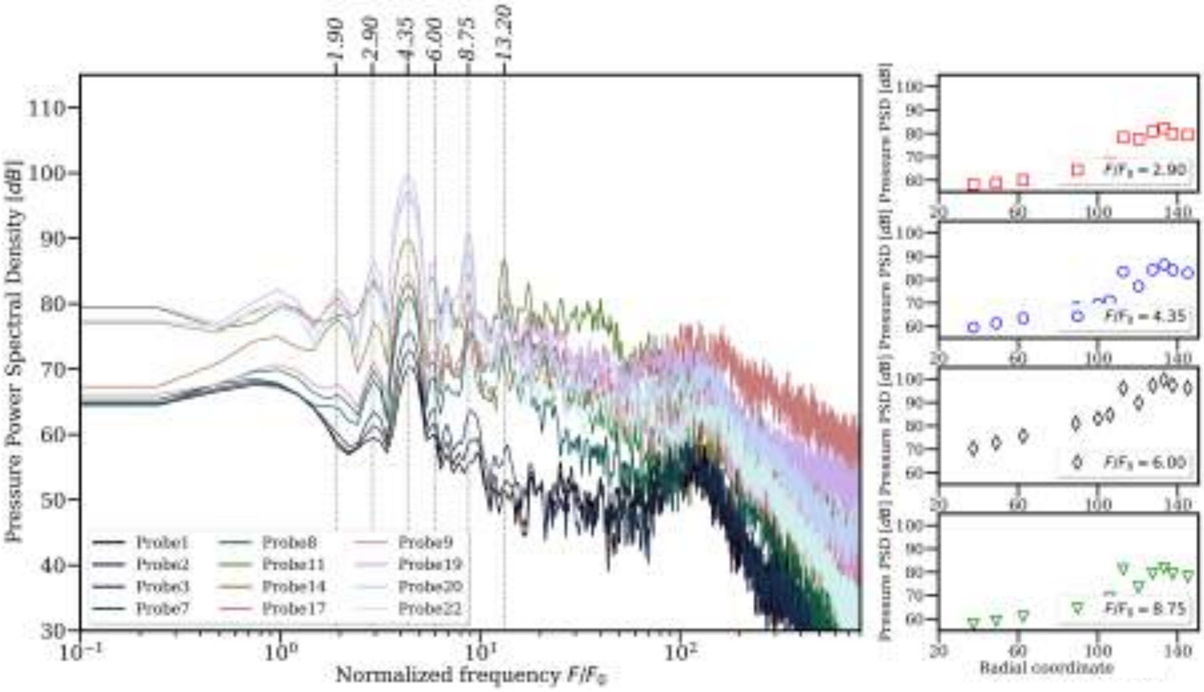

Figure 6.13 – Power Spectral Densities (PSD) of the pressure fluctuations in **Case 2** *(left)* and radial evolutions of the amplitudes of the dominant frequencies *(right)*.

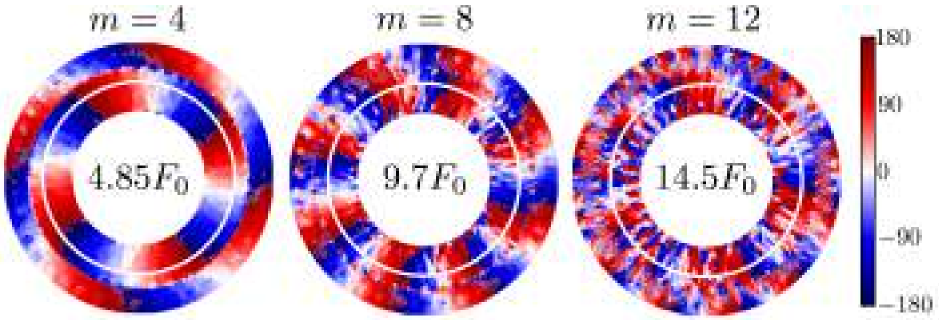

Figure 6.14 – Phase contours of the static pressure of the three main modes obtained through DMD for **Case 1**.

the domain has been decomposed in 4 distinct parts: the upper cavity (C_5), the main annulus (C_2), the throat (C_3) and the rotor/stator wheel space (C_1) as detailed on the top of each figure.

- For **Case 1**: Similarities can be observed with the DMD results of Fig. 6.16. In fact, the characteristic azimuthal wavenumbers $m = 4$ and $m = 8$ respectively for $F/F_0 = 4.85$ and $F/F_0 = 9.56$ are again retrieved in the entire system. In the main annulus, it is also possible with DMT to point out characteristic axial wave numbers: $k = 1$ for $F/F_0 = 4.85$ and $k = 2$ for $F/F_0 = 9.56$. Finally, note that no coherent structures are found in the connection cavity (C_3) and the main annulus (C_2) for

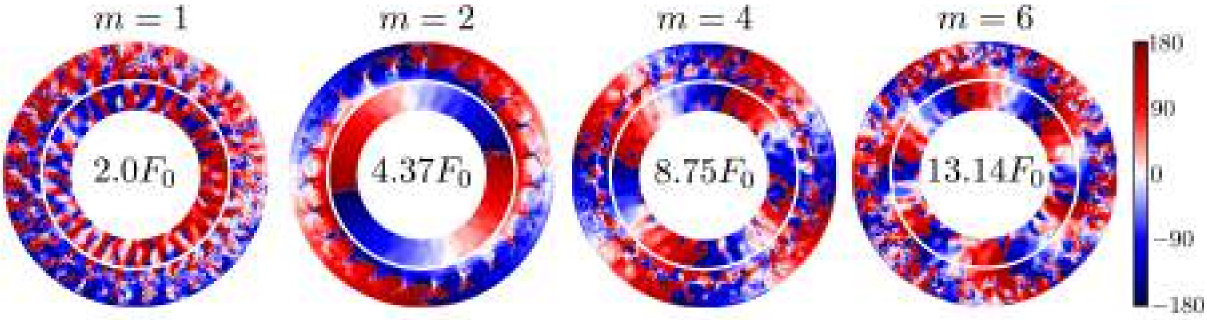

Figure 6.15 – Phase contours of the static pressure of the four main modes obtained through DMD for **Case 2**.

the low frequency mode at $F/F_0 = 1.7$. In cavity $C1$, the modes are observed to evolve in new specific structures. For example, the harmonic of the dominant mode presents a high azimuthal wave number structure ($m \simeq 30$) in the boundary layer of the stator. At the opposite, the low frequency $F/F_0 = 1.7$ is particularly marked by spiral structures with an azimuhtal wave number of $m = 12$. As one can see, these two different azimuthal wavenumbers are relatively close to the ones found for the annular cavity studied in the previous chapters. Such observations are not so surprising since in this particular region, one finds Reynolds numbers and aspect ratios close to the ones of the annular cavity and the mean flow profiles are also found to be in good agreement with the auto-similar profiles of Rogers & Lance (1962) (see Fig. 6.10).

- For **Case 2**: The spatial distributions of each mode are less complex. In fact, in this case, the structures observed with the planar DMD are well identified here in the different parts of the system. For the low frequency, as already observed with DMD, no specific structure is observed. By analyzing the results in the main annulus, one can see that the shocks are marking the modes without impacting their characteristic azimuthal wavenumbers. Note also that no specific axial wavenumber could be distinguished contrarily to **Case 1** where clear helical structures were present. Finally, the dominant mode expresses also in the cavity C_1, featuring a high azimuthal wave number around the hub.

To conclude on this first analysis, LES proves again to be a relevant candidate to capture the pressure band phenomenon in complex rotor/stator cavities as the ones of a space turbopump. In particular, for both cases studied, the multi-frequency feature of this phenomenon and its nature to contaminate the entire system are retrieved. Comparing both cases, it has been confirmed that the stator blades have a low impact on this flow dynamics even though their insertion involves an azimuthal wavenumber shift of each mode. To deeper investigate the mode mechanism of **Case 1**, the GLSA framework is used again in the following section. Indeed, in Chap. 4, this tool proves to be an efficient tool to extract the coherent structure driving the pressure band phenomenon in an academic rotor/stator case and investigate their origin. However, in case of a

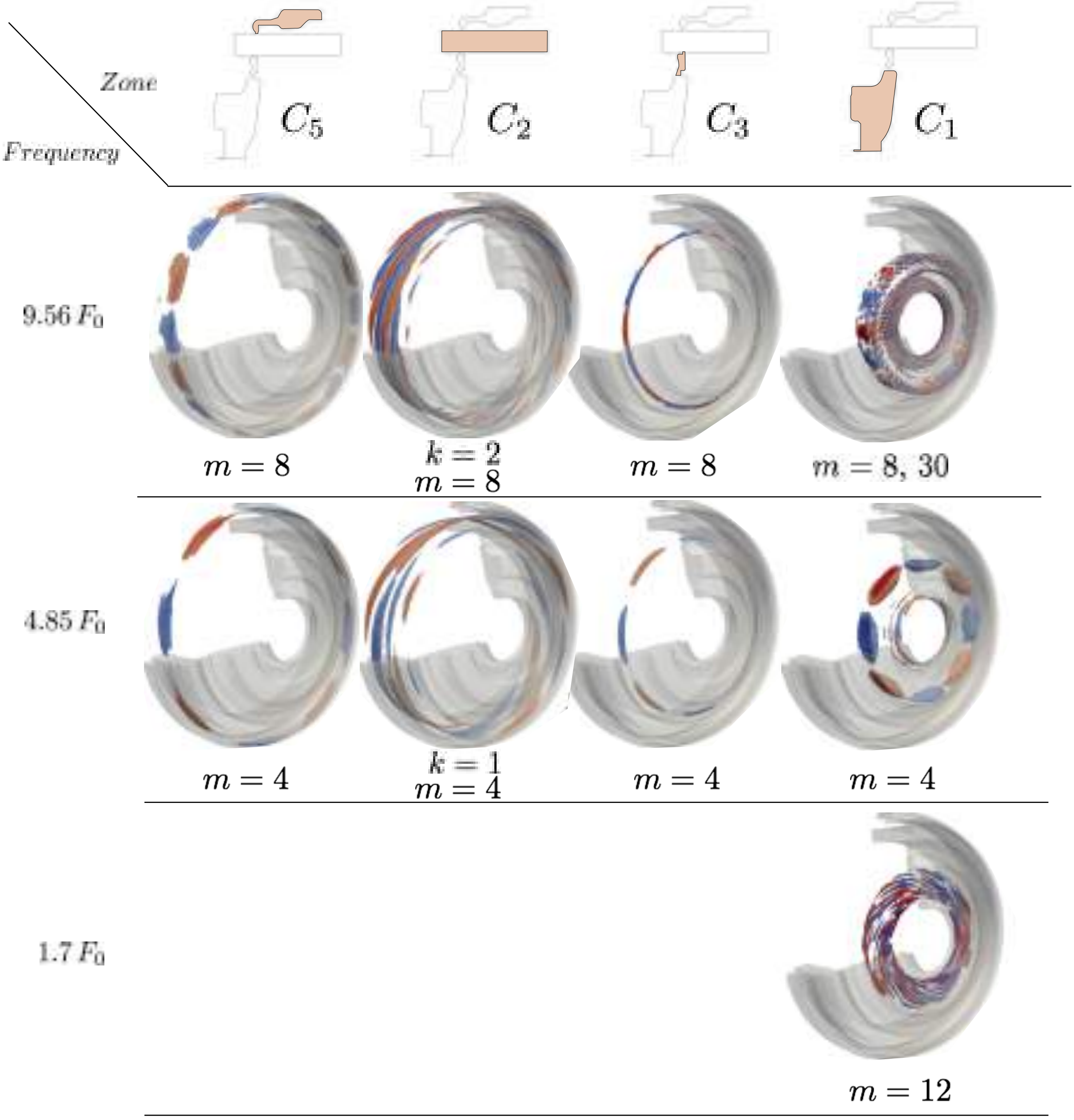

Figure 6.16 – Dynamic Mode Tracking (DMT) of **Case 1**: The axial velocity of the three main frequencies are represented separately from *(left)* to *(right)* in the upper cavity (C_5), the main annulus (C_2) the throat (C_3) and the rotor/stator wheel space (C_1).

highly turbulent flow as the one present in the turbompump, the construction of a linear stability model is still a great challenge for the scientific community. In the next section, a recent stability approach will be introduced to model this complex system. Note that the present LES results are of the utmost importance since the azimuthal wavenumbers found will be taken as input information for the GLSA.

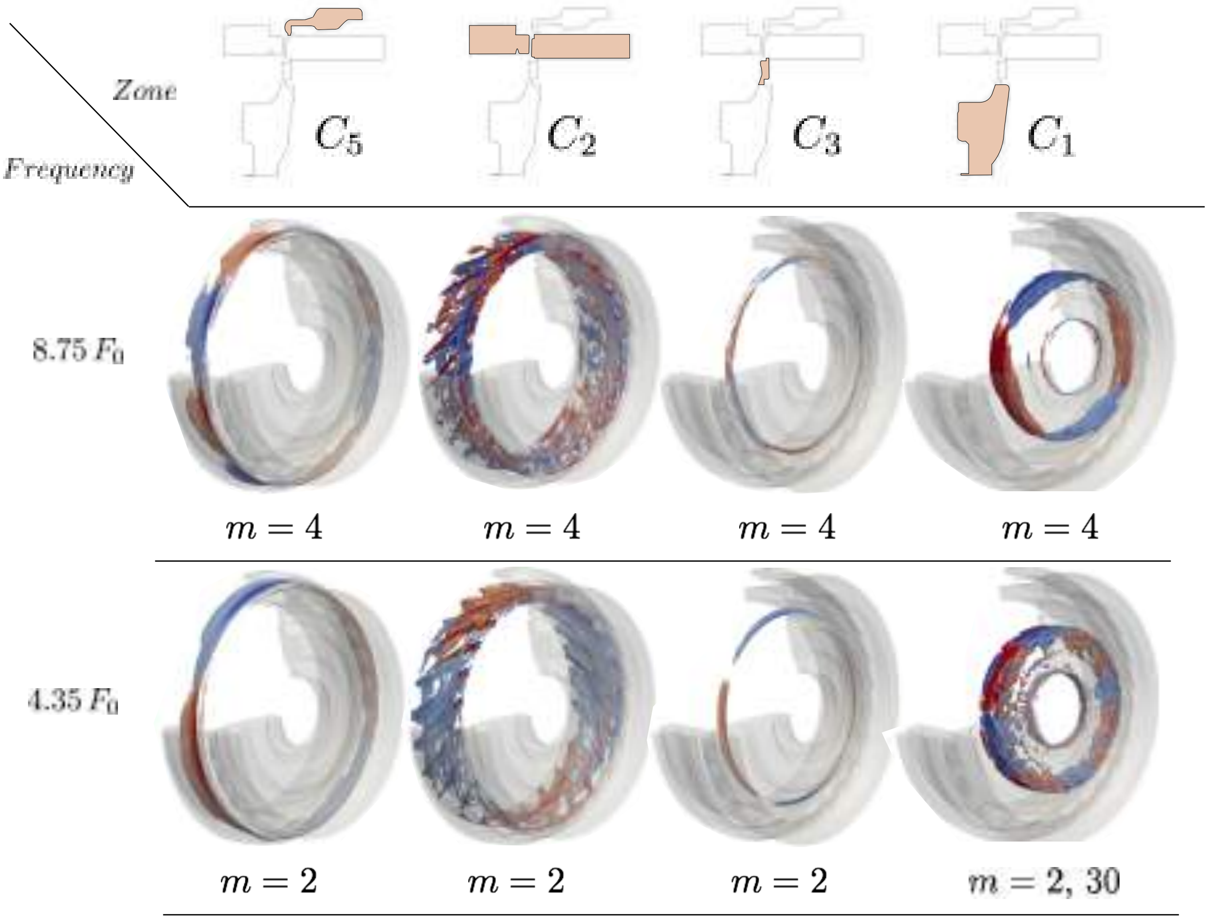

Figure 6.17 – Dynamic Mode Tracking (DMT) of **Case 2**. The axial velocity of the three main frequencies are represented separately from *(left)* to *(right)* in the upper cavity (C_5), the main annulus (C_2) the throat (C_3) and the rotor/stator wheel space (C_1).

6.6 Stability analysis of the turbopump

Linear stability analysis (LSA) was originally derived to investigate the growth of infinitesimal perturbations on stationary laminar base flows. However, the results obtained from this basic model can become innacurate when pertubations reach a finite size or when turbulence is involved. To overcome this limit, linear stability analysis around a mean flow proved to be a promising solution. In fact, as stated in Rukes *et al.* (2016), this approach takes the nonlinear interaction between the coherent structure and the flow implicitly into account. This model found a success for several applications (Barkley (2006); Turton *et al.* (2015)) and enables also to retrieve the pressure band phenomenon in simple rotating cavities of Chap. 4. Contrary to these academic cavities where the flow was in a transitional state, very high Reynolds numbers are found in the turbopump cavities. In this specific case, the stochastic fluctuation interactions can be of first order and were not taken into account with the simple approach used in Chap. 4. To overcome this limit, studies have recently developed a new model describing the coherent structure evolutions by using the triple flow decomposition of Reynolds (1883) instead of a simple one as done in Chap. 4. The resulting equations contain new unknown terms compared to the classical LSA model that correspond to oscillations of the background Reynolds stresses caused by the organized wave. This approach first described in LSA by Reau & Tumin (2002) found a recent success in different applications (Oberleithner *et al.* (2014); Rukes *et al.* (2016); Kaiser & Oberleithner (2017); Tammisola & Juniper (2016)). To complete, the investigation of the pressure band phenomenon through LES, this new GLSA is here discussed and applied to **Case 1** to shed some light on the mode mechanism and origin. This section is organized as follows: First, the governing equations of the coherent perturbations are provided in details Sec. 6.6.1 and applied to **Case 1**. Finally, receptivity and sensitivity analysis, as done in the academic cases, will be conducted to give more insight on the mode origins but also as a guiding tool to propose first solutions to control such flows.

6.6.1 Coherent Stability equations

Contrarly to Chap. 4, a triple decomposition also known as the Reynolds decomposition (Reynolds & Hussain (1972)) is used for all variables so that:

$$g = \bar{g} + \tilde{g} + g' \tag{6.6.1}$$

where $\bar{g}$, $\tilde{g}$ and g' denote respectively the mean flow, the coherent fluctuations and the stochastic fluctuations of a variable g.

By introducing this decomposition in the full Navier-Stokes equations, one can obtain the coherent fluctuation equations by subtracting the time-averaged equations of motion from the phase-averaged equations,

$$\begin{aligned} \frac{\partial \tilde{u}_i}{\partial x_i} &= 0 \\ \frac{\tilde{u}_i}{\partial t} + \bar{u}_j \frac{\tilde{u}_i}{\partial x_j} + \tilde{u}_j \frac{\bar{u}_i}{\partial x_j} &= -\frac{\partial \tilde{p}}{\partial x_i} + \frac{1}{Re} \frac{\partial^2 \tilde{u}_i}{\partial x_j \partial x_j} \\ &+ \frac{\partial}{\partial x_j}(\tilde{u}_i \tilde{u}_j - \overline{\tilde{u}_i \tilde{u}_j}) - \frac{\partial}{\partial x_j}(< u'_i u'_j > - \overline{u'_i u'_j}) \end{aligned} \tag{6.6.2}$$

where u_i is the velocity vector while x_j and t stand for the spatial coordinates and time respectively. Note that here, indices i and j follow the Einstein notation and rule of summation. Likewise, $< \cdot >$ corresponds to the phase average operator so that for any perturbation X of period T,

$$< X > = \tilde{X} + X' = \frac{1}{n} \sum_{p=0}^{n-1} X(\tau + pT),\ \tau \in [0; T] \tag{6.6.3}$$

In the following, the third term on the right hand side of the momentum equations, Eq.(6.6.2), is neglected since one assumes here small perturbations. However, the fourth term which describes the stochastic-coherent interaction, can be of first order in turbulent flows. As Reynolds (1883) or Paredes *et al.* (2016) commented, this term can be understood as the change in Reynolds stresses during a period of the coherent fluctuation. As for RANS or LES equations, a closure problem is therefore generated. Similarly to Kaiser & Oberleithner (2017) and Paredes *et al.* (2016), a Boussineq approximation can be used to relate the stochastic-coherent interaction to the coherent flow strain rates $\tilde{S}_{ij}$ by introducing an eddy viscosity ν_e so that,

$$< u_i'u_j' > - u_i'u_j' = \widetilde{u_i'u_j'} = \nu_e \tilde{S}_{ij}, \tag{6.6.4}$$

and following Ivanova *et al.* (2012), an optimal representation of ν_e can be obtained through a least-square fit over all resolved Reynolds stresses yielding:

$$\nu_e = \frac{(-\overline{u_i'u_j'} + \frac{2}{3}K\delta_{ij}) \cdot (\frac{\partial \bar{u}_i}{\partial x_j} + \frac{\partial \bar{u}_j}{\partial x_i})}{(\frac{\partial \bar{u}_k}{\partial x_l} + \frac{\partial \bar{u}_l}{\partial x_k}) \cdot (\frac{\partial \bar{u}_k}{\partial x_l} + \frac{\partial \bar{u}_l}{\partial x_k})}, \tag{6.6.5}$$

where K is the turbulent kinetic energy and δ_{ij} the Kronecker delta.

In opposition to the most recent studies, the coherent viscosity ν_e is computed in the following based on the available LES predictions and DMT. Indeed, to compute the Reynolds stress tensor $\overline{u_i'u_j'}$ of Eq. (6.6.5), the coherent fluctuations $\tilde{u}_i$ is first evaluated summing the 4 main modes of the system obtained using DMT. Thanks to this knowledge, simple difference with u_i, gives access to the stochastic fluctuations, the cross products $(u_i'u_j')$ and their averaged $(\overline{u_i'u_j'})$. Note also that additionally to the molecular viscosity ν_l and the eddy viscosity ν_e, the mean flow being extracted from a LES, the subgrid viscosity noted ν_{SGS}, which models the interaction of the subgrid scale turbulence with the resolved flow, needs also to be taken into account in the linear stability analysis. It is therefore assumed here, that these three components add yielding a total Reynolds number of the analyzed mean flow of the form,

$$Re_{tot} = \frac{U\,L}{\nu_l + \nu_e + \nu_{SGS}}, \tag{6.6.6}$$

with U and L being the velocity and length scales used to nondimensionalize the equations. In the next section, the corresponding linearized model is applied to **Case 1** to shed some light on the modes driving this turbopump configuration.

6.6.2 GLSA Results

To apply the adapted model presented above, to the turbopump, the global stability solver GIFIE is again used after adaptation for the study. First, a direct comparison of the three viscosities obtained for **Case 1** and needed to formulate the linearized system is given in Fig. 6.18. The laminar viscosity variations are clearly weak and essentially due to the temperature variations across the boundary layers and in the mixing regions, Fig. 6.18(a). When it comes to the mean subgrid scale viscosity ν_{SGS} and eddy viscosity

ν_e, both mark the upper boundary layer of the main annulus where there is a large flow separation as well as strong velocity variations.

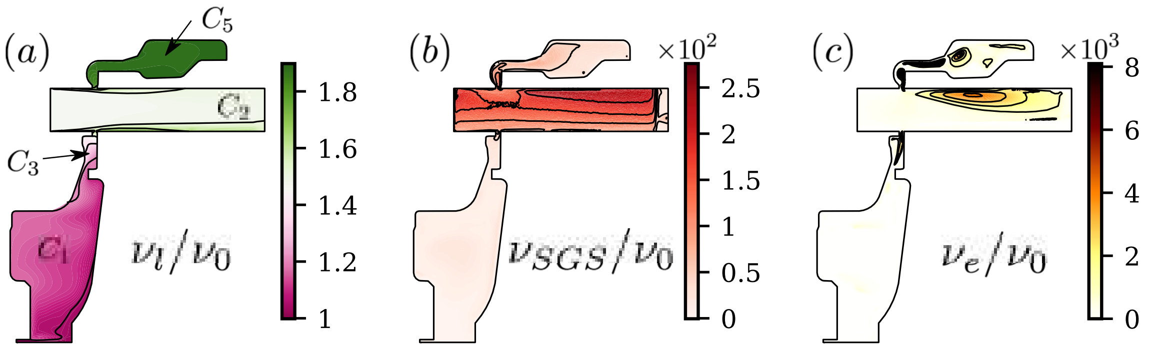

Figure 6.18 – Viscosity comparison: (a) Molecular viscosity ν_l, (b) Subgrid scale viscosity ν_{SGS} (c) Eddy viscosity ν_e. All the results have been normalized by reference viscosity ν_0 of the mixture at a temperature and pressure (T_0, P_0)=(300K, $1.013 \cdot 10^5$ Pa).

In the previous section, DMT and DMD showed that $m = 4$ and $m = 8$ were the two azimuthal wavenumbers marking respectively the dominant mode and its harmonic for **Case 1**. The present stability analysis purpose being, beyond retrieving the mode shapes, to shed some light on their origins, these two characteristic numbers are hence taken as inputs in the present study. Indeed, due to the large size matrices involved, a consequent number of eigenmodes, difficult to sort, are generated through the resolution of the linear problem. By computing the eigenmodes for two different mesh sizes with a small gap, a non negligible number of spurious modes can be highlighted and enables hence to clean a part of the numerical modes from the physical ones. Figures 6.19(a)-(b) show the corresponding clean spectra found respectively for $m = 4$ and $m = 8$ for two sizes of mesh Δh and $\Delta h + \epsilon$. As seen, even after cleaning, for both azimuthal wavenumbers, a specific "arc" branch can be observed in each spectrum. As reviewed in Lesshafft (2018), this specific branch is often linked to spurious modes that are robust to refinement and other numerical parameter variations whenever conducting stability analysis studies (Cerqueira & Sipp (2014); Heaton *et al.* (2009)). In such cases, the modes with the highest amplification rates tend to be non physical. In fact, when performing a stability analysis around a mean flow, one expects to obtain marginally stable modes or at least modes with very low amplification rates (Barkley (2006)). From the obtained spectra, one finds the modes ($\omega/(2\pi F_0)$,m)=(4.79 + i0.09,4) and ($\omega/(2\pi F_0)$,m)=(9.72 + i0.03,8), highlighted by red circles in Fig. 6.19, to be in best agreement with the previous studies and derived knowledge.

The spatial distribution of the modes corresponding to these two frequencies are displayed in Fig. 6.20 where a direct comparison with the 2D shapes obtained with DMT is realized. Note that as shown in Sec. 6.5, these two DMT modes have complex structures and can also be composed of different azimuthal wave numbers. As done in

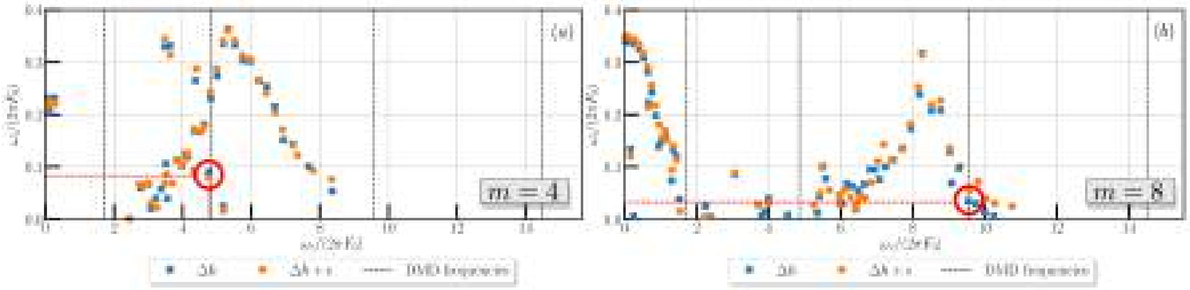

Figure 6.19 – **Case 1** spectrum for (a) $m = 4$ (b) $m = 8$. For each azimuthal value, two different mesh size Δh and $\Delta h + \epsilon$ are displayed to filter spurious modes. Only positive amplification rate mode are given.

Chap. 4, each mode has therefore been Fourier decomposed on an azimuthal basis with $m = 4$ and $m = 8$ respectively for $F/F_0 = 4.85$ and $F/F_0 = 9.56$ to ease the comparison with the present stability analysis. Note also that a none negligible improvement of the GLSA mode shape prediction has been obtained when using the new stability approach taking into account the coherent viscosity. A comparison between the current approach with the one developed in Chap. 4 is proposed in App. F. For the two modes, the main improvement is found in the main annulus where as shown by Fig. 6.18, the coherent viscosity marks the most the system. Furthermore, and contrary to the classical method, the two characteristic axial wavenumbers $k = 1$ and $k = 2$ respectively for the $m = 4$ and $m = 8$ modes are here well retrieved. When it comes to GLSA results compared to DMT:

- $m = 4$ **mode**: When one looks closely to the dominant mode cavities by cavities, the highest amplitudes are found in the C_5 cavity in agreement with DMT. Furthermore, at lower radii, the separation of the top boundary layer of the main annulus C_2 as well as the C_3 cavity behavior are well captured by GLSA. In cavity C_1, the generation of vortices due to the hub leak is also well predicted although their magnitude is found higher with GLSA. Finally, high amplitude spiral structures can be noted in the GLSA results on the stator of cavity C_1, these being not present in the DMT results.

- $m = 8$ **mode**: The main harmonic of the dominant mode although more difficult to obtain with GLSA is also investigated in the following. In fact, when one expected this mode to be fully expressed in the main annulus, the highest amplitudes are found in C_1 where as shown with DMT almost no activity is found for $m = 8$. This can be due to the mode complex structure with multi-characteristc azimuthal wavenumbers that can mark the mean flow and mislead GLSA in recovering the full mode spatial description. Despite this observation, a good dynamics of C_5 is retrieved. Likewise, near the large separation of the upper boundary layer of the main annulus, the characteristic axial wavenumber $k = 2$ is also well captured as well as the small structures in the lower boundary layer.

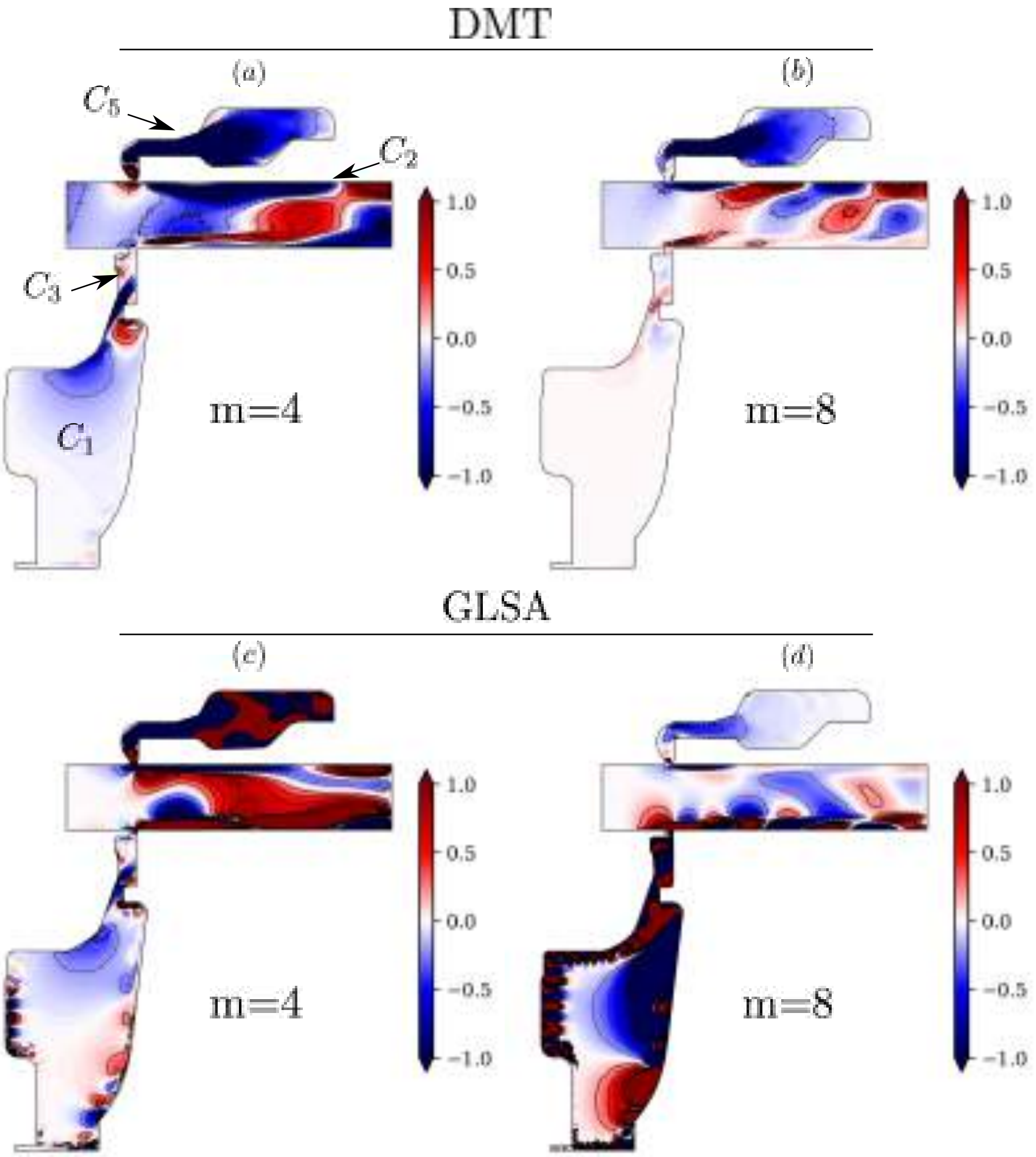

Figure 6.20 – 2D shapes comparison: (a)-(b) DMT results and (c)-(d) global stability results with *(right)* $m = 4$ mode ($F/F_0 = 4.79$). and *(left)* $m = 8$ ($F/F_0 = 9.56$).

Even though the construction of a linear stability model for such complex flow proves here to be challenging, the two main modes of the system could be found with a good agreement with DMT. As shown in the studies on the academic case Chap. 4, the real contribution of GLSA compared to LES is its capacity to exploit adjoint methods to investigate each mode mechanism and set up control strategies. In the following paragraph, receptivity and sensitivity analysis are hence applied to the turbopump, to shed some light on the pressure band phenomenon origins.

Structural sensitivity and receptivity analysis

As explained in Sec. 4.3.2, the adjoint mode results from the resolution of Eq. (4.3.20) and represents the receptivity of the direct mode to external forcing. It can also give, as stated by Chomaz (2005), an indication of the initial condition that most optimally excites the direct mode. The adjoint axial velocity fluctuations for both identified modes by GLSA are shown on Fig. 6.21. In the present case, both modes are not receptive at all in the main annulus of the system where their direct mode axial velocities are maximal. For the first selected mode, $m = 4$, the adjoint expresses mostly in the cavities C_1 and C_5. One can also see that the fluctuations between the at $C_2 - C_5$ connection are particularly high in this zone and would explain why external forcing in this specific region would help modifying this mode. The $m = 4$ mode is also seen to be receptive in the throat (C_3) of the system between the main annulus and the cavity C_1. These results are not surprising and were already observed in a previous study (Pogorelov *et al.* (2018)) where the authors showed that the rim seal of a turbomachinery played a determining role to damp modes of such systems and calibrates the exchanges between the main annulus and the wheel space (C_1). The last local maximum for this adjoint mode is found near the leak on the stator side. These results can be linked to the one found in academic cavities where an injection was added around the hub and for which a complete new dynamics could be obtained with low amplitude inflows. In a similar industrial configuration, Bridel-Bertomeu (2016) showed also that the leak has a major impact on the global modes of the system in particular when it is cold. Finally, for the $m = 8$ mode, similar conclusions can be derived as it is only receptive in the stator boundary layer of cavity C_1.

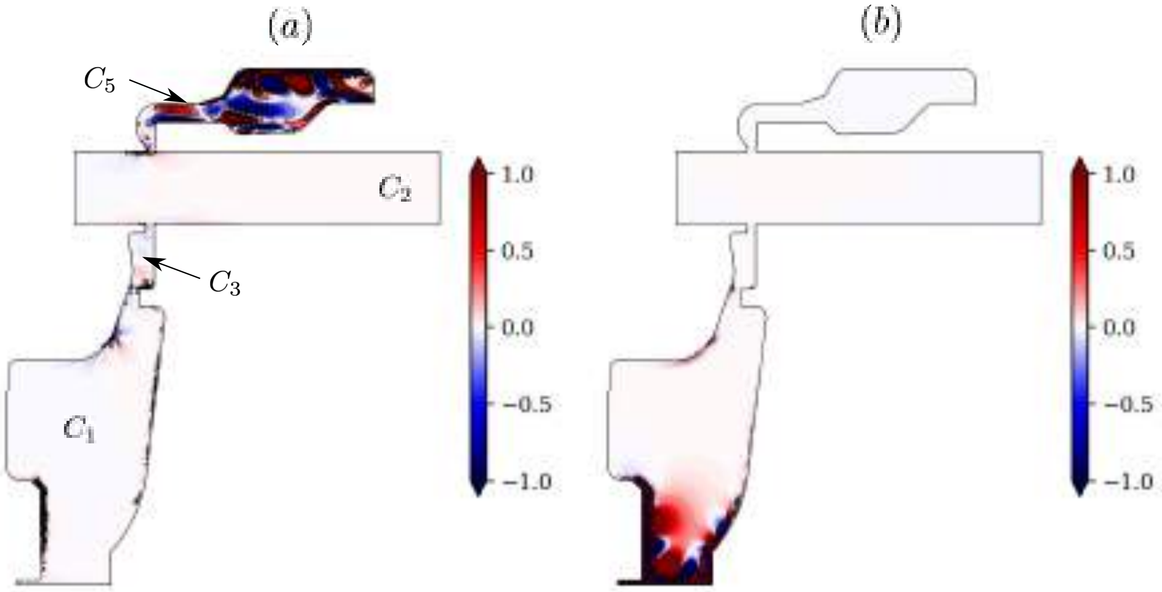

Figure 6.21 – Axial velocity adjoint modes: (a) $m = 4$ ($F/F_0 = 4.79$) and (b) $m = 8$ ($F/F_0 = 9.56$).

To complement these results and based on Giannetti *et al.* (2009), the spatial location where a given mode is triggered, *i.e.* the wavemaker region, is evaluated here through the structural sensitivity, Eq. (4.3.21). Such maps are shown for the two modes of interest in Fig. 6.22. For the most unstable mode $m = 4$, the sensitivity in Fig. 6.22*(a)* shows that the region of most amplification is located near the hub and more precisely at the corner where the leak impacts the rotor. What is remarkable here is that the origin of the mode is far from the main annulus C_2 and cavity C_5 where the mode amplitudes are maximal. A second spot of sensitivity can be observed in cavity C_3. This shows again that this specific cavity plays a clear role in the amplification of the $m = 4$ mode.
For mode $m = 8$, the maximum is found on the stator at $r' = 0.3$. It is however difficult to validate this wavemaker as one showed that the GLSA overestimates the velocity amplitude in this region for this specific mode.

To conclude, GLSA proves here to be a relevant candidate to point out the origin of a complex unsteady phenomenon in an industrial case thanks to adjoint methods. Even though the highly turbulent and multi-azimuthal nature of this specific flow make the construction of a linear stability model a real challenge, first solutions could be highlighted to suppress the pressure band phenomenon in agreement with the literature. As a perspective for future studies on the same application with more robust stability models, sensitivity to base flow modification could be analyzed, as done for the academic cavity in Chap. 5, to set up a more precise control system.

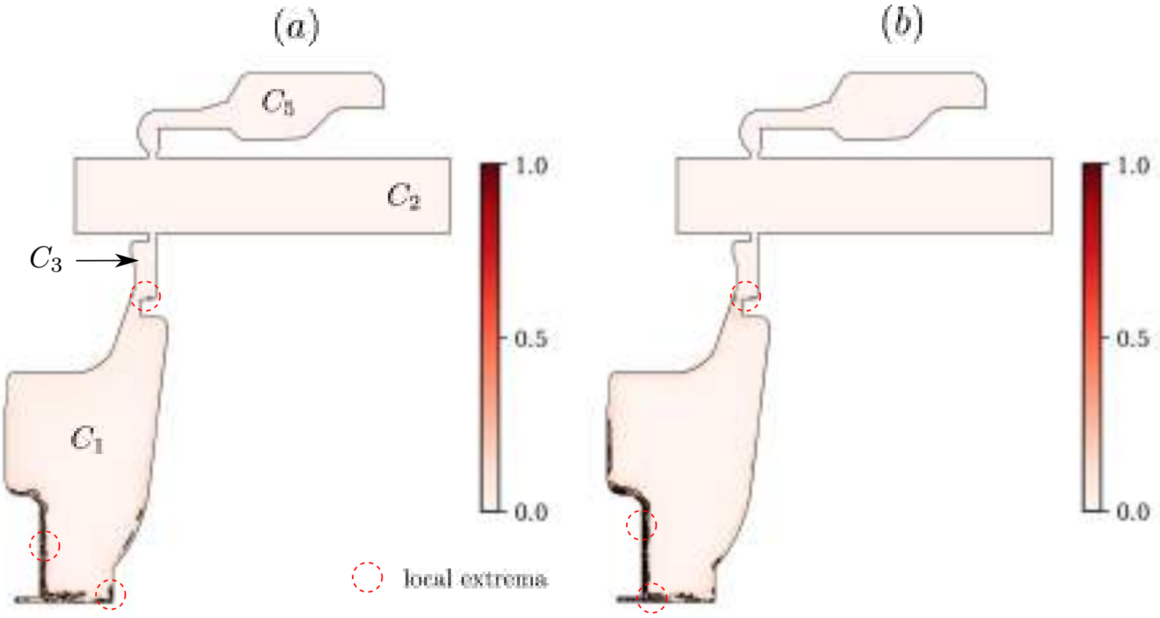

Figure 6.22 – Structural sensitivity: (a) mode $m = 4$ (b) mode $m = 8$.

6.7 Conclusion

This chapter dealt with the investigation of the pressure band phenomenon in a space turbopump turbine. As a follow up from Bridel-Bertomeu (2016) work, the subject is extended here by simulating first a new configuration called **Case 1** where the leak or at least the cavity aspect ratio around the hub is modified. It is shown that this hub modification does not change the overall dynamics of the system. A second configuration called **Case 2** is then studied for which the blades of the stator are taken into account. It is shown that the flow spectrum through this modification becomes richer and quite complex. The main frequencies of **Case 1** are however retrieved in **Case 2** although azimuthal wave number shifts are also observed. More detailed analyses of the mode shapes in the low cavity of each system show that the harmonic of the system can present multi-azimuthal wavenumbers similarly to the cylindrical academic cavity. Finally, **Case 1** is studied further through linear stability analyses. The results show that, due to the large matrix size involved, a very large number of modes can appear making its exploitation difficult. However, a $m = 4$ and $m = 8$ mode can be identified since having the expected frequencies and spatial distribution that are in a good agreement with DMT fields. Complemented by receptivity and sensitivity analyses some light can be furthermore be shed on both mode mechanisms. In particular, the leak and the annular seal of the system, separating the main annulus from the rotor/stator wheel space, appear to be the more receptive regions to an external forcing. One can therefore propose that a modulated leak could be a way to control or at least shift the observed dominant mode. The sensitivity analysis also shows that the modes despite fully expressed in the upper cavities are generated around the hub/stator and are amplified by the annular seal. In agreement with the literature, changing this region of the geometry can therefore be another solution to suppress the pressure band phenomenon.

Conclusions and perspectives

Self-sustained oscillations of rotor/stator cavity flows are well known to industry. In rocket engines, this unsteady phenomenon usually referred to as 'pressure band phenomenon' can be very dangerous and jeopardize the structural integrity of the entire system by damaging turbomachinery components or turbopumps in the context of space applications. Today, the origin of such a flow instabilities and resulting limit-cycle is not well understood. Furthermore, due to the complex geometry of space turbopumps and the highly turbulent flow presents in such systems, a numerical prediction of such phenomenon is still difficult to obtain. The present work aims at capturing such phenomenon but also shed some light on its origin and mechanism with dedicated tools. Finally, one particular interest for the aerospace industry is also to find technical solutions to stablize such an unstable flow.

To address these problematics, an annular rotor/stator cavity has first been investigated in this work as a first order representation of a space turbopump cavity. In the literature, it is well known that despite the simplicity of this configuration, the rotating boundary layers coming from the disks are complex, highly turbulent and three dimensional. Past studies have shown that such flow can not be predicted through Reynolds Averaged Navier-Stokes (RANS) simulations or even the Unsteady Reynolds Averaged Navier-Stokes (URANS) approaches. In this work, Large Eddy Simulations (LES) have been chosen for its well known capacity to simulate highly unsteady flows. Complemented by dedicated tools such as Dynamic Mode Decomposition (DMD) or Power Spectral Density (PSD), one shows that the annular rotor/stator cavity, of interest to the present PhD work, is driven by three dominant modes with three distinct azimuthal wave numbers producing well known spirals or annular patterns. Even though LES proves here to be relevant tool to retrieve the pressure band phenomenon in an academic cavity, no control strategies to suppress or damp this phenomenon could be set up from these results. The first question coming from this latter problematic was how can one control a flow composed of several frequencies ? To answer this question the mode interactions needed first to be understood. To do so, a new tool called Dynamic Mode Tracking and Control (DMT/DMTC) has been developed and implemented during this PhD thesis. Through time filters, this approach enables to extract one or several frequency 3D fields and if needed, through a relaxation term added to the momentum equations, damps also one or several of these identified structures. This method has been incorporated to the AVBP package and recently used on different applications such as the control of numerical instabilities coming from an academic premixed swirl burner, film cooling hole efficiency but also for the investigation of turbulence in the LS89 configuration high-pressure turbine blades. In rotating flow, this strategy enabled, by controlling one by one each mode of the annular cavity, to show that a dominant mode is at the source of the low frequency mode. This important result shows that to control the pressure band phenomenon, one can focus only on the elimination of this dominant frequency. From these results the remaining question was to find the appropriate device to control the flow. To do so a deeper investigation on the mode mechanisms and origins needed to be done. In this context, stability analyses around a mean flow, known to be an efficient tool to analyse oscillating flows, is used on the annular cavity. The three mode limit-cycle obtained through the LES predictions of this cavity is retrieved through a global stability approach thanks to the tool GIFIE created at CERFACS and further developed during this PhD thesis. One shows in particular that this latter approach is a relevant tool to overcome the limits of the local stabilty analysis studied in the previous PhD of Bridel-Bertomeu (2016) on the same configuration. One of the argument justifying the use of stability analysis is its capacity to investigate a mode mechanism through adjoint methods. In this context, two specific tools are used: receptivity and structural sensitivity analysis. When the first one points out the region of a given mode most sensitive to harmonic forcing, structural sensitivity (wavemaker) gives the exact region where a mode is triggered. One found in particular that the dominant mode and the low frequency one depart from the stationary disk boundary layer. To complement the information obtained on each mode' mechanisms, an investigation of the sensitivity tensor and a comparison with a cylindrical cavity flow highlights the fundamental role of the hub on the mode selection. Even though the source of each modes could be found, it is well known that modifying the flow around a mode wavemaker is not always the most optimal way to control it. To define more precisely a device to control the pressure band phenomenon, sensitivity to base flow modifications still obtained in the global stability framework, is analyzed. This tool, implemented in GIFIE during this work, enables to find the optimal location where the mean flow should be modified to stabilized or at least frequency shift a mode. For the annular cavity the external part of the stationary disk boundary layer is found to be the most efficient location to suppress the dominant mode. The strategies and the results are finally validated through a LES introducing suction and injection devices. These indeed enable to suppress all three modes composing the initial limit-cycle thanks to a very low axial velocity, yielding a purely turbulent flow with an overall pressure oscillation level highly decreased.

Regarding the application of such techniques to actual industrial turbine flows such as the one in the space turbopump, several remarks can be made. Even though higher Reynolds numbers, and level of unsteadiness could be noticed in the main annulus of the system, spiral patterns and coherent structures are observed in the rotor/stator wheel space as in the academic cavity. However the interaction of the main flow with the cavity flow generates low azimuthal wavenumbers that are dominant in the whole system. In order to investigate these latter modes, the GLSA framework is reused. Due to the high turbulence level and the non linearities present in the cavities, the classical model used on academic cavities could not be applied. To overcome this limit, a work on the modeling of the equation term linked to the turbulence has been done. An eddy viscosity approach has been proposed and showed an improvement of the results compared to the ones with a classical approach. Furthermore, results of structural sensitivity analysis, pointed out that the leak and the rim seal where the sources of the global modes found in the turbopumps and could be modified to suppress the pressure band phenomenon. Finally, the rim seal type and the presence of the stator/rotor blades are known in gas turbine to play a main role in the ingress of the main annulus flow in the rotor/stator wheel space and hence the generation of hydrodynamic modes. The specific impact of the stator blades is studied in present work. Results shows that even though similar spectrum is obtained for a configuration with or without blades an azimuthal wave number shift has been noted due to the blades.

From a perspective point of view, the results on the industrial cases showed that the main annulus plays a non negligible role on the mode amplifications. An academic cavity connected to an annulus flow or an academic cavity with a radial inflow at the shroud could be useful to study the evolution of the three modes found in this present work in the academic annular case. These configurations could be exploited to better understand the industrial case and the interaction of the wheel space and the main stream of the turbine.

From a GLSA point of view, one shows that the analysis of the coherent fluctuations give an important improvement of the modes shape compared to classical model. However, the mean flow used for this GLSA comes from an LES with wall-law models. A stability model taking into account this two specific features could be built to improve, in particular, the detachment of each mode boundary layers in the main annulus. From a numerical point of view, one of the main challenge found trough the resolution of large eigenvalue matrices is the generation of spurious modes. Pseudo-spectrum could be a solution to sort and extract the physical modes from the numerical ones. Finally, the flow analyses were first conducted to capture the pressure band phenomenon. However the main problem occurring in real cavities is the coupling of the flow with the turbopump structure. To fully answer this problem a model of fluid-structure interaction (FSI) could be set up. A classical global stability framework would be again one of the most promising method to retrieve a self-sustained fluid-structure instability (perturbation growing at large time). In the specific cases of stable system (perturbation decaying at large time), a resolvent analysis could also be studied to determine the optimal external excitation that lead to the largest energetic amplification in the fluid-structure system.

From the different investigations realized during this Ph.D. work the following publications and conferences have been published

Ranked *A* papers

- Queguineur, M., Gicquel, L. Y. M., Dupuy, F., Misdariis, A., Staffelbach, G. Dynamic mode tracking and control with a relaxation method. **Physics of Fluids**, 2019

- Queguineur, M., Bridel-Bertomeu, T., Gicquel, L. Y. M., Stafflebach, G. Large eddy simulations and global stability analyses of an annular and cylindrical rotor/stator cavity limit cycles. **Physics of Fluids**, 2019

- Queguineur, M., T., Gicquel, L. Y. M., Stafflebach, G. Stability and control of an annular rotor/stator cavity limit cycles. **Physics of Fluids**, 2020 *(in preparation)*

Conferences

- Queguineur, M., Bridel-Bertomeu, T., Gicquel, L., Staffelbach, G. Local and Global Stability Analysis of an Academic Rotor/Stator Cavity. Proceedings of **ASME Turbo Expo**, 2018, GT2018-750,
- Queguineur, M., Gicquel, L. Y. M., Stafflebach, G. Modes identification and interactions in a rotor/stator academic cavity. 13th European Turbomachinery Conference on Turbomachinery Fluid Dynamics and Thermodynamics, **ETC**, 2019,
- Queguineur, Gicquel, L. Y. M., Staffelbach, G., Control Strategies of an Academic Rotor/Stator Cavity Through Sensitivity Analysis. Proceedings of **ASME Turbo Expo**, 2019 , GT2019-907

Bibliography

Abdulameer, M A, Garrett, S J, Griffiths, P T & Alvero, B 2016 On the stability of the BEK family of rotating boundary-layer flows for power-law fluids. *Journal of Non-Newtonian Fluid Mechanics* **236**, 63–72. (Cited on page 166.)

Airiau, Christophe, Bottaro, Alessandro, Walther, Steeve & Legendre, Dominique 2003 A methodology for optimal laminar flow control: Application to the damping of Tollmien-Schlichting waves in a boundary layer. *Physics of Fluids* **15** (5), 1131–1145. (Cited on page 91.)

Åkervik, Espen, Brandt, Luca, Henningson, Dan S., Hœpffner, Jérôme, Marxen, Olaf & Schlatter, Philipp 2006 Steady solutions of the Navier-Stokes equations by selective frequency damping. *Physics of Fluids* **18** (6), 2006–2009. (Cited on pages 37, 38, and 59.)

Alveroglu, B, Segalini, A & Garrett, S J 2016 An energy analysis of convective instabilities of the Bödewadt and Ekman boundary layers over rough surfaces. *European Journal of Mechanics B/Fluids* . (Cited on pages 89 and 166.)

Appelquist, E, Schlatter, P, Alfredsson, P H & Lingwood, R J 2015 Global linear instability of the rotating-disk flow investigated through simulations. *J. Fluid Mech.* **765**, 612–631. (Cited on pages 19 and 81.)

Bagheri, Shervin 2013 Koopman-mode decomposition of the cylinder wake. *Journal of Fluid Mechanics* **726**, 596–623. (Cited on page 177.)

Balay, Satish, Abhyankar, Shrirang, Adams, Mark F., Brown, Jed, Brune, Peter, Buschelman, Kris, Dalcin, Lisandro, Dener, Alp, Eijkhout, Victor, Gropp, William D., Karpeyev, Dmitry, Kaushik, Dinesh, Knepley, Matthew G., May, Dave A., McInnes, Lois Curfman, Mills, Richard Tran, Munson, Todd, Rupp, Karl, Sanan, Patrick, Smith, Barry F., Zampini, Stefano, Zhang, Hong & Zhang, Hong 2019 PETSc users manual. *Tech. Rep.* ANL-95/11 - Revision 3.11. Argonne National Laboratory. (Cited on page 67.)

Barbaroux, Pierre 2016 The metamorphosis of the world space economy: investigating global trends and national differences among major space nations' market structure. *Journal of Innovation Economics* **20** (2), 9. (Cited on page 2.)

Barkley, D 2006 Linear analysis of the cylinder wake mean flow. *Europhys. Lett.* **75** (5), 750–756. (Cited on pages 132 and 135.)

Batchelor, G K 1951 Note on a class of solutions of the navier-stokes equations representing steady rotationally-symmetric flow. *Q. J. Mech. Appl. Math.* **4** (1), 29–41. (Cited on pages 18 and 56.)

Beneddine, Samir, Sipp, Denis, Arnault, Anthony, Dandois, Julien & Lesshafft, Lutz 2016 Conditions for validity of mean flow stability analysis. *Journal of Fluid Mechanics* **798**, 485–504. (Cited on page 59.)

Bengana, Y., Loiseau, J.-Ch., Robinet, J.-Ch. & Tuckerman, L. S. 2019 Bifurcation analysis and frequency prediction in shear-driven cavity flow. *Journal of Fluid Mechanics* **875**, 725–757. (Cited on page 59.)

Bödewadt, U T 1940 Die Drehströmung über festem Grunde. *Zeitschrift für Angew. Math. und Mech.* **20** (5), 241–253. (Cited on page 55.)

Boussineq, Joseph 1897 *Théorie de l'écoulement tourbillonnant et tumultueux des liquides dans les lits rectilignes à grande section, Volume 2*, gauthier-v edn. (Cited on page 24.)

Brady, J F & Durlofsky, Louis 1987 On rotating disk flow. *J. Fluid Mech.* **175**. (Cited on page 18.)

Bridel-Bertomeu, Thibault 2016 Investigation of unsteady phenomena in rotor/stator cavities using Large Eddy Simulation. *Ph.D. thesis Institut National Polytechnique de toulouse* (Umr 5563), 118. (Cited on pages 9, 10, 20, 42, 43, 45, 64, 94, 97, 114, 115, 116, 117, 120, 128, 138, 140, 144, 166, and 168.)

Bridel-Bertomeu, Thibault, Gicquel, Laurent & Staffelbach, Gabriel 2016 Wall modeled les and its impact on rotor/stator cavity unsteady features. *ASME Turbo Expo 2016* . (Cited on pages 18, 25, and 28.)

Bridel-Bertomeu, T., Gicquel, L.Y.M. & Staffelbach, G. 2017*a* Large scale motions of multiple limit-cycle high Reynolds number annular and toroidal rotor/stator cavities. *Physics of Fluids* **29** (6). (Cited on page 9.)

Bridel-Bertomeu, Thibault, Gicquel, Laurent & Staffelbach, Gabriel 2017*b* Unsteady macro-structures from large-eddy simulation of industrial turbopump turbine cavity. *AIAA Journal* **55** (7), 2198–2214. (Cited on page 9.)

Burkhardt, Holger, Sippel, Martin, Herbertz, Armin & Klevanski, Josef 2004 Kerosene vs methane: A propellant tradeoff for reusable liquid booster stages. *Journal of Spacecraft and Rockets* **41** (5), 762–769. (Cited on page 6.)

Caraballo, E., Webb, N., Littles, J., Kim, J. H. & Samimys, M. 2009 Supersonic inlet flow control using plasma actuators. *47th AIAA Aerospace Sciences Meeting including the New Horizons Forum and Aerospace Exposition* **1233** (January), 1–14. (Cited on page 88.)

Carini, M., Airiau, C., Debien, A., Ĺeon, O. & Pralits, J. O. 2017 Global stability and control of the confined turbulent flow past a thick flat plate. *Physics of Fluids* **29** (2). (Cited on pages 90 and 93.)

Cerqueira, Stéphane & Sipp, Denis 2014 Eigenvalue sensitivity, singular values and discrete frequency selection mechanism in noise amplifiers: The case of flow induced by radial wall injection. *Journal of Fluid Mechanics* **757** (6), 770–799. (Cited on page 135.)

Chandrasekhar, S 1984 On stars, their evolution and their stability. *Reviews of Modern Physics* **56**, 137–47. (Cited on page 58.)

Chima, R. V. 2002 Computational modeling of vortex generators for turbomachinery. *American Society of Mechanical Engineers, International Gas Turbine Institute, Turbo Expo (Publication) IGTI* **5 B** (April 2002), 1229–1238. (Cited on page 88.)

Chomaz, Jean-Marc 2005 Global instabilities in spatially developing flows: Non-Normality and Nonlinearity. *Annu. Rev. Fluid Mech.* **37** (1), 357–392. (Cited on pages 71, 73, 74, 81, 84, and 138.)

Coles & Hirst 1968 Computation of Turbulent Boundary Layers. *AFOSR-IFP Stanford Conf.* . (Cited on page 118.)

Colin, Olivier & Rudgyard, Michael 2000 Development of High-Order Taylor–Galerkin Schemes for LES. *J. Comput. Phys.* **162** (2), 338–371. (Cited on pages 27, 121, and 171.)

Cooper, Alison J & Carpenter, Peter W. 1997 The stability of rotating-disc boundary-layer flow over a compliant wall. Part 1. Type I and II instabilities. *Journal of Fluid Mechanics* **350**, 231–259. (Cited on page 89.)

Cooper, A. J., Harris, J. H., Garrett, S. J., özkan, M. & Thomas, P. J. 2015 The effect of anisotropic and isotropic roughness on the convective stability of the rotating disk boundary layer. *Physics of Fluids* **27** (1), 1–17. (Cited on page 89.)

Crespo del Arco, Emilia, Serre, Eric, Bontoux, Patrick & Launder, Brian 2005 Stability , transition and turbulence in rotating cavities. In *Instabilities of Flows* (ed. M Rhaman), pp. 141–195. WIT PRESS. (Cited on pages 56 and 76.)

Czarny, O, Iacovides, H & Launder, Be 2002 Precessing vortex structures in turbulent flow within rotor-stator disc cavities. *Flow, Turbul. Combust.* pp. 51–61. (Cited on page 24.)

D'Agostino, Luca, Cervone, Angelo, Torre, Lucio, Pace, Giovanni, Valentini, Dario & Pasini, Angelo 2017 An Introduction to Flow-Induced Instabilities in Rocket Engine Inducers and Turbopumps. *CISM International Centre for Mechanical Sciences, Courses and Lectures* **575**, 65–86. (Cited on page 8.)

Daily, J W & Nece, R E 1960 Chamber dimension effects on induced flow and frictional resistance of enclosed rotating disks. *J. Fluids Eng.* **82** (1), 217–230. (Cited on pages 19, 20, 24, 81, 124, and 125.)

Daniels, W. A., Johnson, B. V., Graber, D. J. & Martin, R. J. 1992 Rim seal experiments and analysis for turbine applications. *Journal of Turbomachinery* **114** (2), 426–432. (Cited on page 115.)

Dapogny, C., Dobrzynski, C. & Frey, P. 2014 Three-dimensional adaptive domain remeshing, implicit domain meshing, and applications to free and moving boundary problems. *Journal of Computational Physics* **262**, 358–378. (Cited on page 119.)

Davies, Christopher & Carpenter, Peter W 2003 Global behaviour corresponding to the absolute instability of the rotating-disc boundary layer. *Journal of Fluid Mechanics* **486**, 287–329. (Cited on pages 58, 89, and 167.)

Davies, Christopher & Thomas, Christian 2016 Global stability behaviour for the BEK family of rotating. *Theor. Comput. Fluid Dyn.* . (Cited on page 58.)

Davies, P. O.A.L. & Yule, A. J. 1975 Coherent structures in turbulence. *Journal of Fluid Mechanics* **69** (3), 513–537. (Cited on page 36.)

Daviller, Guillaume, Brebion, Maxence, Xavier, Pradip, Staffelbach, Gabriel, Müller, Jens-Dominik & Poinsot, Thierry 2017 A mesh adaptation strategy to predict pressure losses in les of swirled flows. *Flow Turbulence and Combustion* **99** (1), 93–118. (Cited on page 119.)

Drazin, P G & Reid, W H 2004 *Hydrodynamic stability*. (Cited on pages 54 and 59.)

Ekman, Vagn Walfrid 1905 On the influence of the Earth's rotation on ocean currents. *Ark. för Mat. Astron. och Fys.* **2**, 1–53. (Cited on pages 54 and 55.)

Faller, Alan J 1963 An experimental study of the instability of the laminar Ekman boundary layer. *J. Fluid Mech.* **15** (4), 560–576. (Cited on page 30.)

Faller, Alan J 1991 Instability and transition of disturbed flow over a rotating disk. *J. Fluid Mech.* **230**, 245–269. (Cited on pages 55, 56, 57, and 58.)

Faller, Alan J & Kaylor, Robert E 1966 A Numerical Study of the Instability of the Laminar Ekman Boundary Layer. *J. Atmos. Sci.* **23** (5), 466–480. (Cited on page 58.)

Favre, Alexandre 1983 Turbulence: Space-time statistical properties and behavior in supersonic flows. *Physics of Fluids* **26** (10), 2851–2863. (Cited on page 22.)

Fiore, Maxime 2019 Influence of cavity flow on turbine aerodynamics. *Ph.D thesis, University of Toulouse* (Umr 5318). (Cited on page 115.)

Gallaire, François & Chomaz, Jean-Marc 2003 Mode selection in swirling jet experiments: a linear stability analysis. *J. Fluid Mech.* **494**, 223–253. (Cited on page 83.)

Garnaud, X., Lesshafft, L., Schmid, P.J. & Chomaz, J.-M. 2012 A relaxation method for large eigenvalue problems, with an application to flow stability analysis. *Journal of Computational Physics* **231** (10), 3912–3927. (Cited on pages 39 and 42.)

Garrett, S. J., Cooper, A. J., Harris, J. H., Özkan, M., Segalini, A. & Thomas, P. J. 2016 On the stability of von Kármán rotating-disk boundary layers with radial anisotropic surface roughness. *Physics of Fluids* **28** (1). (Cited on page 89.)

Giannetti, Flavio & Luchini, Paolo 2007 *Structural sensitivity of the first instability of the cylinder wake*, , vol. 581. (Cited on pages 66 and 74.)

Giannetti, Flavio, Luchini, Paolo & Marino, Luca 2009 Linear stability analysis of three-dimensional lid-driven cavity flow. *atti del XIX Congresso dell'Associazione italiana di meccanica teorica e applicata* . (Cited on page 139.)

Gourdain, N, Gicquel, L, Staffelbach, G, Vermorel, O, Duchaine, F, Boussuge, J-F & Poinsot, T 2009 High performance parallel computing of flows in complex geometries: I. Methods. *Comput. Sci. Discov.* **2**. (Cited on pages 26 and 41.)

Gregory, N, Stuart, J T & Walker, W S 1955 On the stability of three-dimensional boundary layers with application to the flow due to a rotating disk. *Philos. Trans. R. Soc. A Math. Phys. Eng. Sci.* **248**, 155–199. (Cited on pages 30 and 56.)

Gregory, N. & Walker, W. S. 1960 Experiments on the effect of suction on the flow due to a rotating disk. *Journal of Fluid Mechanics* **9** (2), 225–234. (Cited on page 89.)

Haidn, Oskar, Oschwald, M., Clauss, Walter, Arnold, Richard, Sender, Joachim, Preuss, A., Preclik, D., Mäding, C., Görgen, J. & Soller, Sebastian 2008 Lox/methane technology efforts for future liquid rocket engines . (Cited on page 6.)

Healey, J J 2007 Enhancing the absolute instability of a boundary layer by adding a far-away plate. *J. Fluid Mech.* **579**, 29–61. (Cited on pages 18 and 63.)

Heaton, C. J., Nichols, J. W. & Schmid, P. J. 2009 Global linear stability of the non-parallel Batchelor vortex. *Journal of Fluid Mechanics* **629**, 139–160. (Cited on page 135.)

Hecht, F 2012 New development in freefem ++. *Journal of Numerical Mathematics* **20** (3), 251–265. (Cited on page 67.)

HENGLI, LIANG & ZUOYI, CHEN 2002 Characteristic analysis of flow-induced vibrations on inducer of oxygen pump. *Journal of Propulsion and Power* **18** (2), 289–294. (Cited on page 8.)

HILL, D. 1992 A theoretical approach for analyzing the restabilization of wakes. *30th Aerospace Sciences Meeting and Exhibit* (April). (Cited on page 66.)

HO, JOANNA, CORKE, THOMAS C. & MATLIS, ERIC 2016 Effect of wall suction on rotating disk absolute instability. *Journal of Fluid Mechanics* **791**, 704–737. (Cited on pages 89 and 99.)

HUERRE, PATRICK & MONKEWITZ, PETER A. 1990 Local and Global Instabilities in Spatially Developing Flows. (Cited on pages 57, 63, and 95.)

ITOH, MOTOYUKI 1991 On the instability of the flow between coaxial rotating disks. *Bound. Layer Stab. Transit. to Turbul. ASME FED* **114**, 83–89. (Cited on page 63.)

ITOH, MOTOYUKI, YAMADA, YUTAKA, IMAO, SHIGEKI & GONDA, MASAHIRO 1992 Experiments on turbulent flow due to an enclosed rotating disk. *Exp. Therm. Fluid Sci.* **5** (3), 359–368. (Cited on pages 20, 28, and 29.)

IVANOVA, ELIZAVETA, NOLL, BERTHOLD & AIGNER, MANFRED 2012 A numerical study on the turbulent schmidt numbers in a jet in crossflow. *Proceedings of the ASME Turbo Expo* pp. 1–12. (Cited on page 134.)

JAMES, KENNETH R, HARITOS, NICHOLAS, ADES, PETER K, ADES, PETER K, JAMES, KENNETH R & HARITOS, NICHOLAS 2016 Mechanical stability of trees under dynamic loads **93** (10), 1522–1530. (Cited on page 58.)

JEONG, JINHEE & HUSSAIN, FAZLE 1995 On the identification of a vortex. *Journal of Fluid Mechanics* **285** (February), 69–94. (Cited on page 122.)

JORDI, BASTIEN 2015 Steady-state solvers for stability analysis of vortex dominated flows by . (Cited on page 39.)

JORDI, BASTIEN E., COTTER, COLIN J. & SHERWIN, SPENCER J. 2015 An adaptive selective frequency damping method. *Physics of Fluids* **27** (9). (Cited on page 59.)

KAISER, THOMAS & OBERLEITHNER, KILIAN 2017 Stability ans sensitivity analyis of hydrodynamic instabilities in industrial swirled injection systems. *Proceedings of the ASME 2017 Turbomachinery Technical Conference and Expostion GT 2017* . (Cited on pages 133 and 134.)

KOEPPLIN, VIKTOR, HERBST, FLORIAN & SEUME, JOERG R. 2017 Correlation-based riblet model for turbomachinery applications. *Journal of Turbomachinery* **139** (7), 1–10. (Cited on page 88.)

KOLMOGOROV, A. N. 1991 The local structure of turbulence in incompressible viscous fluid for very large Reynolds numbers. *Proceedings of the Royal Society of London. Series A: Mathematical and Physical Sciences* **434** (1890), 9–13. (Cited on page 22.)

KOVASZNAY, L. S. G. 1949 Hot-Wire Investigation of the Wake behind Cylinders at Low Reynolds Numbers. *Proceedings of the Royal Society A: Mathematical, Physical and Engineering Sciences* **198** (1053), 174–190. (Cited on pages 177 and 178.)

LACASSAGNE, LAURA 2017 Simulations et analyses de stabilité linéaire du détachement tourbillonnaire d'angle dans les moteurs à propergol solide. *Ph.D.thesis Institut National Polytechnique de toulouse* . (Cited on page 62.)

LAUNDER, BRIAN, PONCET, SÉBASTIEN & SERRE, ERIC 2010 Laminar, Transitional, and Turbulent Flows in Rotor-Stator Cavities. *Annu. Rev. Fluid Mech.* **42** (1), 229–248. (Cited on page 21.)

LEE, N. K.W. & GREITZER, E. M. 1990 Effects of endwall suction and blowing on compressor stability enhancement. *Journal of Turbomachinery* **112** (1), 133–144. (Cited on page 88.)

LEIBOVICH, S & STEWARTSON, K. 1983 A sufficient condition for the instability of columnar vortices. *Journal of Fluid Mechanics* **126**, 335–356. (Cited on page 83.)

LESSHAFFT, LUTZ 2018 Artificial eigenmodes in truncated flow domains. *Theoretical and Computational Fluid Dynamics* **32** (3), 245–262. (Cited on page 135.)

LESSHAFFT, LUTZ, HUERRE, PATRICK, SAGAUT, PIERRE & TERRACOL, MARC 2006 Nonlinear global modes in hot jets. *Journal of Fluid Mechanics* **554**, 393–409. (Cited on page 62.)

LEU, TZONG SHYNG & HO, CHIH MING 2000 Control of global instability in a non-parallel near wake. *Journal of Fluid Mechanics* **404**, 345–378. (Cited on page 106.)

LILLY, DOUGLAS K 1966 On the Instability of Ekman Boundary Flow. (Cited on page 58.)

LINGWOOD, REBECCA J 1995 Absolute instability of the boundary layer on a rotating disk. *J. Fluid Mech.* **299**, 17–33. (Cited on pages 56 and 81.)

LINGWOOD, R. J 1996 An experimental study of absolute instability of the rotating-disk boundary-layer flow. *Cambridge University Press* **314**, 373405. (Cited on pages 57, 58, and 63.)

LINGWOOD, R. J. 1997 On the effects of suction and injection on the absolute instability of the rotating-disk boundary layer. *Physics of Fluids* **9** (5), 1317–1328. (Cited on page 89.)

Lingwood, R. J. & Garrett, S. J. 2011 The effects of surface mass flux on the instability of the BEK system of rotating boundary-layer flows. *European Journal of Mechanics, B/Fluids* **30** (3), 299–310. (Cited on page 89.)

Lingwood, R. J. & Henrik Alfredsson, P. 2015 Instabilities of the von Kármán Boundary Layer. *Applied Mechanics Reviews* **67** (3), 030803. (Cited on pages 54, 55, 76, and 84.)

Littell, Howard S & Eaton, John K 1994 Turbulence characteristics of the boundary layer on a rotating disk. *J. Fluid Mech.* **266**, 175–207. (Cited on page 18.)

Lopez, Juan M 1998 Characteristics of endwall and sidewall boundary layers in a rotating cylinder with a differentially rotating endwall. *J. Fluid Mech.* **359**, 49–79. (Cited on page 18.)

Lopez, Juan M, Marques, Francisco, Rubio, Antonio M & Avila, Marc 2009 Crossflow instability of finite Bo ¨ dewadt flows : Transients and spiral waves Crossflow instability of finite Bödewadt flows : Transients and spiral waves (November). (Cited on pages 24, 30, 34, and 63.)

Lord, Wesley K., MacMartin, Douglas G. & Tillman, Gregory 2000 Flow control opportunities in gas turbine engines. *Fluids 2000 Conference and Exhibit* (June). (Cited on page 88.)

Lumley, J. L. 1967 The structure of inhomogeneous turbulent flows. *Atmospheric Turbulence and Radio Wave Propagation* . (Cited on page 36.)

Lyapunov, A. M. 1992 The general problem of the stability of motion. *International Journal of Control* **55** (3), 531–534. (Cited on page 58.)

Malik, Mujeeb R 1986 The neutral curve for stationary disturbances in rotating-disk flow. *J. Fluid Mech.* **164**, 275–287. (Cited on page 56.)

Marquet, Olivier, Sipp, Denis & Jacquin, Laurent 2008 Sensitivity analysis and passive control of cylinder flow. *Journal of Fluid Mechanics* **615**, 221–252. (Cited on pages 88, 90, 92, 177, 195, and 196.)

Mathew, Joseph, Foysi, Holger & Friedrich, Rainer 2006 A new approach to LES based on explicit filtering. *International Journal of Heat and Fluid Flow* **27** (4), 594–602. (Cited on pages 37 and 121.)

Mathew, Joseph, Lechner, Richard, Foysi, Holger, Sesterhenn, Joern & Friedrich, Rainer 2003 An explicit filtering method for large eddy simulation of compressible flows. *Physics of Fluids* **15** (8), 2279–2289. (Cited on pages 37 and 121.)

Meliga, P., Chomaz, J. M. & Sipp, D. 2009 Unsteadiness in the wake of disks and spheres: Instability, receptivity and control using direct and adjoint global stability analyses. *Journal of Fluids and Structures* **25** (4), 601–616. (Cited on page 71.)

Mendez, S, Eldredge, J, Nicoud, F, Poinsot, T, Shoeybi, M & Iaccarino, G 2006 Numerical investigation and preliminary modeling of a turbulent flow over a multi-perforated plate. *Center for Turbulence Research Proceedings of the Summer Program* (December 2016), 57–72. (Cited on page 98.)

Merk, Malte, Polifke, Wolfgang, Gaudron, Renaud, Gatti, Marco, Mirat, Clement & Schulle, Thierry 2017 Quantitative Comparisons Between LES Predictions and Experimental Measurements of Sound PressureSpectra in a Confined Swirl Combustor. *AIAA J.* . (Cited on pages 188 and 189.)

Mettot, Clément, Renac, Florent & Sipp, Denis 2014 Computation of eigenvalue sensitivity to base flow modifications in a discrete framework: Application to open-loop control. *Journal of Computational Physics* **269**, 234–258. (Cited on page 90.)

Monkewitz, Peter A., Huerre, Patrick & Chomaz, Jean-Marc 1993 Global linear stability analysis of weakly non-parallel shear flows. *Journal of Fluid Mechanics* **251**, 1–20. (Cited on page 64.)

Nicoud, Franck & Ducros, F 1999 Subgrid-scale stress modelling based on the square of the velocity gradient tensor. *Flow, Turbul. Combust.* **62** (3), 183–200. (Cited on pages 24, 27, and 121.)

Oberleithner, Kilian 2012 On Turbulent Swirling Jets: Vortex Breakdown, Coherent Structures, and their Control. PhD thesis, Technische Universität Berlin. (Cited on page 62.)

Oberleithner, Kilian, Rukes, Lothar & Soria, Julio 2014 Mean flow stability analysis of oscillating jet experiments. *Journal of Fluid Mechanics* **757**, 1–32. (Cited on page 133.)

Odier, Nicolas, Sanjose, Marlene, Gicquel, Laurent, Poinsot, Thierry, Moreau, Stephane & Duchaine, Florent 2019 A characteristic inlet boundary condition for compressible, turbulent, multispecies turbomachinery flows. *Computers & Fluids* **178**, 41 – 55. (Cited on page 118.)

Orr, William M F 1907 The Stability or Instability of the Steady Motions of a Perfect Liquid and of a Viscous Liquid. *Proceedings of the Royal Irish Academy* **27**, 9–68. (Cited on page 62.)

Owen, J. Michael 2011*a* Prediction of ingestion through turbine rim seals-part I: Rotationally induced ingress. *Journal of Turbomachinery* **133** (3), 1–9. (Cited on pages 115 and 128.)

Owen, J. Michael 2011*b* Prediction of ingestion through turbine rim seals-part II: Externally induced and combined ingress. *Journal of Turbomachinery* **133** (3), 31006–1–31006–9. (Cited on page 115.)

Owen, J. Michael 2012 Theoretical modelling of hot gas ingestion through turbine rim seals. *Propulsion and Power Research* **1** (1), 1–11. (Cited on page 115.)

Owen, J M & Rogers, R H 1989 Flow and Heat Transfer in Rotating Disc Systems, Volume 1 : Rotor-stator systems. (Cited on page 18.)

Özkan, M., Thomas, P. J., Cooper, A. J. & Garrett, S. J. 2017 Comparison of the effects of surface roughness and confinement on rotor-stator cavity flow. *Engineering Applications of Computational Fluid Mechanics* **11** (1), 142–158. (Cited on page 90.)

Paranthoën, P., Browne, L. W.B., Le Masson, S., Dumouchel, F. & Lecordier, J. C. 1999 Characteristics of the near wake of a cylinder at low Reynolds numbers. *European Journal of Mechanics, B/Fluids* **18** (4), 659–674. (Cited on page 177.)

Paredes, Pedro, Terhaar, Steffen, Oberleithner, Kilian, Paschereit, Christian Oliver & Theofilis, Vassilis 2016 Global and Local Hydrodynamic Stability Analysis as a Tool for Combustor Dynamics Modeling **138** (February), 1–7. (Cited on page 134.)

Park, D. S., Ladd, D. M. & Hendricks, E. W. 1994 Feedback control of von Kármán vortex shedding behind a circular cylinder at low Reynolds numbers. *Physics of Fluids* **6** (7), 2390–2405. (Cited on page 182.)

Phadke, U.P. & Owen, J.M. 1988 Aerodynamic aspects of the sealing of gas-turbine rotor-stator systems. *International Journal of Heat and Fluid Flow* **9** (2), 98–105. (Cited on page 115.)

Pier, Benoit 2002 On the frequency selection of finite-amplitude vortex shedding in the cylinder wake. *Journal of Fluid Mechanics* **458** (May 2002). (Cited on page 59.)

Pier, Benoît 2003 Finite-amplitude crossflow vortices, secondary instability and transition in the rotating-disk boundary layer. *J. Fluid Mech.* **487**, 315–343. (Cited on page 58.)

Pier, Benoît 2007 Primary crossflow vortices, secondary absolute instabilities and their control in the rotating-disk boundary layer. *Journal of Engineering Mathematics* **57** (3), 237–251. (Cited on page 58.)

Pier, Benoît 2013 Transition near the edge of a rotating disk. *Journal of Fluid Mechanics* **737**, 1–9. (Cited on page 19.)

Pier, Benoit, Huerre, Patrick, Chomaz, Jean Marc & Couairon, Arnaud 1998 Steep nonlinear global modes in spatially developing media. *Physics of Fluids* **10** (10), 2433–2435. (Cited on page 58.)

Pierrehumbert, R, T & Widnall, E 1982 The two- and three-dimensional instabilities of a spatially periodic shear layer **114**. (Cited on page 64.)

Pogorelov, Alexej, Meinke, Matthias & Schr, Wolfgang 2018 Large-Eddy Simulation of the Unsteady Full 3D Rim Seal Flow in a One-Stage Axial-Flow Turbine . (Cited on pages 115, 128, and 138.)

Poinsot, T J & Lele, S K 1992 Boundary Conditions for Direct Simulation of Compressible Viscous Flows. *J. Comput. Phys.* **101**, 104–129. (Cited on page 118.)

Poncet, Sébastien, Serre, Éric & Le Gal, Patrice 2009 Revisiting the two first instabilities of the flow in an annular rotor-stator cavity. *Phys. Fluids* **21**, 1–30. (Cited on page 76.)

Pope, Stephen B 2001 *Turbulent flows*. Cambridge: Cambridge University Press. (Cited on pages 21, 36, and 104.)

Prandtl, L. 1904 Ueber flussigkeitsbewegung bei sehr kleiner reibung. *Verhandl. III, Internat. Math.-Kong., Heidelberg, Teubner, Leipzig, 1904* pp. 484–491. (Cited on page 88.)

Qadri, Ubaid Ali, Mistry, Dhiren & Juniper, Matthew P. 2013 Structural sensitivity of spiral vortex breakdown. *Journal of Fluid Mechanics* **720**, 558–581. (Cited on pages 71, 73, 74, and 83.)

Queguineur, Matthieu, Bridel-Bertomeu, Thibault, Gicquel, Laurent & Staffelbach, Gabriel 2018 Local and Global Stability Analysis of an Academic Rotor/Stator Cavity. *Proceedings of ASME Turbo Expo 2018: Turbine Technical Conference and Exposition* **GT2018-750**. (Cited on pages 67, 92, and 97.)

Queguineur, Matthieu, Bridel-Bertomeu, Thibault, Gicquel, L.Y.M. & Stafflebach, Gabriel 2019 Large eddy simulations and global stability analyses of an annular and cylindrical rotor/stator cavity limit cycles. *Phys. Fluids* (August), 1–40. (Cited on page 68.)

Rannacher, Rolf 2000 Finite Element Methods for the Incompressible Navier-Stokes Equations. *In Fundam. Dir. Math. fluid Mech.* pp. pp. 191–293. (Cited on page 67.)

Rayleigh, John William Strutt 1883 Investigation of the character of the equilibrium of an incompressible heavy fluid of variable density. *Proceedings of the London Mathematical Society* **14**, 170–177. (Cited on page 53.)

Reau, Nicolas & Tumin, Anatoli 2002 Impact of Harmonic Perturbations on a Turbulent Mixing Layer. *European Journal ofMechanics B/Fluids* **21**, 143–155. (Cited on page 133.)

Reynolds, Osborne 1883 An experimental investigation of the circumstances which determine whether the motion of water shall be direct or sinuous, and of the law of resistance in parallel channels. *Philos. Trans. R. Soc.* **174**, 935–982. (Cited on pages 53, 133, and 134.)

Reynolds, WC & Hussain, A 1972 The mechanics of an organized wave in turbulent shear flow. Part 3. Theoretical models and comparisons with experiments. *Journal of Fluid Mechanics* **54**, 263–288. (Cited on page 133.)

Rogers, M H & Lance, G N 1962 The axially symmetric flow of a viscous fluid between two infinite rotating disk. *Proc. R. Soc. A Math. Phys. Eng. Sci.* **266**, 109–121. (Cited on pages 28, 29, 124, 125, 126, and 130.)

Roman, J. E., Campos, C., Romero, E. & Tomas, A. 2019 SLEPc users manual. *Tech. Rep.* DSIC-II/24/02 - Revision 3.11. D. Sistemes Informàtics i Computació, Universitat Politècnica de València. (Cited on pages 67 and 68.)

Roussopoulos, Kimon 1993 Feedback control of vortex shedding at low Reynolds numbers. *J.\ Fluid Mech.* **248**, 267–296. (Cited on page 182.)

Rukes, Lothar, Paschereit, Christian Oliver & Oberleithner, Kilian 2016 An assessment of turbulence models for linear hydrodynamic stability analysis of strongly swirling jets . (Cited on pages 132 and 133.)

Sagaut, Pierre 2006 *Large Eddy Simulation for Incompressible Flows*, 3rd edn. Springer Berlin Heidelberg. (Cited on pages 20, 24, 26, and 119.)

Schlichting, H. & Gersten, K. 2001 *Boundary Layer Theory*, , vol. 9. (Cited on pages 26 and 56.)

Schmid, Peter J 2010 Dynamic mode decomposition of numerical and experimental data. *J. Fluid Mech.* **656**, 5–28. (Cited on pages 27 and 32.)

Schouveiler, L 2001 Instabilities of the flow between a rotating and a stationary disk. *J. Fluid Mech.* **443**, 329–350. (Cited on pages 18, 20, 34, 63, and 124.)

Seguí, Luis M., Gicquel, L. Y.M., Duchaine, F. & De Laborderie, J. 2018 Importance of boundary layer transition in a high-pressure turbine cascade using les. *Proceedings of the ASME Turbo Expo* **2C-2018**, 1–10. (Cited on page 26.)

Serre, Eric, Crespo Del Arco, Emilia & Bontoux, Patrick 2001*a* Annular and spiral patterns in flows between rotating and stationary discs. *J. Fluid Mech.* **434**, 65–100. (Cited on pages 27, 46, and 124.)

Serre, E, Hugues, S, Crespo Del Arco, E, Randriamampianina, a. & Bontoux, P 2001*b* Axisymmetric and three-dimensional instabilities in an Ekman boundary layer flow. *Int. J. Heat Fluid Flow* **22** (1), 82–93. (Cited on pages 24, 30, and 42.)

Serre, Eric, Tuliszka-Sznitko, Ewa & Bontoux, Patrick 2004 Coupled numerical and theoretical study of the flow transition between a rotating and a stationary disk. *Phys. Fluids* **16** (3), 688. (Cited on page 24.)

Séverac, Éric, Poncet, Sébastien, Serre, Éric & Chauve, Marie Pierre 2007 Large eddy simulation and measurements of turbulent enclosed rotor-stator flows. *Phys. Fluids* **19** (8), 1–47. (Cited on pages 18, 20, 21, 24, 28, 29, and 81.)

Sippel, Martin & Klevanski, Josef 2004 Preliminary definition of an aerodynamic configuration for a reusable booster stage within tight geometric constraints. *European Space Agency, (Special Publication) ESA SP* (563), 21–27. (Cited on page 4.)

Smagorinsky, J 1963 General Circulation Experiments with the Primitive Equations I : the basic experiment. *Mon. Weather Rev.* **91** (3), 99–164. (Cited on page 27.)

Smith, Newell H 1947 Exploratory investigation of laminar-boundary-layer oscillations on a rotating disk. *Tech. Rep.* NACA No. 1227. Langley Memorial Aeronautical Laboratory, Langley Field, Va. (Cited on pages 30 and 56.)

Sommerfeld, A 1908 Ein beitrag zur hydrodynamischen erklaerung der turbulenten fluessigkeitsbewegungen. *Proc. 4th Int. Congr. Math. III* **174** (1883), 116–124. (Cited on page 62.)

Stephen, S. O. 2017 Effects of partial slip on viscous instabilities in rotating-disc boundary-layer flows. *8th AIAA Theoretical Fluid Mechanics Conference, 2017* (December), 1–4. (Cited on page 89.)

Stewartson, K 1953 On the flow between two rotating coaxial disks. *Proc. Camb. Philol. Soc.* **49**, 333–341. (Cited on page 18.)

Strykowski, Pj J & Sreenivasan, Kr R 1990 On the formation and suppression of vortex 'shedding' at low Reynolds numbers. *Journal of Fluid Mechanics* **218**, 71–107. (Cited on page 90.)

Stuart, J T 1954 On the effects of uniform high suction on the steady flow of a non-newtonian liquid due to a rotating disk. *Mech. Appl. Maths V* **7** (4), 446–457. (Cited on pages 89 and 99.)

Su, Wen Tao, Li, Xiao Bin, Li, Feng Chen, Wei, Xian Zhu, Zheng, Zhi Ying & Zhang, Xin 2013 Comparisons of les and RANS computations with PIV experiments on a cylindrical cavity flow. *Advances in Mechanical Engineering* **2013**. (Cited on page 21.)

Sutton, George P. & Seifert, Howard S. 1950 *Rocket Propulsion Elements*, 7th edn., , vol. 3. (Cited on page 8.)

Taira, Kunihiko, Brunton, Steven L., Dawson, Scott T. M., Rowley, Clarence W., Colonius, Tim, McKeon, Beverley J., Schmidt, Oliver T., Gordeyev, Stanislav, Theofilis, Vassilios & Ukeiley, Lawrence S. 2017 Modal Analysis of Fluid Flows: An Overview pp. 1–43. (Cited on pages 32 and 36.)

Tammisola, O & Juniper, Matthew P. 2016 Coherent structures in a swirl injector at Re = 4800 by nonlinear simulations and linear global modes. *J. Fluid Mech.* **792**, 620–657. (Cited on page 133.)

Tatro, P R & Mollo-Christensen, E L 1967 Experiments on Ekman layer instability. *J. Fluid Mech.* **28** (03), 531–543. (Cited on page 58.)

Taylor, C. & Hood, P. 1973 A Numerical Solution of the Navier-Stokes Equations Using the Finite Element Technique. *Computers and Fluids* **1** (1), 73–100. (Cited on page 67.)

Theofilis, Vassilios 2011 Global Linear Instability. *Annual Review of Fluid Mechanics* **43** (1), 319–352. (Cited on pages 36 and 64.)

Thomas, Christian & Davies, Christopher 2010 The effects of mass transfer on the global stability of the rotating-disk boundary layer. *Journal of Fluid Mechanics* **663**, 401–433. (Cited on page 89.)

Thomas, Christian & Davies, Christopher 2013 Global stability of the rotating-disc boundary layer with an axial magnetic field. *Journal of Fluid Mechanics* **724**, 510–526. (Cited on page 89.)

Tuliszka, Ewa, Serre, Eric & Bontoux, Patrick 2002 On the nature of the boundary layers instabilities in a flow between a rotating and a stationary disc. *Comptes Rendus M{é}canique* **330** (2), 91–99. (Cited on page 63.)

Tuliszka-Sznitko, E & Zielinski, Artur 2007 Instability of the flow in rotating cavity. *J. Theor. Appl. Mech.* **45** (3), 685–704. (Cited on page 24.)

Tuliszka-Sznitko, E, Zielinski, A & Majchrowski, W 2009 Large Eddy Simulation of transitional flows in rotor/stator cavity. *Arch. Mech.* **61** (2), 95–120. (Cited on page 24.)

Turton, Sam E., Tuckerman, Laurette S. & Barkley, Dwight 2015 Prediction of frequencies in thermosolutal convection from mean flows. *Physical Review E - Statistical, Nonlinear, and Soft Matter Physics* **91** (4), 1–10. (Cited on pages 59 and 132.)

Venkatachala, B. J. & Nath, G. 1980 Mass transfer effects on the generalised vortex flow over a stationary surface with or without magnetic field. *Proceedings of the Indian Academy of Sciences Section C: Engineering Sciences* **3** (3), 211–223. (Cited on pages 89 and 101.)

Viazzo, Stéphane, Poncet, Sébastien, Serre, Eric, Randriamampianina, Anthony & Bontoux, Patrick 2012 High-order Large Eddy simulations of confined rotor-stator flows. *Flow, Turbul. Combust.* **88** (1-2), 63–75. (Cited on page 18.)

Von Kármán, Theodore 1921 Über laminare und turbulente reibung. *Zeitschrift für Angew. Math. und Mech.* **1** (4), 233–251. (Cited on page 55.)

Williamson, C. H.K. 1988 Defining a universal and continuous Strouhal-Reynolds number relationship for the laminar vortex shedding of a circular cylinder. *Physics of Fluids* **31** (10), 2742–2744. (Cited on pages 177 and 178.)

Wilson, Lynn O. & Schryer, N. L. 1978 Flow between a stationary and a rotating disk with suction. *Journal of Fluid Mechanics* **85** (3), 479–496. (Cited on page 90.)

Wu, Xiaohua & Squires, Kyle D. 2000 Prediction and investigation of the turbulent flow over a rotating disk. *Journal of Fluid Mechanics* **418**, 231–264. (Cited on page 21.)

Appendix

Appendix A

Local stability governing equations of enclosed cavity

A.1 General Local stability equations

The general stability equations in cylindrical coordinate corresponding to the dispersion problem Eq. (4.3.9) are:

$$\left(\frac{1}{r}+i\alpha\right)\hat{u}_r+\frac{mi}{r}\hat{u}_\theta+\hat{u}_z^{'}=0, \tag{1.1.1}$$

$$\begin{aligned}\nu\hat{u}_r^{''}+\left(\omega i-\alpha^2\nu-\frac{\nu}{r^2}m^2+\frac{\nu}{r}\alpha-\frac{i\nu}{r^2}-U_bi\alpha-\frac{V_bmi}{r}\right)\hat{u}_r-W_b\hat{u}_r^{'}=\\ -\hat{u}_zU_b^{'}+\left(\frac{2V_b}{r}-\frac{\nu im}{r^2}\right)\hat{u}_\theta+\alpha i\hat{p},\end{aligned} \tag{1.1.2}$$

$$\begin{aligned}\nu\hat{u}_\theta^{''}+\left(\omega i-\alpha^2\nu-U_bi\alpha-\frac{U_b}{r}-\frac{V_bim}{r}-\frac{m^2\nu}{r^2}+\frac{i\alpha\nu}{r}-\frac{\nu}{r^2}\right)\hat{u}_\theta-W_b\hat{u}_\theta^{'}=\\ +\frac{\hat{p}}{r}im-V_b^{'}\hat{u}_z-\frac{V_b}{r}\hat{u}_r,\end{aligned} \tag{1.1.3}$$

$$\begin{aligned}\nu\hat{u}_z^{''}+\left(\omega i-\alpha^2\nu+\frac{i\alpha\nu}{r}-\frac{m^2\nu}{r^2}-U_bi\alpha-W_b^{'}-\frac{V_b}{r}im\right)\hat{u}_z-W_b\hat{u}_z^{'}=\\ -\frac{\hat{p}^{'}}{r},\end{aligned} \tag{1.1.4}$$

where $'$ denotes the partial derivative with respect to z and ν the kinematic viscosity.

A.2 Local stability equations of the BEK model

As stated Chap. 4, the stability of the BEK flows has always been an essential step to understand more complex rotating flows like the one encountered in cavities. The local stability analysis of the BEK family has received recently a particular attention in Bridel-Bertomeu (2016). Even if the structures of boundary layers and its transition is not perfectly understood yet, some studies try to find solutions to stabilize this kind of flows. As an example, recently, Abdulameer *et al.* (2016) have investigated the stability of the BEK boundary layer family under stationary convective disturbances for shear thinning power-law fluids. They showed that this kind of fluid has a stabilizing effect on both type I and type II instabilities. On the other hand, Alveroglu *et al.* (2016) looked at the impact of the roughness (grooves) on the stability of the BEK family. He concluded that the surface roughness is an effective passive flow control mechanisms for engineering flows like rotor/stator systems.

Governing equations

This paragraph sums up the construction of BEK family equations with a local stability approach. For the problem under consideration, the local Reynolds number defined in Sec. 4.2 is needed and is usually constructed using :

$$Re_\delta = r_a Ro \tag{1.2.1}$$

where r_a corresponds to the dimensionless radius where the local stability is applied.

The method described in the previous section is used here to compute the perturbation equations of the BEK model. To do so, the dimensionless form of the mean flow velocity $[U^*, V^*, W^*]$ and pressure P^* profiles,

$$\begin{cases} U^*(z^*) &= \dfrac{U}{r\Delta\Omega} = \dfrac{U}{r\tilde{\Omega}Ro} \\ V^*(z^*) &= \dfrac{V}{r\Delta\Omega} = \dfrac{V}{r\tilde{\Omega}Ro} \\ W^*(z^*) &= \dfrac{W}{L\Delta\Omega} = \dfrac{U}{L\tilde{\Omega}Ro} \\ P^*(z^*) &= \dfrac{P}{\rho L\Delta\Omega^2} = \dfrac{P}{\rho L\tilde{\Omega}^2 Ro^2} \end{cases} \tag{1.2.2}$$

where z^* stands for the axial coordinate normalized by $L = (\nu/\Omega)^{1/2}$.

are introduced in the momentum and continuity equations Eqs. (4.3.1)-(4.3.4) and linearized around the base flow. To validate the separability of the equations in r , θ and

t, the parallel flow approximation is applied. This assumption is equivalent to replacing r by Re_δ in the resulting equations and neglecting the Re_δ^{-2} or smaller terms.

Finally, the normal mode formulation of (4.3.16) is introduced to obtain the following set of equations:

$$\left\{\begin{aligned}
&\left(i\alpha + \frac{Ro}{Re_\delta}\right)\hat{u}_r + \beta\hat{u}_\theta - \hat{u}_z' i = 0,\\[2ex]
&\hat{u}_r'' - \left(\alpha^2 + \beta^2 + iRe_\delta(\alpha U_b + \beta V_b) - iRe_\delta\omega + RoU_b + T_3\right)\hat{u}_r - RoW_b\hat{u}_r'\\
&\qquad\qquad = i(2RoV_b + Co + T_2)\hat{u}_\theta - iU_b' Re_\delta\omega + i\alpha Re_\delta p,\\[2ex]
&\hat{u}_\theta'' - \left(\alpha^2 + \beta^2 + iRe_\delta(\alpha U_b + \beta V_b) - iRe_\delta\omega + RoU_b + T_3\right)\hat{u}_\theta - RoW_b\hat{u}_\theta'\\
&\qquad\qquad = i(2RoV_b + Co + T_2)\hat{u}_r - iV_b' Re_\delta\omega + i\beta Re_\delta p,\\[2ex]
&\hat{u}_z'' - \left(\alpha^2 + \beta^2 + iRe_\delta(\alpha U_b + \beta V_b) - iRe_\delta\omega + RoW_b' + T_1\right)\hat{u}_z - RoW_b\hat{u}_z'\\
&\qquad\qquad = Re_\delta p,
\end{aligned}\right. \tag{1.2.3}$$

where $\beta = m/Re_\delta$ and $\qquad T_1 = \dfrac{i\alpha}{Re_\delta}, \qquad T_2 = -\dfrac{2im}{Re_\delta^2}, \qquad T_3 = \dfrac{1}{Re_\delta^2} - T_1$

Recent studies on rotating boundary layers coupled with stability analysis have been able to find new properties and deeper understanding about turbulence transition. Davies & Carpenter (2003) studied the effect of spatial inhomogeneity on the global response of the locally absolutely unstable flow. They showed that for both the Von karman and Ekman layers the laminar to turbulent transition obtained experimentally corresponds to the onset of absolute instabilities with very close Reynolds Number.

However they have also demonstrated that convective behavior dominates at all Reynolds numbers even for strong absolutely unstable regions and is the main source of the global behavior.

A.3 Local stability equations of an enclosed rotor/stator cavity

For these specific cases, one defines the interdisk distance h as the reference scale and the dimensionless radius $r_a = r/h$ the position where the local stability analysis is conducted. The velocity scale will be $r_a\Omega_d$, while the time scale is $h/r_a\Omega_d^*$ and $\rho^* r_a^2 \Omega_d^2$ is the reference pressure. One recalls that in that case the local Reynolds number is defined as $Re = r_a = r/h$ and the global Reynolds number is Re_h. With these definitions, the system reads,

$$\begin{cases} \left(i\alpha + \dfrac{1}{r}\right)\hat{u}_r + \beta\hat{u}_\theta - i\partial_z\hat{u}_z = 0, \\ \\ \partial_{zz}\hat{u}_r - \left(\alpha^2 + \beta^2 + irRe_h\left(\alpha U_b + \beta V_b\right) - irRe_h\omega + T_3\right)\hat{u}_r - \sqrt{Re_h}W_b\partial_z\hat{u}_r \\ \qquad = i(2Re_h + 2Re_hV_b + T_2)\hat{u}_\theta - ir\partial_zU_bRe_h\omega + i\alpha rRe_hp, \\ \\ \partial_{zz}\hat{u}_\theta - \left(\alpha^2 + \beta^2 + irRe_h\left(\alpha U_b + \beta V_b\right) - irRe_h\omega + Re_hU_b + T_3\right)\hat{u}_\theta - \sqrt{Re_h}W_b\partial_z\hat{u}_\theta \\ \qquad = i(2Re_hV_b - 2Re_h + T_2)\hat{u}_r - ir\partial_zV_bRe_h\omega + i\beta rRe_hp, \\ \\ \partial_{zz}\hat{u}_z - \left(\alpha^2 + \beta^2 + irRe_h\left(\alpha U_b + \beta V_b\right) - irRe_h\omega + Ro\partial_zW_b + T_1\right)\hat{u}_z - \sqrt{Re_h}W_b\partial_z\hat{u}_z \\ \qquad = rRe_hp, \end{cases} \tag{1.3.1}$$

where $\beta = m/Re_\delta$, $T_1 = \dfrac{i\alpha}{r}$, $T_2 = -\dfrac{2im}{r^2}$ and $T_3 = \dfrac{1}{r^2} - T_1$. ∂_z and ∂_{zz} are respectively the first and second derivative with respect to z.

Based on this local approach all reported mode features can be predicted as demonstrated in Bridel-Bertomeu (2016) by all the couples (α, m) and for a fixed interdisk Reynolds Number Re_h.

A.4 Global stability equations of an enclosed rotor/stator cavity

Introducing the normal modes in the linearized Naviers-Stokes equations, one obtains a dispersion problem of the form:

$$\left\{\begin{array}{l}
\left(\partial_r + \frac{1}{r}\right)\hat{u}_r + i\frac{m}{r}\hat{u}_\theta + \partial_z\hat{u}_z = 0, \\
\\
\left(-i\omega + U_b\partial_r + i\frac{m}{r}V_b + W_b\partial_z + \partial_r U_b - \frac{1}{Re}\left(\partial_{zz} - \frac{m^2}{r^2} + \partial_{rr} + \frac{\partial_r}{r} - \frac{1}{r^2}\right)\right)\hat{u}_r \\
\qquad\qquad + \frac{2m}{r^2 Re}\hat{u}_\theta + \partial_z U_b\hat{u}_z + \partial_r\hat{p} = 0 \\
\left(-i\omega + U_b\partial_r + i\frac{m}{r}V_b + W_b\partial_z + \partial_r U_b - \frac{1}{Re}\left(\partial_{zz} - \frac{m^2}{r^2} + \partial_{rr} + \frac{\partial_r}{r} - \frac{1}{r^2}\right)\right)\hat{u}_\theta \\
\qquad\qquad - \frac{2m}{r^2 Re}\hat{u}_r + \partial_r V_b\hat{u}_r + \partial_z V_b\hat{u}_z + i\frac{m^2}{r^2}\hat{p} = 0 \\
\left(-i\omega + U_b\partial_r + i\frac{m^2}{r^2}V_b + W_b\partial_z + \partial_z W_b + \frac{1}{Re}\left(\partial_{zz} + \frac{m^2}{r^2} - \partial_{rr} + \frac{\partial_r}{r}\right)\right)\hat{u}_z \\
\qquad\qquad \partial_r W_b\hat{u}_r + \partial_z\hat{p} = 0,
\end{array}\right. \tag{1.4.1}$$

where ∂_r and ∂_{rr}, are respectively the first and second derivatives respectively with r. This set of equations can be solved numerically as before.

Appendix B

DMT/DMTC validations and sensitivity analysis

A.1 Validation test cases of the Dynamical Mode Tracking (DMT)

This section evaluates the efficiency of the method through different types of CFD examples. The first case is a $1D$ closed cavity within which 3 linearly independent (low amplitude) acoustic eigenmodes are present. The purpose of this simple case is to show the capability of DMT to identify these modes. The second example focuses on the vortex shedding of a cylinder wake. The specific test is used to compared DMD and DMT. For both cases, a sensitivity analysis to the bandwidth filter β is provided to illustrate its impact on found features.

A.1.1 Case 1: $1D$ cavity problem

The test case corresponds to a $1D$ cavity where acoustic eigenmodes are added at initialization and then left free to resonate into a closed domain. Here, Euler equations are used in place of NS to comply with the original linear and isentropic assumptions: *i.e.* without dissipation. For the CFD prediction, the cell centered scheme TTGC (Colin & Rudgyard (2000)) (third order in time and space) is chosen to reduce numerical dissipation as much as possible. For this specific numerical experiment, the length of the cavity is unity ($l = 1$ m) with no mean flow and a uniform mean atmospheric pressure. The modes initially imposed are the cavity $1^{st}, 3^{rd}$ and 5^{th} eigenmodes. They are initialized with the same velocity amplitude $\frac{p'}{\rho c}$, where c stands for the speed of sound so that at $t^* = \frac{t\,c}{l} = 0$,

$$u(x) = \frac{p'}{\rho c}\left[\sin(\pi x^*) + sin(\pi 3x^*) + sin(\pi 5x^*)\right], \tag{2.1.1}$$

with $p' = 10\,Pa$ the acoustic pressure fluctuations and $x^* = \frac{x}{l}$ the 1D coordinate. For this specific problem, the eigen frequencies follow,

$$f^{(n)} = n\,c/2\,l \;\; n = 1, 3, 5. \tag{2.1.2}$$

Figure B.1(a) shows the 3 mode velocity amplitudes imposed at $t^* = 0$. The resulting spectrum issued by the temporal recording of the flow issued by CFD at the probe S_{AC} (all mode common velocity antinode $x^* = 0.5$ Fig. B.1(a)) is shown in Fig. B.1(b) for the time duration $t^* = [0, 70]$. All frequencies f^* ($f/f^{(1)}$) between 0 and 5 are displayed in this figure and the velocity has been normalized by the initial velocity amplitude $\frac{p'}{\rho c}$ to ease the results visualization. The spectrum obtained confirms the expected results and a low dissipation level of the CFD simulation. On this basis, DMT is first used to extract the modes from the total field issued by the CFD simulation. To do so, a 2^{nd} order ordinary differential equation (Eq. (3.3.4)) is defined for each of the three modes and simultaneously activated at $t^* = 0$ for all points of the computational domain. In this case, using Eq. (3.3.4), each parameter couple is set to $(\beta^{(n)} = 40, \omega_0^{(n)} = 2\pi\, f^{(n)})$.

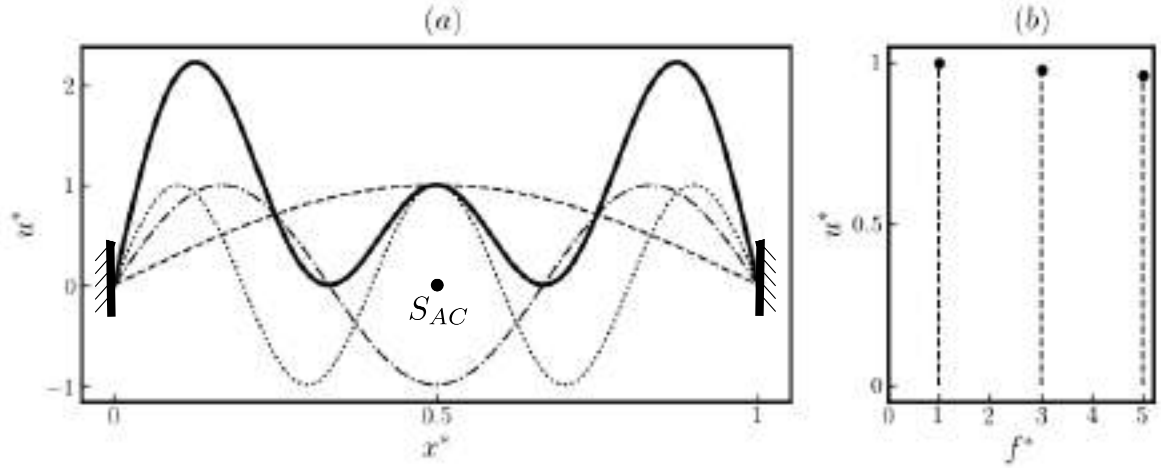

Figure B.1 – Modes description: *(a)* Spatial distribution of normalized initial velocity profile u^* with (- -), the fundamental mode ($f^{(1)}$), (-·-), the 3^{rd} harmonic ($f^{(3)}$), (·····), the 5^{th} harmonic ($f^{(5)}$) and (—), the total resulting velocity field. S_{AC} corresponds to a probe located at the common mode antinode $x^* = 0.5$ *(b)* Fast Fourier Transform (FFT) at the probe S_{AC} between $t^* = [0, 70]$.

Note that for this particular case where $\beta^{(n)} = 40$, the frequency bandwidth of the associated filter is $9.5Hz$. Likewise, from Eq. (3.3.7), $\tau^*_{90\%} = \tau_{90\%} c/l = 26.2$.

First the system response and convergence is illustrated on Fig. B.2 by showing the differential system evolution as a function of time for the three modes. Here the diagnostic relies on the evaluation of the non dimensionalized velocity fluctuation, $u^*_n = (u - \bar{u}^{(n)})/\frac{p'}{\rho c}$, at the probe S_{AC} as a function of normalized time, t^*. For all three modes, associated velocity fluctuations magnitude is in good agreement with the initialization, confirming the capacity of DMT to recover the right modes in terms of amplitude as time advances. In fact, $\tau^*_{90\%}$ is found equal to 26.2 which is in agreement with the analytical expression Eq. (3.3.7) (26.39). Fig. B.2 also confirms that the speed convergence is independent of the frequency of the mode to be tracked. In terms of spatial shape, Fig. B.3, each mode structure is captured in approximately 2 periods and can be compared at the limit cycle of the differential systems, *i.e*: $t^* = 71.5$ to the theoretical solution.

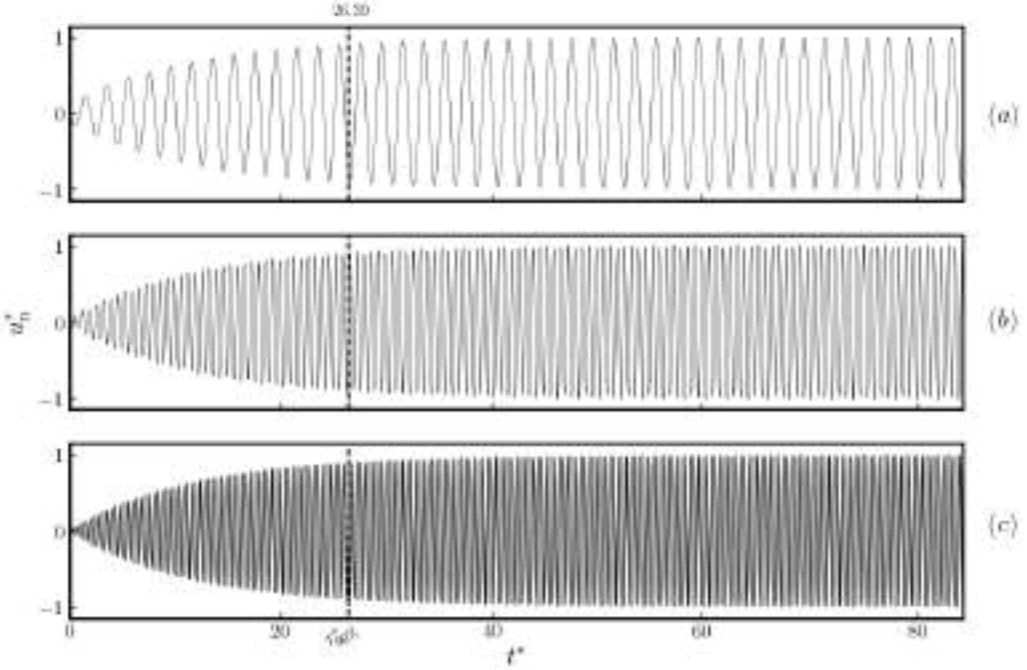

Figure B.2 – Mode tracking: Evolution of the normalized fluctuating velocity profile u_n^* over time of *(a)* the fundamental mode ($f^{(1)}$), *(b)* the 3^{rd} harmonic ($f^{(3)}$), *(c)* the 5^{th} harmonic ($f^{(5)}$), at probe S_{AC}.

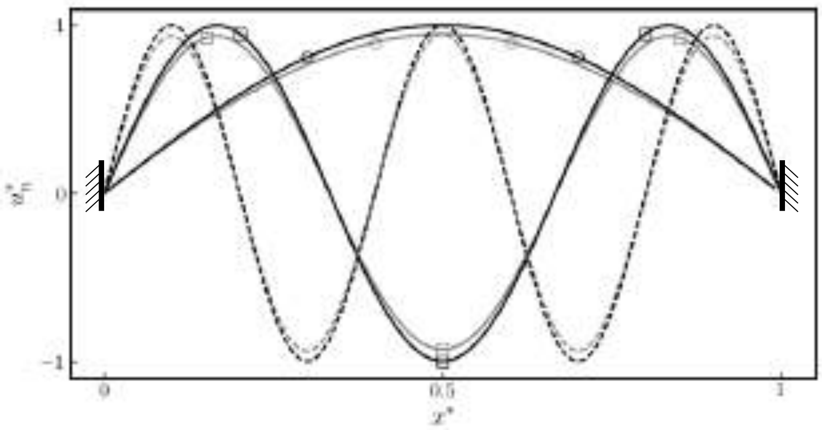

Figure B.3 – Retrieved spatial structure of the modes: Comparison between the exact solution *(black)* and results of DMT *(gray)* at $t^* = 71.5$. Adimensionlized fluctuating velocity profile over time of (-⊖-), the fundamental mode ($f^{(1)}$),(-⊟-), the 3^{rd} harmonic ($f^{(3)}$), (- -) and the 5^{th} harmonic ($f^{(5)}$).

Again excellent agreement is found and differences can be attributed to the nature of any numerical scheme or to the bandwidth of the band-stop filter as designed here. Indeed, contrary to the ideal filter shown in Fig. 3.2, even far from the central frequency f_0 the gain of the filter is never equal to zero which can impact the amplitude of the modes obtained. This impact is for example observed in Fig. B.2(b) where the envelop of the reported signal is slightly modulated by the fundamental frequency.

Concerning the associated CPU coast, the computation has been realized on a mesh composed of 1998 cells (3000 nodes) using 2 Intel Xeon E5-2605 24 cores processors running at 2.4Ghz. For 3 tracked frequencies, the overhead for this case is an increase by 1.1% in comparison to the simulation without DMT. Naturally, the problem size is reduced here which coincides with a low total cost. A more complex $2D$ flow problem is addressed in Sec. A.1.2 in order to evaluate the method more significantly, as well as its cost.

An explicit assessment of the effect of the filter bandwidth is investigated in the following by systematically changing the value of β to be $[10, 20, 40, 60, 100]$. To evaluate the temporal response of the system for all cases, one defines $Ev^{(n)}$ as the kinetic energy of the n^{th} mode,

$$Ev^{(n)} = \int_V \rho \frac{(u - \bar{u}^{(n)})^2}{2} dv \;\; n = 1, 3, 5 \; , \tag{2.1.3}$$

and is then followed in time where V is the "volume" of the computational domain. Note that by construction, at $t^* >> \tau^*_{90\%}$, all modes should have the same kinetic energy noted hereafter Ev_0.

The adimensionalized energy envelop $Ev^{(n)}/Ev_0$ is given in Fig. B.4 for 5 values of β. As anticipated, the time needed to converge increases when reducing the filter bandwidth. Note that in order to capture 90% of all mode amplitudes functions of β, simulations are here 4 times longer than the one presented in Fig. B.2. From such a test, one can conclude that, for high values of β $[40, 60, 100]$, the three modes are well retrieved. Note that, the drawback of using high β values is that non negligible gains for frequencies around the one of interest exist. As a consequence, the tracked mode can be slightly modulated by the surrounding frequencies if present.

Figure. B.4(a) and B.4(b) indicate that the amplitudes of the fundamental and the 3^{rd} harmonic are not necessarily well retrieved. This is attributed to the fact that the gain of the associated band-stop filters is not low enough around the frequency of interest. Because the 5^{th} harmonic has a frequency 5 times higher than the fundamental frequency, it is easier to obtain a more precise estimate of its frequency through the use of a FFT applied to the CFD prediction. The final shapes of the 3 different modes for all β are displayed in Fig. B.5. Overall, all global shapes are well retrieved for all the cases, the amplitude presenting potential discrepancies as detailed before.

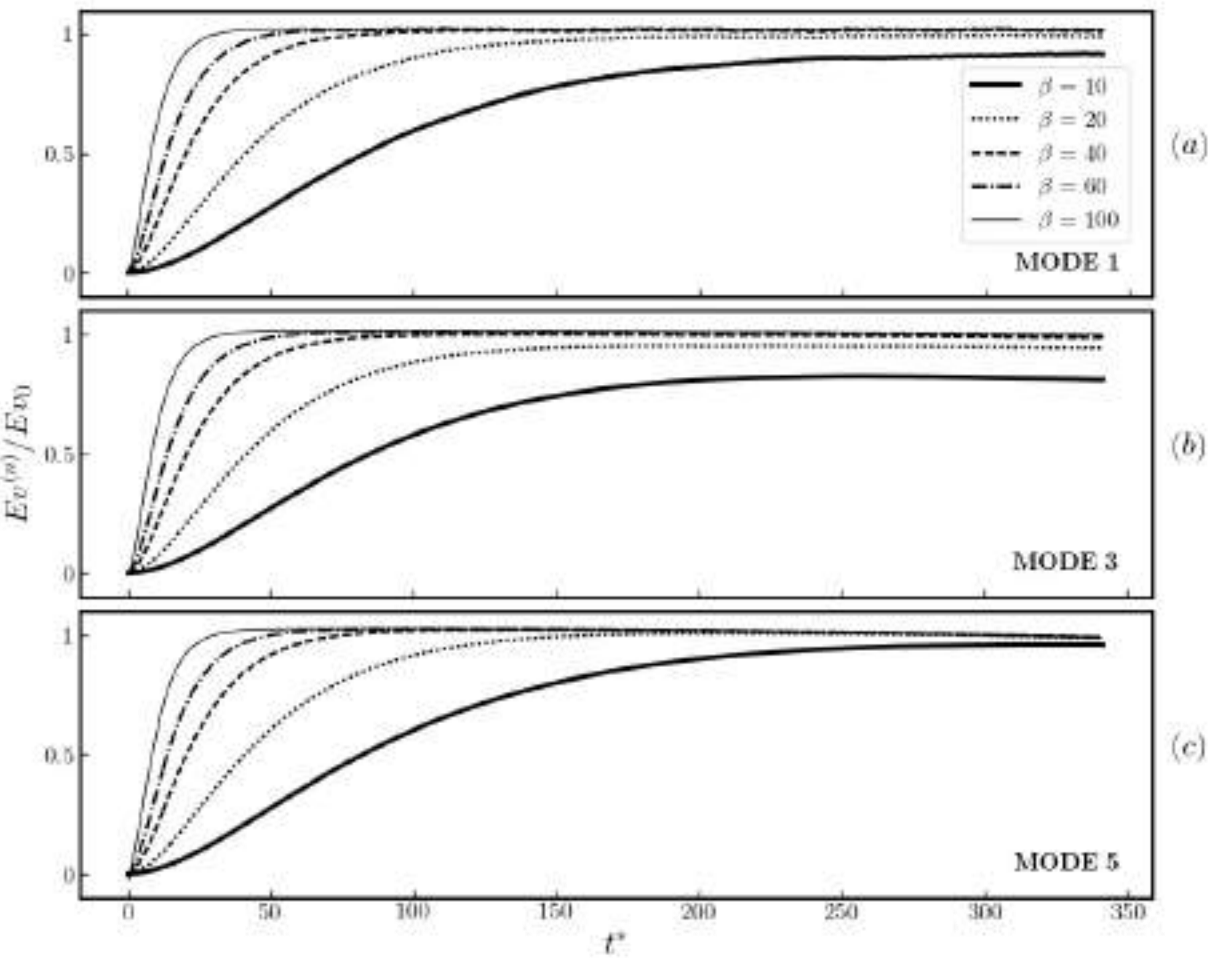

Figure B.4 – Impact of the bandwidth filter β: Normalized kinetic energy integrated over the domain over time with *(a)* the fundamental mode ($f^{(1)}$), *(b)* the 3^{rd} harmonic ($f^{(3)}$), *(c)* the 5^{th} harmonic ($f^{(5)}$). 5 values of β have been tested: $\beta = 10$ (━), $\beta = 20$ (·····), $\beta = 40$ (- -), $\beta = 60$ (·-·), $\beta = 100$ (—).

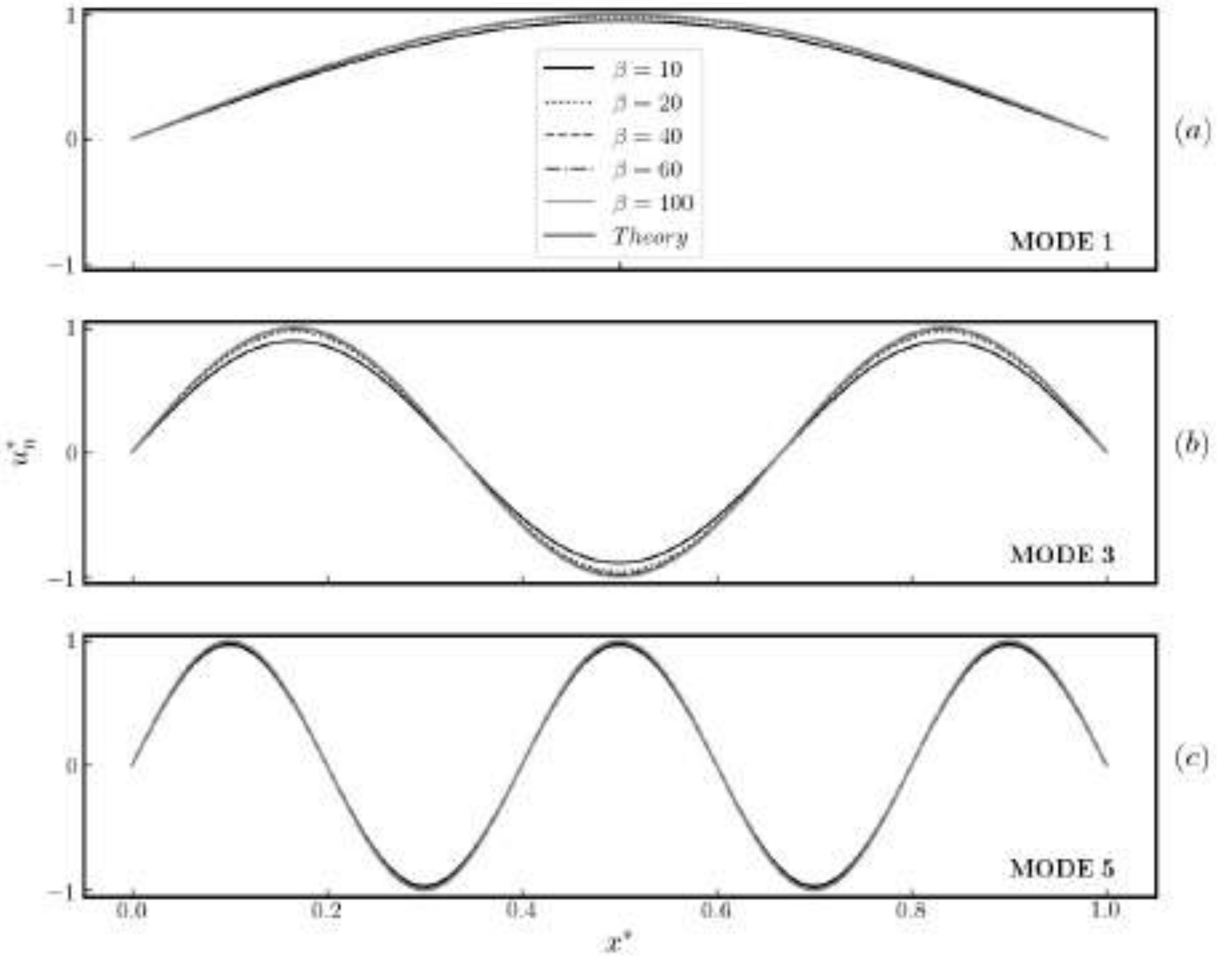

Figure B.5 – Impact of the bandwidth filter β on the final modes shape: Normalized velocity over the domain with *(a)* the fundamental mode ($f^{(1)}$), *(b)* the 3rd harmonic ($f^{(3)}$), *(c)* the 5th harmonic ($f^{(5)}$). 5 values of β have been tested: $\beta = 10$ (▬), $\beta = 20$ (·····), $\beta = 40$ (- -), $\beta = 60$ (·-·), $\beta = 100$ (—). The maximum amplitude found after convergence of the filter is displayed for each mode.

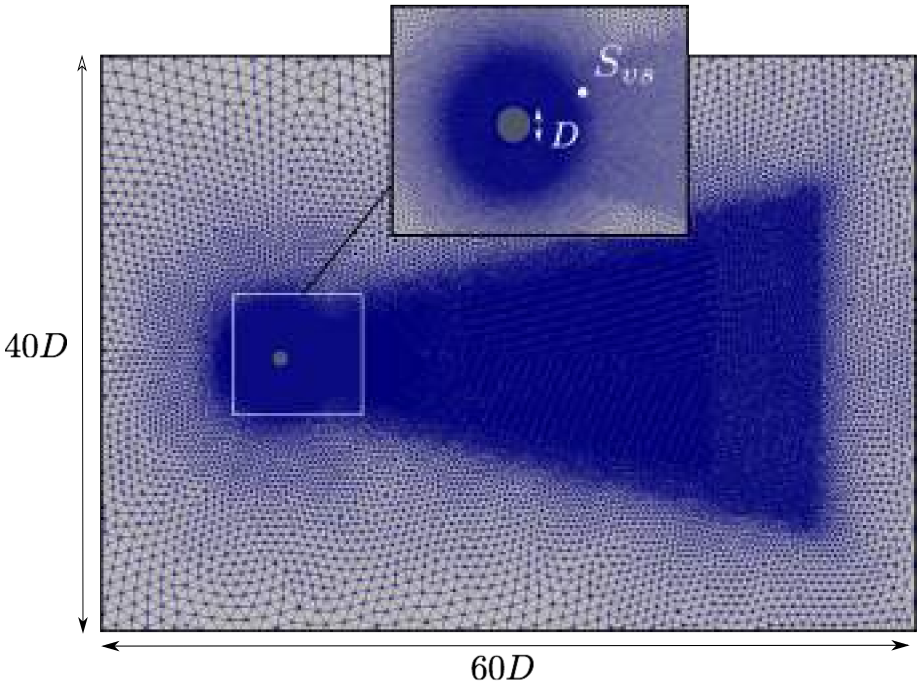

Figure B.6 – Flow domain and mesh used for the DNS flow prediction. S_{vs} corresponds to a probe used to evaluate the convergence of DMT.

A.1.2 Case 2: Cylinder wake flow instability

DMT is now applied to the fundamental flow dynamic problem that is the vortex shedding of a cylinder wake. This system is still an open subject of research and often used as a classical test for new modal analyses or flow control (Bagheri (2013); Marquet *et al.* (2008)). Figure B.6 shows the computational domain and mesh used for the NS simulation of the present problem. The Reynolds number is here defined as $Re_D = U_0 D/\nu$ where ν is the kinematic viscosity, U_0 the undisturbed mean velocity and D the cylinder diameter. The specific value of $Re_D = 56$ is selected as it is close to the onset of instability and for which a large amount of data is available in the literature (Kovasznay (1949); Paranthoën *et al.* (1999); Williamson (1988)). Coordinates and time are normalized respectively by D and U_0/D so that $(x^*, y^*) = (x/D, y/D)$ and $t^* = tU_0/D$.

Flow predictions obtained by use of DNS (without activation of DMT) are first compared to the Kovasznay experiment (Kovasznay (1949)). Figure B.7 shows the comparison of axial mean velocity profiles $U(y^*)$ normalized by U_0, *i.e* $U^*(y^*) = U/U_0$ for several axial positions: $x^* = 2, 3.5, 5, 8, 12, 20, 40$. Good general agreement is found. Discrepancies at $x^* = 40$ are due to the fact that this axial coordinate corresponds exactly to the limit of the domain where an interaction of the structures with boundary condition is present. Similarly, the non-dimensionalized Root Mean Square (RMS), $100U_{RMS}/U_0$ noted u'^*, are compared on Fig. B.8 with the same conclusion. Note that room for improvement is noticeable but considered outside the scope of the present discussion. To complement this finding, the Strouhal number of the vortex shedding defined as $St(Re_D) = fD/U_0$ is reported in Table B.1 and compares within 1% to experimental findings. In this case, f

Source	$St(56)$
Present work	0.130
Williamson Williamson (1988)	0.1316
Kovasznay Kovasznay (1949)	0.1306

Table B.1 – Comparison of the Strouhal number St obtained with the present work and from literature.

is retrieved directly from the FFT of a numerical probe located in the cylinder wake and noted S_{vs} in Fig. B.6.

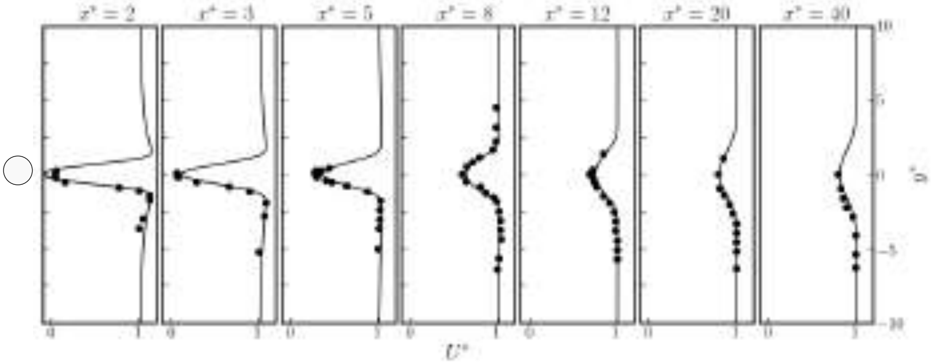

Figure B.7 – Mean axial velocity profile U^* at $x^* = 2, 3.5, 5, 8, 12, 20, 40$ with (●) Kovasznay experiments and (—) present study.

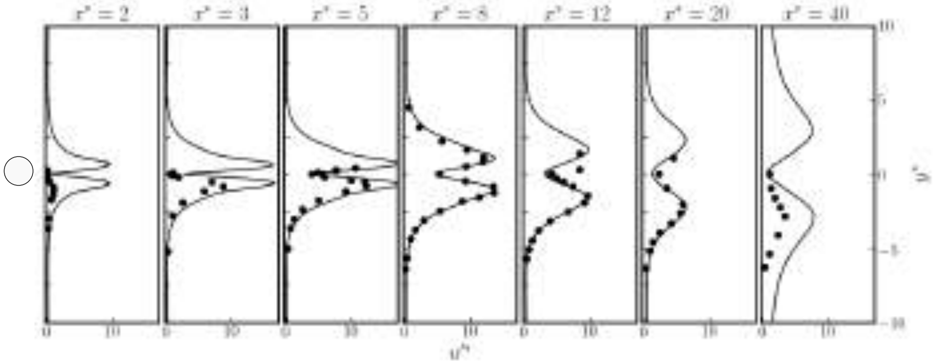

Figure B.8 – RMS axial velocity profile u'^* at $x^* = 2, 3.5, 5, 8, 12, 20, 40$ with (●) Kovasznay experiments and (—) present study.

DMT is now applied for the reported Strouhal number along with $\beta = 40$ to evaluate the capacity of the approach in retrieving this feature. Note that with these parameters, the associated filter is selective enough to avoid capturing any harmonics of the primary instability. The probe S_{vs} is first used to analyse the filter convergence, Fig. B.9. The axial velocity associated to the vortex shedding is defined as u^*_{vs} so that $u^*_{vs} = \frac{u-\bar{u}}{(u-\bar{u})_{max}}$. 90% of the vortex shedding amplitude at this station is retrieved after a $t^*_{90\%} = 187.5$ which is in good agreement with the expression derived in Sec. (3.3) which yields $t^*_{90\%} = 191.9$. In parallel and for comparison, a series of flow snapshots extracted from the CFD simulation are gathered and analyzed *a posteriori* with DMD. For this latter, only a small region around the cylinder wake is retained to avoid any noise issues, a problem *a priori* not present with DMT as parameterized here. Figure B.10 shows a comparison of the mode shapes reported by DMD (that also finds the frequency contrarily to DMT) and DMT with on the left, the axial velocity and on the right, the transverse velocity component. Both velocity fields are for each case normalized by their respective peak values. Such a comparison confirms that DMT and DMD are in full agreement when it comes to the spatial capturing of the instability: *i.e.* the vortex shedding.

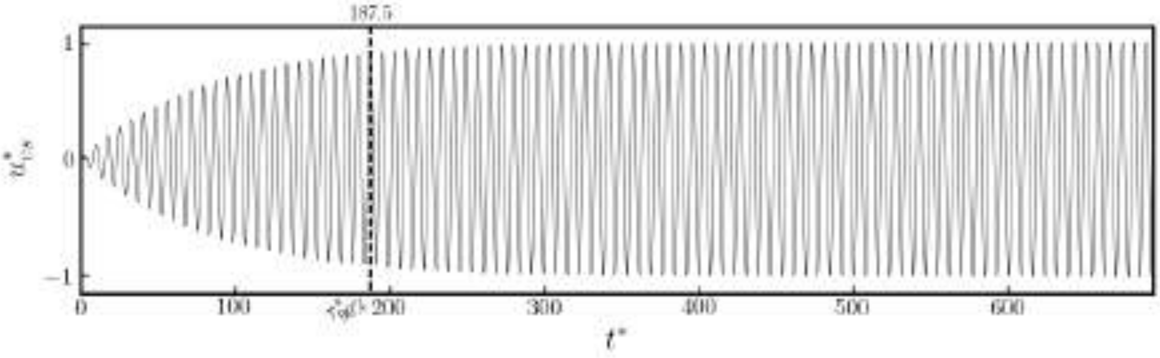

Figure B.9 – Mode tracking: Evolution of the normalized axial velocity u^*_{vs} associated to the vortex shedding frequency at the probe S_{vs}.

In terms of added computational cost, contrarily to the previous case, the current simulation is obtained with a highly refined $2D$ mesh composed of $159,000$ cells ($90,000$ nodes). If simulated by use of 2 Intel Xeon E5-2605 24 cores processors running at 2.4Ghz, the total CPU cost obtained for the results exposed in Fig. B.10 is $4.3h - CPU$. Activating DMT with only one tracked frequency results for this problem into an 1.1% increase of the total CPU cost. Just like for the acoustic cavity case, a sensitivity of the mode amplitude and its convergence to bandwidth filter variations is realized. Results are displayed in Fig. B.11 for 4 values of β $[10, 40, 60, 100]$. Note that for all these tests, the simulation time prior to the activation of DMT has been long enough to obtain a precise frequency of the vortex shedding and a well established limit cycle. As a consequence, for any β the expected kinetic energy of the mode is retrieved. This flow has furthermore

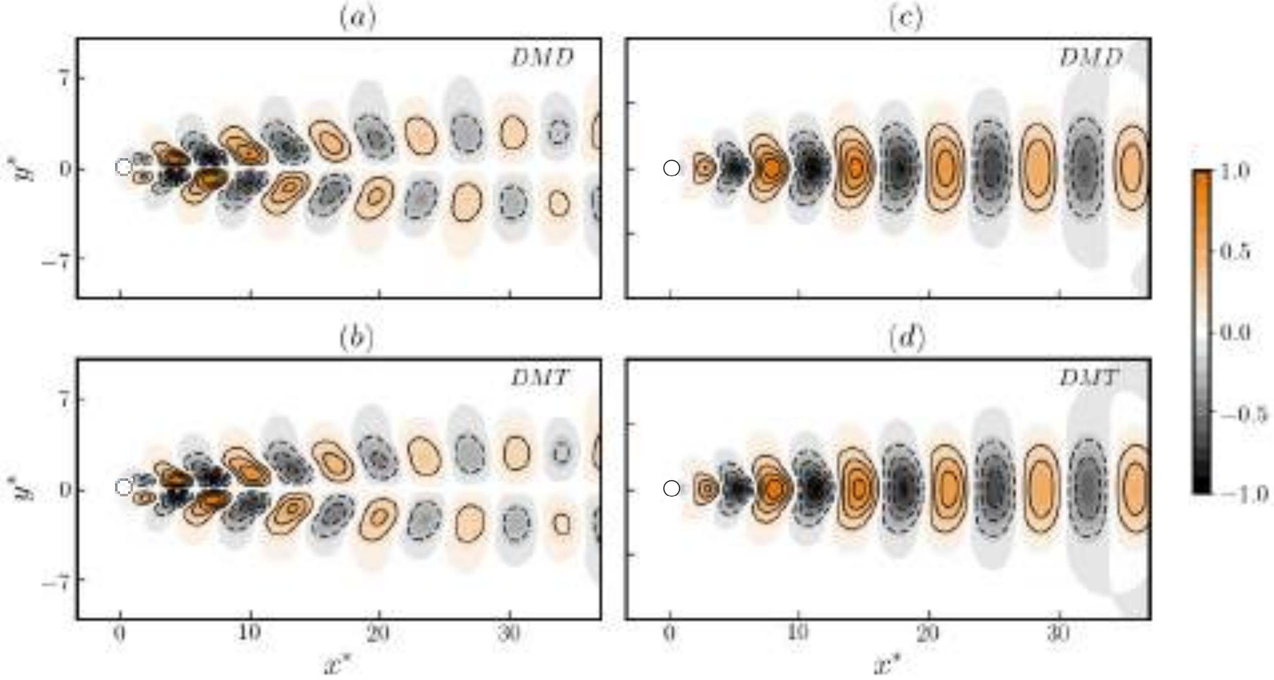

Figure B.10 – Contours of non dimensional velocity associated to the vortex shedding with on the left, the axial and on the right, the transversal velocity components with *(a)*-*(c)*, DMD and *(b)*-*(d)*, DMT. All fields are here normalized by their respective maximum velocity value.

the particularity of being single frequency for a large range of Reynolds numbers. A large bandwidth filter can hence be taken to have a quick convergence of the tracking without impacting the amplitude of the mode looked upon.

A.2 Validation test cases of the Dynamical Mode Tracking and Control (DMTC)

As discussed earlier, one interest behind DMT and its "on-the-fly" ability to identify modes is that it easily provides access to control strategies. To illustrate such features, **Case 1** is first addressed, a relaxation term being added to the F operator, Eq (3.2.1) in complement to DMT. Then the same process is repeated for **Case 2**.

A.2.1 Case 1: Control of the $1D$ cavity problem

The problem at hand being totally linear (linear acoustics), no interaction between modes is expected. DMTC is hence used to introduce the effect of the different parameters and the behavior of the method. For the analysis, only the 3^{rd} harmonic is intended to be suppressed. For the exercise, the final state obtained with DMT at $t^* = 84.4$ is taken as the initial solution for the simulation with DMTC. Activating DMTC introduces a feeback

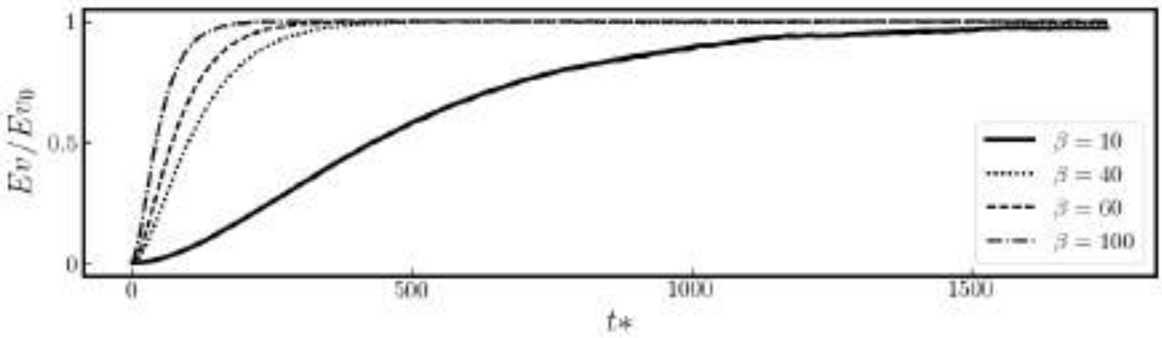

Figure B.11 – Impact of the bandwidth filter β: Normalized kinetic energy of the vortex shedding integrated over the domain over time with $\beta = 10$ (▬), $\beta = 40$ (·····), $\beta = 60$ (- -) and $\beta = 100$ (·-·).

for NS equation and as such, a specific temporal evolution is expected. Figure B.12(a) shows this evolution through the kinetic energy (Eq. (2.1.3)) of each mode. Note here that due to the narrow filter bandwidth, the fundamental mode and the 5^{th} harmonic energies remain constant, in agreement with the intent of controlling only mode 3. Results are here obtained with a small relaxation value, $\chi^{(3)} = 20$ and $\beta^{(n)} = 40$. Contrary to DMT, which is converged here, control or more precisely damping of the mode introduces an additional time scale. One defines $t^*_{10\%}$ the settling time, after DMTC activation, for a controlled mode to decrease and remain under 10% of its initial amplitude (Ev_0 in Fig. B.12(a)). For the present case $t^*_{10\%}$ is found for the 3^{rd} harmonic equal to 79.3, *i.e*, three times $t^*_{90\%}$ (time required for DMT to recover 90% of the mode amplitude). After convergence of the coupled system, an FFT of the signal recorded at S_{AC} and issued by the new CFD prediction Fig B.12(b), confirms that the 3^{rd} harmonic has been completely suppressed as desired. The spatial distribution of the modes after activation of DMTC are displayed Fig. B.13 for 4 characteristic times A, B, C, D as defined in Fig B.12(a). The different instants are chosen such that the three modes reached their highest amplitude. The results previously described in terms of energy are retrieved here for the three mode: *i.e* the 3^{rd} harmonic is completely removed without affecting the two remaining modes. Regarding CPU cost of this simulation, the computation has been again realized on the same mesh composed of 1998 cells (3000 nodes) using 2 Intel Xeon E5-2605 24 cores processors running at 2.4Ghz. The total CPU time obtained for the results exposed in the Figs. B.12 and B.13 is 440 min, *i.e*, 2.2% higher than the basic case without DMTC or DMT.

An explicit assessment of the relaxation coefficient effect introduced with DMTC is investigated in the following by systematically changing the value of χ to be $[20, 40, 30, 60, 100, 500]$ for a fixed $\beta = 40$. The subsequent temporal evolution of adimensionlized Energy $Ev^{(n)}$ is given in Fig. B.14. For all simulations presented for this sensitivity analysis, DMT results at $t^* = 84.4$ and obtained for $\beta = 40$ (Fig. B.2) are used as input. As shown in Fig. B.14(a) and Fig. B.14(c), for all χ the non damped modes amplitudes are well retrieved. Concerning the controlled mode (Mode $f^{(3)}$) Fig. (B.14)b, the speed at which this mode is damped appears to depend on χ but has an upper bound. The other information provided by Fig. B.14(b) is that different temporal transients are

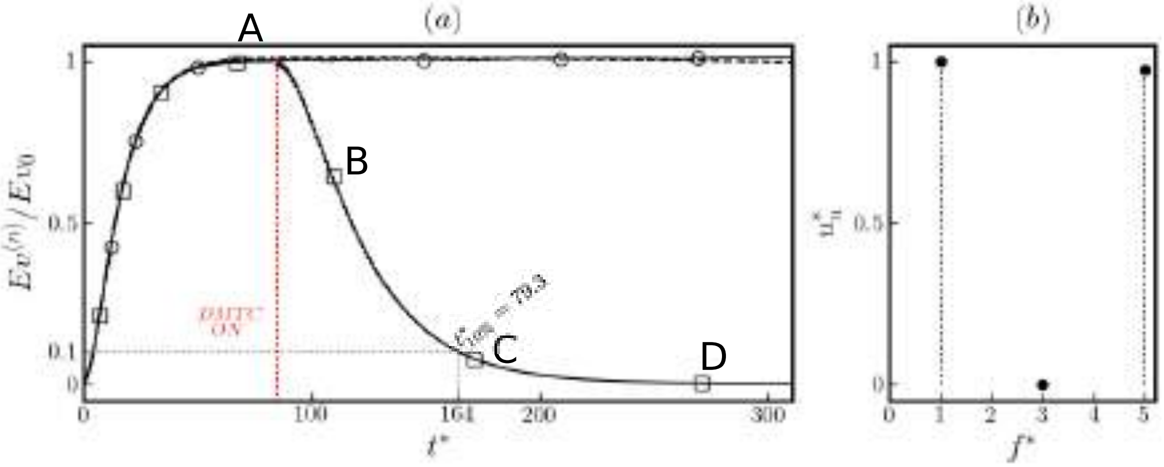

Figure B.12 – Mode damping: *(a)* Kinetic energy integrated over the domain over time $Ev^{(n)}/Ev_0$ (for a given mode n) with (-○-) the fundamental mode ($f^{(1)}$), (-□-) the 3^{rd} harmonic ($f^{(3)}$), (- -) the 5^{th} harmonic ($f^{(5)}$). The evolution of the 3^{rd} harmonic spatial distribution at characteristic instants A, B, C, D is displayed on Fig. B.13. *(b)* FFT at probe S_{AC} post damping for $t^* = [220, 320]$. Parameters of DMTC are $\beta^{(n)} = 40$ and $\chi^{(3)} = 20$.

to be expected and these will be strongly dependent on χ and β. In that respect, for $\chi > 30$, transitional growths have been observed without affecting the results. More details on the sensitivity of the system response issued by the damping of the 3^{rd} harmonic to the bandwidth of the filter variations for a fixed relaxation coefficient are exposed in appendix A.3.

A.2.2 Case 2: Control of the cylinder wake flow instability

The previous case was totally linear and hence easy to control. Hydrodynamic instabilities like the vortex shedding studied previously is the result of a saturation process of a linearly unstable mode among many that can interact and tend to different limit-cycles depending on the initial base flow and external actions impairing the system. In this context, studies have been dedicated to closed loop control to suppress or disphase the vortex shedding. In most cases, this type of control enables to damp the main frequency for a given Reynolds number but also the new generated states to finally get a steady flow (Roussopoulos (1993); Park *et al.* (1994)). In comparison, DMTC intends to suppress only one frequency for one state. An analysis of the state generated after DMTC activation is conducted here in order to validate the theory exposed Sec. 3.4.

For that purpose, the results of DMT in Sec. A.1.2 are used here and DMTC is activated at $t^* = 696$, keeping $\beta = 40$ and using a relax coefficient $\chi = 40$. Figure B.15(a) displays the results of the velocity $u^* = u/U_0$ recorded at probe S_{vs} and for which a post damping FFT is presented in Fig. B.15(b) considering only the new converged limit cycle.

Results confirm that the signal is quickly damped and that the system converges to a new state with another instability after a transitional phase. As introduced in

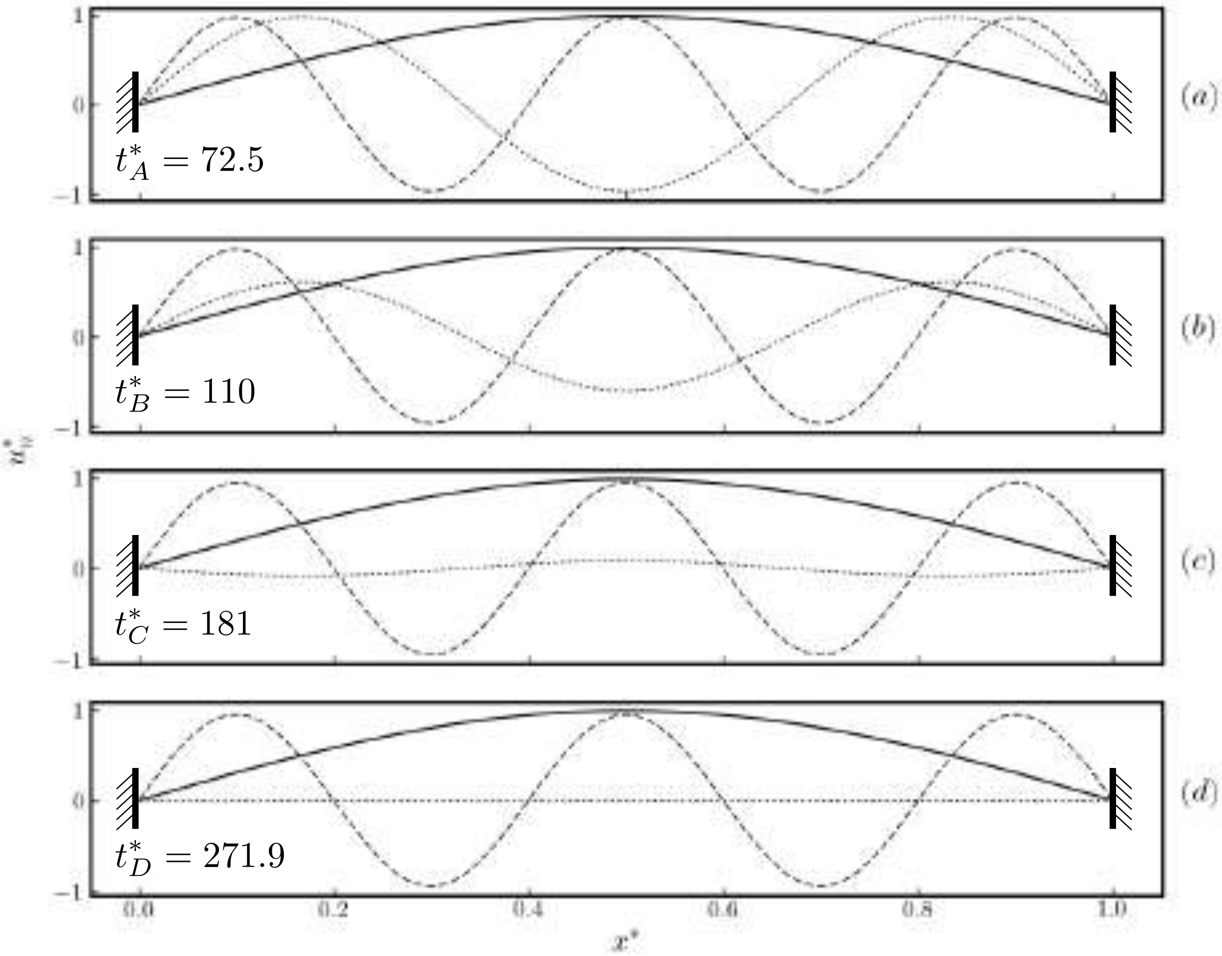

Figure B.13 – Spatial distribution of the normalized velocity profile u_n^* after DMTC with (—), the fundamental mode ($f^{(1)}$), (····), the 3^{rd} harmonic ($f^{(3)}$), (·-·), the 5^{th} harmonic ($f^{(5)}$) at *(a)* $t_A^* = 72.5$, *(b)* $t_B^* = 110$, *(c)* $t_C^* = 181$ and *(d)* $t_D^* = 271.9$ (See Fig. B.12).

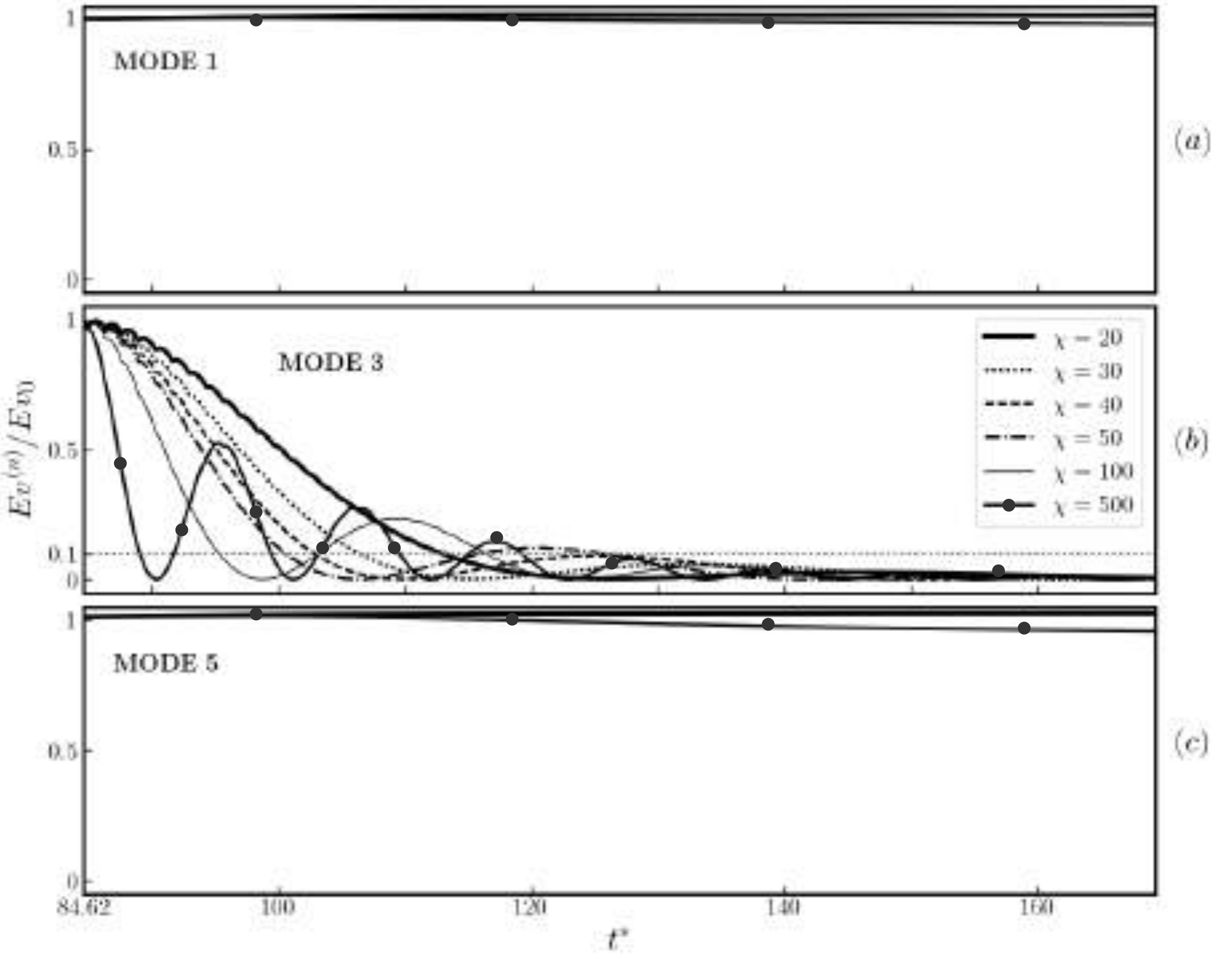

Figure B.14 – Impact of the relaxation coefficient χ during the damping of the 3rd harmonic: Adimensionlized kinetic energy integrated over the domain over time with *(a)* the fundamental mode ($f^{(1)}$), *(b)* the 3rd harmonic ($f^{(3)}$), *(c)* the 5th harmonic ($f^{(5)}$). 6 values of χ have been tested: $\chi = 20$ (▬), $\chi = 30$ (·····), $\chi = 40$ (- -), $\chi = 50$ (·-·), $\chi = 100$ (—) , $\chi = 500$ (-●-).

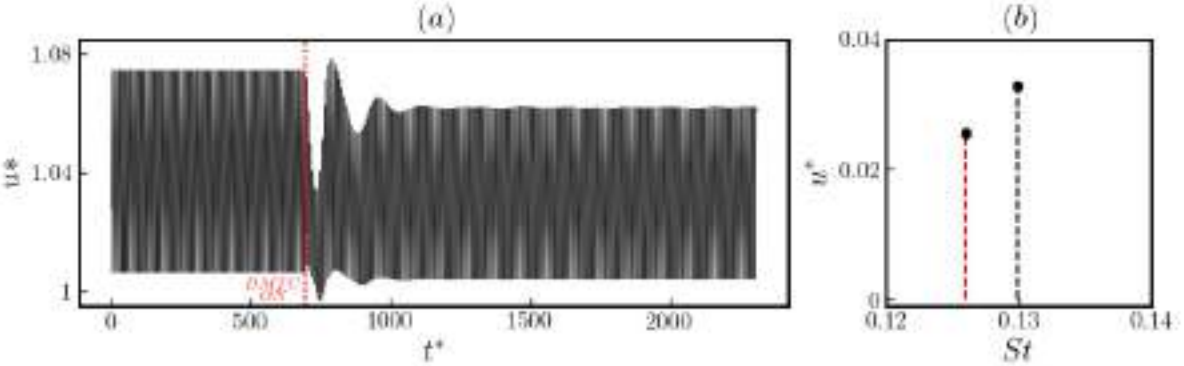

Figure B.15 – Damping of the vortex shedding: *(a)* Evolution of the axial velocity, *(b)* FFT of the signal prior (- -) and post (- -) DMTC activation at probe S_{vs}.

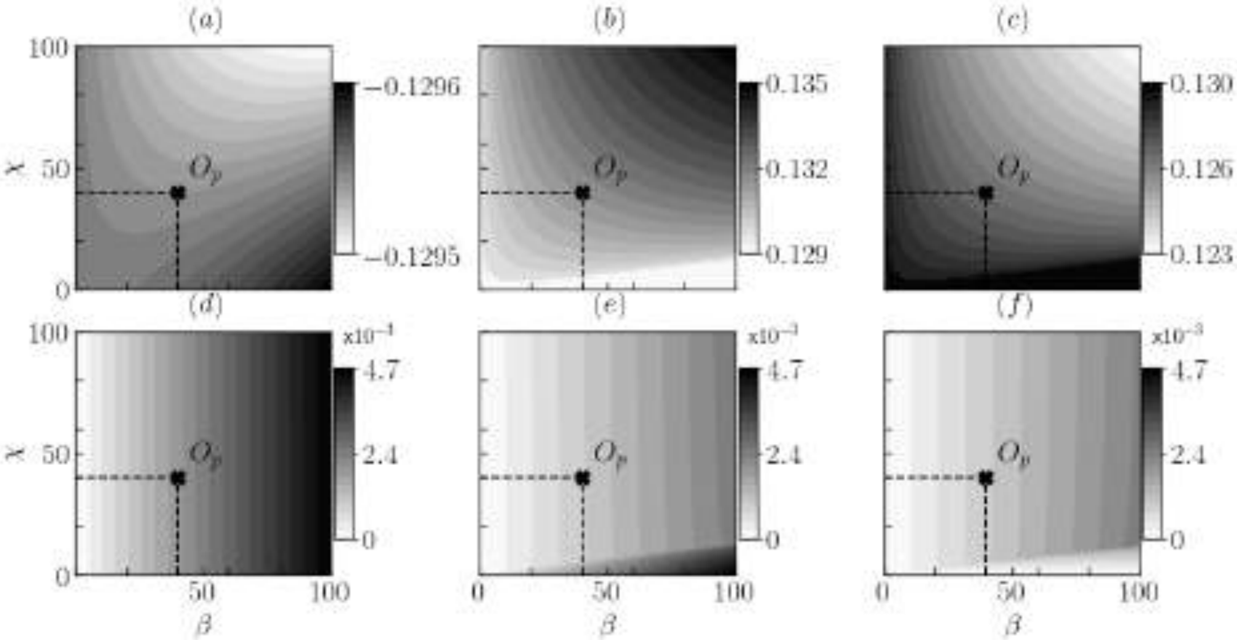

Figure B.16 – (β,χ) Mapping of the three complex frequencies found after DMTC for $St = 0.13$: *(a-c)* represents the Strouhal number (real part) and *(d-f)* the growth rate (imaginary part) normalized by D/U_0, for each eigenvalue. O_p corresponds to the operating point of interest.

Sec. 3.4, eigenmodes of the new state can be predicted by finding the roots of the 3^{rd} order polynomial exposed in Eq. (3.4.7). To do so, one first assumes that $\omega = \omega_0$ which is equivalent to say that the real frequency of the initial system ω is known. For the case under study, a first hand view of the effect of DMTC and the potential emergence of a specific mode different from ω_0 as a function of the (β,χ) couple can be obtained. Figure B.16 shows such mappings for $(\beta, \chi) \in ([0, 100], [0, 100])$ for a fixed Strouhal number $St = 0.13$, *i.e*, a pulsation ω_0 corresponding to the vortex shedding for $Re = 56$. For that case, the real parts obtained for each eigenvalue normalized by D/U_0 correspond to the expected new Strouhal numbers issued by the activation of DMTC, Fig. B.16*(a-c)*. The imaginary parts, *i.e* the growth rate are also accessible and displayed in Fig. B.16*(d-f)* with the same normalization. First, it is noted that the first eigenvalue, Fig. B.16(a), has a negative Strouhal number and is hence not a possible solution of the new state. The two remaining eigenvalues have a positive Strouhal number and a positive growth rate for all the range of parameters studied. This latter information suggests that for all sets of parameters (β,χ), two instabilities are prone to appear under the activation of DMTC. For the specific case ($\beta = 40, \chi = 40$) defined by O_p in Fig. B.16, a Strouhal number of 0.1321, Fig. B.16(b) and 0.127 Fig. B.16(c) are expected. One can notice here that these specific values coincide with the bandwidth filter limits and a good agreement is found between the third Strouhal number eigenvalue and our simulation (0.1265). Note finally, that similar values of growth rates are found for both identified new eigenvalues: 0.97×10^{-3} for the first eigenvalue and 0.95×10^{-3} for the third.

The acoustic cavity and the cylinder wake were used to give better insight into

DMT/DMTC and show the different parameters and their impact on the results. The following section intends to demonstrate in a real case how this new tool could be applied to analyze a complex system but also how it can be used to correct a wrong prediction in a CFD simulation.

A.3 Sensitivity of DMTC to the bandwidth filter β

An explicit assessment of the filter bandwidth effect on the control of the 3^{rd} harmonic is investigated in the following by systematically changing the value of β to be $[10, 20, 40, 60, 100]$. The envelop of the adimensionlized Energy $Ev^{(n)}$ is given in Fig. B.17 for 5 values of β. Since the time necessary to converge is reduced by increasing the bandwidth, DMT has been first applied to our case from $t^* = 0$ to $t^* = 338$ in order to obtain 90% of the mode amplitudes for any bandwidth (see Sec. A.1.1). DMTC is applied from $t^* = 338$ on. Here again, for small values of β, transitional growth can appear. For the 5^{th} harmonic, high dissipation can be observed: this is only due to numerical scheme and the long simulation time. The same dissipation could be observed for the same simulation time without DMTC. Contrary to the sensitivity to the relax coefficient χ, one can see in Fig. B.17(b) that the time $t^*_{10\%}$ defines Sec. A.2.1 constantly increases with β.

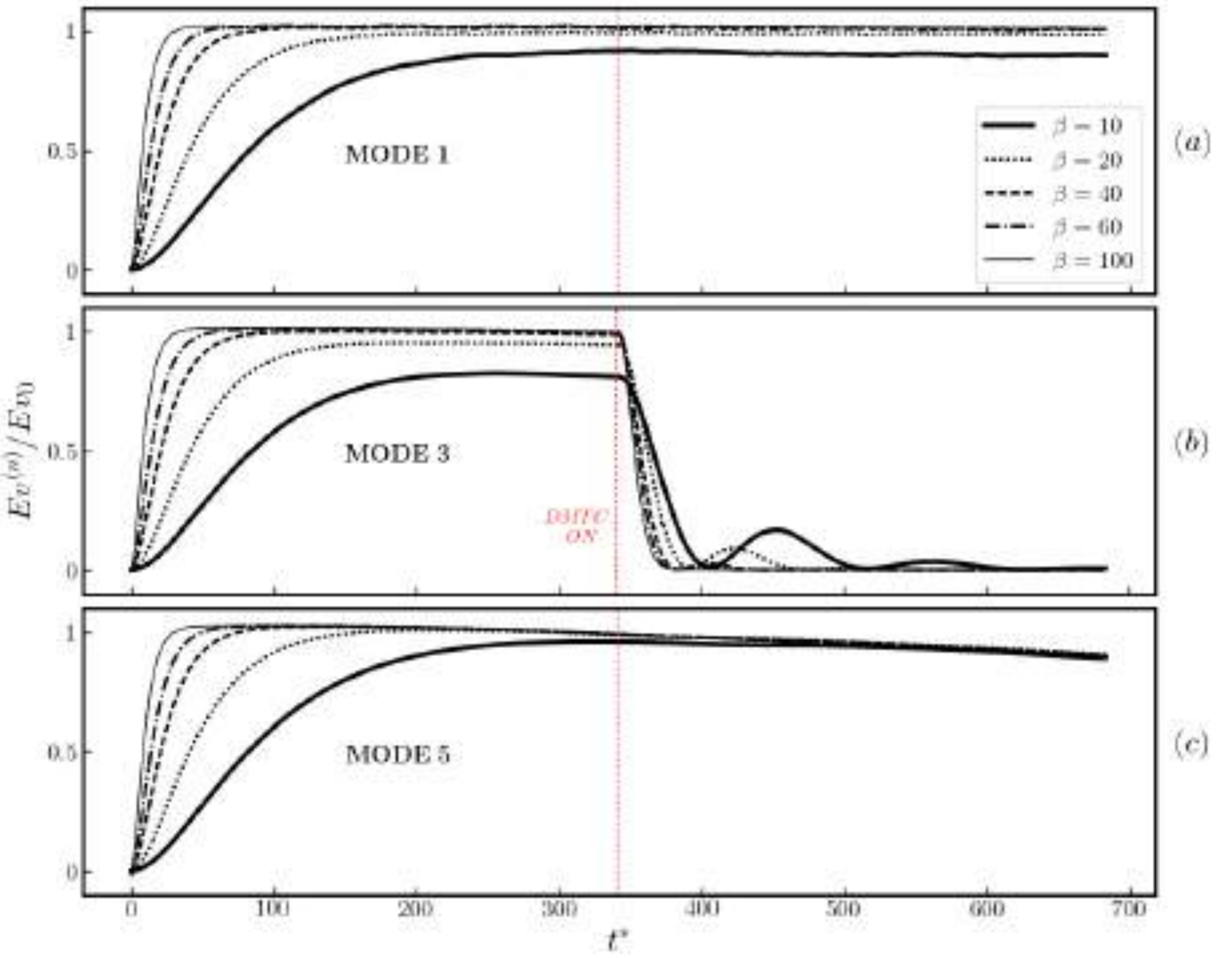

Figure B.17 – Impact of the bandwidth filter β during the damping of the 3^{rd} harmonic: Adimensionlized kinetic energy integrated over the domain over time with *(a)* the fundamental mode $f^{(1)}$, *(b)* the 3^{rd} harmonic $f^{(3)}$, *(c)* the 5^{th} harmonic $f^{(5)}$. 5 values of β have been tested: $\beta = 10$ (━), $\beta = 20$ (·····), $\beta = 40$ (- -), $\beta = 60$ (·-·), $\beta = 100$ (—).

A.4 DMTC Application example for complex flows

The last case studied here is a full 3D simulation of an academic premixed swirl burner. The purpose of this case is to show how DMT helps analyzing a numerical prediction and its limit-cycle in terms of composition and activity. DMTC is then used to deal with such flow predictions exhibiting artificially induced instabilities so that a more relevant flow is obtained. Note that all the details about this complex system, Fig. B.18(a), are not provided here and can be retrieved in the paper of Merk *et al.* (2017). For this specific burner, Large Eddy Simulation (LES) has been performed on the flow domain shown in Fig. B.18(b) and the probe S_b located in the confinement chamber, Fig. B.18(b), is used to evaluate the activity within the system. Note that such a flow is highly complex since resulting of the use of complex configuration and complex physics. Indeed, the flow is fully turbulent and reacting. The operating condition for this CH_4/Air premixed flame are displayed in Fig. B.18(c).

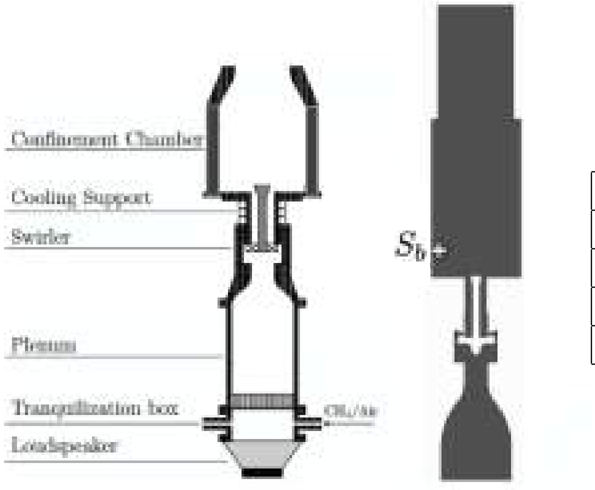

(a) (b)

Operating conditions	
Equivalence ratio, ϕ	0.82
Inlet Bulk velocity, U_{bulk}	5.44 m/s
Flame power,P_{th}	5,4 KW
Swirl Number, S	0.8

(c)

Figure B.18 – Presentation of the system: *(a)* Sketch of the experimental set up, *(b)* Cut of the flow domain used for the Large Eddy Simulation (LES) with S_b a probe in the confinement chamber and *(c)* Table of the main operating conditions of the system.

Due to the complexity of initializing such a complex flow problem, undesired steady state solutions are often obtained for such simulation. In fact, acceptable states are usually the result of expert choices either in guessing a suitable initial solution for the simulation or through the used of guided boundary conditions settings, artificial damping, coarse meshes, etc. For this specific case, first hand initialization of the simulation, resulted in the triggering of a high frequency thermo-acoustic instability that appears with a high amplitude, hence distorting the analysis of this known stable swirled flow and flame.

This high frequency instability, corresponds to a transverse mode of the chamber and can be retrieved with Helmoltz solvers. Note that, this physical mode of the system is

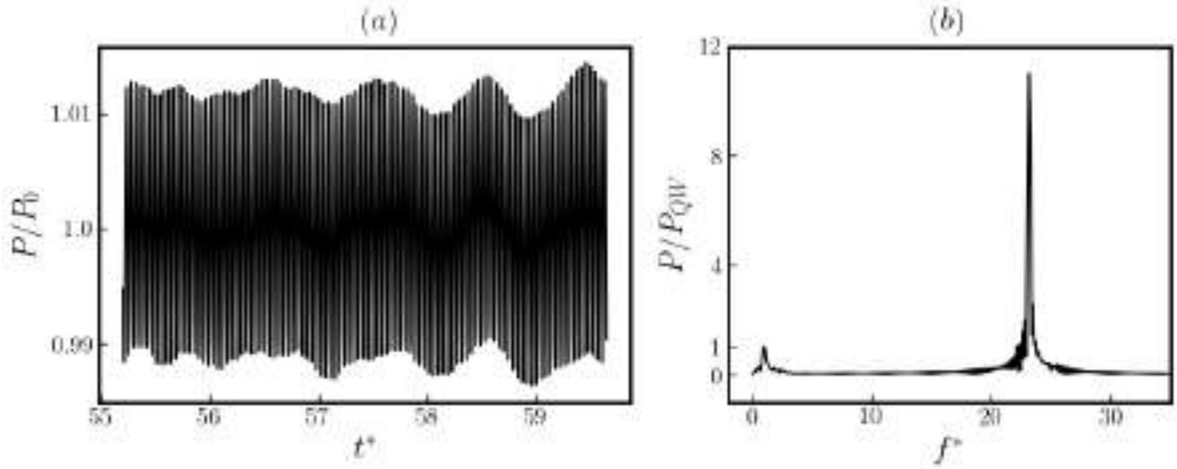

Figure B.19 – Activity of the system: *(a)* Adimensionalized pressure, P/P_0, over time with P_0 the atmospheric pressure *(b)* FFT on probe S_b (see Fig. B.18(*(b)*))

not observed in practice in experiments due to the low pass nature of the flame, the dissipation created by the vibrations of the chamber walls and the non reflective inflow and outflow conditions at this frequency.

Figure B.19(a) illustrates the pressure signal recorded over time and adimensionalized by the atmospheric pressure P_0 at probe S_b (Fig. B.19(a)) along with its FFT in Fig. B.19(b). Note that only the limit-cycle is represented here and both time and frequency have been adimensionalized by the frequency of the quarter wave mode f_{QW} of the configuration so that $f^* = f/f_{QW}$ and $t^* = t.f_{QW}$. The 1/4 wave mode is likely to appear based on experimental findings and reported boundary conditions effects: *i.e* depending on the exhaust lengthMerk *et al.* (2017). In fact, 1/4 wave mode is present in the issued LES (first peak of Fig. B.19(b)) but the high frequency triggered mode with a frequency $f^* = 23$ has an amplitude 10 times higher than the one of the quarter wave mode precluding any analysis.

Use of DMT is first discussed and illustrated in this context. In that case, the unwanted frequency $f^* = 23$ being far from the ones representing the expected physics, one can choose a very large filter bandwidth $\beta = 1000$ corresponding to a bandwidth $\Delta f^* = 0.795$ around the tracked mode. Convergence of DMT of these settings is reported on Fig. B.20. Due to the very large filter bandwidth, 90% of the mode amplitude is obtained after only 17 periods or $t^*_{90\%} = 58.76$, which is in good agreement with the time evaluated using Eq. (3.3.7) yielding $t^*_{90\%} = 58.82$. Equivalently to previous observations, the analysis of fields issued by $(q - \bar{q})$ provides good information about the spatial distribution of the mode in time.

For illustration, the adimensionalized total energy associated to this mode fluctuations: *i.e* $(\rho E - \overline{\rho E})$ noted $E_T/E_{T,max}$ is shown at two instants in Fig. B.21. A longitudi-

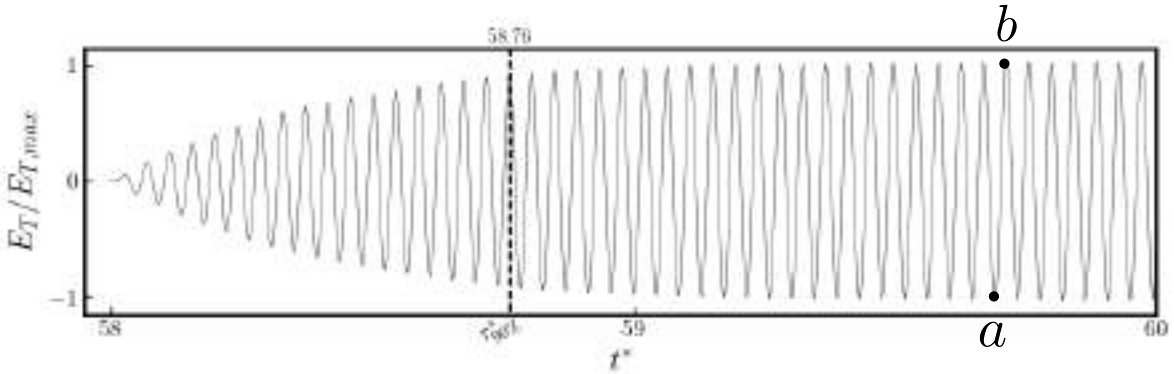

Figure B.20 – Mode tracking: Evolution of adimenzionalied energy $E_T/E_{T,max}$ associated to the unwanted mode at the probe. Spatial distribution at points a and b are displayed in Fig. B.21.

nal and a transverse cut are displayed to point out the rotating nature of the mode. Note that the difference $(\rho E - \overline{\rho E})$ is representative of the mode pressure fluctuation. The nodal plane (*in white* in the Fig. B.21) positioned along the central axis of the burner indicates that the flow feature looked for corresponds to the first transverse mode of the chamber. From the longitudinal cut, one can also see that the mode expresses itself everywhere in the combustion chamber. It also interacts with the flame, indicating a potential thermo acoustic loop explaining the self sustained activity and presence in the limit cycle . Note finally that the plenum, volume prior the combustor, is absolutely not marked by the mode which confirms that the inlet boundary condition is not active for that mode and changing its acoustic impedance will have no impact.

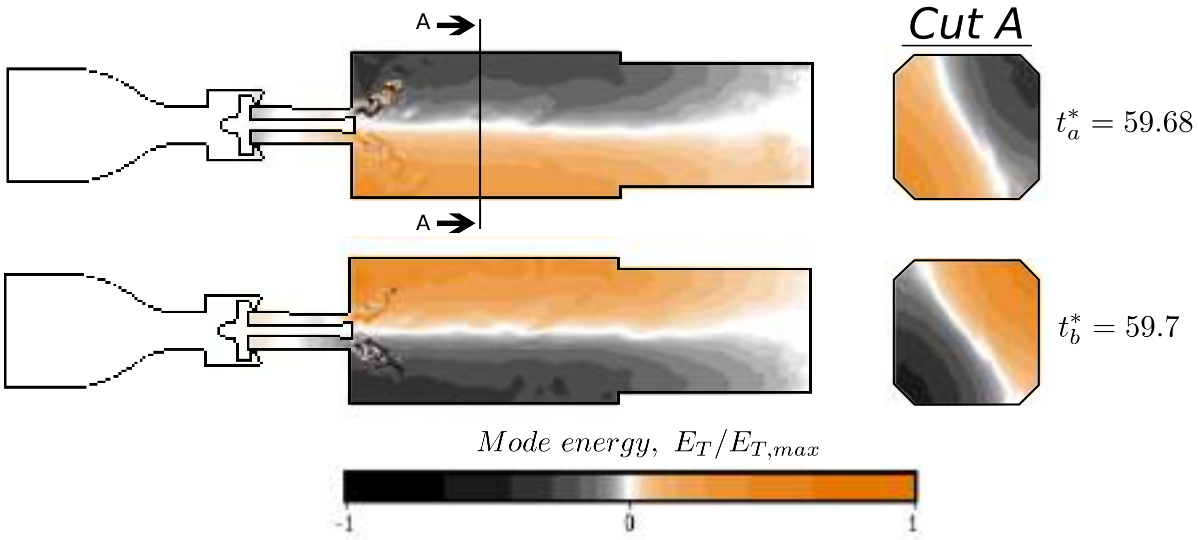

Figure B.21 – Spatial distribution of the unwanted mode adimensionalized energy $E_T/E_{T,max}$ on two cuts at characteristic times $t^*_a = 59.68$ and $t^*_b = 59.7$ defined in Fig B.20.

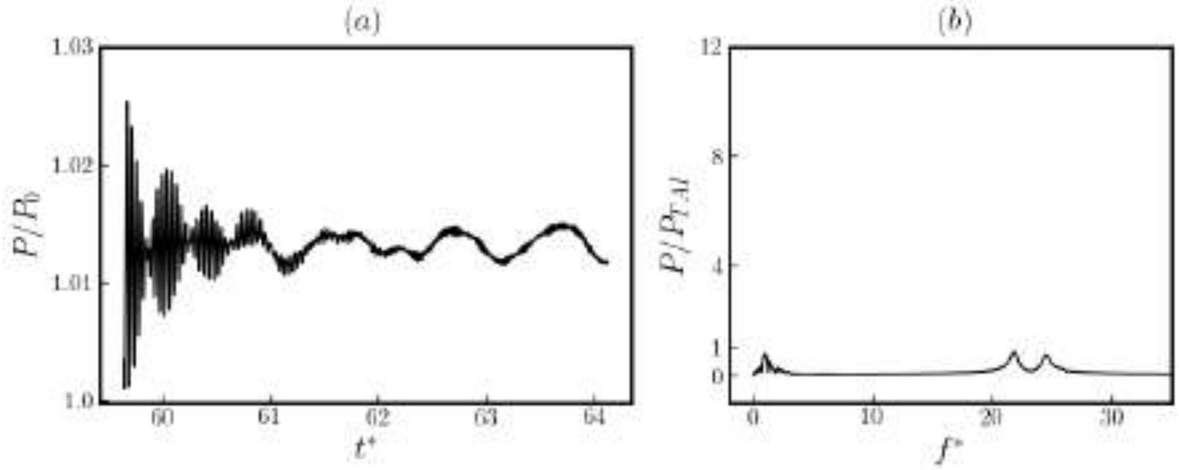

Figure B.22 – Damping of the main instability: *(a)* Adimensionalized pressure, P/P_0, over time with P_0 the atmospheric pressure *(b)* FFT on probe S_b (see Fig. B.18(*(b)*))

DMTC is then activated from the last solution at $t^* = 59.7$ obtained with the DMT. A high relaxation coefficient $\chi = 200$ is used for this test in order to have fast convergence. Following this activation, the adimensionalized pressure evolution over time is shown Figure B.22(a). The results demonstrate again that after 2 periods of the 1/4 wave mode, the high frequency is being damped. The FFT in Fig. B.22(b) of the pressure spectrum recorded in the LES at probe S_b for the window of interest, shows that the quarter wave mode amplitude is slightly affected and residues of high frequency activities around the spurious mode are present.

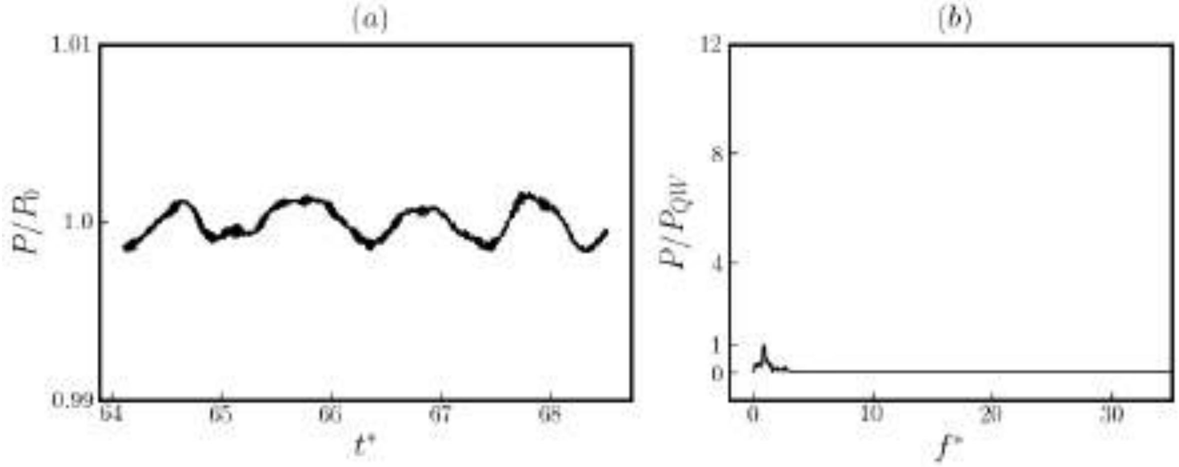

Figure B.23 – Deactivation of DMTC: *(a)* Adimensionalized pressure, P/P_0, over time with P_0 the atmospheric pressure *(b)* FFT on probe S_b (see Fig. B.18(*(b)*))

Finally, it is important to note that DMTC is a fully time dependent system which provides the spatial map of a controlled oscillation as it evolves with time. Consequently all the transient description is accessible. This property is demonstrated by Fig. B.24. Starting with the instantaneous field of oscillations at $t^* = 59.68$ as in Fig. B.21, the level of spatial oscillations is rapidly seen to decrease to finally disappear at later instants Fig. B.24(*bottom*).

Residues corresponding to the damped frequency can be observed around the flame. This is explained by the broadband nature of combustion and to the fact that it responds constantly at this frequency. Such results also confirm that even though frequencies around the limits of the filter bandwidth could appear, it is not the case here and the unwanted frequency has been completely removed. For this specific burner configuration, since it is suspected beforehand that the high frequency oscillation was artificially triggered by the numerical strategy adopted, it seems important to confirm that the newly obtained limit cycle is stable. To do so, DMTC is switched off at $t^* = 64.2$ to see how the solution evolves. Results Fig. B.23 confirmed the finding and the unwanted mode remained absent, allowing the analysis of the quarter wave mode without potential interference. All discussed computations have been realized on a 3D mesh composed of 7.1 million cells (1.3 million nodes) with 15 Intel Xeon E5-2605 24 cores processors running at 2.4Ghz. The total CPU time obtained for the results with tracking and control of only one frequency is $2050\,h$, *i.e*, 3.5% higher than the basic case without DMT or DMTC activated.

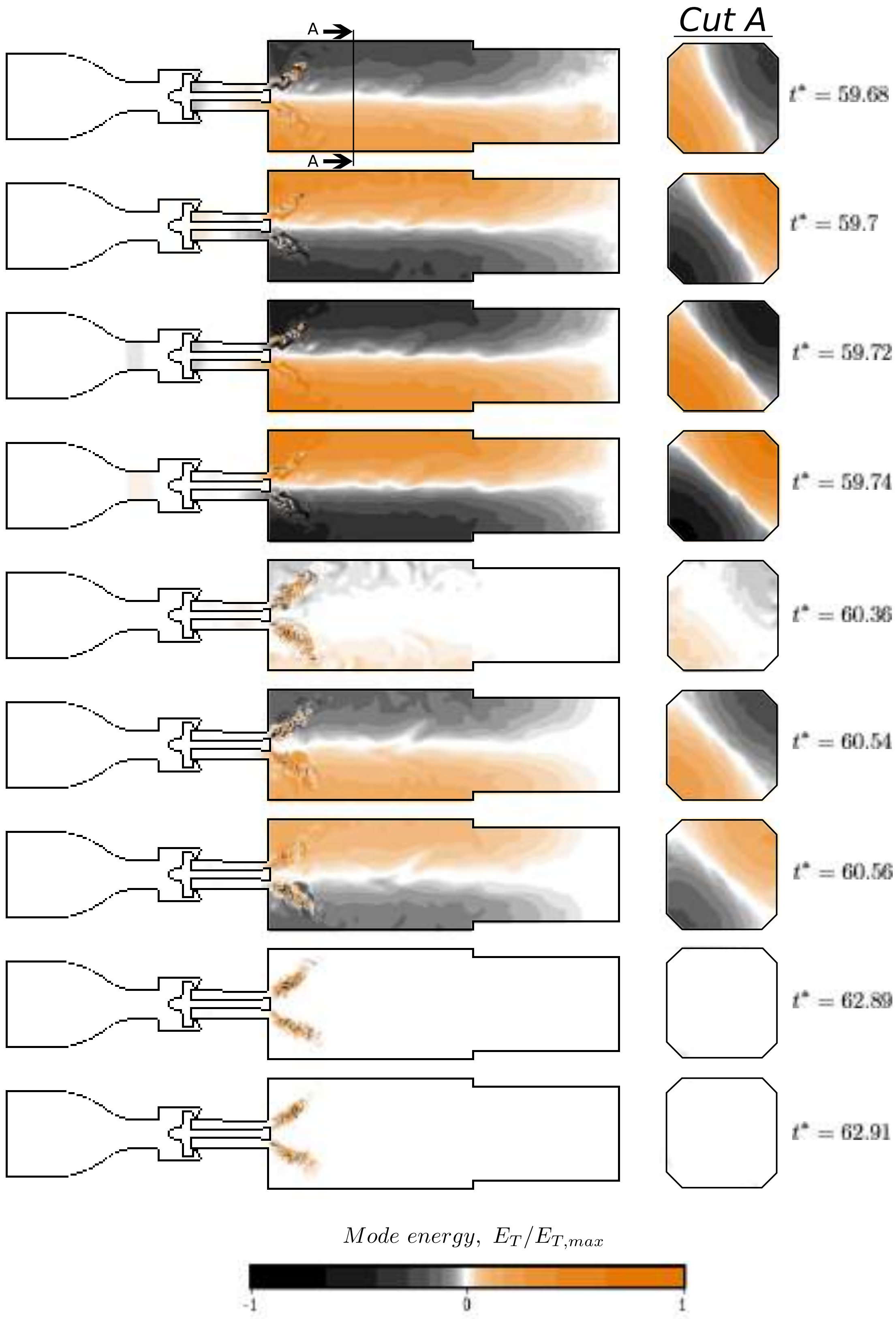

Figure B.24 – Mode energy: Instantaneous solution of $E_T/E_{T,max}$ of the high frequency instability for characteristic instants.

Appendix C

Sensitivity to base flow modification validations

A.1 Cylinder wake sensitivity to base flow modification

This section evaluates the efficiency of the code GIFIE to give a sensitivity to base flow modification map for a cylinder wake at a Reynolds nymber of $Re = 47$. Fig. C.1 compares the current results Fig. C.1 *(left)* with the results of the original paper on the method (Marquet *et al.* (2008)) Fig. C.1 *(right)*. Figure C.1 *(upper)* and Fig. C.1 *(lower)* represent respectively the growth rate sensitivity and frequency sensitivity to a base flow modification. The global map is well retrieved with also the local maxima. From the growth rate sensitivity (Fig. C.1 *(upper)*), one retrieves that the flow can be stabilized ($\delta\omega_i < 0$) by taking a δU purely axial oriented downstream and applied in the the axis of the bubble reciculation at $(x, y) = (1.1, 0)$. For this same modification the frequency sensitivity (Fig. C.1 *(lower)*) shows that the frequency shift will be positive and hence the vortex shedding frequency will be increased.

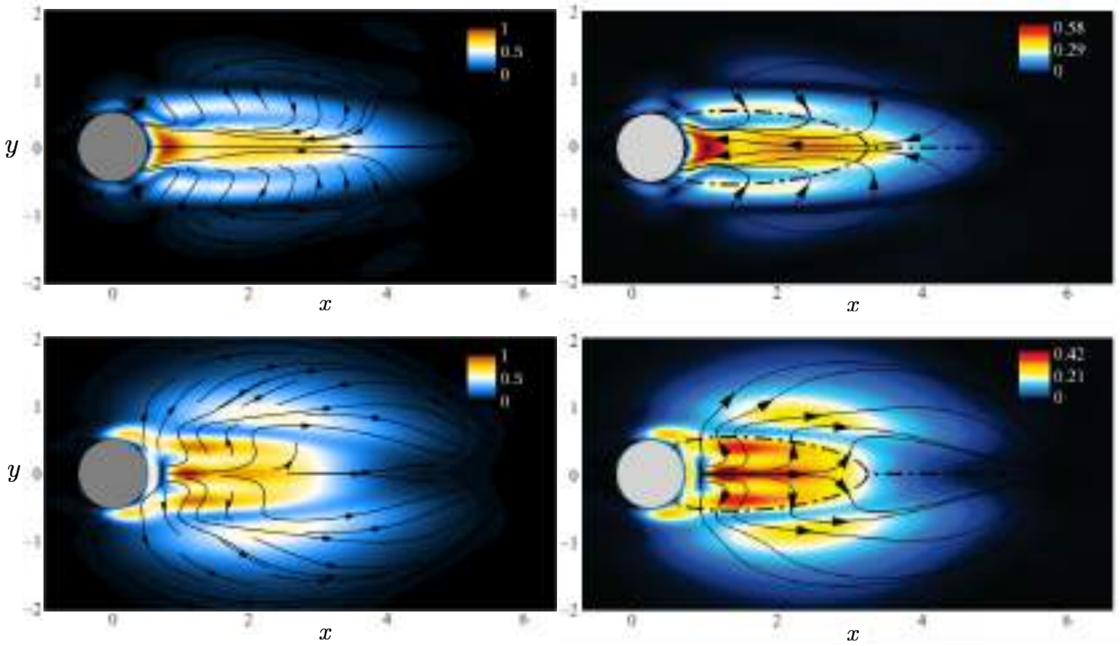

Figure C.1 – Sensitivity to base flow modifications of a cylinder wake at Re=47 with on *(right)* results from Marquet *et al.* (2008) and *(left)* the current results. The *(upper)* and *(lower)* figures corresponds respectively to the grow rate sensitivity and frequency sensitivity to a base flow modification. The mgnitude is represneted in colors and orientation in colors. Note that the current results have been normalized by its ∞-norm.

Appendix D

Sensitivity to base flow modification validations

A.1 Power Spectral Density of a control annular cavity

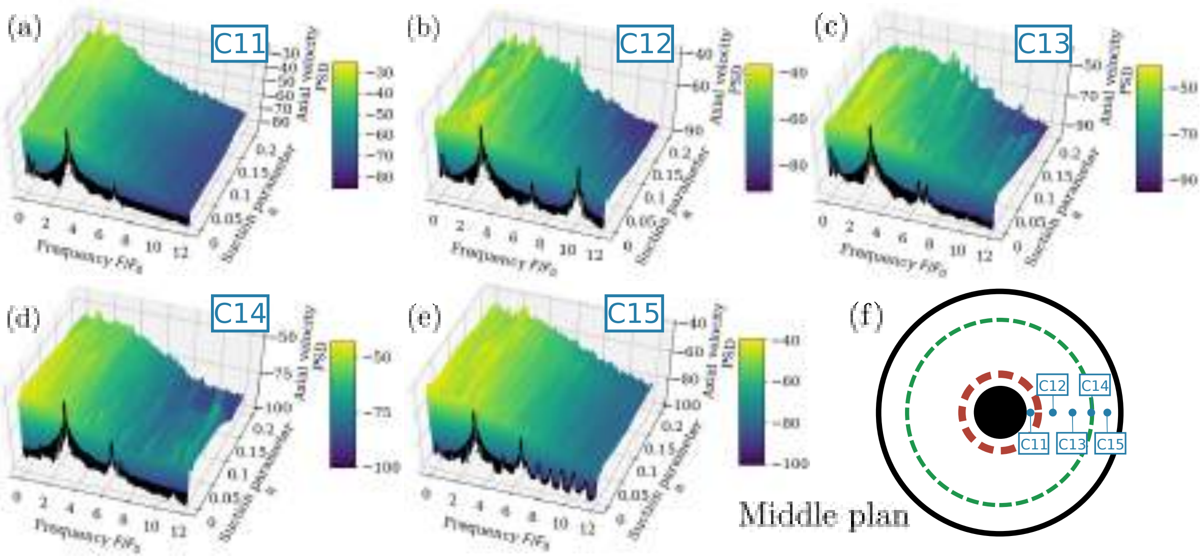

Figure D.1 – Probes Axial velocity PSD of the controlled cavity function of the suction amplitude a in a mid cavity plan: (a) probe $C11$ ($r = 0.08$) (b) probe $C12$ ($r = 0.12$) (c) probe $C13$ ($r = 0.16$) (d) probe $C14$ ($r = 0.20$) (e) probe $C15$ ($r = 0.24$) . In each plots the black contour represent the results obtained for the non controlled cavity. (f) Schematic of the probes $C11$ to $C15$ probes.

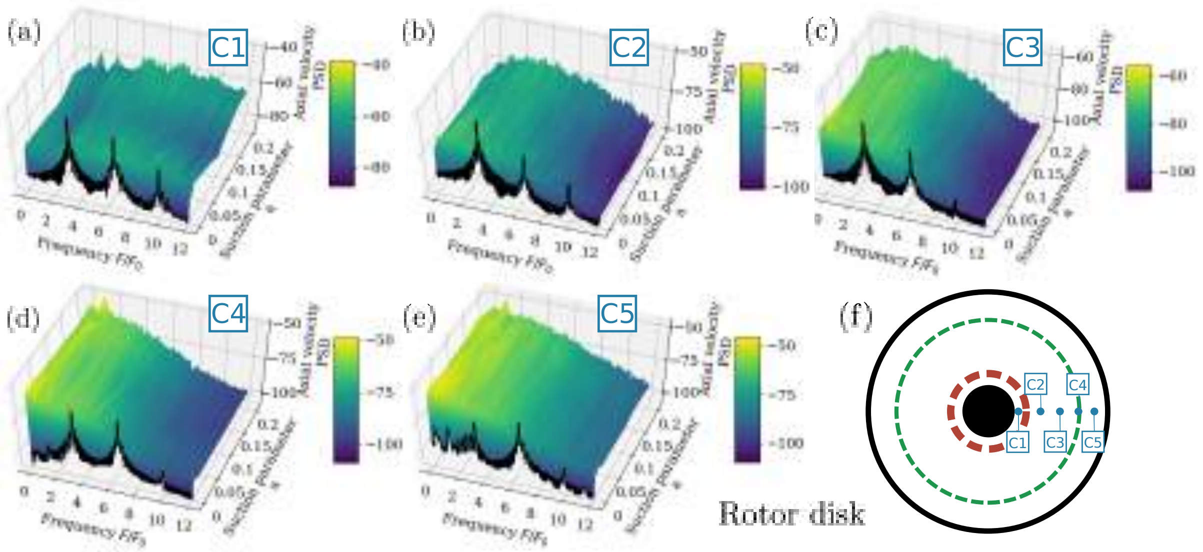

Figure D.2 – Probes Axial velocity PSD of the controlled cavity function of the suction amplitude a in the rotor disk: (a) probe $C1$ ($r = 0.08$) (b) probe $C2$ ($r = 0.12$) (c) probe $C3$ ($r = 0.16$) (d) probe $C4$ ($r = 0.20$) (e) probe $C5$ ($r = 0.24$) . In each plots the black contour represent the results obtained for the non controlled cavity. (f) Schematic of the probes $C1$ to $C5$ probes.

Appendix E

Local and global stability analysis comparison in an annular rotor/stator cavity

Proceedings of ASME Turbo Expo 2018: Turbine Technical Conference and Exposition
GT2018
June 11-15, 2018, Oslo, Norway

GT2018-75008

LOCAL AND GLOBAL STABILITY ANALYSIS OF AN ACADEMIC ROTOR/STATOR CAVITY

Matthieu Queguineur *
CFD Team CERFACS
Toulouse, France
Email: queguineur@cerfacs.fr

Thibault Bridel-Bertomeu
Laurent Gicquel
Gabriel Staffelbach
CFD team CERFACS
Toulouse, France

ABSTRACT

Self-sustained oscillations of rotor/stator cavity flows are well known to industry. This unsteady phenomenon can be very dangerous and jeopardize the structural integrity of aeronautical engines by damaging turbomachinery components or turbopumps in the context of space applications. Today, the origin of such flow instability and resulting limit-cycle is not well understood and still difficult to predict numerically. In order to have more insight of this phenomenon dynamic, an academic rotor/stator cavity is investigated in the present paper. The main motivation of this study is to highlight the benefit of conjunct numerical strategies relying on Large Eddy Simulations (LES) and flow stability analyses to understand driving instability mechanisms. More specifically, results of a local and global methods are devised and compared to a Dynamic Mode Decomposition (DMD) of LES predictions. Good agreements between the stability methods studied and the present features in the LES limit-cycle are found. On this basis, a sensitivity and receptivity analysis of the flow is realized to point the origin of the two most unstable modes: i.e the position within the flow where the problem issues.

NOMENCLATURE

Acronyms

CFD	Computational Fluid Dynamics
DNS	Direct Numerical Simulation
DMD	Dynamical Mode Decomposition
LES	Large Eddy Simulation
LSA	Linear Stability Analysis
TTGC	Two-Step Taylor Galerkin C
WALE	Wall Adaptative Local Eddy-viscosity

Greek letters

Ω	Rotor rotation rate	$[rad.s^{-1}]$
δ	Boundary layer characteristic scale	$[m]$
ν	Kinematic viscosity	$[m^2s^{-1}]$
ω	Complex frequency	$[-]$
ω_0	Absolute complex frequency	$[-]$
α	Complex wave number	$[-]$
$\nabla\cdot$	Divergence operator	$[m^{-1}]$
∇	Gradient operator	$[m^{-1}]$
∇^2	Laplace operator	$[m^{-2}]$

---

[*] Address all correspondence to this author.

Symbols

$\mathbb{C}$	Complex numbers set	$[-]$
h	Cavity height	$[m]$
r	Radial coordinate	$[m]$
z	Axial coordinate	$[m]$
t	Time	$[s]$
R_0	Internal radius cavity	$[m]$
R_1	External radius cavity	$[m]$
G	Aspect ratio	$[-]$
R_m	Curvature parameter	$[-]$
Re_G	Global Reynolds number	$[-]$
Re	Local Reynolds number	$[-]$
Re_h	Scale of boundary layers	$[-]$
U	Global velocity flow	$[m.s^{-1}]$
P	Global pressure flow	$[kg.m^{-1}.s^{-2}]$
$U_{b,i}$	Base flow velocity components	$[m.s^{-1}]$
P_b	Base flow pressure	$[kg.m^{-1}.s^{-2}]$
p	Pressure perturbations	$[kg.m^{-1}.s^{-2}]$
u_i	Perturbations velocity components	$[m.s^{-1}]$
D	Dispersion relation	$[-]$
m	Azimuthal wavenumber	$[m.s^{-1}]$
$\mathbb{S}$	Sensitivity	$[-]$
F	Frequency	$[Hz]$
F_0	Frequency of the rotor	$[Hz]$
$\mathscr{L}$	Direct problem operator	$[-]$

Subscript

$\langle\cdot\rangle_i$	Imaginary part
$\langle\cdot\rangle_r$	Real part
$\langle\cdot\rangle_0$	Zero group velocity
$\langle\cdot\rangle_G$	Zero group velocity

Superscripts

$\langle\cdot\rangle^+$	Adjoint

1 INTRODUCTION

Space engine design still remains a source of challenges for researchers and engineers today. Each phenomenon and components needs to be precisely analysed due to the complexity of the fluid mechanisms that operate such devices. For example, experimental campaigns have often evidenced undetermined unsteady phenomena around the cavity of space turbopump turbine. Some of them are called 'Pressure bands phenomenon' are characterized by dominant frequencies which can be measured everywhere in the cavity. These self-sustained oscillatory motions of the fluid can, under certain circumstances, become dangerous and if uncontrolled, impact the structural integrity of the engine. Although highly complex in the end application, this specific phenomenon has recently been retrieved in academic rotor/stator cavities as described by Bridel [3].This simple configuration is investigated again in the present paper .

Rotating flows over a single disk have been an interesting subject for fundamental fluid mechanics but also for industrial purpose for a long time [Ekman [10], Karman [34], Bodewadt [2]]. Recent studies have been focused on enclosed rotor/stator systems [Lingwood [19],Itoh [16] with a renewed interest. From an experimental point of view, the complete study of Schouveiler *et al.* [29] or Lopez [20] detail the different transitions scenario possible as a function of geometrical parameters and Reynolds number Re_G. From the Linear Stability Analysis (LSA) point of view, the first studies were done between two infinite disks. In that cases, auto similar Batchelor profiles were applied for the base flow [Itoh [16]]. However, for rotating cavity boundary layer, Healey [12] has demonstrated that walls and hence confinement have a non negligible impact on the waves that grow and propagate in the crosstream direction. Tuliszka [32] confirmed this phenomenon by extending the work of Itoh [16] and Lingwood [19] to rotor/stator systems. In this specific analysis, good agreement was found between a Direct Numerical Simulation (DNS) and a local stability analysis. Finally, the existence of the spiral paterns and travelling circular waves as descibed in Schouveiler [29] were confirmed. The present study follow on from one of the most recent studies done by Bridel [3]. Based upon the conjunct use of Large Eddy Simulations (LES)[Sagaut [26, 27]], dedicated post processing techniques and local stability analysis, Bridel *et al.* [3] managed to expand our understanding of the dynamics of such systems and highlight the potential sources at the origin of the observed instabilities. To do so, first, Dynamical Mode Decomposition (DMD) of Schmid [28] enabled to show that the full dynamics of the flow can be linked to only three dominant modes and that the fluctuations from the stationnary disc is the source of the spiral patterns that cover all the inviscid core flow which then reach the rotating disc boundary layer and destabilize it. Second, local stability analyses based on the parallel flow assumption and realized on a 1D base flow were conducted and helped identifying the location of the instability triggering mechanism. Note that, although powerful, such analysis can be restrictive for complex systems with, for example, recirculations or boundary detachment situations. With the increase of computing power in the 1980s, global stability has offered the possibility to extend the local approach to 2D base flows. This paper intends to combine both stability methods to go deeper into the understanding of the instability mechanisms occurring in annular rotor/stator cavities. One of the main benefits of a global approach is the possibility to conduct more easily receptivity and sensitvity analysis as descibed first in Giannetti [11].Those tools provide more information on the origin of the instabilities and thereby select a control strategy to apply to the flow.

The document is organized as follows. The system configuration is presented in Section 2. Linear stability analysis theory with both local and global approaches are explained in Section 3. Then, a description of the base flow obtained from LES is given and discussed in Section 4. Stability results are analyszed in section 5, starting with the local approach followed by the global results to finally finish with the sensitivity/receptivity analyses

2 CONFIGURATION OF INTEREST

The study is conducted on the same annular academic cavity of Bridel *et al*. [3] originally introduced by Tuliszka [32]. Figure 1 represents this simple cavity with associated geometrical characteristics. The upper disk is stationnary and the lower rotating at the speed Ω. If one defines h the height of the cylindrical cavity, R_1 the external radius and R_0 the internal radius, several characteristic numbers are usually used to fully describe a rotor/stator systems.

The aspect ratio, defined as $G = h/R_1$, is the most important one. The curvature paramater defined as $R_m = (R_1 + R_0)/(R_1 - R_0)$ has also been identified to be of importance. Finally, 3 Reynolds numbers need to be defined. The first one, $Re_G = \Omega R_1^2/\nu$, will correspond to the classical Reynolds number of a system with ν the kinematic viscosity of the flow. The second one, $Re_h = (h/\delta)^2$, will be related to the boundary layers with $\delta = (\nu/\Omega)^{1/2}$. Finally, in order to apply local stability analyses a 'local Reynold number' is usually introduced (Bridel [3].Follwing the work of Itoh [16] and Tuliszka [33], let r be the radius at which our local analysis will be applied. By taking h the reference length scale, $r\Omega$ the velocity scale, $\rho r^2\Omega^2$ the reference pressure and the time scale $h/r\Omega$, an artificial Reynolds number can be simply reduced to $Re = r/h$. Table 1 sums up all geometric and physical features of Tuliszka cavity.

Feature	Symbols	Value
Internal radius	R_0	71 mm
External radius	R_1	250 mm
Height	h	35 mm
Aspect ratio	G	0.2
Curvature	R_m	1.8
Rotation rate	Ω	315 rad/s
Global Reynolds number	Re_G	10^5

TABLE 1: Geometric and physical features of Tuliszka annular cavity.

3 LINEAR STABILITY ANALYSIS

In fluid dynamics, a system can be said stable in the sense of Lyapunov [21], if an infinitesimal perturbation on its 'base flow' stays infinitesimal over time or if the perturbed flow stays around the base flow. In addition to telling if a flow is stable or unstable, the main goal of a linear stability analysis is to give the physical features of the response of a little perturbation around the base flow: frequency, amplification rate (also called growth rate), spatial and temporal evolution. This section intends to introduce the main stability notions and the two methods used in this study in the particular case of a rotating flow. The interested reader can find more information about this theory in Drazin and Reid [9]. For both local and global approaches, one can define, $\mathbf{p}$ and $\mathbf{u} = (u_r, u_\theta, u_z)^T$ respectively the pressure and velocity perturbations. While $\mathbf{U} = (U_{b,r}, U_{b,\theta}, U_{b,z})^T$ and P_b stand for the base flow variables such that the global flow $(\mathbf{U}, \mathbf{P})$ can be reconstructed as:

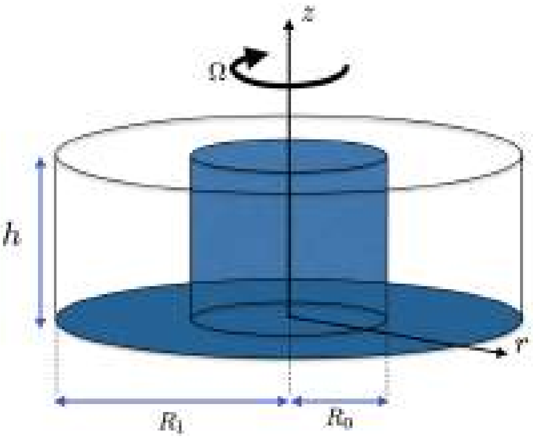

FIGURE 1: Scheme of the academic annular rotor-stator cavity of Tuliszka (Not to scale): 🟦 rotating parts, ⬜ stationnary parts.

$$\begin{cases} \mathbf{U}(r,\theta,z,t) = U_{b,i} + u_i(r,\theta,z,t), \\ \mathbf{P}(r,\theta,z,t) = P_b + p(r,\theta,z,t). \end{cases} \tag{1}$$

The stability of the base flow is obtain by resolving the incompressible Navier-Stokes equations of the perturbation linearized about the base flow. The perturbation evolution is therefore obtained by solving the following differential equations in cylindrical coordinates (r, θ, z) :

$$\begin{gathered} \nabla \cdot \mathbf{u} = 0, \\ \frac{\partial \mathbf{u}}{\partial t} + \nabla \mathbf{u} \cdot \mathbf{U}_b + \nabla \mathbf{U}_b \cdot \mathbf{u} + \nabla \mathbf{p} - \frac{1}{Re_G} \nabla^2 \mathbf{u} = 0, \end{gathered} \tag{2}$$

Where, $\nabla \cdot x$, ∇x and $\nabla^2 x$ denote respectively the divergence gradient and Laplace operators in cylindrical coordinates.

Local stability analysis

Flow stability was particularly difficult to study in the past because of the lack of computation resources or even analytical tools. Hence most of the investigations assumed that the wavelength of the underlying instability mechanism was short compared to the typical scale over which the flow develops along the streamwise direction. Under such an assumption, usually called 'parallel flow', a rotating base flow around an axis z will take the form $(U_{b,i}(z), P_b(z))$.

Normal modes: The set of linearized equations corresponding to eq. (2) are separable in r, θ and t. Hence the perturbations can be represented with a normal mode formulation of the form :

$$[u_r, u_\theta, u_z, p]^T = [i\hat{u}_r, \hat{u}_\theta, \hat{u}_z, \hat{p}]^T(z)exp[(i(\alpha r + m\theta - \omega t)], \quad (3)$$

where $\hat{u}_r$, $\hat{u}_\theta$, $\hat{u}_z$ and $\hat{p}$ stand for the eigenfunctions.

In this case, a given mode is said to be normal because it is considered independent of the other modes of the system. Each mode is hence represented by a pair of parameters (α, ω) with α a complex wavenumber $\alpha = \alpha_r + i\alpha_i$ and ω a complex frequency $\omega = \omega_r + i\omega_i$. With this notation, α_r corresponds to the wavenumber of the perturbation and α_i the amplification rate in space of the mode. A similar physical interpretation of ω can be given *i.e* ω_r represents the real frequency and ω_i the amplification rate in time of the mode. Finally m acts for the azimuthal wavenumber. Modes corresponding to $m = 0$ will be axisymmetric and for $|m| > 0$ modes will show spirals patterns with $m-$arms.

By introducing this normal mode decomposition in the linearized equations, we can obtain a dispersion relation expressed as,

$$D(\omega, \alpha, \hat{q}) = 0. \quad (4)$$

From this expression three types of analyses can be conducted:

Temporal analysis: The purpose of this analysis is to find the complex frequency ω by fixing a real wavenumber ($\alpha \in \mathbb{R}$). In other words, find the response of the flow to an α given spatial excitation. The dispersion problem issues by Eq. (4) can be reduced to the following eigenvalue problem (EVP) :

$$A\hat{q} = \omega B\hat{q}, \quad (5)$$

where $\hat{q} = [\hat{u}_r, \hat{u}_\theta, \hat{u}_z, \hat{p}]^T$ is the problem eigenvector.

The growth of the infinitesimal perturbation $\hat{q}$ is then governed by $\mathfrak{Im}(\omega) = \omega_i$ (imaginary part of ω). Indeed for an $\omega_i > 0$, the base flow is said linearly and locally unstable. The perturbation grows exponentially with time and the contrary for $\omega_i < 0$. In the particular case where $\omega_i = 0$, the base flow will be said neutrally stable and the associated perturbations will not change with time. Temporal analyses are well suited for bounded flows for which located perturbations can't spatially grow. However, even if this type of analysis can give the evolution of a local perturbation in time, it does not provide information about the global behavior of the flows. The term 'global mode', will be widely used in the next sections of this study and is usually referred as a perturbation that evolves in space and time to a point where it impacts the entire flow field (non local).

Spatial analysis: In this case the unknown parameter is the wavenumber α. We look for the response of the flow to time periodic oscillations. Hence by fixing $\omega \in \mathbb{R}$, the dispersion relation (4) becomes a eigenvalue problem with quadratic terms in α formulated as:

$$A\hat{q} = \alpha B\hat{q} + \alpha^2 C\hat{q}. \quad (6)$$

Note that for this specific problem the expression involving $\hat{p}$ does not have terms in α^2 so taking $\phi = \alpha\hat{u}_i$ we can formulate the problem to obtain:

$$\begin{bmatrix} A & 0 \\ 0 & I \end{bmatrix} \begin{bmatrix} \hat{q} \\ \phi \end{bmatrix} = \alpha \begin{bmatrix} B & C \\ -I & 0 \end{bmatrix} \begin{bmatrix} \hat{q} \\ \phi \end{bmatrix} \quad (7)$$

or,

$$A^{'}\tilde{q} = \alpha B^{'}\tilde{q}, \quad (8)$$

with $\tilde{q} = [\hat{q}, \phi]^T$.

Spatial analyses have proven to be very efficient for open flows. The main benefit over temporal analyses is that it enables reconstruction of the a 2D global shape of a global mode. Many studies have been done with this type of analysis during the last decades. One can cite the work of Oberleithner [22] on swirling jet and vortex breakdown or more recenlty the work of Laccasagne [18] on the stability of corner shedding vortices in solid-propellant rockets.

Spatio-temporal analysis: In the two last paragraphs , two types of analyses have been presented, one for bounded flows and one for open flows. In some cases, some spatially developing flows can sustain self-excited global modes without external forcing and characterized by a dominant frequency ω_G. Huerre & Monkewitz [15] have shown that a global mode comes from a region of what we call 'absolute instabilities'. In that case, in order to find such particular instabilities, a spatio-temporal analysis is performed to study the local group velocity of the flow.

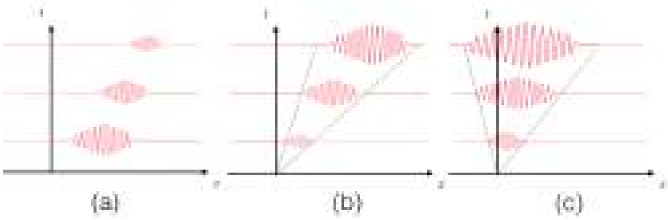

FIGURE 2: The 3 types of responses of a perturbation: (a) Stable, (b) Convectively unstable, (c) Absolutely unstable

Absolute and Convective instabilites

An absolute instability corresponds to a perturbation moving with zero group velocity and is marked by a saddle point of ω in the complex α-plane. In other word, for this type of study, the wavenumber is taken complex ($\alpha \in \mathbb{C}$) and here again one tries to find an eigenvalue ω_0 solution of the following eigenvalue problem:

$$\begin{cases} A\hat{q} = \omega_0 B\hat{q} \\ c = \left.\dfrac{\partial \omega}{\partial \alpha}\right|_{\omega_0} = 0 \end{cases} \tag{9}$$

The sign of the resulting ω_0 will give the behavior and evolution of the local pertubation as shown in the Fig. 2. In the particular case (b) for which $\omega_0 < 0$, the perturbation is amplified and is convected away from its source, the base flow is said convectively unstable (locally). At the opposite, for $\omega_0 > 0$ (c), the perturbation will expand around its local source and perturb all the flow, the base flow is said absolutely unstable (locally).

Construction of a global mode:

The origin of the oscillation or in other words the perturbation which triggers a global mode is usually called the *wavemaker* and is represented by ω_g. The reconstruction of a 2D global mode is a complex process that can be summed up in five steps:

1- Maximum temporal growth rate at X_1: The first step is to do a simple temporal analysis on an arbitrary slice X_1 to find the maximum growth rate $\omega_{max,1}$. Chomaz *et al*. [6] showed that this value will represent the upper part of the absolute instabilities rate at this location.

2- Saddle-point at X_1: The second step is to do a spatio-temporal analysis to find the saddle point at the same slice X_1.

3- Saddle-points at all X: From the saddle point found at X_1, it is possible to track all the saddle points at each X location. The curve $\omega_0(X)$ will represent all the candidates that can be the wavemaker.

4 -Wavemaker $\omega_s(X_s)$: The curve $\omega_0(X)$ is usually fitted around its maximum by a Padé polynomial and extended to the complex X-plane. Cooper *et al*. [7] have shown that this type of polynomial has a good behavior during their expansion in the complex plane. Here again the wavemaker indeed corresponds to the saddle point (Chomaz [6]) that is:

$$\frac{\partial \omega_0}{\partial X}(X_s) = 0, \tag{10}$$

with $\omega_g = \omega_0(X_s)$

5- Reconstruction: Finally a spatial analysis is realized at $\omega = \omega_g$ and the global mode shape is reconstruced by applying the following expression (Huerre *et al* [15]):

$$u_i(r,\theta,x,t) = \Re\left(\hat{u}_i exp\left[i\left(\int_0^r \alpha(\xi)d\xi + m\theta - \omega t\right)\right]\right) \tag{11}$$

with $u_i : [u_r, u_\theta, u_x]$ and $\hat{u}_k$ the eigenvectors $[i\hat{u}_r, \hat{u}_\theta, \hat{u}_x]$ associated to $\alpha(r)$

Global stability analysis

The analysis introduced so far relied on the parallel flow assumptions. Unfortunately for many applications such an assumption does not hold anymore. Weakly non-parallel flow theory has hence been created to go over this problem. As an example the Parabolised Stability Equations (PSE) proved to be efficient to capture simple boundary layers. However, the resulting method was not powerful enough to capture recirculations and boundary detachment flow situations. It is only in the 1980s with the advances in computing science and computing power that the local stability theory has been able to be extended to two dimensional base flows. Pierrehumbert & Widnall [25] performed the first global stability analysis based on the solution of the EVP pertaining to the essentially 2D basic states of shear layer vortices. The interested reader can refer to Theophilis [31] for a complete review of the global stability studies.

Governing Equations:

The construction principle of a global stability analysis remains the same as the local approach. However, one assumes here a 2D base flow such as:

$$\begin{aligned} \mathbf{U} &= (U_{b,r}(r,z), U_{b,\theta}(r,z), U_{b,z}(r,z))^T, \\ P &= P_b(r,z), \end{aligned} \tag{12}$$

and a normal modes decomposition to read,

$$[u_r, u_\theta, u_z, p]^T = [\hat{u}_r, \hat{u}_\theta, \hat{u}_z, \hat{p}]^T(r,z) exp[(i(m\theta - \omega t)], \tag{13}$$

The 2D global modes are hence here obtained directly by resolving an eigenvalue problem. The main drawbacks of this method are the loss of the notion of absolute instability and the possibility to conduct spatial stability analysis.

Boundary conditions: For the global approach as well as the local one (but only at $z = 0$ and $z = h$) Dirichlet conditions are applied on the velocity perturbations $\hat{u}_i$ while Neumann conditions are used for the pressure p.

Sensitivity and Receptivity

As described in the last section, fluid systems can be characterized by their stability behavior. Nevertheless, a simple global analysis is usually not enough to describe the entire flow. In fluid dynamics, adjoint approaches are often used for optimal design methods. It gives indeed new insight in the system and can be interpreted as a sensitivity measure of the flow robustness to changes, an information of importance to design control strategies, for example. In such a context, the direct eigenvalue problem can be reformulated as :

$$\mathscr{L}\hat{q} = \omega\hat{q}, \tag{14}$$

where $\mathscr{L}$ stands for the direct problem operator and $\hat{q}$ the eigenvalue unknown vector. Adjoint modes are hence easily accessed and satisfy the following relation:

$$\mathscr{L}^{+}\hat{q}^{+} = \omega^{*}\hat{q}^{+}, \tag{15}$$

where $\mathscr{L}^{+}$ is the adjoint operator of $\mathscr{L}$ and $\omega^{*} = \Re(\omega) - i\Im\mathfrak{m}(\omega)$,the complex conjugate of ω.
In stability analysis, the adjoint eigenmodes represent the receptivity of the flow. This characteristic has been introduced by Hill [14]. It is usually defined as the response to additive changes to the governing equations, *i.e* modeling external sources of influence (such as free-stream turbulence or wall roughness) or the optimal initial condition which will excite the most global mode. This tool is hence essential for active control.

As a complement to receptivity, the structural sensitivity describes the response to structural changes in the governing equations, while modelling the internal sources of influence (such as base-flow modifications or changes in the geometry). Following the definition given by Giannetti [11], the structural sensitivity is given as the overlap of the direct and adjoint modes:

$$\mathbb{S}(r,z) = \frac{\parallel \hat{q}^{+} \parallel_2 \parallel \hat{q} \parallel_2}{|< \hat{q}^{+}, \hat{q} >|}, \tag{16}$$

where $< \cdot, \cdot >$ denotes the inner product defined as $< a,b >= \int a \cdot b\, dS$ and $\parallel \cdot \parallel_2$ stands for the L_2-norm.

According to Giannetti the location of maximum structural sensitivity will correspond to the greatest drift of the eigenvalues for a given modification of the system. This maximum is usually defined as the trigger of a global mode and can be assimilated to the notion of wavemaker described in the local stability approach.

4 BASE FLOW

Large eddy simulations of the Tuliszka cavity have been conducted recently by Bridel *et al*. in [4]. Self-sustained oscillations of the fluids have been observed in the form of dominant frequencies present in all the cavity. As shown by Arco [8], the stationnary disc has been found unstable to spiral and circular waves whereas the rotor only with the presence of a shaft. Finally, the dynamics of the fluid has been more deeply studied by applying a Dynamical Mode Decomposition. Three main global unstable modes have been observed to drive all the dynamics of the flow. The most unstable mode is defined as the *stator mode* because it is particularly marked around the boundary layer of the stationnary disc ($z = h$). The second global mode is referred as the *rotor mode* for the same reason. The last one is an axisymmetric mode corresponding to an azimuthal wave number of $m = 0$ and will not be studied in the present study. Stability analyses are used here to go deeper in the mechanisms of these instabilities and find its origin. As said previously, in linear stability theory, all analyses have to be done around a base flow solution of the steady Navier Stokes equations. For simple cases, analytical solutions are usually taken. However for more complex flows, the mean flow has proved to be a good substitute to the base flow(Pier [24]). This last choice is still a great subject of debate (Beneddine *et al*. [1]) but out of the scope of the present discussion. Indeed, even if the mean flow is, most of the time, not a solution of the steady Navier-Stokes equations, it still enables to take into account a part of the non-linearities of the flow (Pier [24]).

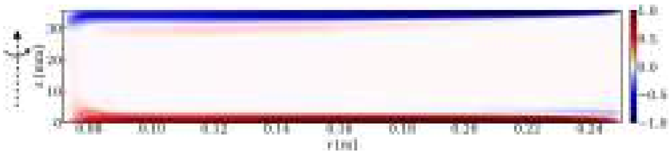

FIGURE 3: 2D Base flow contours : Time and azimuthal averaged LES radial velocity non-dimensionalized by its ∞-norm, $U_{b,r}/max(U_{b,r})$

Following the work of Bridel *et al*. [3], LES results have been time and azimuth averaged to conduct the stability analysis.

Figure 3 presents the 2D profile of the radial velocity that has been used for the global approach. As shown in Figure 4 Good agreement were found with the results of Severac [30] and the auto-similar profile of Owen & Rogers [23].

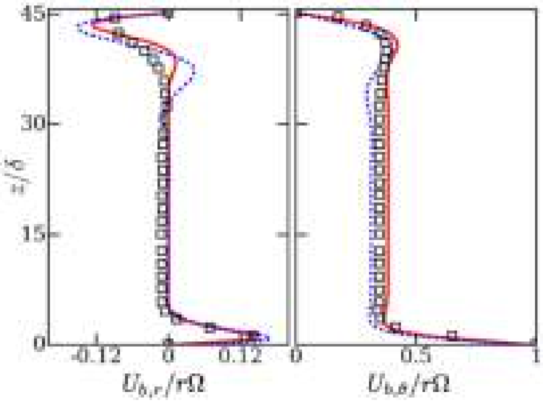

FIGURE 4: Base flow at $r/R_1 = 0.5$: Dimensionless mean radial velocity *(left)*, azimuthal velocity *(right)* with our LES results (—), Severac [30] experiment (□) and Owen & Rogers [23] (- -)

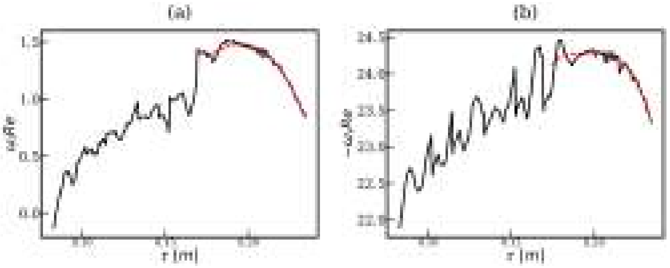

FIGURE 5: Stator mode: Radial evolution of the absolute (a) Temporal amplification $\omega_{0,i}Re$ (b) Temporal frequency $-\omega_{0,r}Re$

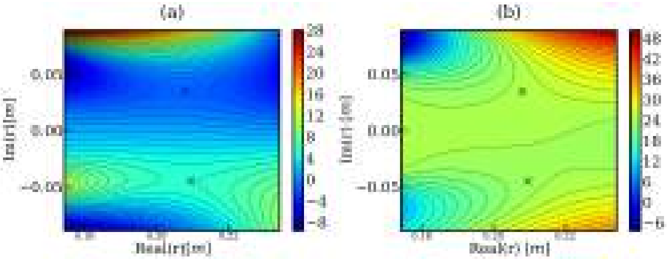

FIGURE 6: Stator mode: Isocontours of (a) absolute amplification $\omega_{0,i}Re$, (b) absolute temporal frequency $-\omega_{0,r}Re$ for the continued function $\omega_0(r)$ in the complex $r-$plane

5 STABILITY RESULTS

Local stability

The local stability analysis has been conducted with the code ***AVLP*** developed by Bridel [3] during his PhD at CERFACS. This code has been implemented to study any kind of axisymmetric flow where the assumption of parallel flow is reasonably valid. The azimuthal numbers $m = 29$ and $m = 12$ have been taken as inputs for the local stability analysis respectively for the stator and rotor modes as evidenced by the LES analysis.

As described in section 3, to reconstruct a global mode with a local stability analysis, 5 steps need to be followed. After finding the maximum temporal growth at mid radius and then the saddle point at the same location, all the saddle points have been found for all radii of the cavity. Results of the intermediate steps are displayed here only for the stator mode. We can note in Figure. 5 that the amplification rate is always greater than 0 which denotes that the flow is absolutely unstable everywhere. At the opposite, the rotor (not shown here) presents few regions of absolute instabilities around the shroud. Following the method first used by Chomaz [6], a Padé polynomial of the form P/Q with P of degree n and Q $n-1$ is used to fit the saddle point curve around the maximum. The resulting red dashed curve in Fig. 5 is found for a degree $n = 16$ for the stator and $n = 13$ for the rotor. Figure 6 corresponds to the expansion of those curves in the complex plane (see section 3) for the stator mode. In case where several saddle points are found, Chomaz [6] shows that the wavemaker will correspond to the eigenvalue with the real part closest to the imaginary axis. This method has been validated by Juniper [17] and applied here for the stator mode. The saddle point here at $r_s = r/R_1 = 0.836$ represents the wavemaker location associated to the stator global mode. By taking F_0 the rotor frequency and by reporting this result on the Figure. 5, a real frequency of $F/F_0 = -\mathfrak{Re}(\omega_G Re)/2\pi F_0 = 3.85$ and a global growth rate of $\mathfrak{Im}(\omega_G Re)/2\pi F_0 = 0.218$ are found at r_s. The DMD of Bridel [3] found a global frequency of the mode $m = 29$ equal to $F/F_0 = 3.6$ which is in good agreement with the present result.

The same process has been applied for the rotor mode. The wavemaker has been identified at the position $r_s = 0.856$ for a global frequency of $F/F_0 = 0.34$ and a growth rate of 0.086. Here again a good agreement is found with the DMD frequency of the mode $m = 12$: $F/F_0 = 0.35$.

Global Stability

The global stability analysis has been conducted with the code ***GIFIE*** developed by Bridel *et al.* [3]. The eigenvalue problem is discretized using FreeFEM++ [13] an open source software tool solving differential equations and performs the finite element method on triangle shaped elements in two dimensions. The resolution of the eigenvalue problem is done with the packaging SLEPc and PETSc. Any kind of incompressible base flow can be studied with this solver and, as for AVLP, has the possibility to run analyses in parallel.

Mapping of the unstable mode

All the azimuthal modes m between 0 and 40 have been computed and analyzed in this first paragraph. Figure 7 *(a)* represents the maximal growth rate found at each m and the frequency in *(b)*. Unlike the local analysis, the global approach finds an unstable mode for almost each azimuthal wavenumbers. However 3 different zones can be identified. The axisymmetric mode $m = 0$, a peak at $m = 11$ and a bump around $m = 30$ which agree with Bridel's DMD (see Table 2). The most unstable mode is found for $m = 35$ but those between 29 and 36 have almost the same growth rate and, as the frequency is increasing linearly with m in this region, we retrieve a 2D global mode with the same shape but shifted in-space. From now, the study will therefore be conducted only on the rotor mode $m = 12$ and $m = 29$ like the local approach to ease the comparison between the two methods.

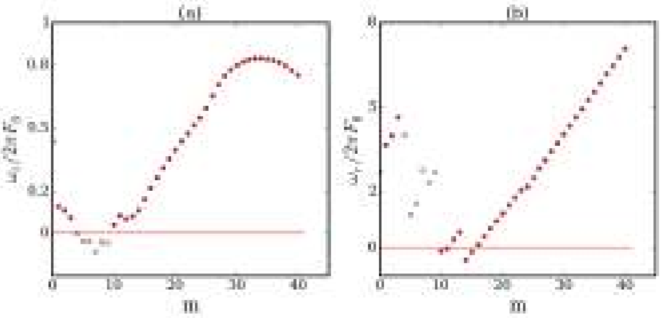

FIGURE 7: Mapping of all the most unstable modes at each azimuthal number m with (a) The temporal amplification $\omega_i/2\pi F_0$ and (b) The temporal frequency $\omega_r/2\pi F_0$

2D Global modes comparison: Figure 9 and 8 show the results obtained for the 3 methods in order DMD (*upper*), local (*middle*) and global (*lower*) approaches respectively for the rotor mode and stator mode. A good agreement is found between the three cases for the stator. In case of the rotor mode, one can see in the Figure 9 (*middle*) that the local stability result has been voluntarily cropped around the hub for $r \in [0, 0.05]$. Indeed around this region a strong recirculation appears to drive the main perturbations and the local approach is violated is this zone. However the results of the rotor mode of the global stability analysis and the DMD are in good agreement and the same dynamics is retrieved. One can especially see that the perturbations for this mode come from the stationnary disk to finally be at its maximun next to the shroud on the rotating disk. This observation highlights that an interaction between the two main modes is inevitable but will not investigated here.The limits of the local approach to analyze complex flows have been made clear.

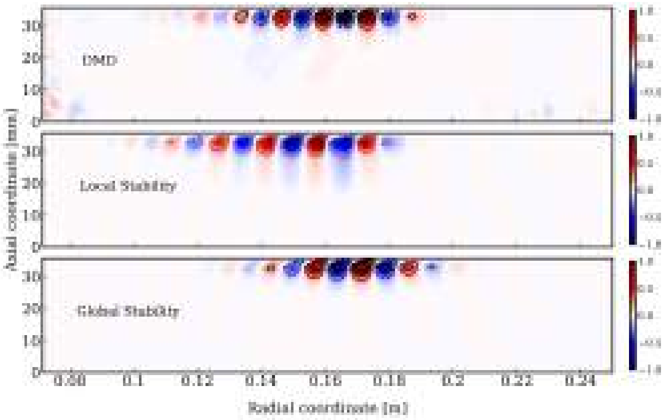

FIGURE 8: 2D shape of stator mode ($m = 29$): axial velocity fluctuations for upper) DMD, *(middle)* Local stability, *(lower)* Global stability

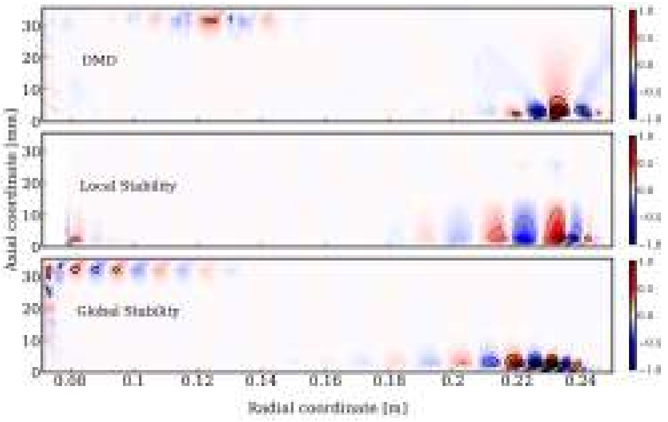

FIGURE 9: 2D shape of rotor mode ($m = 12$): axial velocity fluctuations for upper) DMD, *(middle)* Local stability, *(lower)* Global stability

Receptivity and sensitivity Figure 11 *(upper)* presents the results of the adjoint eigenvalue problem for mode $m = 12$ while Fig. 10 *(upper)* those of the stator. For both modes, the region of maximum receptivity is not located at the same location of maximum amplitude of the direct mode. This phenomenon has been point out by Chomaz [5] and corresponds to a convective non-normality effect. In other word the base flow advection can have a non negligible impact on the modes shape and magnitude.

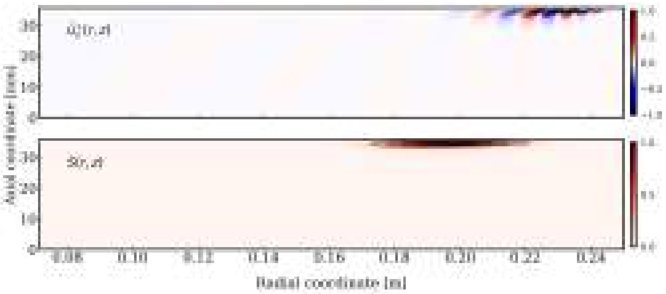

FIGURE 10: Stator mode , *(upper)* receptivity of velocity axial fluctuation $\hat{u}_z^+(r,z)$, *(lower)* Structural sensitivity $\mathbb{S}(r,z)$

At the end, the receptivity of the axial velocity of the stator mode shows that to force or control a global mode at first order, harmonic pulsations need to be introduced near the shroud on the stationary disk. The analysis of the receptivity is done here for the axial velocity but the same study could be realized on the pressure and the others velocity components but are not treated here.

Figure 11 *(lower)* and 10 *(lower)* present respectively the structural sentivity of the rotor and the stator mode. The sensitivity maximum for the rotor mode is unexpectedly located on the stationary disk at $(r,z) = (0.133, 0.0345)$ whereas for the stator mode, it is located not far from the shroud on the stationary disk $(r,z) = (0.195, 0.034)$. The rotating disk seems to be the source of the two main unstable modes and this result tends to confirm the amplification of the rotor mode along the hub before to reach its maximum amplitude in this limit cycle.

6 CONCLUSION

Flow instabilities can have a real impact in the structural integrity of turbomachinary components. Their control is a primary subject but a better understanding of how they work is first mandatory. Our study was focused on "the pressure bands " phenomenon which can be retrieved in academic annular cavities. Through the now well known cavity of Tuliszka, this work aimed to, first, compare local and global stability approaches but also to improve our understanding of rotating flows on rotor/stator cavity. Table 2 sums up the results obtained during our study and good agreement between the local analysis, global analysis and the dynamic mode decomposition of [3] are found. For the stator, the global 2D shape is well reproduced and the wavemaker found in both stability analyses coincide precisely. In case of the rotor, the two approaches have predicted a reasonably good shape of the global mode near the shroud but the local approach has naturally difficulties next to the hub where a recirculation of the flow is present. The wavemaker has been localized near the shroud whereas the global approach found it more near the hub. The global approach has furthermore given new insight on the source of the rotor mode by combining those results with sensitivity analyses. At the end, the literature and our study on the academic cavity have shown clearly the limits of a local stability analysis. In fact, the parallel flow assumption does not enable to retrieve exactly the shape of a global mode in zones where the base flow is particularly complex. The two methods present two different ways to find the trigger of a global mode. However, the process in case of a local approach relies on complex mathematical concepts and needs rigorous attention to be able to retrieve the good results. In terms of control, the receptivity and the sensitivity analyses are clearly interesting tools. With the global approach, the results showed a good agreement with the literature and confirmed that the global modes come from the boundary

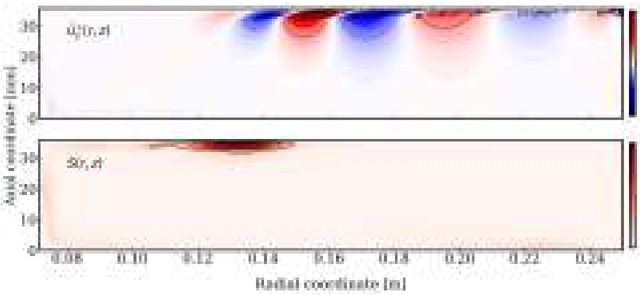

FIGURE 11: Rotor mode , *(upper)* receptivity of velocity axial fluctuation $\hat{u}_z^+(r,z)$, *(lower)* Structural sensitivity $S(r,z)$

	GIFIE		AVLP		DMD	
Mode	Rotor	Stator	Rotor	Stator	Rotor	Stator
$\omega_r Re/(2\pi F_0)$	0.304	3.72	0.34	3.85	0.35	3.6
$\omega_i Re/(2\pi F_0)$	0.070	0.740	0.086	0.218	not comparable	
r/R_1 at $\mathbb{S}_{max}$	0.524	0.784	0.856	0.836	-	-

TABLE 2: Sum up of the stability results compared to DMD. Dimensionless frequency, amplification and wavemaker

layers. However an adjoint mode with a local approach would involve complicated mathematical concepts and so has not been addressed in the present study. Finally if the global approach seems to be the most promising method, the local approach can not be forgotten. The notion of absolute instability gives indeed a lot of physical insights that we can not retrieve with the global approach.

ACKNOWLEDGMENT

The first author was partly supported by a grant from CNES and Ariane Group. We would like to thank Ariane Group and CNES for the PhD opportunity and their scientific investment in the project. Parts of the computations have been carried out on the IBM x3570 supercomputer at the IDRIS (CNRS, Orsay, France) computing centre (program 100191), and on the BullX B720 cluster at the CINES (MESR, Montpellier, France) computing centre (program fac6074).

REFERENCES

[1] Beneddine, S., Sipp, D., Arnault, A., Dandois, J., and Lesshafft, L. Conditions for validity of mean flow stability analysis. *Journal of Fluid Mechanics 798* (2016), 485–504.

[2] Bödewadt, U. T. Die Drehströmung über festem Grunde. *Zeitschrift für Angew. Math. und Mech. 20*, 5 (1940), 241–253.

[3] Bridel-Bertomeu, T. *Doctorat de l'université de toulouse*. PhD thesis, CERFACS, 2016.

[4] Bridel-Bertomeu, T., Gicquel, L., and Staffelbach, G. Large scale motions of multiple limit-cycle high Reynolds number annular and toroidal rotor/stator cavities. *Physics of Fluids 29*, 6 (2017).

[5] Chomaz, J.-M. Global instabilities in spatially developing flows: Non-Normality and Nonlinearity. *Annu. Rev. Fluid Mech. 37*, 1 (2005), 357–392.

[6] Chomaz, J.-M., Huerre, P., and Redekopp, L. G. A frequency selection criterion in spatially developing flows. *Stud. Appl. Math. 84* (1991), 119–144.

[7] Cooper, A. J., and Crighton, D. G. Global modes and superdirective acoustic radiation in low-speed axisymmetric jets. *Eur. J. Mech. B/Fluids 19*, 5 (2000), 559–574.

[8] Crespo del Arco, E., Serre, E., Bontoux, P., and Launder, B. Stability , transition and turbulence in rotating cavities. In *Instabilities of Flows*, M. Rhaman, Ed. WIT PRESS, 2005, pp. 141–195.

[9] Drazin, P. G., and Reid, W. H. *Hydrodynamic stability*. 2004.

[10] Ekman, V. W. On the influence of the Earth's rotation on ocean currents. *Ark. för Mat. Astron. och Fys. 2* (1905), 1–53.

[11] Giannetti, F., and Luchini, P. *Structural sensitivity of the first instability of the cylinder wake*, vol. 581. 2007.

[12] Healey, J. J. Enhancing the absolute instability of a boundary layer by adding a far-away plate. *J. Fluid Mech. 579* (2007), 29–61.

[13] Hecht, F. New development in freefem ++. *Journal of Numerical Mathematics 20*, 3 (2012), 251–265.

[14] HILL, D. A theoretical approach for analyzing the restabilization of wakes. *30th Aerospace Sciences Meeting and Exhibit*, April (1992).

[15] Huerre, P., and Monkewitz, P. a. Local and Global Instabilities in Spatially Developing Flows. *Conference on Boundary Layer Concepts in Fluid Mechanics 22* (1990), 473–537.

[16] Itoh, M. On the instability of the flow between coaxial rotating disks. In *Bound. Layer Stab. Transit. to Turbul. ASME FED* (1991), vol. 114, pp. 83–89.

[17] Juniper, M. P. The local and global stability of confined planar wakes at intermediate Reynolds number. *J. Fluid Mech.* (2011), 218–238.

[18] Lacassagne, L. Simulations et analyses de stabilité linéaire du détachement tourbillonnaire d'angle dans les moteurs à propergol solide. *Ph.D.thesis Institut National Polytechnique de toulouse* (2017).

[19] Lingwood, R. J. Absolute instability of the boundary layer on a rotating disk. *J. Fluid Mech. 299* (1995), 17–33.

[20] Lopez, J. M., and Weidman, P. D. Stability of stationary endwall boundary layers during spin-down. *J. Fluid Mech. 326* (1996), 373–398.

[21] Lyapunov, A. M. The general problem of the stability of motion. *International Journal of Control 55*, 3 (1992), 531–534.

[22] Oberleithner, K. *On Turbulent Swirling Jets: Vortex Breakdown, Coherent Structures, and their Control*. PhD thesis, Technische Universit{ä}t Berlin, 2012.

[23] Owen, J. M., and Rogers, R. H. Flow and Heat Transfer in Rotating Disc Systems, Volume 1 : Rotor-stator systems, 1989.

[24] Pier, B. On the frequency selection of finite-amplitude vortex shedding in the cylinder wake. *Journal of Fluid Mechanics 458*, May 2002 (2002).

[25] Pierrehumbert, R, T., and Widnall, E. The two- and three-dimensional instabilities of a spatially periodic shear layer.

[26] Sagaut, P. *Large eddy simulation for incompressible flows*. Springer, 2002.

[27] Sagaut, P., and Deck, S. Large-eddy simulation for aeronadymics: status and perspectives. *Phil. Trans. R. Soc. Lond. 367* (2009), 2849–2860.

[28] Schmid, P. J. Dynamic mode decomposition of numerical and experimental data. *J. Fluid Mech. 656* (2010), 5–28.

[29] Schouveiler, L. Instabilities of the flow between a ro-

tating and a stationary disk. *J. Fluid Mech. 443* (2001), 329–350.

[30] SÉVERAC, É., PONCET, S., SERRE, É., AND CHAUVE, M. P. Large eddy simulation and measurements of turbulent enclosed rotor-stator flows. *Phys. Fluids 19*, 8 (2007), 1–47.

[31] THEOFILIS, V. Global Linear Instability. *Annual Review of Fluid Mechanics 43*, 1 (2011), 319–352.

[32] TULISZKA, E., SERRE, E., AND BONTOUX, P. On the nature of the boundary layers instabilities in a flow between a rotating and a stationary disc. *Comptes Rendus Mécanique 330*, 2 (jan 2002), 91–99.

[33] TULISZKA-SZNITKO, E., AND SOONG, C. Y. Instability of non-isothermal flow between coaxial rotating disk. In *Eur. Congr. Comput. Methods Appl. Sci. Eng.* (2000).

[34] VON KÁRMÁN, T. Über laminare und turbulente reibung. *Zeitschrift für Angew. Math. und Mech. 1*, 4 (1921), 233–251.

Appendix F

Linear stability models comparison

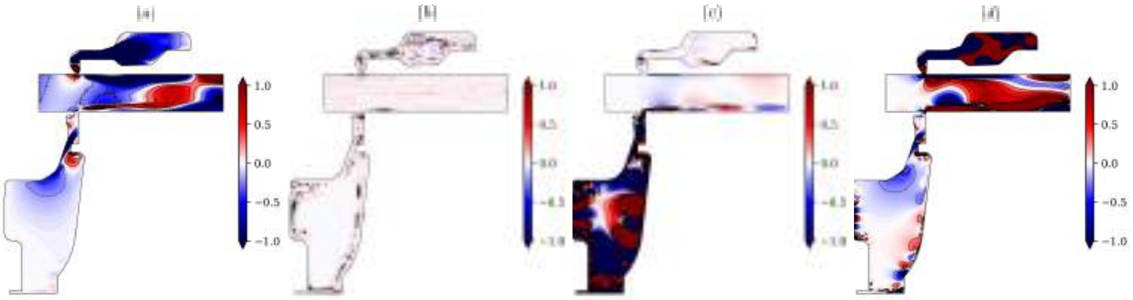

Figure F.1 – Stability model comparison: (a) Mode $F/F_0 = 4.85$ obtained with DMT (b) Mode $(F/F_0, m) = (4.69, 4)$ $\nu = \nu_l$, (c) Mode $(F/F_0, m) = (4.53, 4)$ $\nu = \nu_l + \nu_{SGS}$, (d) Mode $(F/F_0, m) = (4.69, 4)$ $\nu = \nu_l + \nu_{SGS} + \nu_e$

This appendix presents a comparison of the 3 stability models tested on the turbopump cavity. Only results of the $m = 4$ mode is presented here. DMT result obtained for the frequency $F/F_0 = 4.85$ presented Fig. F.1(a) is taken as the reference. Note that this turbopump mode being complex the $m = 4$ contribution has been extracted from DMT thanks to a Fourier decomposition as realized in Sec. 4.4.2. Fig. F.1(b) was obtained with the exactly same model used for the academic cavity in Chapter 4, Fig. F.1(c) was obtained with the same model as Fig. F.1(b) with the addition of the subgrid model viscosity ν_t. Finally Fig. F.1(c) presents the last results obtained with the model introduced in Sec.6.6.1. Contrary to the academic case the subgrid viscosity is none negligible in the turbopumps LES. The addition of this component to the stability equations acts as a numerical instabilities cleaner. However one can see even though the global mode shape has been improved the highest amplitudes modes were retrieved in the low cavity contrary to the DMT results. Furthermore the separation of rotating boundary layers in the vein is still not well predicted. Finally, the addition of the coherent viscosity help improving the ratio of amplitudes of the modes between the lower ccavity and the vein. Furthermore as shown Fig. 6.18(c) this viscosity marked particularly the upper boundary layer of the vein and as consequence help improving its separation shape.

Résumé court

Cette thèse présente une étude détaillée sur le phénomène de 'bandes de pression' connu pour être dangereux pour les turbopompes de moteur cryogénique. Ce phénomène, particulièrement difficile à prédire numériquement, apparait en particulier dans les cavités de type rotor/stator sous forme de spirales et d'anneaux dans les couches limites tournantes. Dans ce travail, les avantages des Simulations des Grandes Echelles (SGE) et Analyses Globales de Stabilité Linéaire (GLSA) sont utilisés pour mettre en avant l'origine des oscillations de ces écoulements. Deux configurations sont présentement étudiées : une cavité de type rotor/stator académique et une turbine de type industriel de turbopompe. Dans les deux cas, la SGE munie d'outils de post-traitement adaptés, a permis de retrouver les structures cohérentes de ces écoulements, aussi appelées modes d'écoulement, dictant toute la dynamique de ces cavités. Dans le cas de la configuration académique, la GLSA a permis de trouver l'origine de chaque mode ainsi que de proposer des stratégies de contrôle de ces écoulements. L'utilisation de systèmes d'aspiration et de soufflage se sont montrés être les solutions les plus optimales pour supprimer le phénomène de bandes de pression et ont été validés à travers une SGE.

Short abstract

This thesis provides a detail investigation of the 'pressure band phenomenon' known to be dangerous for space turbopumps. This specific phenomenon appears in rotor/stator cavities under the form of spiral or annular patterns in rotating boundary layers and is difficult to predict numerically. In the present work, the conjunction of Large Eddy Simulations (LES) and Global Linear Stability Analysis (GLSA) is used to give more insight on these oscillatory motions of the flow. Two specific configurations are studied: Academic smooth rotor/stator cavities and a real industrial turbine. In both cases, LES with dedicated post-processing tools enables to retrieve the coherent flow structures also referred to as flow modes driving each cavity. In case of the academic cavity, GLSA reveals the origin of each mode and possible control strategies. Suction and injection through the stationary disk show to be the more optimal solutions to suppress the pressure band phenomenon and were validated through a LES.